THE CONTROL OF BOUNDARY LAYERS AND CHANNEL FLOWS USING PLASMA ACTUATORS

By

PAUL MARKEY RIHERD II

A DISSERTATION PRESENTED TO THE GRADUATE SCHOOL
OF THE UNIVERSITY OF FLORIDA IN PARTIAL FULFILLMENT
OF THE REQUIREMENTS FOR THE DEGREE OF
DOCTOR OF PHILOSOPHY

UNIVERSITY OF FLORIDA

2013

I dedicate this to my family and my fiancée, for always being patient with me.

ACKNOWLEDGMENTS

There are many people that should be thanked for their assistance and insight as I have worked and researched at the University of Florida. I would like to thank Dr. Subrata Roy for his guidance and endless patience with me as a student. I would also like to thank Drs. Miguel Visbal and Don Rizzetta for their support during the several summers I spent working with them at AFRL in Ohio. Similarly, I would like to thank Steve Wilkinson for the chance to learn and work at NASA at LaRC in Virginia for a summer.

I would also like to thank the many other graduate students at APRG for making it such a unique and welcoming place to work. In particular, I would like to thank Ryan Durscher, Chin-Cheng Wang, Tomas Houba, Ariel Blanco, and Navya Mastanaiah for the multitude of conversations, lunches, and shared problem solving that led to this point.

This work would also not be possible without the support of UF's High Performance Computing center. The help provided to me by Charles Taylor and Craig Prescott has been essential in the writing and running of codes in this research.

Finally, I would like to thank my family and my fiancée, Megan Wallis, for their endless patience as I slowly moved through graduate school. Their support in particular has made the difficulties of graduate school much easier to bear.

TABLE OF CONTENTS

page

CHAPTER

APPENDIX

LIST OF TABLES

LIST OF FIGURES

Abstract of Dissertation Presented to the Graduate School
of the University of Florida in Partial Fulfillment of the
Requirements for the Degree of Doctor of Philosophy

THE CONTROL OF BOUNDARY LAYERS AND CHANNEL FLOWS USING PLASMA ACTUATORS

By

Paul Markey Riherd II

December 2013

Chair: Subrata Roy
Major: Mechanical Engineering

Dielectric barrier discharge actuators can be used to control boundary layer and channel flows. These actuators introduce a body force to the flow, adding momentum and vorticity in a beneficial manner for control purposes. The key contributions of this study are an increased understanding of how plasma actuators can be used to modify the stability properties of a laminar boundary layer, characterization of how serpentine geometry plasma actuators can be used to generate boundary layer streaks, and an exploration the bulk flow properties and flow structure of plasma driven channel flows.

Linear stability analyses of a plasma modified boundary layer have been performed, indicating that plasma actuators can be used to stabilize or destabilize a laminar boundary layer, depending on the magnitude and orientation of the actuator. The local and global stability properties of plasma modified boundary layers have been characterized, and evidence for additional instability modes has been discovered. It is also shown through numerical simulations that when the electrode geometry of these actuators is modified in a sinuous manner, boundary layer streaks can be generated, opening additional avenues for control using this class of actuators. The use of these actuators to drive a channel flow is demonstrated experimentally. Empirical relationships are drawn, based upon the data collected. Characterization of these channel flows is also performed using numerical simulations and experimental techniques.

CHAPTER 1
INTRODUCTION

Fluid flow is present in many of the technologies and natural phenomena that are used and experienced everyday by individuals worldwide, as well as in the components of the physical infrastructure required for a modern world. The range of phenomena which comprise fluid flow is incredibly diverse and is present on the length scales ranging from the mean free path between colliding gas molecules up to the size of galaxies. On a more tangible scale, the flow of gases and liquids are important to many modern technologies. These flows comprise the movement of water and fuel in pipes and around cars, planes, boats, and trains as they move people and goods from one location to the next.

While many of these technologies involving fluid flow work adequately without any adjustments, there may be significant gains to be made by using passive and active methods of flow control to manipulate these flows. The motivation for implementing flow control within these technologies is for more optimal devices, by making them more energy efficient, more reliable, expanding the envelope of operating conditions, or generally pushing the technologies under consideration towards a more desired state. In particular, though a wide variety of passive and active flow control devices exist (Cattafesta & Sheplak, 2011), plasma based control devices have shown promise for flow control applications.

In this study, several facets of flow control are examined. One aspect of flow control that is examined is the control of the laminar to turbulent transition process of simple flows using Dielectric Barrier Discharge (DBD) plasma actuation. The final goal of the applied flow control will be to either accelerate or delay the onset of transition and the flow becoming turbulent. Either result may be desired, depending on the circumstances of the flow and the goals of the applied control. An application for a relatively new class of plasma actuator (i.e. the serpentine geometry plasma actuator) is also examined. This particular type of actuator is intended to be more versatile than the standard geometry actuator, and the potential for this type of actuator geometry to generate boundary layer streaks for the control of laminar boundary layers is explored. Another aspect of control that is examined is the application of DBD plasma actuators to drive low speed channel flows. The intended impact of this examination is to develop small devices which can pump fluid for heat and mass transfer applications in small environments.

DBD actuators have been successful in demonstrating flow control in laboratory scale experiments and numerical simulations. To speak generally, this class of actuators possesses a very broad range of applicability. In addition to the multitude of applications for DBD devices, trends and relationships regarding the behavior of the body force, flow fields, power consumption, and performance characteristics have been examined, which can be found in the many reviews of these devices (Corke *et al.*, 2010; Moreau, 2007; Roth *et al.*, 1998, 2000; Wang *et al.*, 2013). There is extensive literature examining the effectiveness of these actuators for separation control over humps (Rizzetta & Visbal, 2010; Schatzman & Thomas, 2008) and airfoils (Greenblatt *et al.*, 2008; Post & Corke, 2004; Rizzetta & Visbal, 2007, 2011). Drag reductions, noise control, and vortex shedding control have also been examined for blunt bodies (Jukes & Choi, 2009; Rizzetta & Visbal, 2009; Sung *et al.*, 2006). Laminar and turbulent boundary layer control have been examined, including uses of these actuators for closed (Grundmann & Tropea, 2008*a*,*b*, 2009) and open loop (Duchmann *et al.*, 2013*a*, 2012, 2010, 2013*b*; Gibson *et al.*, 2012; Grundmann & Tropea, 2009) hydrodynamic stability control. While the applications have typically been limited to flows of less than 50 m/s, there are some studies which indicate that these actuators have been used for supersonic flow control (Im *et al.*, 2010; Schuele, 2011), where the freestream flow velocities have been upwards of 700 m/s.

Some of the benefits of DBD plasma actuators are that they have extremely quick response times (on electronic, rather than mechanical time scales (Corke *et al.*, 2010)), they can be constructed in a way so that they are surface compliant (and should have no impact on the flow when they are not active or act as a type of surface roughness (Corke *et al.*, 2010)), they can be pulsed and duty cycled at a wide bandwidth of frequencies (which offers an opportunity to use these actuators to instigate certain instabilities, such as the Tollmien-Schlichting wave (Riherd & Roy, 2013*c*; Rizzetta & Visbal, 2011; Visbal *et al.*, 2006; Visbal, 2010)), among other benefits. The downsides of this type of devices are that they are not very energy efficient and that they have only limited control authority. The benefits of these actuators suggest that they can be used for some very specialized flow control applications, but the downsides limit what these applications can be, especially from the perspective of economic feasibility.

Going forward in this field, there are a number of obstacles that must still be overcome in the development of these actuators and their applications, including improving the efficiency of these actuators in the context of fluid dynamics. Kriegseis *et al.* (2013*b*) predicts that for there to be an overall power savings using these actuators, the effect on the flow must be amplified many times over the power actually delivered to the flow by the actuators. This necessary amplification must overcome the extremely low efficiency of the actuators in delivering power to the flow, as it is predicted that only about 0.1% of the power supplied to the actuator reaches the flow. There are significant losses in power due to the ionization process and weak momentum transfer between the charged particles in the plasma and the uncharged particles in the gas. This exceedingly low efficiency drives the need for innovative applications that take advantage of the flow's natural reaction to modification by plasma actuation, otherwise net power savings will not be feasible. Without these improvements in performance, this type of plasma actuator may not become economically feasible for wider use.

The performance of these actuators at ground testing conditions appears to work in many experimental settings, but there are physical limitations to the stability of the plasma discharge as these devices are operated at higher and higher voltages (Durscher *et al.*, 2012). Beneficially, this effect appears to be temperature and pressure dependent, and ground testing conditions are suggested to be highly non-ideal. Rather, flight conditions appear to be more appropriate for the operation of these plasma actuators due to the decreased temperature and pressure, which allow for a greater discharge (Soni & Roy, 2013; Valerioti & Corke, 2012), even though there is a drop in actuator performance when the freestream velocity is increased (Kriegseis *et al.*, 2013*a*).

The objective of this dissertation is to present research exploring how plasma actuation can be applied to control boundary layer and channel flows. The results of this work add to the existing literature regarding the use of these actuators for flow control and indicate the versatility of these actuators continues to expand. The key findings from this work are that DBD plasma actuators have the potential to modify the stability of laminar boundary layers, delaying or accelerating the onset of turbulence, depending on how they are oriented. In particular the effects of flow-wise actuation have been examined, and it is shown the two instabilities important to laminar boundary layers, Tollmien-Schlichting waves and boundary layer streaks, are stabilized. Furthermore, the flow fields generated by the use of serpentine plasma actuators in laminar boundary layer have also been characterized. From this characterization, it is found that these actuators can generate boundary layer streaks. While these streaks are normally considered an instability, when they are introduced very carefully to a flow field, they can be used to stabilize or destabilize the flow, indicating that this type of actuator could be used for multiple flow control applications. Finally, the application of using DBD actuators to drive small scale channel flows has been examined using experimental methods and numerical simulations. The system properties and the flow structure of these channels have been examined.

This dissertation is structured in the following manner. In Chapter 2, the relevant fluid mechanics are reviewed. The effects of using steady, linear geometry plasma actuation for the control of the hydrodynamic stability of laminar boundary layers are considered using local stability analysis in Chapter 3. Furthermore, the local stability problem is expanded upon using a model of a boundary layer modified by plasma actuation, allowing for a more rapid analysis of the boundary layer stability. A foundation for studying this problem in a two-dimensional environment is also established. In Chapter 4, the framework for studying the effects of plasma actuation on two-dimensional boundary layers is expanded upon. A method of bi-global stability analysis is presented, and two different instability mechanisms are examined. With the use of flow wise oriented plasma actuation, stabilization of both instability mechanisms is predicted numerically. Plasma actuators with complex, serpentine geometries are examined for their potential role in laminar boundary layer flow control in Chapter 5. The flow fields generated by this type of plasma actuation are characterized, and motivation for examining their stability properties for transition control is also presented. The concept of a “plasma channel” is introduced in Chapter 6. Experimental results are presented demonstrating its effectiveness and characterizing the bulk flow properties of a finite length channel. In Chapter 7, the plasma channel concept is further extended. Properties inside of the channel are characterized and discussed, rather than the bulk flow properties. Numerical simulations and experimental validation are performed in order to study the flow inside of the channel. Finally, a summary and conclusions of the completed research are presented in Chapter 8.

CHAPTER 2
OVERVIEW OF RELEVANT FLUID MECHANICS

The flow of liquids and gases can become extremely complicated, depending on the density and temperature of the fluid, as well as the length and time scales involved. For a majority of the flows relevant to modern technologies and phenomena experienced by individuals, a continuum model of fluid dynamics (i.e. the compressible Navier-Stokes equations) can be used (White, 2006). For the compressible Navier-Stokes equations, the continuity, momentum, and energy equations for the fluid are

$$\frac{\partial \rho^*}{\partial t^*} + u_i^* \frac{\partial \rho^*}{\partial x_i^*} + \rho^* \frac{\partial u_i^*}{\partial x_i^*} = 0 \tag{2–1a}$$

$$\rho^* \left(\frac{\partial u_i^*}{\partial t^*} + u_j^* \frac{\partial u_i^*}{\partial x_j^*} \right) = -\frac{\partial p^*}{\partial x_i^*} + \frac{\partial \tau_{ij}^*}{\partial x_j^*} + f_i^* \tag{2–1b}$$

$$\rho^* \left(\frac{\partial h^*}{\partial t^*} + u_i^* \frac{\partial h^*}{\partial x_j^*} \right) = \frac{\partial p^*}{\partial t^*} + u_j^* \frac{\partial p^*}{\partial x_j^*} + \frac{\partial}{\partial x_i^*} \left(k^* \frac{\partial T^*}{\partial x_i^*} \right) + \tau_{ij}^* \frac{\partial u_i^*}{\partial x_j^*} + u_i^* f_i^* \tag{2–1c}$$

where * indicates dimensional values. x_i represents the Cartesian coordinate system, u_i represents the components of the velocity vector, τ_{ij} represents the shear stress tensor, and p, h, T and ρ represent the pressure, enthalpy, temperature, and density. f_i represents the body force vector. In terms of the physical coefficients, μ and λ represent the dynamic and bulk viscosities, while k represents the thermal diffusivity. The enthalpy of the fluid is defined as

$$h^* = e^* + \frac{p^*}{\rho^*} \tag{2–2}$$

where e is the internal energy density. The shear stresses on the fluid are defined as

$$\tau_{ij} = \mu^* \left(\frac{\partial u_i^*}{\partial x_j^*} + \frac{\partial u_j^*}{\partial x_i^*} \right) + \delta_{ij} \lambda^* \frac{\partial u_j^*}{\partial x_j^*} \tag{2–3}$$

where δ_{ij} is the Dirac delta function. To close this system, an equation of state is necessary. For gases, the ideal gas law is often used, which is

$$p^* = \rho^* R^* T^* \tag{2–4}$$

where R is the individual gas constant, which depends on the molecular weight of the gas.

For the present study, the flows under investigation are of relatively low velocity and possess only small variations in density. As such, it is assumed that they can be modeled using an incompressible, continuum model of fluid mechanics. While this assumption filters out a great deal of what is possible in the broader sense of fluid mechanics, it will still capture the essential physics of the problems under investigation. These assumptions allow for the flows to be examined using the Incompressible Navier-Stokes (INS) equations, which only involves the velocity fields and the pressure in the domain and are defined using index notation as

$$\frac{\partial u_i^*}{\partial x_i^*} = 0 \tag{2–5a}$$

$$\frac{\partial u_i^*}{\partial t^*} + u_j^* \frac{\partial u_i^*}{\partial x_j^*} = -\frac{1}{\rho^*}\frac{\partial p^*}{\partial x_i^*} + \nu^* \frac{\partial^2 u_i^*}{\partial x_j^{*2}} + \frac{f_i^*}{\rho^*} \tag{2–5b}$$

The fluid's density (ρ) and kinematic viscosity (ν) are assumed to be constant. Non-dimensionalizing the flow field by its characteristic length (L) and velocity scales (u_∞), such that

$$u = \frac{u^*}{u_\infty^*} \qquad x_i = \frac{x_i^*}{L^*} \qquad p = \frac{p^*}{\rho^* u_\infty^{*2}} \qquad t = \frac{t^* L^*}{u_\infty^*} \qquad f_i = \frac{f^*}{\rho^* u_\infty^{*2}} \tag{2–6}$$

it can be found that for most incompressible flows, only a single non-dimensional parameter is necessary, the Reynolds number (Reynolds, 1883), which is defined as

$$Re = \frac{u_\infty^* L^*}{\nu^*} \tag{2–7}$$

Using this non-dimensionalization, the INS equations can be recast as

$$\frac{\partial u_i}{\partial x_i} = 0 \tag{2–8a}$$

$$\frac{\partial u_i}{\partial t} + u_j \frac{\partial u_i}{\partial x_j} = -\frac{\partial p}{\partial x_i} + \frac{1}{Re}\frac{\partial^2 u_i}{\partial x_j^2} + f_i \tag{2–8b}$$

This simplified model of the fluid mechanics is restricted to low speed flows with negligible density variations, but those are the conditions expected in the present work. Even under these “limited” conditions, a wide variety of physical phenomena have been documented.

Fluid flows can largely be classified into three distinct categories, laminar, transitional, and turbulent. Reynolds (1883) was the first to make a scientific distinction of this type. He did so by using dye to visualize the motion of fluid in a pipe, observing that the flow in the pipe appeared “direct” (laminar) at low velocities, but “sinuous” (turbulent) at higher velocities.

The simplest flows are laminar flows, of which there are a number of exact solutions to the Navier-Stokes equations. These laminar flows are characterized as consisting of a relatively simple flow structure, the streamlines of these flows are largely parallel. In a laminar flow, if any vortical structures exist, then they exist at discrete time and length scales. Turbulent flows are quite the opposite, being highly unsteady, random (often chaotic), and possessing a range of vortical structures that can exist on a discrete and continuous range of time and length scales. These flows have traditionally been studied using statistical methods. In more recent decades, with the advent of high quality experimental methods, such as Particle Image Velocimetry (PIV), and improvements in the scale and accuracy of Computational Fluid Dynamics (CFD) methods, the individual structures in a turbulent flow have also garnered attention. Comparatively less explored transitional flows occupy an intermediate place between laminar and turbulent flows and are subject to a wide range of phenomena. These flows will be dicussed in greater detail in Section 2.3.

2.1 Boundary Layer Flows

Boundary layer flows are those which impose high levels of shear stress near a no-slip boundary condition along a surface (i.e. $u_i = 0$). This is in contrast to free shear layers, such as jets and plumes which exhibit concentrations of shear stress, but do not involve a no-slip condition. Fluid movement through pipes, channels, and around flat surfaces are examples of boundary layer flows. However, over time, unless otherwise specified, the term boundary layer flow has taken on the meaning of a spatially developing, semi-bounded flow with a no-slip surface on one side, a freestream velocity far from this surface, and spanning some distance in the directions parallel and span-wise normal to the flow.

At low Reynolds numbers, incompressible, boundary layer flows are well described by the Falkner-Skan-Hartree (FSH) similarity solution (Falkner & Skan, 1931; Hartree, 1937). A special case of the FSH boundary layers is the Blasius boundary layer, which describes the flow over a flat plate with no pressure gradient (i.e. a plate is perfectly aligned with an oncoming flow) and no cross flow components. For boundary layers, there are three heights which are considered important (Figure 2-1). The 99% height ($\delta_{99\%}$) defines the outer range of the boundary layer. The displacement height (δ^*) describes the virtual change to the surface geometry due to the boundary layer displacing fluid. Finally, the momentum height (θ) is also important, as it's the streamwise rate of change ($\frac{d\theta}{dx}$) is directly tied to the skin friction on a flat surface. These boundary layer heights are defined as

$$\delta_{99\%} = y|_{u(y)=0.99} \tag{2–9a}$$

$$\delta^* = \int_0^\infty \left(1 - \frac{u\left(y\right)}{u_\infty}\right) dy \tag{2–9b}$$

$$\theta = \int_0^\infty \frac{u\left(y\right)}{u_\infty} \left(1 - \frac{u\left(y\right)}{u_\infty}\right) dy \tag{2–9c}$$

At higher Reynolds numbers, a boundary layer will eventually become turbulent (Figure 2-2). Even though there is no exact solution to the Navier-Stokes equations describing a turbulent boundary layer, there is still a high degree of similarity between turbulent boundary layers at varying Reynolds numbers. Examples include the turbulent flows in pipes and channels (Nagib & Chauhan, 2008). With turbulent boundary layers, there are additional velocity, length, and time scales, based on the shear stress at the

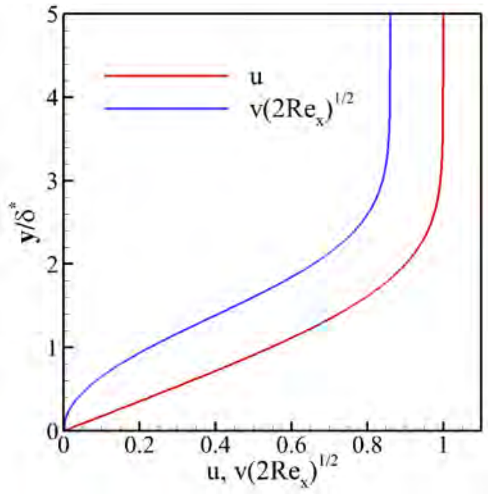

Figure 2-1. Blasius boundary layer velocity profile for the streamwise and wall normal velocities. Calculated using Blasius boundary layer equations (White, 2006).

wall. The dimensional (*) and non-dimensional forms of these scales are

$$u_\tau^* = \sqrt{\nu \left.\frac{\partial u^*}{\partial y^*}\right|_w} \qquad u_\tau = \sqrt{\frac{1}{Re}\left.\frac{\partial u}{\partial y}\right|_w} \tag{2–10a}$$

$$\delta_\tau^* = \frac{\nu}{u_\tau^*} \qquad \delta_\tau = \frac{1}{Re\ u_\tau} \tag{2–10b}$$

$$t_\tau^* = \frac{\nu}{u_\tau^{*2}} \qquad t_\tau = \frac{1}{Re\ u_\tau^2} \tag{2–10c}$$

Using these viscous velocity, length, and time scales, the flow can be put in terms of the wall units such that

$$u^+ = \frac{u^*}{u_\tau^*} = \frac{u}{u_\tau} \tag{2–11a}$$

$$y^+ = \frac{y^*}{\delta_\tau^*} = \frac{y}{\delta_\tau} \tag{2–11b}$$

$$t^+ = \frac{t^*}{t_\tau^*} = \frac{t}{t_\tau} \tag{2–11c}$$

When the turbulent boundary layer is scaled by the viscous length scale, it can be decomposed into three parts, a viscous wall layer, where viscous dissipation dominates, an outer layer, which is dominated by inviscid convective effects, and a buffer layer where both of these effects are present. For an attached boundary layer with no pressure gradient (White, 2006), these are roughly

$$\text{viscous wall layer:} \qquad 0 \le y^+ < 5 \qquad u^+ = y^+ \tag{2–12a}$$

$$\text{buffer layer:} \qquad 5 < y^+ < 70 \tag{2–12b}$$

$$\text{overlap layer} \qquad 70 < y^+ \qquad u^+ = \frac{1}{\kappa} \ln y^+ + B \tag{2–12c}$$

where $\kappa = 0.384$ and $B = 4.17$. While a turbulent flow can be roughly described by these regions, Spalding's "Law of the Wall" (1961) and the more sophisticated model developed by Monkewitz *et al.* (2007) are able to describe the mean turbulent velocity profile which smoothly transitions from the wall to the free stream for large Reynolds numbers.

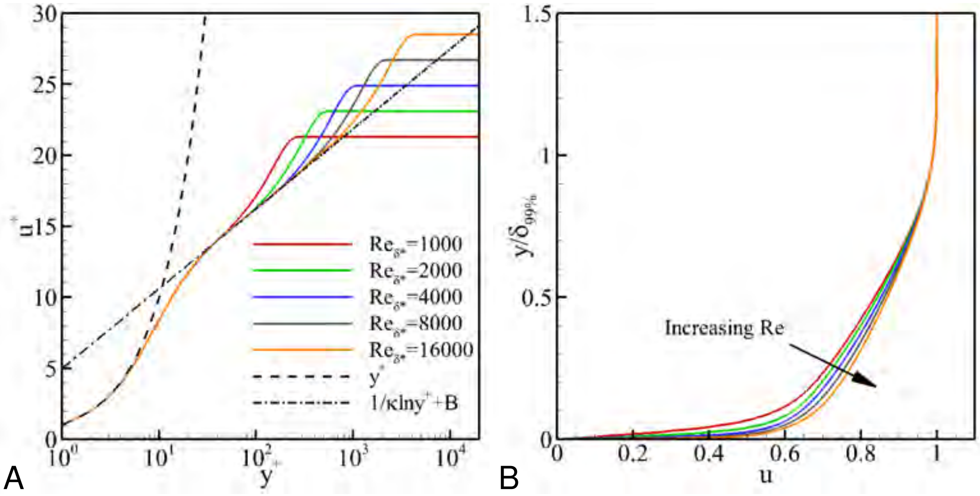

Figure 2-2. Turbulent boundary layer velocity profiles A) at various Reynolds numbers in terms of shear units and B) scaled by their boundary layer heights. Created using the method of Monkewitz *et al.* (2007).

2.2 Channel Flows

The term “channel flow” commonly refers to a bounded, laminar or turbulent, pressure or gravity driven flow between two infinitely wide, parallel plates. Here, the flow properties are simplified once the flow is sufficiently far from any inlets or outlets, as the mean properties in the stream-wise direction become fully developed ($\frac{\partial(\bar{\cdot})}{\partial x} = 0$). As such, stream-wise varying effects can be ignored in these flows, allowing for even more basic study of fluid dynamic phenomena than in a boundary layer.

The laminar, pressure (or gravity) driven channel flow has an exact solution. If a constant pressure gradient of $\frac{\partial p}{\partial x} \neq 0$, full development of the flow velocities $\left(\frac{\partial u_i}{\partial x}\right)$, and no slip conditions at the channel walls are assumed, then all of the stream-wise varying terms in the Navier-Stokes equations can be neglected. Under these conditions, the the Navier-Stokes equations simplify down to

$$\frac{\partial u}{\partial t} = \frac{1}{Re_h}\frac{\partial^2 u}{\partial y^2} - \frac{\partial p}{\partial x} \tag{2–13}$$

where $Re_h = \frac{u^*_\infty h^*}{\nu^*}$ (h being the channel half height). Equation 2–13 can be treated as a diffusion equation with an included source term. Coupled with no-slip boundary conditions at the channel surfaces ($y = \pm h = \pm 1$), and assuming a steady flow, the velocity profile of the channel flow is such that

$$u(y) = 1 - y^2 \tag{2–14}$$

where u is normalized by the centerline velocity, p is normalized by the dynamic head, and $\partial p/\partial x = \frac{2}{Re_h}$. In the unsteady case, a solution is also possible using the separation of variables technique (White, 2006). In addition to this simplest example of a pressure driven channel flow, variations involving moving walls (Poiseuille, 1840), expanding or contracting channel walls (Hamel, 1917; Jeffery, 1915), sidewalls (commonly referred to as duct flows, (Berker, 1963)), and porous blowing on both walls (Berman, 1953) have also been examined and found to have exact solutions, among others.

Similarly to how the stability of boundary layer flows is dependent on the Reynolds number, the hydrodynamic stability properites of are channel flows are also Reynolds number dependent. Furthermore, as boundary layer flows will eventually becomes a turbulent flow as the Reynolds number increases, so do channel flows. At sufficiently high Reynolds numbers, the turbulent boundary layer profile described for the boundary layer flows also applies to channel flows, though the coefficients involved are different ($\kappa = 0.37,\ B = 3.7$ for Equation 2–12, (Nagib & Chauhan, 2008)). For the most fundamental studies of turbulent flows, channel flows are often used, as this type of flow is usually well developed along the length of the flow, which simplifies data collection in experiments and the boundary conditions that must be applied in numerical simulations.

2.3 Hydrodynamic Stability and Turbulent Flows

Transitional flows are those which are characterized as undergoing the change from being an unstable laminar flow, sensitive to small perturbations, to one which is fully turbulent. How this change occurs depends on the particular flow and the perturbations it is exposed to. The earliest methods of examining the stability of these flows were based on determining if the eigenmodes of the linearized Navier-Stokes equations (based around a steady base flow) are stable or not (Rayleigh, 1880, 1887). Eigenvalue methods are still employed for modern research, though more sophisticated methods have also been developed, allowing for a greater understanding of many different instability mechanisms.

For an incompressible flow, let $\bar{u}_i = [\bar{u}, \bar{v}, \bar{w}]^T$ represent the steady base flow velocities and $\tilde{u}_i = [\tilde{u}, \tilde{v}, \tilde{w}]^T$ and $\tilde{p}$ represent the perturbation velocities and pressure, respectively so that $u_i = \bar{u}_i + \tilde{u}_i$ and $p = \bar{p} + \tilde{p}$. Linearizing the INS equations (Equation 2–8), the linearized, incompressible Navier-Stokes equations are given as

$$\frac{\partial \tilde{u}_i}{\partial x_i} = 0 \tag{2–15a}$$

$$\frac{\partial \tilde{u}_i}{\partial t} + \bar{u}_j \frac{\partial \tilde{u}_i}{\partial x_j} + \tilde{u}_j \frac{\partial \bar{u}_i}{\partial x_j} = -\frac{\partial \tilde{p}}{\partial x_i} + \frac{1}{Re}\left(\frac{\partial^2 \tilde{u}_i}{\partial x_j^2}\right) \tag{2–15b}$$

If an oscillatory temporal nature is assumed to the perturbations, such that

$$\mathbf{u} = \begin{bmatrix} \tilde{u} \\ \tilde{v} \\ \tilde{w} \\ \tilde{p} \end{bmatrix} = \exp\left(-i\omega t\right) \begin{bmatrix} u' \\ v' \\ w' \\ p' \end{bmatrix} = \exp\left(-i\omega t\right) \mathbf{u}' \tag{2–16}$$

Equations 2–15-2–16 can be put into the form

$$\mathbf{A}\mathbf{u} = i\omega \mathbf{B}\mathbf{u} \tag{2–17}$$

where **A** and **B** represent appropriate operator matrices, respectively. Furthermore, if the flow is sufficiently simple (one-dimensional, slowly developing, and parallel to the direction of flow, that is $\bar{u} = \bar{u}(y),\ \bar{w} = \bar{w}(y),\ \frac{\partial(\bar{\cdot})}{\partial x} =, \frac{\partial(\bar{\cdot})}{\partial z} = v = 0$) and the perturbation is assumed to be periodic, except for in the non-homogeneous direction (i.e. $\mathbf{u} = \exp\left(i\left(\alpha x + \beta z - \omega t\right)\right)\mathbf{u}'$), then this system of equations can be simplified down to the Orr-Sommerfeld equation for wall normal velocity, v', (Equation 2–18a) and the Squire equation for the wall normal vorticity, ω_y', (Equation 2–18b).

$$\left((i\omega + i\alpha\bar{u}) \left(\frac{\partial^2}{\partial y^2} - k^2 \right) - i\alpha \frac{\partial^2 \bar{u}}{\partial y^2} - \frac{1}{Re} \left(\frac{\partial^2}{\partial y^2} - k^2 \right)^2 \right) v' = 0 \tag{2–18a}$$

$$\left((-i\omega + i\alpha\bar{u}) - \frac{1}{Re} \left(\frac{\partial^2}{\partial y^2} - k^2 \right) \right) \omega_y' = -i\beta \frac{\partial \bar{u}}{\partial y} v' \tag{2–18b}$$

Depending on the desired analysis, these equations can be used to evaluate the spatial (complex $\alpha = \alpha_R + i\alpha_I$, real $\omega = \omega_R$) or temporal (complex $\omega = \omega_R + i\omega_I$, real $\alpha = \alpha_R$) stability modes as an eigenvalue problem for α or ω.

For inviscid flows ($\frac{1}{Re} \rightarrow 0$), the Rayleigh equations are a simplification of the Orr-Sommerfeld and Squire equations. These equations are

$$\left((i\omega + i\alpha\bar{u}) \left(\frac{\partial^2}{\partial y^2} - k^2 \right) - i\alpha \frac{\partial^2 \bar{u}}{\partial y^2} \right) v' = 0 \tag{2–19a}$$

$$\left(-i\omega + i\alpha\bar{u}\right)\omega_y' = -i\beta\frac{\partial\bar{u}}{\partial y}v' \tag{2–19b}$$

From the Rayleigh equation, several simplified theorems of flow stability have been developed. Rayleigh (1880) theorized that for an inviscid flow to be unstable, there must be an inflection point in the flow's velocity profile (i.e. $\frac{\partial^2\bar{u}}{\partial y^2} = 0$ and $\frac{\partial\bar{u}}{\partial y} \neq 0$). Fjørtoft (1950) expanded on this theorem, determining a more rigorous inviscid instability requirement. This additional requirement is that at some point in the velocity profile

$$\frac{d^2\bar{u}}{dy^2}\left(\bar{u} - \bar{u}_s\right) < 0 \tag{2–20}$$

must be satisfied, where $\bar{u}_s$ is the steady, streamwise velocity at the inflection point. Examining the complex phase velocities that instabilities travel at in a velocity profile, Howard (1961) determined that all of the phase velocities of the perturbations (where the phase velocity of a perturbation is defined as $c = c_R + ic_I = \frac{\omega}{\alpha}$) should exist within some circle of potential values, which are dependent on the minimum and maximum of the velocity profile, such that

$$\left(c_R - \frac{1}{2}\left(\bar{u}_{max} + \bar{u}_{min}\right)\right)^2 + c_I^2 \leq \left(\frac{1}{2}\left(\bar{u}_{max} - \bar{u}_{min}\right)\right)^2 \tag{2–21}$$

Examining the results of eigenmode growth from the Orr-Sommerfeld-Squire equations provides stability results of questionable accuracy when compared to experimental results for simple problems. For some problems, these equations accurately describe some of the stability mechanisms present in some problems (such as FSH boundary layers), but do not address the entire spectrum of effects that may occur. For other problems, the results are less accurate. For example, this eigenvalue analysis incorrectly addresses the critical points of stability in some flows (such as Poiseuille flow), and predicts absolute stability for others (pipe flow and Couette flow) when experimental evidence shows that they are most definitely unstable, even at low Reynolds numbers. Because of this, it was long assumed that perturbation growth, not accurately captured by the Orr-Sommerfeld equations, was due to non-linear effects instead (Trefethen *et al.*, 1993).

In the late 1980s and early 1990s, Farrell and his co-workers (1992; 1988) developed a method to study the optimally transient growth of perturbations for viscous flows. Previous attempts at studying transient mechanism had predicted that short term instability growth could be important in otherwise stable flows (Ellingsen & Palm, 1975; Gustavsson, 1979; Salwen & Grosch, 1981; Thomson, 1887). This method predicted that even at low Reynolds numbers, linear growth mechanisms would be able to amplify the energy contained in small perturbations by several orders of magnitude, even though the perturbations would eventually decay to the least stable or most unstable eigenmode. Trefethen *et al.* (1993) introduced an additional method which showed that certain time periodic body force distributions would be able to produce similar levels of amplification. These methods provide sufficient evidence that linear growth mechanisms are highly relevant to the early stages of the laminar to turbulent transition process, even when traditional eigenvalue methods suggest that the flow is stable. An overview of these methods is provided in Table 2-1.

Depending on the magnitude of the primary instabilities, these initial instabilities can also be prone to secondary and higher instabilities (Herbert, 1988), and can lead to even faster rates of instability growth. Once the perturbations relevant to linear growth are sufficiently amplified, they enter the non-linear regime, where they normally break down to form a turbulent flow.

Non-linear stability analysis also presents itself as a diverse problem, and the theories and methods used vary widely, depending on the desired outcome, and whether the transition effects incorporated into the method qualified as weakly or fully non-linear. While the early stages of transition are fairly well understood, less is known about these later stages and how a deterministic flow with discrete frequency oscillations becomes a more random flow with a continuum of frequency oscillations.

Table 2-1. Overview of different linear stability methods.

Stability analysis:	Eigenvalue problem	Optimal Initial Value Problem	Forcing Response	
Form:	Initial condition response: $\mathbf{u} = \exp(i\omega t)\,\mathbf{u}_0$		Forcing response $\mathbf{u} = (\mathbf{A} - \omega\mathbf{B})^{-1}\,\mathbf{f}$	
Growth:	Long term dynamics $(t \to \infty)$	Short term dynamics based on the initial condition, $\mathbf{u}_0$	Optimal periodic response	Case specific periodic response
Output:	Exponential growth rates as $t \to \infty$	Maximum growth of the kinetic energy over a finite amount of time for an optimum initial condition	Maximum growth in the system for an optimal forcing	Response of the system to a specific forcing *(i.e. response to control)*
Stability is based on:	Growth of a single eigenmode	Non-modal growth of some initial condition	SVD of the resolvent	Application of the resolvent

The study of what happens in the non-linear regime is presently a topic of intense research and beyond the scope of the present study.

Different types of stability analysis will often predict similar physical behavior, but this is not always the case. Sometimes several different behaviors in the flow can be shown to be unstable. This indicates that there may be multiple paths for a flow's transition to turbulence, and that the transition process can occur at different rates, depending on which path is taken. This is a very important result to note, as the perturbations which a flow will experience in many applications scenarios (such as in a boundary layer over an aircraft wing or the flow of chemicals in pipe) do not always match up with those seen in experiments or in simplified theories. When these perturbations do match up, it is often due to their introduction into the flow by some sort of actuator, not necessarily the natural environment in which the flow exists. That there exists a certain randomness to which transition path is selected is important for flow control applications, as it indicates that there may be a way to control the transition path selected by the flow, providing an entry point for flow control. This particular subset of flow control is defined as “transition control.”

One important consideration for the application of transition control is to determine what path a flow will take while transitioning from laminar to turbulent. The relevant path to transition is determined by what perturbations exist in the environment, and at what magnitude they exist at. How the flow responds to a specific type of perturbation is defined as the flow’s “receptivity” to that type of perturbation (Morkovin, 1969). A given flow will experience a variety of perturbations, and may also be subject to controlled perturbations through some flow control actuator. Depending on the perturbation, the flow may experience some combination of modal and non-modal, primary, secondary, transient, or by-pass transition mechanisms.

For a boundary layer flow, the receptivity chart for different types of perturbations is shown in Figure 2-3. For boundary layers with no cross-flow, the different transition paths have been described by Reshotko (2001). In path (A), the transition is initiated by the growth of small TS waves, which then become unstable on their own due to secondary instabilities before eventually becoming turbulent. Path (B) indicates a situation where transient growth instigates the modal growth of the TS wave. Path (C) designates a situation where the exponential growth of instabilities is only of minor importance, and that the rapid, algebraic growth of a perturbation eventually causes it to become unstable to its own secondary instabilities and break down. Paths (D) and (E) indicate the scenarios where large freestream perturbations either excite and breakdown algebraic instabilities, or directly transition the flow by generating a turbulent spot. These latter paths require perturbations of significant magnitude.

The TS mode is traditionally the one most widely studied for boundary layer flows. This transition path is usually initiated by small surface perturbations, which grow and

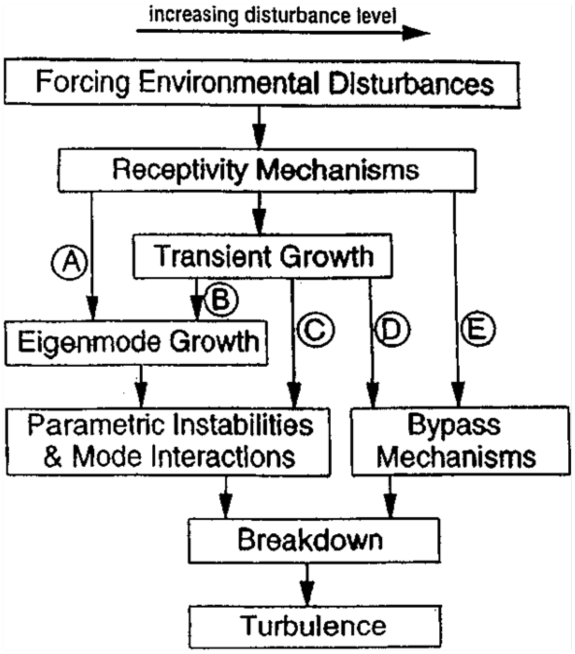

Figure 2-3. Diagram of the transition paths which the flow is receptive to based on the magnitude and nature of the perturbation for boundary layers. From Morkovin *et al.* (1994).

decay at exponential rates along the length of the boundary layer flow. Once the TS mode reaches a sufficient amplitude, the later stages of transition begin (as indicated in Figure 2-3). Two-dimensional TS modes have been widely examined in the reported literature, as Squire's theorem indicates that two-dimensional instabilities are the most amplified modal instabilities (for parallel, fully developed flows) (Squire, 1933). While viscosity is normally taken to be a stabilizing effect in fluid flows, with regard to the TS wave, the viscosity plays a necessary part of the destabilizing effect. This type of perturbation only grows when the local boundary layer Reynolds number (i.e. Re_{δ^*}) has a large, but finite value. As $Re_{\delta^*} \rightarrow \infty$, the TS wave becomes stable again (Wazzan *et al.*, 1968).

An example of the TS wave can be seen in Figure 2-4. The TS wave can be classified as a wall mode, due to its location within the boundary layer. While the wave extends far away from the boundary layer, the magnitude of the perturbation decays rapidly away from the wall. In general, the wavelength of the most unstable TS mode is approximately $20\delta^*$ long (White, 2006).

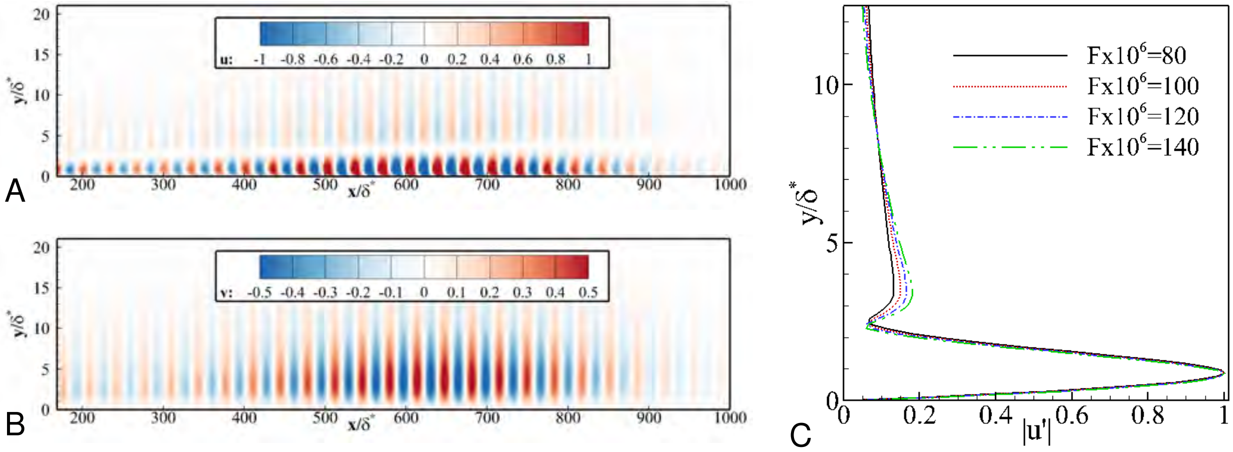

Figure 2-4. TS wave components of A) u-velocity and B) v-velocity at a non-dimensional frequency of $F \times 10^6 = 140.0$, where $F = \frac{\omega_R}{Re}$. The inlet Reynolds number is $Re_{\delta^*} = 500$ C) Boundary layer profiles from a spatial stability analysis for a Reynolds number of $Re_{\delta^*} = 500$.

While the TS mode is an example of an instability where the theoretical results (Schlichting, 1933; Tollmien, 1929) overlap with the experimental results (Ross *et al.*, 1970; Schubauer & Skramstad, 1947), the overlap between the results has not been free of controversy. Experimental methods tend to measure the critical Reynolds number to be lower than what the local, linear stability analyses predict it to be (Ross *et al.*, 1970; Schubauer & Skramstad, 1947). As the theory based methods became more sophisticated in taking the two-dimensional nature of the flow into account using parabolic equations (Bertolotti *et al.*, 1992; Gaster, 1974), and as computational methods became more robust (Bertolotti *et al.*, 1992; Fasel, 1976), the data continued to favor linear stability theory (though discrepancies are noted at higher frequencies). However, out of this disagreement, several facts have been identified.

1. The metric used to quantify perturbation growth matters (Fasel & Konzelmann, 1990; Gaster, 1974). The u-velocity and v-velocity components of the TS mode grow at similar, but not identical rates. Consequently, the energy growth of the TS wave, whether at some distance away from the wall or integrated along a line

normal to the wall also grows at its own rate. As such, the spatial amplification rate must be well defined in order to perform meaningful comparisons with other studies. The neutral stability curve can be sensitive to which metric is used.

2. The location of the perturbation measurement along the height of the boundary layer also matters (Fasel & Konzelmann, 1990). The growth of the perturbation occurs at different rates depending on where the instability is measured in the boundary layer.The neutral stability curve can be sensitive to where data is collected.

3. Agreement between the different methods is better at lower non-dimensional frequencies than at higher non-dimensional frequencies (Bertolotti *et al.*, 1992).

4. The perturbation introduced to the flow matters (Bertolotti *et al.*, 1992). Depending on the perturbation, transient or non-linear effects may be introduced into the boundary layer.

Eventually, it was determined that the differences between the theoretical, numerical, and the experimental results was due to a spatial transient growth mechanism (Bertolotti *et al.*, 1992). Transient growth mechanisms usually can be minimized, but not eliminated in experimental studies. Only in numerical simulations can a perturbation be defined that does not project onto any transient instabilities.

Two empirically derived conclusions have arisen from studying the TS wave for boundary layers. The first result is known as the “universal correlation” for boundary layer (Wazzan *et al.*, 1979). Based on a broad set of experiments and stability calculations of boundary layers, it was found that the shape factor of the boundary layer ($H = \delta^*/\theta$) is the primary variable of importance when determining the critical Reynolds number (specifically, Re_{δ^*}). The critical Reynolds number for all of the flows examined (including subsonic, supersonic, flows with adverse/favorable pressure gradients, etc.) appears to collapse to a single line when compared by the shape factor of the boundary layer (Figure. 2-5).

Another empirically based result is that once the TS wave has been amplified to a certain amount, the flow will transition quickly. While not entirely accurate, as the TS mode does not instantly transition from organized arrays of spanwise voritices to a fully

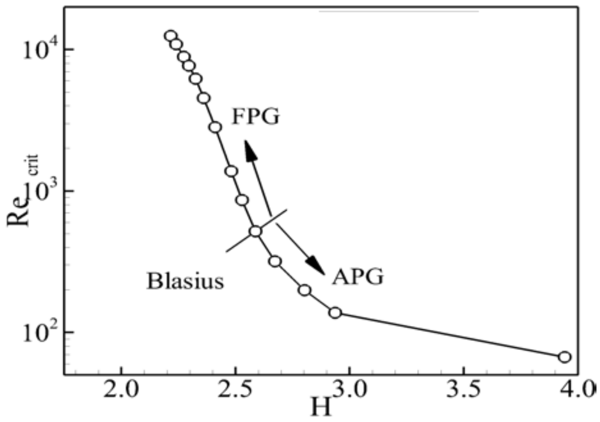

Figure 2-5. Universal correlation of the critical Reynolds number. After the Falkner-Skan data in White (2006).

turbulent flow, the later stages of transition occur fairly quickly, so this approximation is not too unrealistic. The magnitude of exponential amplification required to assume that transition will occur is referred to as the N-factor. The total amplification of the perturbation can be defined through temporal stability analysis (van Ingen, 1956) as

$$\frac{A}{A_0} = \exp\left(\int_{x_{crit.}}^{x_{trans.}} \alpha c_i dt\right) = \exp\left(\int_{x_{crit.}}^{x_{trans.}} \omega_i dt\right) \approx \exp(9) \tag{2–22}$$

or through spatial stability analysis (Jaffe *et al.*, 1970) as

$$\frac{A}{A_0} = \exp\left(-\int_{x_{crit.}}^{x_{trans.}} \alpha_i dx\right) \approx \exp(10) \tag{2–23}$$

where $x_{crit.}$ is the point where the instability begins to grow at a certain frequency (i.e. ω_R) and $x_{trans.}$ refers to the point where the flow can be considered fully turbulent for a certain perturbation frequency. $\frac{A}{A_0}$ refers to the relative magnitude of the perturbation to its initial magnitude (A_0) at $x_{crit.}$. The right hand side terms of Equation 2–22 is $\exp(9) \approx 8000$ and Equation 2–23 is $\exp(10) \approx 22000$ refer to the total amplification of the modal instability which must occur for transition to occur. The amplification required for the flow to become fully turbulent depends on a number of factors (freestream turbulence levels, surface imperfections, vibrations of the boundary layer surface, etc.), but can be assumed to be of the order 10^4. The N-factor is defined as $\ln\left(\frac{A}{A_0}\right)$. While the spatial stability method of determining the N factor is the more physically accurate method, the temporal stability is more commonly used, as it is easier to calculate using linear stability methods.

The N-factor analysis of the TS wave, while useful in application, does not present a physically accurate description of the later stages of the transition process. Once the TS mode of a certain frequency reaches a critical magnitude with respect to the free stream velocity, it becomes susceptible to secondary instabilities (Herbert, 1988). In the TS wave path to transition, these secondary instabilities present themselves as Lambda (Λ) shaped vortices in the boundary layer, repeating in the spanwise direction. Interestingly, this secondary instability mechanism can be manifested in two different ways. The less unstable orientation of the Λ vortices occurs when the vortices exist in a staggered pattern (H-type, Figure 2-6A and B), such that two streamwise adjacent Λ vortices are staggered 180 degrees out of phase with each other. The more unstable orientation of the Λ vortices occurs when the vortices are aligned with each other (K-type, Figure 2-6C and D).

At higher disturbance levels, the transition of the flow from laminar to turbulent is likely to be initiated by a different path to transition (shown as Path (C) in Figure 2-3). Instead of the modal growth of the TS wave in the boundary layer, perturbations from the free-stream initiate non-modal growth of vortical structures in the boundary layer. Transient instability analysis (Butler & Farrell, 1992) indicates that streamwise oriented vortex streaks are the most amplified mode over a finite length of time. These long ($\alpha << \beta$) structures consist of counter rotating streamwise oriented vortices, which generate very large variations in the streamwise velocity ($|u'| >> |v'|, |w'|$), as they transport streamwise momentum into and out of the boundary layer (Figure 2-7). The energy contained in these non-modal structures can be amplified by up to three orders of magnitude by these transient amplification mechanisms.

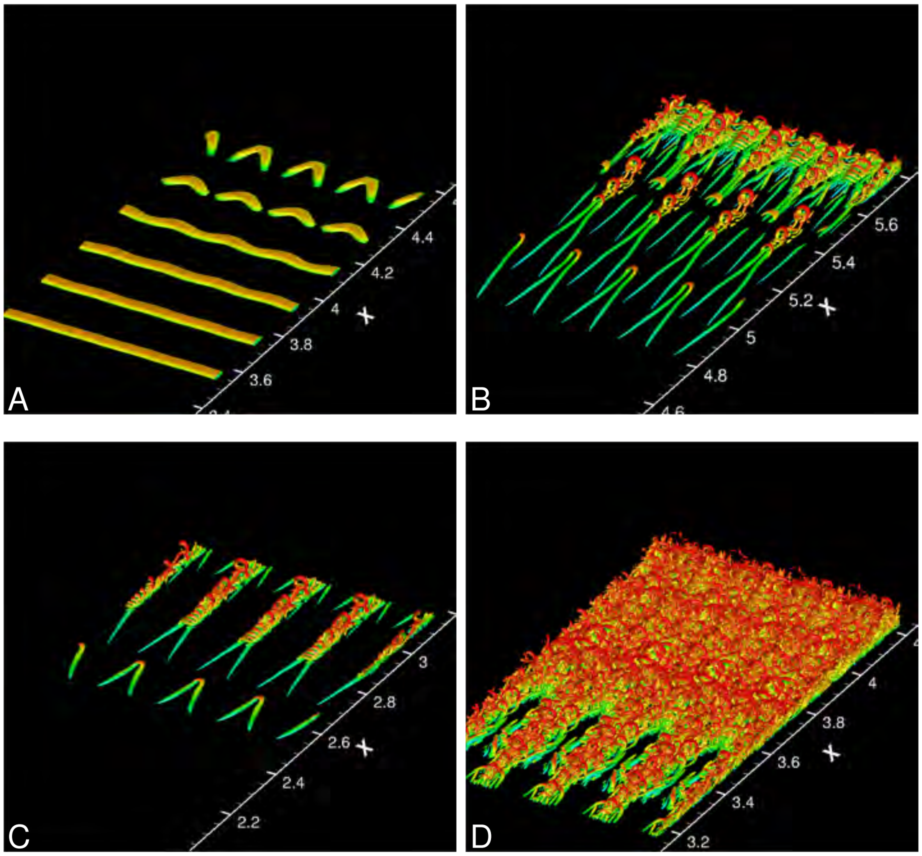

Figure 2-6. Examples of secondary instabilities for TS wave. A,B) H-type and C,D) K-type Λ vortices in a controlled transition scenario from Sayadi *et al.* (2011).

Just as the TS wave is subject to secondary instability growth and eventual breakdown of the organized flow features in the boundary layer, these streamwise boundary layer streaks are also subject to their own secondary instability and breakdown mechanisms. A number of different fundamental and subharmonic effects have been identified by Andersson *et al.* (2001) using an inviscid instability analysis and viscous DNS, which display reasonable agreement with the existing experimental studies.

A third and equally important path to transition is that due to "bypass" transition (which includes paths (D) and (E) in Figure 2-3). This path to transition is usually initiated by larger perturbations in the flow. In bypass transition, these large perturbations usually manifest themselves as turbulent spots, without having to first be amplified by any other instability mechanism (Figure 2-8). While the full details of bypass transition

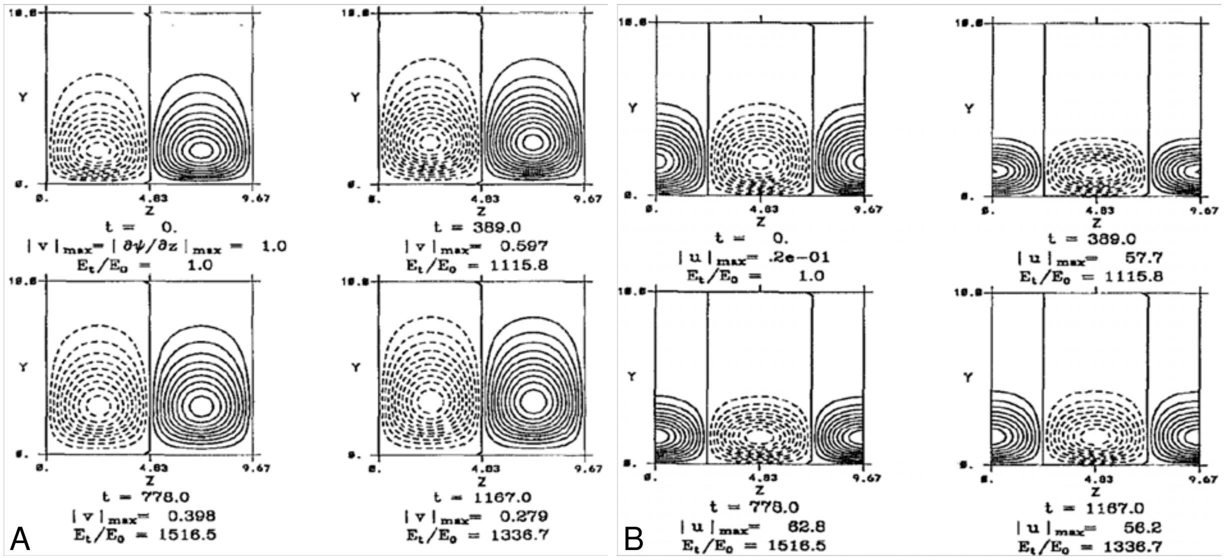

Figure 2-7. Examples of streamwise vortex streaks in a boundary layer. The A) stream function indicating streamwise oriented vorticity and B) the streamwise velocity component as they grow in magnitude. From Butler & Farrell (1992).

are not fully understood at this time, it is hypothesized that bypass transition is strongly related to the spatial optimally growing perturbations (Tumin & Reshotko, 2001).

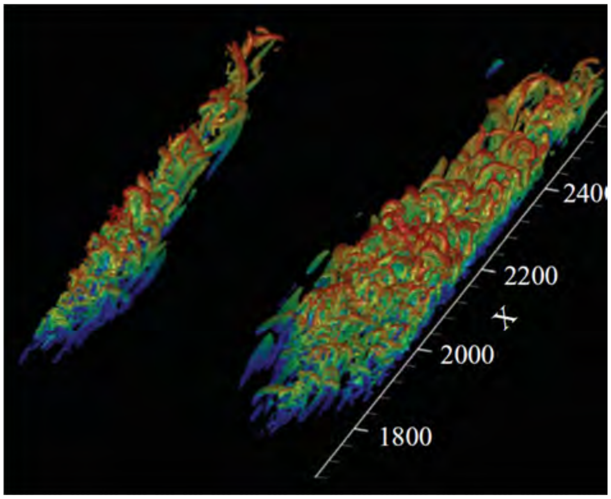

Figure 2-8. Example of by-pass transition generating a turbulent spot. From Wu & Moin (2009)

With the proper application of transition control, specific perturbations can be introduced to the flow, and with the proper feedback system, existing perturbations may be canceled. Passive and active, closed and open loop flow control systems have all been implemented using a variety of different type of sensors and actuators (Cattafesta & Sheplak, 2011). In doing this, the laminar to turbulent transition process can be controlled, accelerating or decelerating the process as desired.

Given enough time, and if the instabilities in the flow are sufficiently large, a flow will eventually reach a turbulent state. With the advent of high performance computing, which allows for simulations to provide the entire flow field at specific instances in time, specific phenomena in the flow can be identified. However, this has only been the case in the last few decades. Before computational fluid dynamics (CFD) became a viable tool for examining turbulent flows, statistical methods were commonly used to examine the properties of turbulent flows. As such, the statistical properties such as the mean, variance, co-variances and frequency spectra (both temporal and spatial) of the flow have been used to characterize and explore turbulent flows. One statistical property in particular, the $\overline{u'v'}$ Reynolds stress, has been successful in describing the unsteady mixing that occurs in a turbulent flow. Statistical descriptions of a turbulent flow eliminate the overwhelming details of examining the multitude of individual vortical structures that exist in the flow, and simplify the analysis, allowing for the focus to be placed on more application relevant and more easily quantified properties such as turbulent mixing, skin friction, or the production and dissipation of turbulent kinetic energy.

In addition to the statistical methods that have been employed, advances have been made in understanding the individual coherent flow structures in a turbulent flow. The most prevalent structures in a turbulent boundary layer or channel flow are hairpin vortices (Figure 2-9). Other coherent structures also exist, such as streamwise vortices, which occasionally "burst" and eject low speed turbulent flow away from the surface of a boundary layer. Much effort has gone into the study of the hairpin structures in particular, and they have been found to be generated either directly by some means of perturbation in the flow (Acarlar & Smith, 1987*a*,*b*), as well as through various transition processes, include primary to secondary wall mode transition (Tollmein-Schlitching

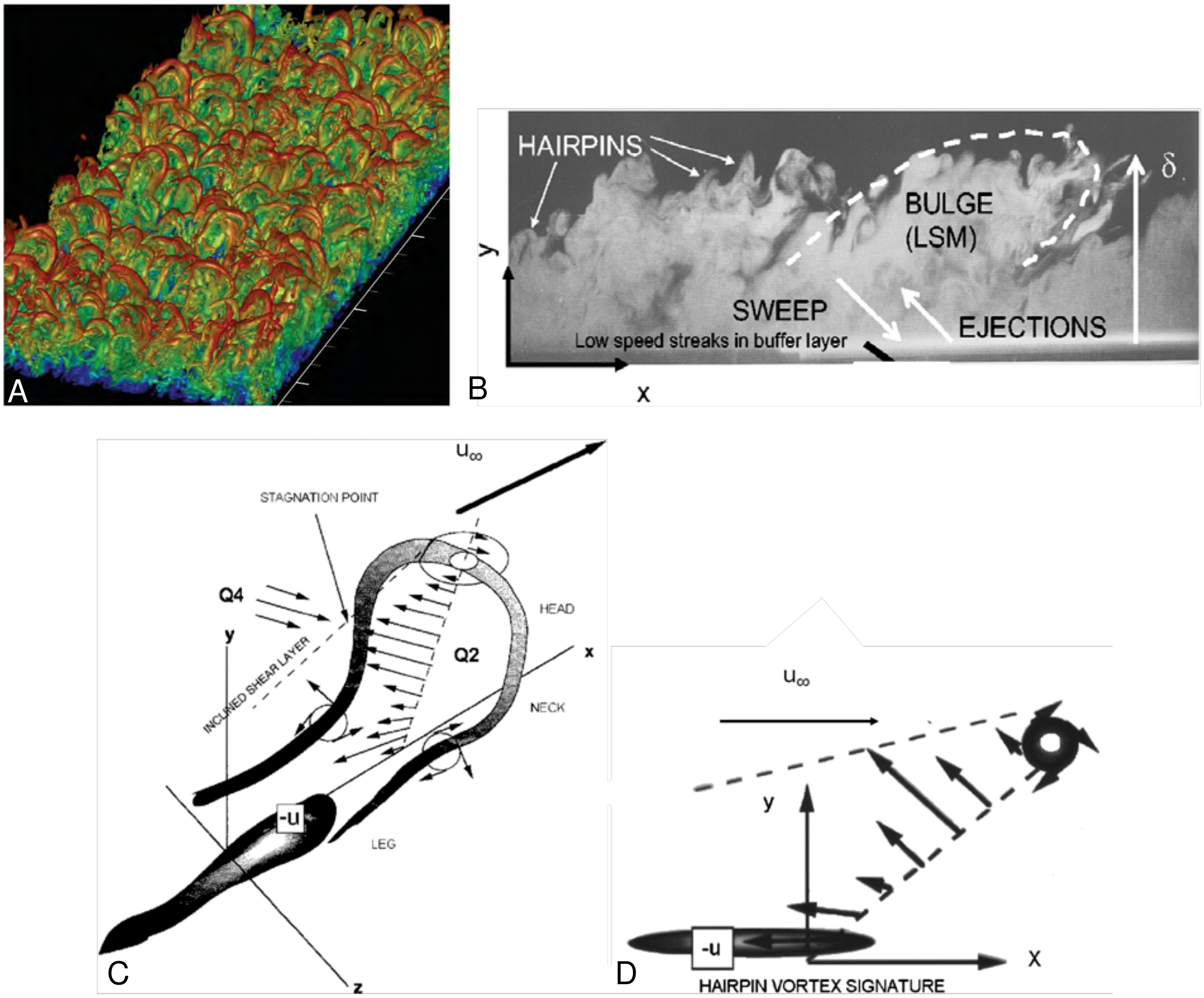

Figure 2-9. Visualization of turbulent structures in a flat plate boundary layer. A) Hairpin structures in a turbulent zero pressure gradient flat plate boundary layer using the Q-criterion. From Wu & Moin (2009). B) Ejection and sweep events in a turbulent boundary layer. From Falco (1977). C) Schematic of a hairpin vortex and D) sideview of a hairpin vortex along the center of the structure. From Adrian *et al.* (2000)

waves + harmonic or subharmonic secondary instabilities (Sayadi *et al.*, 2011)), and bypass transition (Wu, 2010; Wu & Moin, 2009).

The organization of these structures has also been examined (Adrian, 2007), as well as the manner in which individual structures reproduce to form ”packets” of hairpin structures (Zhou *et al.*, 1999). It has been determined that individual hairpin vortices can generate extended trains of hairpin vortices. This natural amplification of the turbulence structure suggests an entry point for future flow control efforts for turbulent boundary layers.

These turbulent motions can be quantified by what “quadrant” (Wallace *et al.*, 1972) they belong to, where, depending on the sign (positive or negative) of the streamwise and wall normal components, the fluid at a specific point can be classified as ejections $(u\,(-)\,v\,(+))$, a sweep $(u\,(+)\,v\,(-))$, wallward interactions $(u\,(-)\,v\,(-))$, or outward interactions $(u\,(+)\,v\,(+))$. Wallace *et al.* (1972) measured these effects using hot-wire anemometry, and concluded that the ejections and sweeps contribute most greatly to the generation of the Reynolds stress, while the wallward and outward interactions subtract (to a lesser degree) from the Reynolds stress. With the availability of high-quality PIV data it has been found that these sweeps and ejections largely correspond to packets of hairpin vortices in the boundary layer (Adrian, 2007).

2.4 Implementation of DBD Body Force Into Navier-Stokes Equations

DBD plasma devices consist of two electrode asymmetrically placed across a solid dielectric, with components ranging in size from from mm to μm (Roth *et al.*, 1998, 2000; Zito *et al.*, 2012). The electrodes are then powered using a high voltage, high frequency signal (on the order of $0.1 - 10kV_{pp}$ and $1 - 100kHz$). This signal generates an electric field, which ionizes the working gas and though the Townsend ionization process and secondary emission processes, sustains the plasma. This alternating electric field is then able to add momentum to the charged particles via the electro-hydrodynamic force $(f_i = qE_i)$. In turn, the charged particles impart momentum to the un-charged particles, eventually resulting in the formation of a wall jet in the region of the DBD actuator (Opaits *et al.*, 2010).

Various methods of simulating the first principles plasma discharge process have been developed (Boeuf *et al.*, 2007; Roy, 2005), though this type of calculation does require significant computational expense. When it comes to coupling the plasma actuation to the fluid flow, the plasma is most often treated as a non-thermal body force, applied through the f_i term in the Navier-Stokes momentum equations (Equation 2–8). First principles models have been employed to serve as the body force in CFD simulations (Gaitonde *et al.*, 2006), though simpler body force models are more commonly used.

The simpler body force models can be grouped into a number of different types. The earliest and simplest, phenomenological models of the body force were based on observation of that the plasma actuators added momentum to the flow (Shyy *et al.*, 2002). These models assume that the plasma region generates a body force distributed over a certain area, and that it is strongest near the electrodes, and weakest at the edge of the plasma. While these models are not the most robust models with respect to the physics that are represented, they do generate a wall jet downstream of the plasma actuator, providing a low order approximation of the desired effect. More robust models assume a load distribution of charged particles (Suzen *et al.*, 2005), and calculate the electric field to generate the body force. Experimental measurements of the velocity field around the plasma actuator allow for the body force to be calculated before being employed as part of CFD simulations (Kotsonis *et al.*, 2011; Kriegseis *et al.*, 2013*c*). When it comes to balancing the ease of use and physical robustness of the different types of models, approximated body force distributions may be the best. Approximated body force distributions generate the distributed body force based on numerical simulations (Singh & Roy, 2008) or experimental results (Maden *et al.*, 2012) of the DBD actuator. These distributions are usually defined as continuous polynomial or exponential functions with respect to x and y, allowing them to be easily implemented into computational tools, without the need for interpolating existing data onto a new domain.

All of these different methods have their pros and cons with respect to evaluating the body force distribution and implementing it for some use. A recent study by Maden *et al.* (2012) compared a number of different body force models, and measured the differences in the velocity field in and around the plasma region. Their study found that there are slight differences in the flow fields generated by the different models in the near plasma region. However, that study also found that when the models are properly calibrated the results are nearly independent of the body force model outside of the plasma body force region.

CHAPTER 3
LOCAL STABILITY ANALYSIS OF A OF A PLASMA ACTUATED BOUNDARY LAYER

In the past few years, one emerging application of DBD plasma actuators has been to control the laminar to turbulent transition process in boundary layer flows. There are advantages to using these actuators to control the laminar to transition process over other types of actuators. That these actuators can be flush mounted certainly poses itself as an advantage, as this means that the actuator cannot accidentally disrupt the flow when it is inactive, but only modifies the flow when it is activated. Furthermore, this type of actuator can be run continuously or in a duty cycled manner, which allows for it to be used in different operational modes, depending on the relevant flow conditions.

Grundmann & Tropea (2008*b*, 2009) used DBD actuators in a flow wise (co-flow) orientation with continuous actuation, constantly adding momentum into the boundary layer. Operating the actuators in this manner, they were able to delay the transition by 200mm for a 10m/s flow. Duchmann *et al.* (2012) made PIV measurements of the TS wave in the region around the plasma actuator, and showed a significant reduction in the wave amplitude and changes to the wave speed relative to the flow without plasma actuation.

Some theoretical work was also performed describing how momentum addition using EHD devices modifies the boundary layer and its stability properties. For example, flow stabilization downstream of the plasma actuator has been predicted for co-flow oriented momentum addition using local stability analysis and employing boundary layer profiles from experiments (Duchmann *et al.*, 2013*a*) and CFD simulations (Riherd & Roy, 2013*b*; Riherd *et al.*, 2012, 2013). More robust work using bi-global stability calculations for TS waves and boundary layer streaks has also been performed, identifying the exact stabilization mechanisms (Riherd & Roy, 2013*a*,*b*,*d*). The details of that work is described in Chapter 4.

With regard to specific applications beyond a flat plate, Séraudie *et al.* (2011) have examined the effects of using DBD plasma actuators for the flow over an ONERA-D airfoil at an angle of attack (which generated an adverse pressure gradient over a majority of the chord). Their study employed low velocity wind tunnel testing and LST to predict the transition points of the flow, using a model similar to what has been developed in this study. Recently, flight tests using continuous plasma actuation have been performed (Duchmann *et al.*, 2013*b*). These flight tests demonstrated a transition delay of 3% of the chord length for a small aircraft for a high Reynolds number flow ($Re_x \approx 1.15 \times 10^6$).

Active flow control approaches have also been examined, Grundmann & Tropea (2008*a*,*b*, 2009) used these devices as a method of transition delay in an adverse pressure gradient boundary layer as part of a closed loop control system to cancel oncoming Tollmien-Schlichting (TS) waves. It was found that pulsed DBD actuators could be used to accurately inject momentum into the boundary layer, canceling the TS waves. Dadfar *et al.* (2013) examined this problem from a the perspective of a implementing a more robust feedback control problem using linear quadratic controllers, and predicted that the disturbances could be mitigated by ≈60-75% of their magnitude. Hanson *et al.* (2010*a*,*b*) have performed some preliminary work into the use of streamwise oriented DBD actuators for the control of transient instabilities, which should ideally lead to the generation of closed loop flow control applications. While active flow control approaches such as these may ultimately lead to increased energy savings relative to continuous forcing approaches, there is a much higher level of complexity in implementing this type of approach, which my be prohibitive for applications in the near future.

In this chapter, the effects of a plasma actuator in a laminar boundary layer are examined. Simulations at low Reynolds numbers have been performed. Based on the results of these simulations, different spatial regions in the boundary layer are identified from their local flow characteristics. A local, temporal stability analysis is then used to examine the stability of this region, focusing on the onset of the unstable TS mode.

Based on the different types of boundary layer velocity profiles seen in these low Reynolds number simulations, a low order model of the boundary layer velocity profile is then constructed. Using the same local, temporal stability analysis, this general model is used to perform a wide parametric study of the plasma actuated boundary layer. In this parametric study, both co-flow and counter flow oriented plasma actuation are examined. Evidence for an inviscid instability mode and an absolute instability is discovered. The data from this model is also found to predict dramatic changes in the critical stability point of the boundary layer, but the results are still in line with the "universal correlation" of Wazzan *et al.* (1979).

3.1 Baseline Flow Modification

As a starting point for the stability analysis, the effect of the DBD actuation on the ZPG boundary layer have been simulated numerically. This is done using the Implicit Large Eddy Simulation/Direct Numerical Simulation (ILES/DNS) Navier-Stokes solver FDL3DI (Rizzetta *et al.*, 2008), details of which are provided in Appendix C. A two dimensional mesh (801×151) is used, which resolves the near wall boundary layer, the effects of a sharp leading edge, and the steady addition of momentum through a body force term. At the location of plasma actuation, there are 62 points in the boundary layer ($\delta_{99\%}$) for the Reynolds number tested as part of this study. This mesh is finer than required and is able to capture the flow adequately near regions of high gradients, particularly for the thin boundary layer near the plate leading edge. The mesh is geometrically stretched near the boundaries in order to prevent the effects of reflections that could potentially bounce off of the farfield boundaries and interfere with the flow. A schematic of the domain used can be seen in Figure 3-1A.

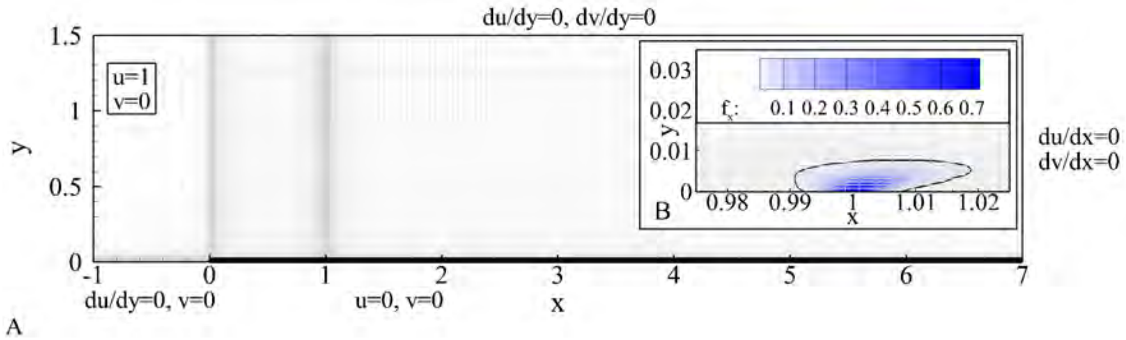

Figure 3-1. Schematic of the mesh used for computations. A) The two-dimensional domain and velocity boundary conditions used for the baseline flow modifications, and B) a close up of the co-flow oriented body force used within the boundary layer. Every fourth grid point is shown.

3.1.1 Boundary Conditions

The intent of these simulations is to model the effects of a plasma modified boundary layer as part of an incompressible flow. However, the simulation tool used, FDL3DI, is a compressible flow solver. While setting the freestream Mach number to an appropriately low value of ($M_\infty = 0.1$) allows for minimal compressibility effects in the domain, there are some boundary condition concerns that have to be addressed.

The velocity boundary conditions are the simplest to understand and implement, as they are the same regardless of compressibility. On the surface of the plate, no slip conditions are applied ($u = v = 0$). Upstream of the plate, a symmetry plane is assumed ($v = \frac{\partial u}{\partial y} = 0$). At the inlet, a freestream velocity condition is applied ($u = 1, v = 0$). For the farfield normal to the plate and downstream out boundaries, first order accurate Neumann boundary conditions are applied to u and v. These boundary conditions take the form of $u_n = u_{n-1}$, where n and $n - 1$ indicate the grid points at the boundary and the first point inside of the boundary. At this level of accuracy, this condition is equivalent to low order approximation (i.e. nearest neighbor). While this may imply that there is additional error to the flow, these boundaries are significantly far away from the area of interest and should not have a significant impact.

The pressure boundary conditions are not as well defined for the case of the incompressible flow, but nonetheless, there is an intuitive way to apply them. Upstream of the plate, the pressure is set to a constant value p_∞. As the boundary layer is a zero pressure gradient, it is expected that the freestream pressure gradient along the length of the plate is zero (i.e. $\frac{\partial p}{\partial x} = 0$). While this assumption will not be adequate near the surface of the plate when there is a plasma actuator, it should suffice for the farfield. As such, the pressure for the farfield boundary away from the surface is constant as well, resulting in $p = p_\infty$. This boundary condition is also applied at the outlet of the domain, so that there is no pressure gradient driving the flow. For the surface, the assumption used to generate the Blasius boundary layer, $\frac{\partial p}{\partial y} = 0$, is employed along the length of the plate (using a third order accurate biased finite difference stencil, $\frac{\partial p}{\partial y}|_j \approx \frac{1}{\Delta y} - \frac{11}{6}p_j + 3p_{j+1} - \frac{3}{2}p_{j+2} + \frac{1}{3}p_{j+3}$). This boundary condition also suffices as a boundary condition for the pressure upstream of the plate.

Density boundary conditions also need to be defined. It is assumed that at the inlet and in the farfield, the plate has no influence on the density, so density is assumed to be constant ($\rho = \rho_\infty = 1$). Upstream of the plate, a symmetry condition is applied using a third order accurate stencil (i.e. $\frac{\partial \rho}{\partial y} = 0$). Over the length of the plate a constant wall temperature condition is applied, as such the density is proportional to the pressure at the surface of the plate. Whilte is assumption may or may not be accurate due heating at the wall by the plasma actuator, temperature effects are intentionally neglected in order to simplify the problem. At the outlet, the first order Neumann boundary condition is applied, which doubles as a first order interpolation of the density at the outlet.

3.1.2 Calibration of the Plasma Model

The plasma actuation is modeled using an approximate body force distribution based on first principle simulations of the plasma discharge (Singh & Roy, 2008) (Figure 3-1B) in a manner consistent with the description in Rizzetta *et al.* (2008). The same set up is used with no slip conditions ($u = v = 0$) for the left, right, and bottom boundaries and a no shear condition on the upper boundary, leading to a quiescent condition over a majority of the domain. The plasma actuator is run at various magnitudes with quiescent initial and a mix of no slip/no shear boundary conditions. The magnitude of the plasma actuation is proportional to the parameter D_c, which relates the magnitude of the body force to the dynamic pressure (i.e., $D_c = \frac{|f_0|L}{\rho u_\infty^2}$). The effect of the actuation on the flow is then characterized by the maximum velocity seen in the wall jet (u_p, shown in Figure 3-2). A linear interpolation is then used to control the body force for the simulation under non-quiescent conditions. The magnitude of the implemented force is characterized by the non-dimensional parameter

$$\gamma_0 = \frac{\bar{u}_p\big|_{x_0}}{\bar{u}_\infty} \tag{3–1}$$

This parameter is selected in order to focus solely on the fluid dynamic effect of the plasma actuation and its influence on the flow stability, ignoring the electrical inputs such as voltage, frequency and the waveform driving the device. The values of γ_0 are calibrated for the Reynolds number tested as part of this study.

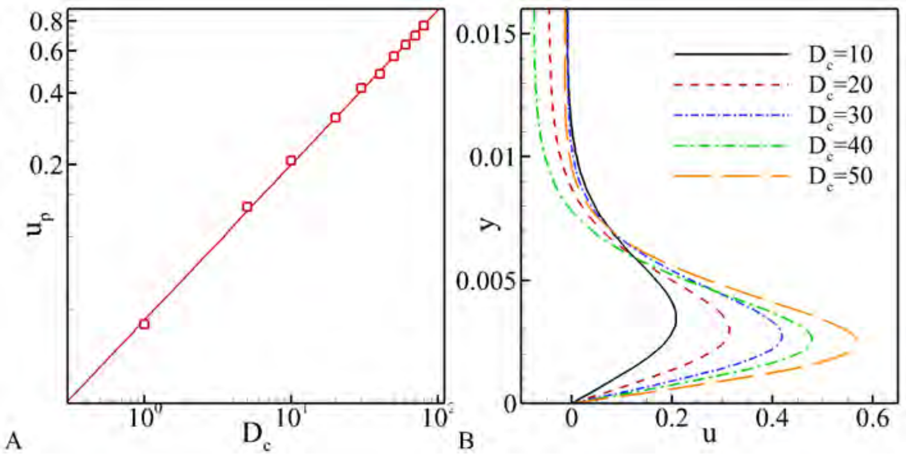

Figure 3-2. Calibration data for the plasma actuation. A) Values of u_p used to calibrate D_c. B) Velocity profiles at a location downstream of the plasma actuation for various values of D_c.

3.1.3 Simulated Baseflows

In the simulations, the body force is placed at a position corresponding to $Re_x = 100,000$ ($Re_{\delta *} = 543$) in a boundary layer flow. This actuator location is in the transitional regime, which is useful for understanding how the momentum addition modifies the laminar to turbulent transition in the critical domain.

The first thing that should be noticed is that the addition of momentum into the boundary layer modifies the boundary layer flows (Figure 3-3A-C). Slightly upstream of the actuator, the flow is pulled downwards into the wall as if there were boundary layer suction present (Figure 3-3D). However, as the pressure data in Chapter 6 will show, there is a local pressure rise about the actuator, contrary to the common belief (Corke *et al.*, 2010). Immediately downstream of the device, the boundary layer profile shows several inflection points, which suggests that inviscid instabilities may become important (Figure 3-3E), as they satisfy Fjørtoft's criteria (Equation 2–20). Further downstream of this, the profiles return to something resembling the Blasius profile, though fuller than that of the initial flow (Figure 3-3F).

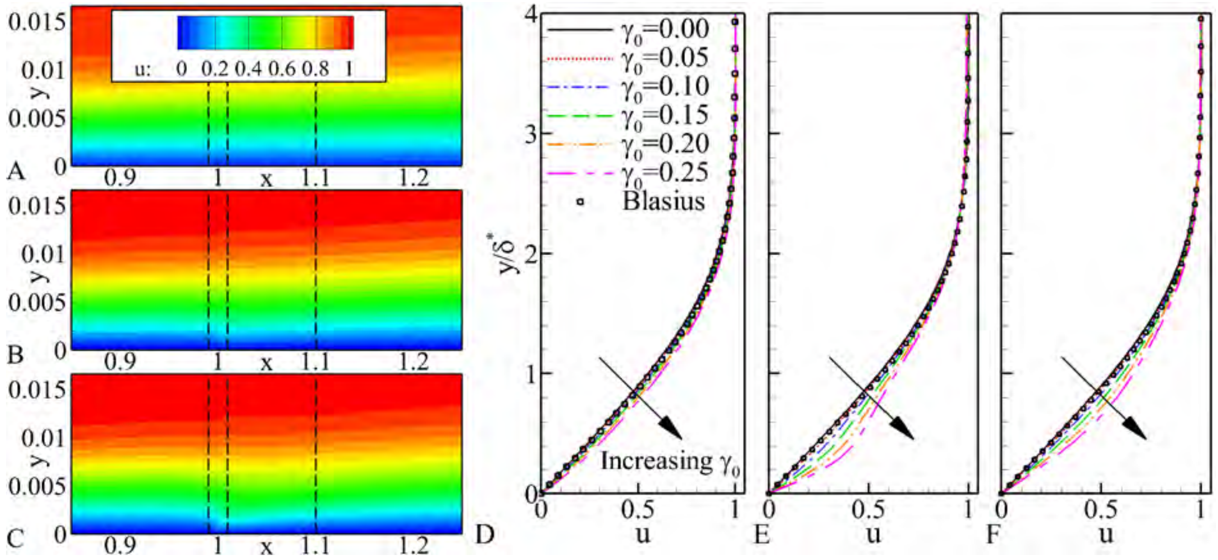

Figure 3-3. Velocity fields around the plasma actuators for A) $\gamma_0 = 0.00$, B) $\gamma_0 = 0.10$, and C) $\gamma_0 = 0.20$. Boundary layer profiles at D) $x = 0.99$, E) $x = 1.01$, and F) $x = 1.10$ are also shown. The dashed lines in A-C) indicate locations where the boundary layer profiles are extracted from, and are shown in D-F).

There is expected to be some impact on the pressure fields in these flows as well. It is known from hydrodynamic stability theory that for laminar boundary layers (White, 2006), flows with a a positive pressure gradient (i.e. a decelerating flow, such as an expanding nozzle) will be less stable, while flows with negative pressure gradients (i.e. an accelerating flow, such as on a forward facing ramp) will be more stable. Comparing the surface pressures with and without plasma actuation (Figure 3-4A), there is a slowly developing, reduction in the pressure upstream of the body force (due to entrainment effects accelerating the flow). Right at the actuator, there is a very rapid jump in the surface pressures, which then slowly decays as the flow develops downstream. This rapid rise in the pressure is likely due to various effects resisting the acceleration of the flow by the body force. Examining a slice of the flow outside of the boundary layer (Figure 3-4B), comparable effects can still be seen, bu the sudden rise is less rapid, and the magnitude of the effects is reduced, indicating that these changes to the pressure field are localized to the boundary layer.

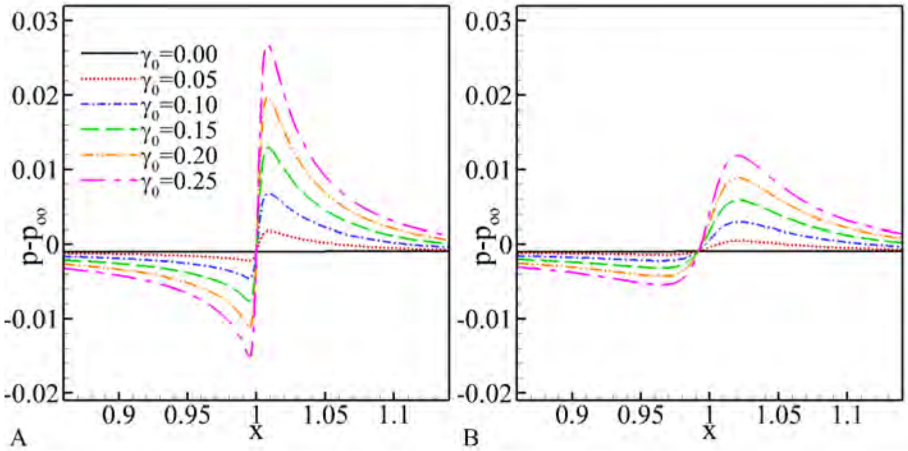

Figure 3-4. Pressure on and near the surface around the plasma actuator. A) Surface pressure and B) pressure collected at a height of 0.02, which is outside of the boundary layer and body force region.

It is expected that these pressure gradients have some impact on the stability of the flow. Upstream and downstream of the actuator, the pressure gradient is negative, which corresponds to the stabilization. This stabilizing effect is complicated by non-parallel and flow development effect, so this implication on the flow's stability should be interpreted with caution until quantitatively analyzed (see Section 3.2). The even more complex region to understand is the region right around the plasma actuator. Due to two-dimensional flow field in this region, the impact of the pressure gradient on its own may or may not be of importance relative to other effects in the flow field.

As the boundary layer velocity profiles are modified due to the addition of momentum into the boundary layer, the displacement and momentum deficit of the boundary layer should be altered as well. It can be seen in Figure 3-5 that there is a monotonic response of the boundary layer heights to the magnitude of the body force. There are some localized effects near the boundary layer, in which the boundary layer height may rise ($\delta_{99\%}, \theta$) due to modifications very near to or away from the wall or fall (δ^*) due to a reduction in the boundary layer momentum deficit. Overall, there is a drop in the boundary layer heights downstream with the addition of momentum into the boundary layer.

All of these effects suggest that there are 3 different locations important to the stability of these devices (Figure 3-5). There is the region upstream of the devices (I), which may now be slightly more stable due to the entrainment of fluid into the boundary layer. There is the region over and immediately downstream of the device (II), which shows signs of inviscid instability due to Fjørtofts criteria. Finally, there is the region far downstream of the device (III), which should be more stable due to a reduced boundary layer height caused by the injection of momentum into the boundary layer by the plasma actuator.

As important as changes to the boundary layer heights may be, the changes to the boundary layer profiles are even more important. The "fullness" of the boundary layer profile can be measured by the boundary layer shape factor ($H = \frac{\delta^*}{\theta}$). A lower shape factor indicates a "fuller," more stable boundary layer profile, and even small changes to the shape of the velocity profile may incur very large changes to the critical Reynolds

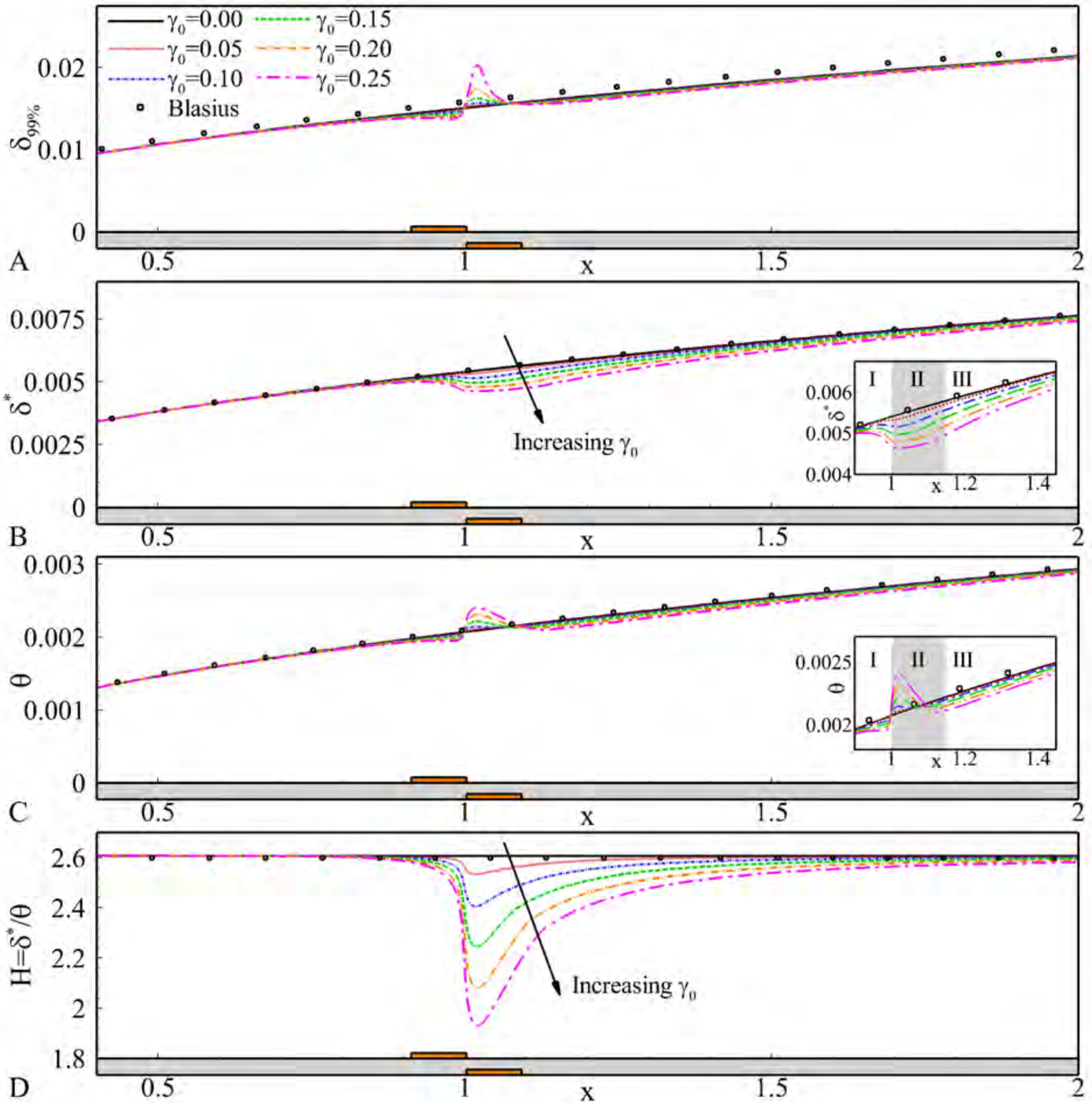

Figure 3-5. Boundary layer heights and shape factor as a function of the velocity ratio, γ_0, for values ranging from 0 to 0.25 - A) $\delta_{99\%}$, B) δ^*, C) θ, and D) the shape factor, $H = \delta^*/\theta$, along with a comparison to the analytical solution for the case of $Re_{act} = 100,000$. Inlays show a zoomed in view near the actuator location.

number of the boundary layer (Wazzan *et al.* (1979), Figure 2-5). It can be seen in Figure 3-5D that the addition of momentum into the boundary layer can induce large changes to the shape factor. Based on these two results, it is expected that the changes to the shape of the boundary layer profiles by the momentum addition will induce a stabilizing effect in the plasma modified boundary layer flows.

3.2 Local Linear Stability Theory

3.2.1 Numerical Model of the Eigenvalue Problem

Linear stability theory can be used to predict the existence and growth rates of instabilities that may manifest themselves in the boundary layer. In order to perform this type of analysis, it must be assumed that the flow is slowly developing and parallel to the surface. Two metrics have been developed, $E_{\|}$ and E_d, which quantify the validity of these assumptions. These metrics are defined as

$$E_{\|} = \max_{y\in(0,\infty)} \left(\tan^{-1} \left| \frac{\bar{v}}{\bar{u}} \right| \right) \tag{3–2}$$

and

$$E_d = \max_{y\in(0,\infty)} \left| \frac{\partial \bar{u}}{\partial x} \right| \tag{3–3}$$

and quantify the parallel flow and slowly developing assumptions, respectively. These assumptions are quantified in Figure 3-6. This flow, while it does exhibit some rapid spatial changes and non-parallel behavior near the actuator, can be considered a slowly developing, parallel flow over the remainder of the domain. As such, one dimensional, linear stability theory can be applied, except for near the actuator. In order to understand the effects near the actuator, a bi-global stability method is employed, the results of which are discussed in Chapter 4.

For the present local stability analysis, the method described in Appendix A is employed. This model focuses on only fluidic effects; there is no feedback mechanism between the fluid and plasma present in this analysis. In order to check for the accuracy and convergence of the solution, a grid resolution study has been performed. Two separate cases, one examining the TS mode, the other examining a “fast” mode, which will be explained in more detail in Section 3.3, have been examined. The convergence of the most unstable eigenvalue can be found in Table 3-1 and Figure 3-7. The order

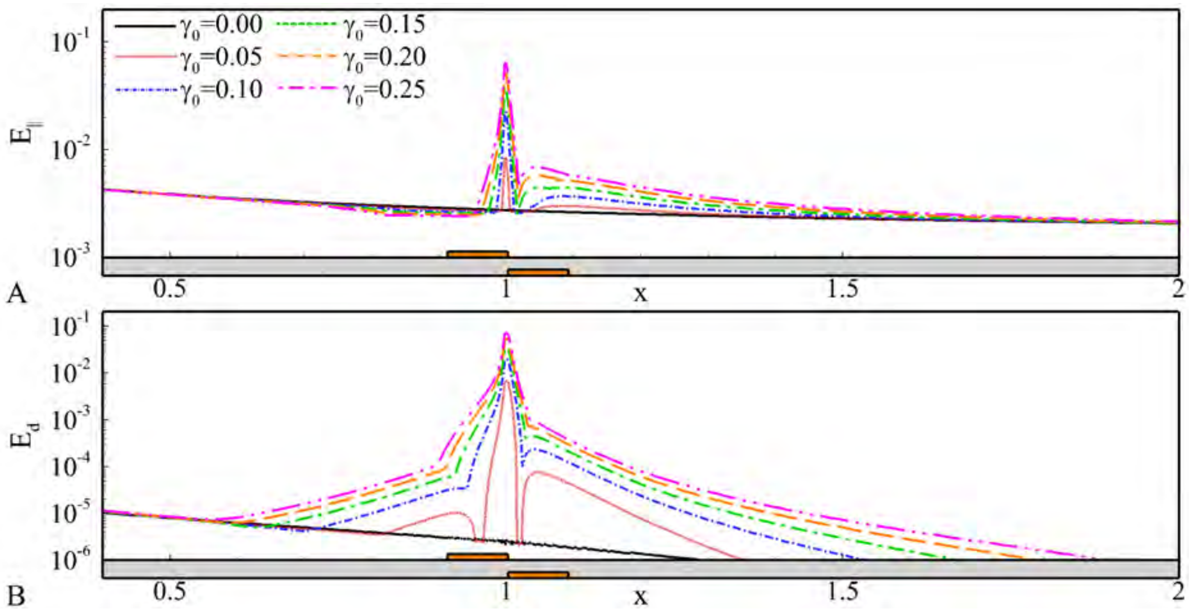

Figure 3-6. Evaluation of parallel flow approximation. A) $E_{\parallel}$ and B) E_d for the flow fields calculated in Section 3.1.3 for velocity ratios of $\gamma_0 = 0$ to $\gamma_0 = 0.35$.

of accuracy of the stencils employed for the calculations were second and fourth order accurate, respectively. The convergence of the unstable eigenmodes, reflects this, as it converges at a rate between n_y^{-2} and n_y^{-4}.

Examining this convergence data, the grid resolution of $n_y = 201$, $\Delta y = 0.0581\delta^*_{Blasius}$ appears to be in the asymptotic error range. This grid density should be sufficient resolution for the present method. Furthermore, this grid density provides a result in an appropriate amount of time to perform a wide parametric study.

Table 3-1. Convergence of the most unstable eigenvalue for two sample cases. For both cases, $Re_{\delta^*,Blasius} = 1000$, $\alpha = 0.3$.

n_y	Blasius, ω_{TS}	Model $(\eta = 1, \gamma = 0.25)$, ω_{Fast}
51	$0.11238325236 - 0.00090042619i$	$0.23306979831 + 0.00220664208i$
71	$0.11017358051 + 0.00059957882i$	$0.23281253531 + 0.00242939870i$
101	$0.10924347588 + 0.00163256137i$	$0.23273816623 + 0.00249039239i$
142	$0.10898287015 + 0.00213952218i$	$0.23272109814 + 0.00250492030i$
201	$0.10892701325 + 0.00235576622i$	$0.23271726363 + 0.00250853091i$
283	$0.10892058760 + 0.00243347102i$	$0.23271652043 + 0.00250929338i$
401	$0.10892145449 + 0.00246038133i$	$0.23271638394 + 0.00250945035i$
566	$0.10892233968 + 0.00246910010i$	$0.23271636662 + 0.00250947873i$
801	$0.10892273162 + 0.00247197532i$	$0.23271636809 + 0.00250948486i$

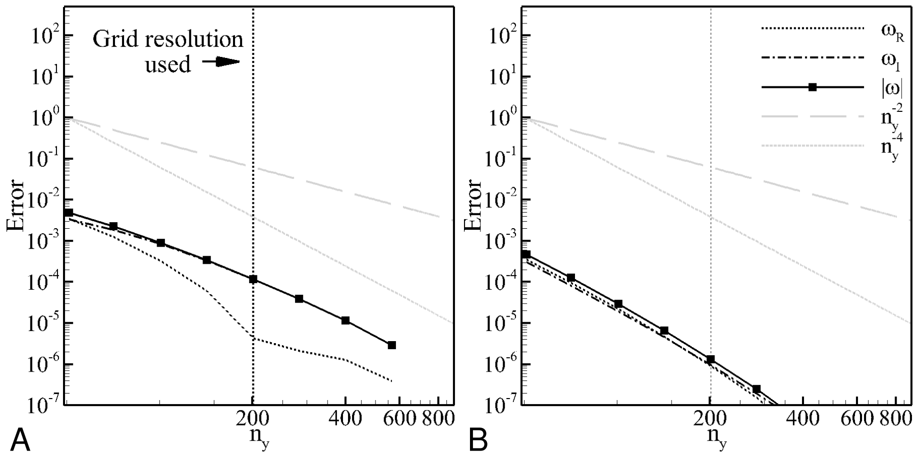

Figure 3-7. Grid convergence of the critical eigenvalue for two different boundary layer instabilities. A) Blasius boundary layer profile and B) a boundary layer profile generated by the model ($\eta = 1.0, \gamma = 0.25$). For both cases, $Re_{\delta^*,Blasius} = 1000$, $\alpha = 0.3$. The vertical line indicates the grid resolution used for the present study.

3.2.2 Co-Flow Actuation

Velocity profiles from Section 3.1 were extracted from 160 points in the flow ($0 < Re_x < 4Re_{x,act}$) and examined using the eigenvalue analysis as provided. Only two-dimensional, non-oblique modes have been examined ($\beta = 0$). Sufficiently far upstream of the flow modification, the stability properties are unchanged. However, the stability is modified in the regions near and downstream of the body force. The extracted eigenvalues for the case of $Re_{x,act} = 100,000$ at $Re_x = 120,000$ can be seen in Figure 3-8. The critical eigenvalue moves monotonically in the complex plane of ω from unstable to stable as γ_0 increases (Figure 3-8B). Neutral stability diagrams are shown in Figure 3-9 for the different values of γ_0 examined. Again, a monotonic behavior is found to exist, where the higher levels of actuation have a more profound effect on the stability characteristics (either stabilizing or destabilizing depending on the specific eigenmode). It can be seen that as the value of γ_0 and amount of momentum transfer is increased, the ‘thumb’ region typically associated with instabilities in the ZPG boundary layer is moved farther and farther downstream. This indicates that the boundary layer stability is successfully being reinforced by the use of DBD actuation.

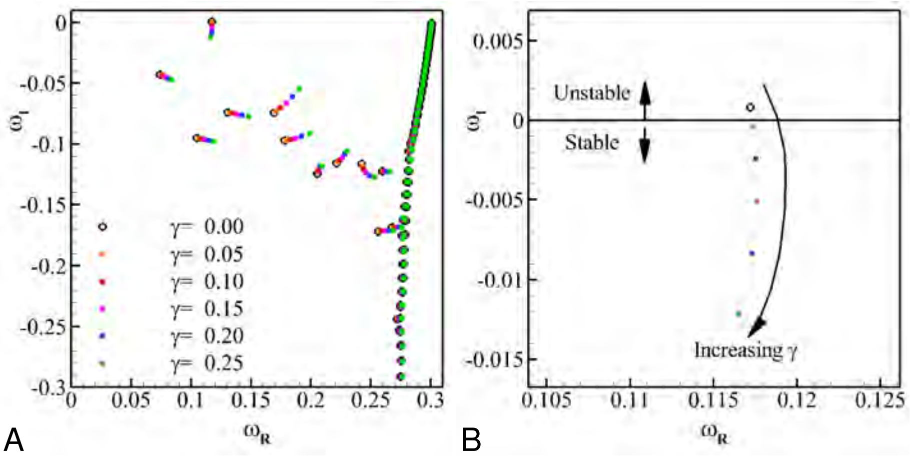

Figure 3-8. Computed eigenspectra downstream of the palsma actuator at $Re_x = 120,000$, $\alpha = 0.3$ A). A close-up of the TS wave eigenvalue is also shown B).

It can be seen that LST predicts increased flow stabilization in terms of Re_x (Figure 3-10) as well as $Re_{\delta*}$ in the neutral stability curves (Figure 3-9). Furthermore, this flow stabilization extends beyond the near actuator region, to points where the assumptions required for the one-dimensional stability analysis are valid. The reasons for this flow stabilization are likely to be due to two different effects, both of which are coupled to each other and the addition of momentum into the boundary layer. The addition of momentum into the boundary layer is shown to reduce the boundary layer displacement height (Figure 3-5B). In turn, this reduces the local boundary layer Reynolds number, which delays the onset of perturbation growth in the boundary layer. The second source of stabilization results from the momentum addition modifying the boundary layer velocity profiles (Figure 3-3). By adding momentum to the flow, the boundary layer profiles are made fuller, and the shape factor, H, is modified. This parameter has been shown to be very important in identifying the onset of the perturbation growth in boundary layers through a universal correlation between the critical Reynolds number and the shape factor (Wazzan *et al.*, 1979), where a decreased shape factor implies

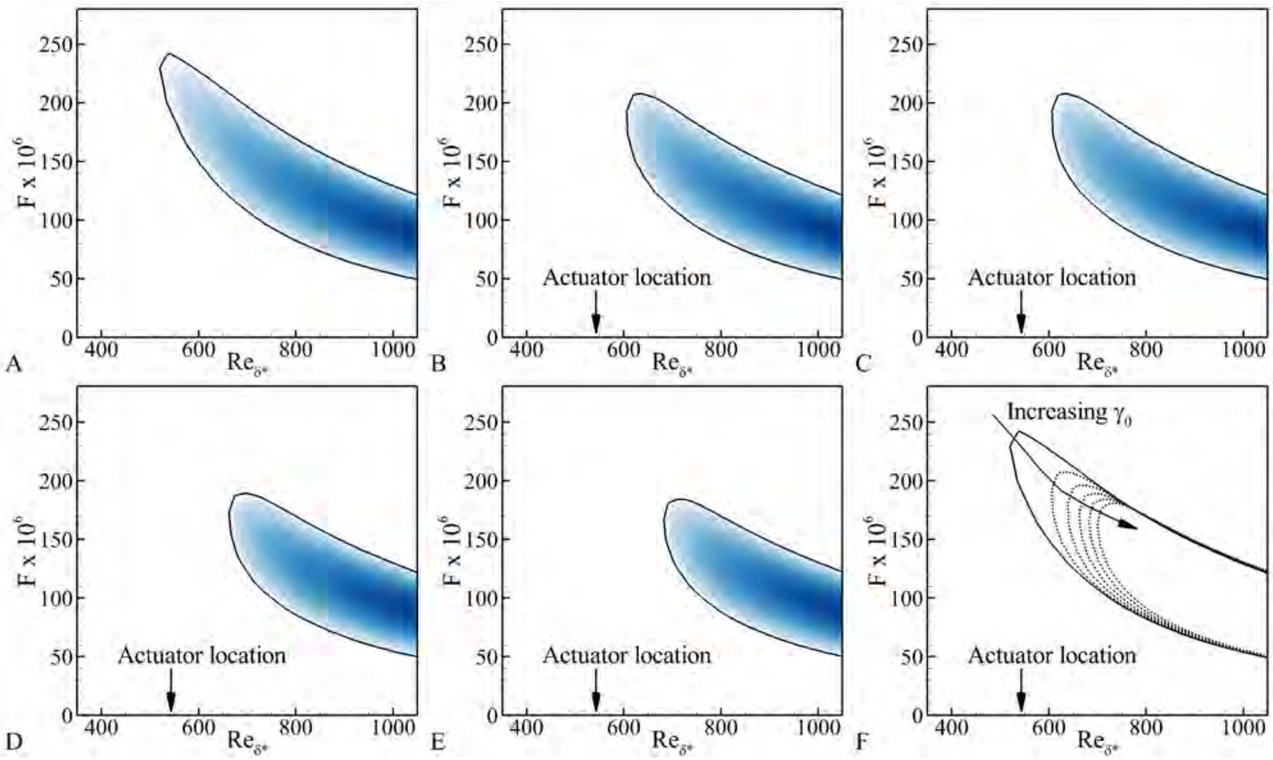

Figure 3-9. Stability diagrams of the modified boundary layer flows when the actuator is placed at $Re_x = 100,000$ for A) $\gamma_0 = 0.00$, B) $\gamma_0 = 0.05$, C) $\gamma_0 = 0.10$, D) $\gamma_0 = 0.15$, and E) $\gamma_0 = 0.20$. In A-E), the line of neutral stability is marked. $F = Real\left(\omega\right)/Re_{\delta^*}$. F) Neutral stability curves for values of γ_0 ranging from 0.00 to 0.25 with a spacing of 0.05

transition delay of the TS wave. Fortunately, the manner in which momentum is added into the boundary layer reduces the shape factor, thus delaying the critical onset of the TS wave's growth.

3.3 A Model of the Local Boundary Layer Profiles

While these simulated flows allow for analysis under these specific flow scenarios, knowledge of the stability of a boundary layer modified by an arbitrary level of plasma actuation is also desirable. In order to examine the effects of a more general modified boundary layer, a low order model approximating the boundary layer velocity profiles can be developed. It is known that under quiescent conditions, plasma actuation is able to create wall jets, which match the Glauert wall jet similarity solution sufficiently far downstream (Opaits *et al.*, 2010). The current simulations (Figure 3-3) as well as past

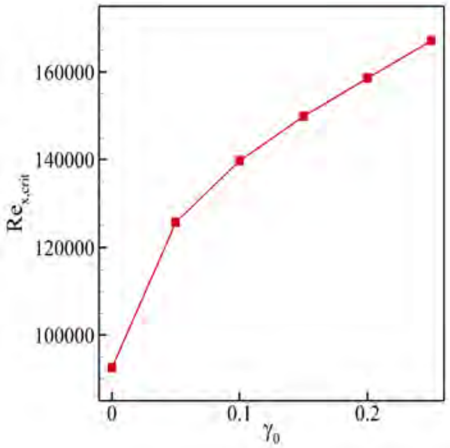

Figure 3-10. Critical values of Re_x for the actuated flow.

numerical and experimental results (B.Jayaraman *et al.*, 2007; Moreau, 2007) suggest that the momentum addition into the boundary layer can form wall jet-like effects if the levels of actuation are high enough. Even for lower levels of actuation, the momentum addition is still seen. This suggests that a superposition of a boundary layer and wall jet velocity profile should suffice to approximate the effects of plasma actuation on a ZPG boundary layer. That is,

$$\bar{u}_{comb.} = \bar{u}_{Boundary\ \ layer} + \bar{u}_{Wall\ \ jet} \tag{3–4}$$

In order to manipulate this model, base flow solutions for the boundary layer and wall jet profiles are necessary, as well as two non-dimensional parameters in order to scale the size and velocity magnitude of the momentum injection relative to the boundary layer. The Blasius boundary layer (Blasius, 1908) and Glauert wall jet (Glauert, 1956) similarity solutions are logical choices for the ZPG boundary layer, though there is no suggestion that the superposition of these solutions will result in an exact solution to the Navier-Stokes equations, only an approximation.

Concerning the non-dimensional parameters, while the global value of γ_0 can be used to characterize an entire two-dimensional flow field, but when examining individual

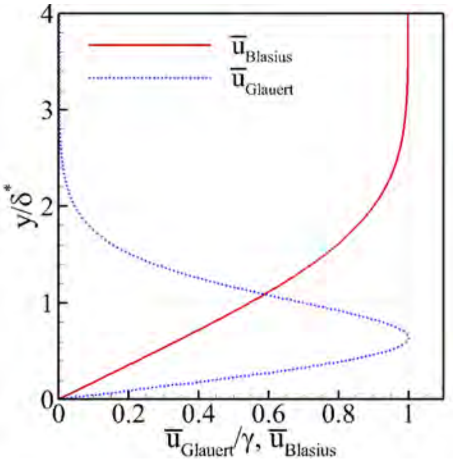

Figure 3-11. Components of the plasma modified boundary layer flow model.

boundary layer profiles it is more useful to define a localized velocity ratio parameter,

$$\gamma = \frac{\bar{u}_p\left(x\right)}{\bar{u}_\infty}. \tag{3–5}$$

which is more closely tied to the momentum addition that exists in the boundary layer profile downstream of the plasma actuator. This locally varying value of γ is a function of the global magnitude of the momentum injection (as characterized through γ_0) as well as the convective and diffusive transport of the momentum in the boundary layer, which will vary as one moves away from the actuator location. The momentum injected by the wall jet

$$\delta_p^* = \int_0^\infty \frac{\bar{u}_{WJ}\left(y\right)}{\bar{u}_p} dy \tag{3–6}$$

and momentum deficit of the boundary layer (i.e. the displacement boundary layer height) can be formulated as length scales

$$\delta_{BL}^* = \int_0^\infty 1 - \frac{\bar{u}_{BL}\left(y\right)}{\bar{u}_\infty} dy \tag{3–7}$$

to form a relative length scale such that

$$\eta = \frac{\delta_p^*}{\delta_{BL}^*} \tag{3–8}$$

which is also a local parameter, due to the development of the boundary layer and wall jet components in the flow. These non-dimensional parameters can then be applied to the initial model from Equation 3–4 such that

$$\bar{u}\left(y\right) = \bar{u}_{Blasius}\left(y\right) + \gamma\bar{u}_{Glauert}\left(\frac{y}{\eta}\right) \tag{3–9}$$

The product of the two non-dimensional parameters developed here can be used to generate a third physically important parameter, μ, where

$$\mu = \eta\gamma \tag{3–10}$$

this parameter is the ratio of the momentum injected into the boundary layer by the plasma body force as compared to the momentum deficit in the boundary layer. While the total amount of momentum replaced is definitely important, exactly how this momentum is added into the boundary layer also matters. Momentum addition outside of the boundary layer will not likely be helpful, nor will momentum addition that occurs at too near to the surface. Therefore, it is not only the velocity ratio or total momentum addition that will affect the boundary layer stability, but both of these parameters, improper application of which could be counter productive.

Applying this model, a wide range of potential boundary layer profiles can be created. These boundary layer profiles are approximately matched to specific parameters from the simulations performed. The results of this show that there is a reasonably good agreement between the velocity profiles created by the model and those from the CFD simulations (Figure 3-12A and B). Agreement is good near the wall, near the region of maximum velocity, and into the farfield. However in the intermediate region where the wall jet dissipates momentum into the boundary layer, there is a noticeable discrepancy. As this discrepancy appears to be diffusive in nature, it is likely to vary depending on the local Reynolds number of the boundary layer velocity profile, which is not something that the current model takes into effect. There also appears to be a discrepancy in the inflection points between the model and the extracted boundary layer profiles, as shown using the second derivative of the velocity profile in Figure 3-12C. The inflection points in the model velocity profiles do not occur at the same location in the boundary layer as those in the simulated velocity profiles, though they are still within $0.25\delta^*_{BL}$. This discrepancy in the location of boundary layer inflection points has implications with respect to the existence and importance of inviscid instabilities to the boundary layer. This discrepancy seems to be smaller farther downstream of the actuator location, as the local value of the boundary layer ratio, η, has increased and the velocity ratio, γ, has decreased. As one moves farther and farther downstream of the actuator, the trends of η increasing and γ decreasing continue, due to the dissipation of momentum away from the wall.

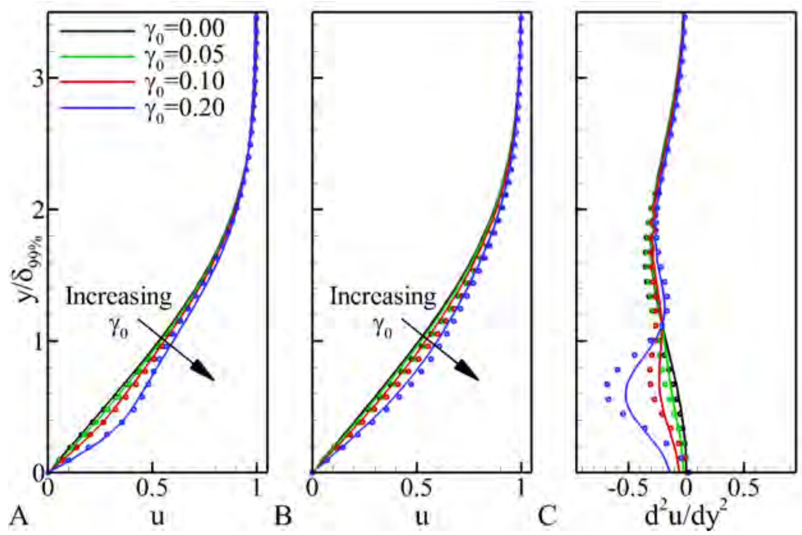

Figure 3-12. Comparisons between the simulated and modeled velocity profiles are shown for the downstream profiles at A) x=0.01 and B) x=1.1 presented in Figure 3-3. The values of γ_0 listed indicate which CFD simulation the velocities fields are being extracted from and matched to. The values of γ and η vary in order to fit to the model. C) A comparison of the second derivative of $\bar{u}$ at x=1.1 for the boundary layer profiles extracted from the CFD and generated by the model.

Agreement between the boundary layer profiles is better farther downstream of the actuators (at $x = 1.1$, as compared to $x = 1.01$, Figure 3-12A and B), where the boundary layer profiles do not exhibit a large overshoot due to momentum addition. The local parameters for the model are $\gamma < 0.20$ and $0.64 < \eta < 0.83$ at $x = 1.01$ (Figure 3-12A) and $\gamma < 0.14$ and $1.00 < \eta < 1.15$ at $x = 1.1$ (Figure 3-12B). The co-flow boundary layer profiles seen farther downstream of the plasma actuator are much more similar to those in the common literature than those seen very close to the plasma actuator, as such, calculations using the low order model of the boundary layer profile will use comparable values of γ and η.

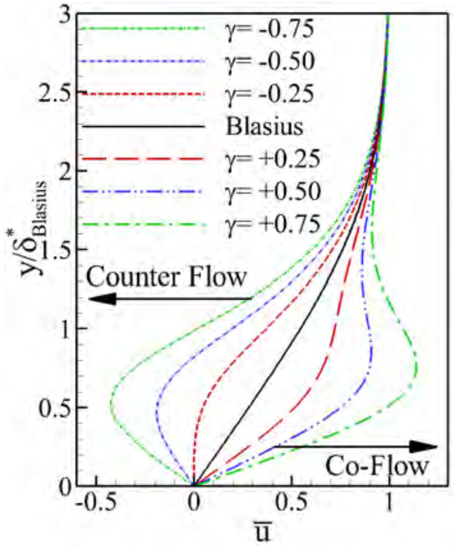

Figure 3-13. Boundary layer profiles used in the calculations, with $\eta = 1.0$ and varying values of γ.

It should be noted that there are now two displacement boundary layer heights relevant to the boundary layer stability, both of which are important for different reasons. From a flow control perspective, the scaling based on the boundary layer component (δ^*_{BL}, i.e. the Blasius boundary layer) of the combined velocity profile is most relevant. Holding this boundary layer height constant, momentum can be added or subtracted from the flow and the changes in the boundary layer's stability properties can be examined. When it comes to understanding the relevant physics, the displacement boundary layer height based on the combined boundary layer velocity profile (δ^*) is more relevant, as it is this boundary layer height defined by the velocity profile.

3.3.1 Additional Instability Modes

In addition to the viscid, convective instability associated with boundary layers (the TS mode), additional instabilities may also be present.

Previous studies of the effect of DBD actuation on boundary layer stability have focused on the co-flow orientation of the plasma actuation for flow stabilization. However, there are instances where flow destabilization is a goal of flow control. In these instances, operating the plasma actuator in a counter flow manner may be of use. Just as co-flow actuation injects momentum into the boundary layer and stabilizes it, counter flow actuation removes momentum from the boundary layer and should destabilize the boundary layer. In addition to removing momentum, for high enough levels of counter flow actuation (that is large, negative values of γ), flow separation and reversal may occur. This flow reversal, while not a requirement of an absolute instability, suggests that one may be present, adding another instability mode to the existing convective instability associated with ZPG boundary layers. Flow regimes (with respect to γ and η) at which flow reversal may occur are shown in Figure 3-14, which are evaluated using the present model of the plasma modified boundary layer profile.

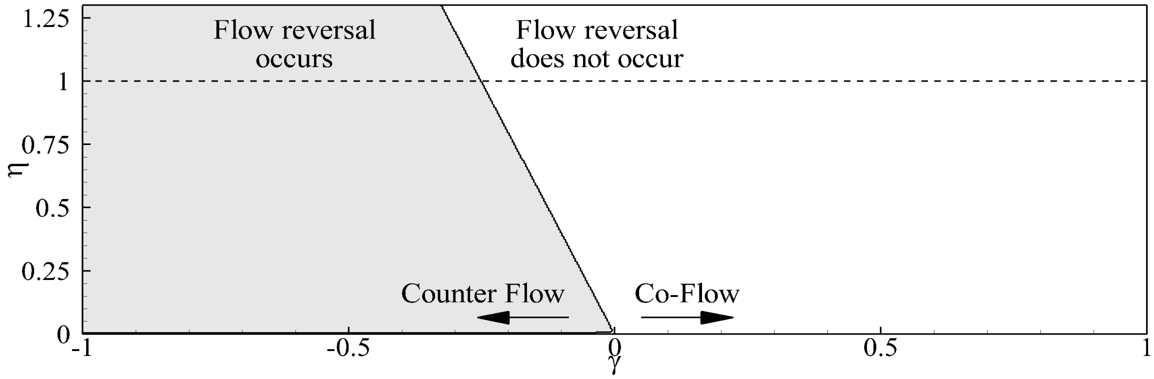

Figure 3-14. Region where flow reversal occurs in the boundary layer profile.

Examining the different boundary layer velocity profiles generated by the simulation and the model, it can be seen that inflection points may occur in the velocity profile (Figure 3-12C). While an inflection point does not necessarily indicate that an inviscid instability is present, it does raise suspicions that one may exist. Fjørtoft's criterion is a stricter condition for the presence of an inviscid instability (Equation 2–20). Applying this criterion to the many boundary layer profiles computed for determining whether flow reversal had occurred, it can be seen that there is only a small region in the (γ, η) plane where Fjørtoft's criterion is not met (Figure 3-15). This result suggests that the region for stabilizing flow control is limited, and that only slight levels of co-flow actuation can be used for this purpose. If too large of a co-flow actuation is applied, then inviscid instabilities will become a significant problem.

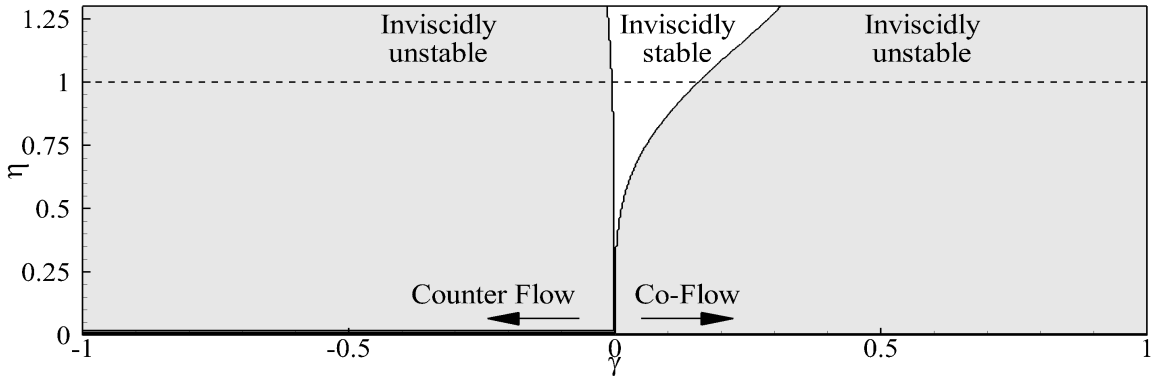

Figure 3-15. Region where Fjørtoft's criterion is met.

3.3.2 Comparison Between Computed Boundary Layer Profiles and The Model

Before performing a large number of calculations, it would be beneficial to compare the stability properties of the computed boundary layer profiles with those generated by the model. This comparison would be beneficial in establishing the validity of the present model for this type of calculation. For this calculation, the boundary layer profiles shown in Figure 3-12B have been chosen for examination. At this point, $Re_x = 110,000$ and $Re_{\delta*} = 556$. While these profiles may not be the most optimal due to their closeness to the plasma actuator, they exhibit enough variation in the boundary layer profile to determine whether or not the model and the computed boundary layer profiles predict similar behavior. The exact parameters used for the model are given in Table 3-2.

Table 3-2. Parameters to compare the boundary layer velocity profile flow model to the simulated flows.

Case	γ	η
γ_0=0.05	0.0126	1.333
γ_0=0.10	0.0360	1.318
γ_0=0.15	0.0656	1.298
γ_0=0.20	0.0989	1.183

In comparing the result of the two models, it should be noted that both the eigenmodes and the eigenvalues should be considered, as they together predict the relevant physics. Comparing the eigenvalues (Figure 3-16), it can be seen that the error of the real and imaginary components is less than 20% of the magnitude of the critical eigenvalue, and for most of the comparison cases is less than 10%, especially at higher wavenumbers. Further comparing the results, it can be seen that the general trends of the frequency and growth rate with regard to the increase in the magnitude of the plasma actuation (increasing γ_0), as well as the streamwise wave number, are comparable for the boundary layer profiles extracted from the CFD simulations and for the model.

Examining the eigenmodes (Figure 3-17), it can be seen that the general shape of the eigenmode is comparable for the boundary layer profiles extracted from the CFD simulations and those generated by the model.

3.3.3 Linear Stability Using the 1D Flow Model

The hypotheses developed in Section 3.3.1 suggest that a number of different effects could occur to the flow stability as a function of the local velocity ratio, γ. Different instabilities may occur, and significant changes to the nature of the instabilities may occur as the effect of the momentum injection is varied. For these calculations, the model of the boundary layer flow developed in Section 3.3 is used, as it affords more ease and flexibility in generating boundary layer profiles than the CFD based approach used in Section 3.2.

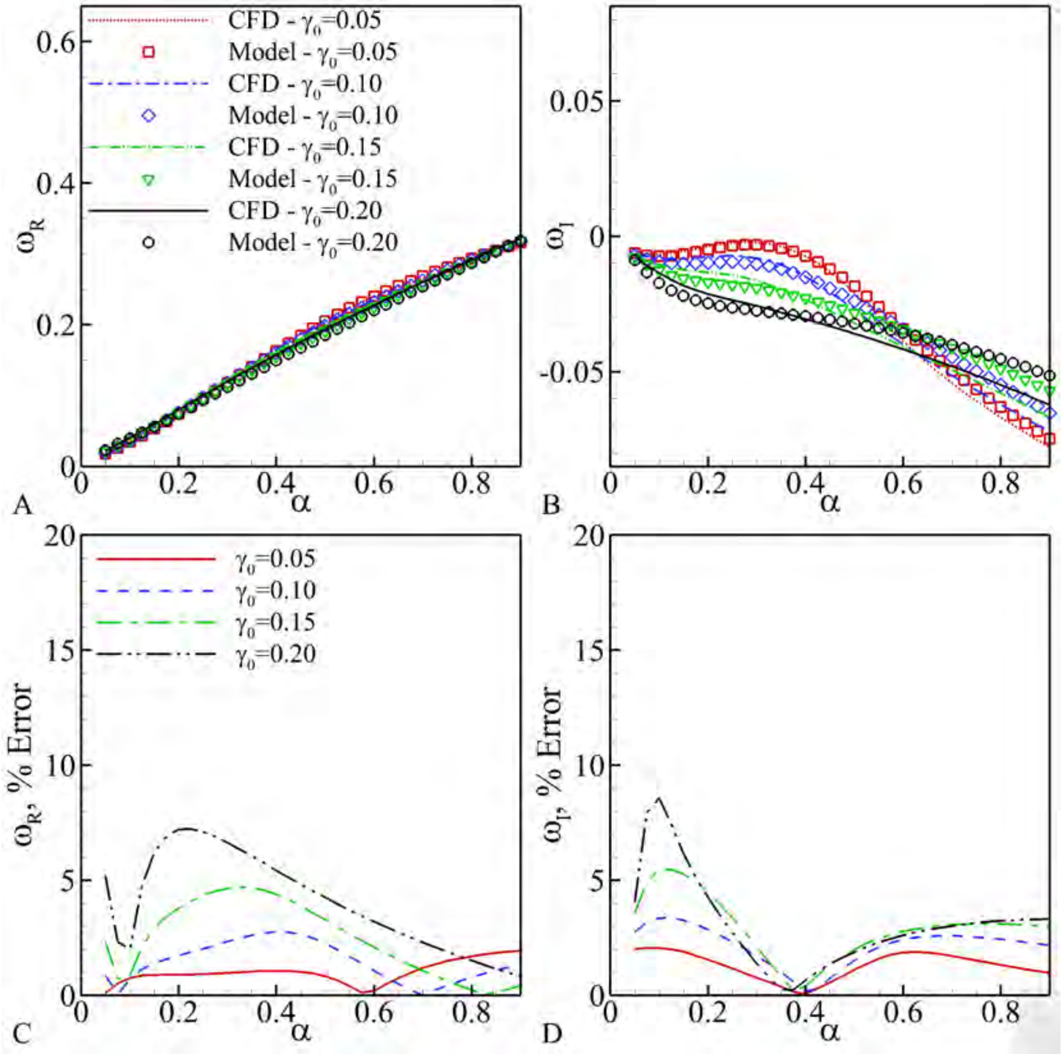

Figure 3-16. Comparison and error between the critial eigenvalues of boundary layer profiles from the simulations and the model. A) Real and B) imaginary components of the critical eigenvalues and percentage error of the C) real and D) imaginary components of the eigenvalue for the boundary layer profiles extracted from the CFD simulations and the model of the boundary layer profile.

In order to determine which instabilities may exist, a parametric study is presented in order to determine the effects of co-flow and counter flow actuation on the different eigenmodes of the boundary layer. The eigenvalues of the flow are computed for the case of $\eta = 1.0$ and $\alpha = 0.3$ for various Reynolds numbers and varying the level of actuation from $\gamma = -0.5$ to $\gamma = 0.5$. The value of γ for which the eigenvalues are computed has been varied slowly ($\Delta\gamma = 0.02$) in order to ensure that smooth behavior

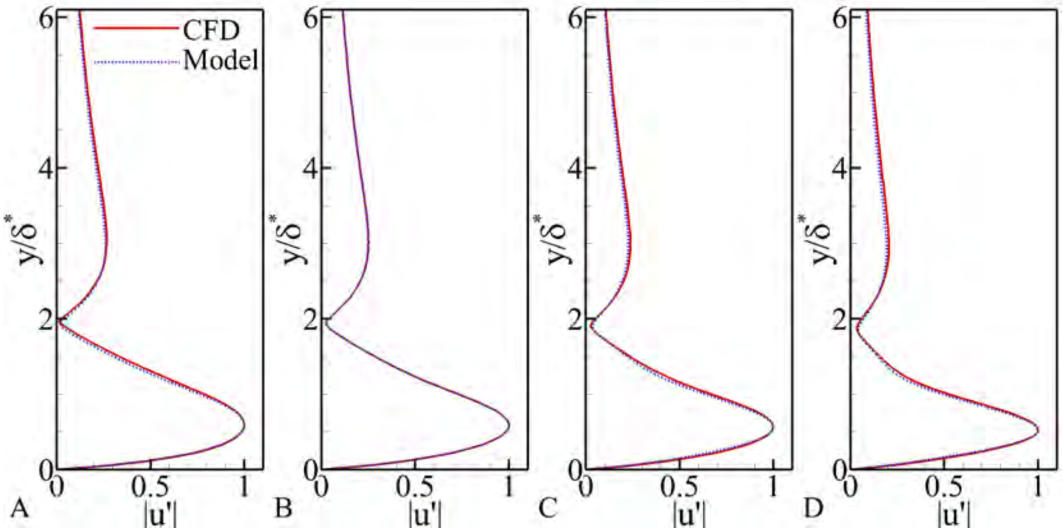

Figure 3-17. Comparison of the eigenmodes from the simulations and the model. A) $\gamma_0 = 0.05$, B) $\gamma_0 = 0.10$,C) $\gamma_0 = 0.15$ and D) $\gamma_0 = 0.20$ for $\alpha = 0.3$ for the boundary layer profiles shown in Figure3-12B.

exists. It can be seen that at the lowest Reynolds number examined ($Re_{\delta*} = 150$, Figure 3-18A), that the most unstable mode for a given value of γ varies continuously as γ varies from -0.5 to 0.5. However, at a higher Reynolds number ($Re_{\delta*} = 450$ and 600, Figures 3-18C and D), the most unstable mode changes as the value of γ is increased from -0.5 to 0.5. At the higher Reynolds number, the TS mode becomes more stable as co-flow actuation is applied and is destabilized as counter flow actuation is applied. Even though the TS mode is stabilized as co-flow actuation is applied, a different mode, which had previously been very stable, becomes unstable as this type of flow control is utilized.

It could be assumed that these eigenmodes are moving in the complex plane as the dispersion relationship which controls them is varied with respect to the Reynolds number. However, it can be seen that these two branches of the dispersion relationship intersect (Figure 3-18B) and then trade portions of their branch to each other as the Reynolds number is changed. The critical point at which this occurs is $Re_{\delta*,\ Blasius} = 315$ and $\gamma = 0.0675$ at the point $\omega = 0.155 - i0.495$ for the wavenumber $\alpha = 0.3$ (this value of α was not optimized to find the absolute lowest value of $Re_{\delta*}$ where this effect occurs). There may be a number of different implications with this branch switching. The implication most relevant to this study is that at very low Reynolds numbers, only a single eigenmode is relevant to the stability of these combined wall jet and boundary layer flows, but at moderate to high Reynolds numbers, two separate modes exist that are connected to each other.

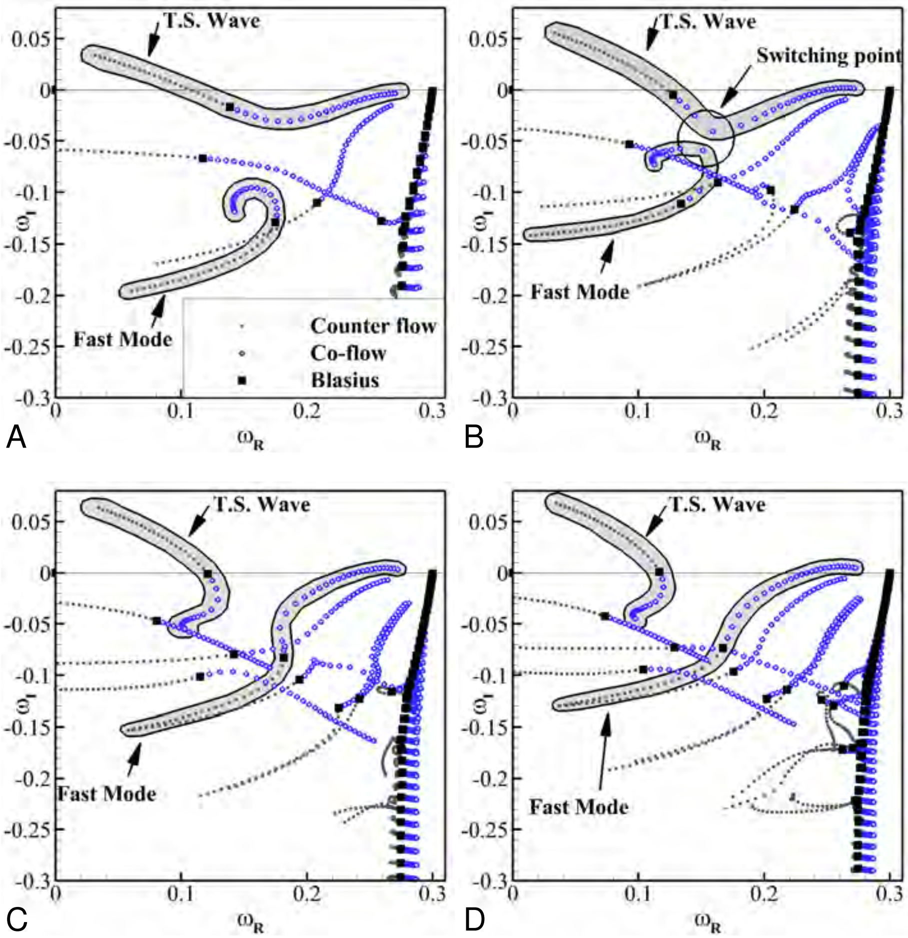

Figure 3-18. Eigenspectra of the model as a function of γ ($-0.5 < \gamma < 0.5$) for $\alpha = 0.3$ and a boundary layer height ratio of $\eta = 1.0$ for A)$Re_{\delta^*,Blasius} = 150$, B)$Re_{\delta^*,Blasius} = 300$, C)$Re_{\delta^*,Blasius} = 450$, and D)$Re_{\delta^*,Blasius} = 600$. Grey dots indicate eigenvalues for a certain counterflow velocity profile. Black dots indicate eigenvalues for a certain co-flow velocity profile.

3.3.4 Co-Flow Actuation ($\gamma > 0$)

Examining the effects of co-flow actuation, it is expected that this manner of operation will stabilize the boundary layer up to a certain point, above which, inviscid instabilities will become relevant and the flow will be destabilized. Neutral stability curves have been calculated for the cases of positive γ and are shown in Figure 3-19. Two different scalings based on the displacement boundary layer height and the displacement height of Blasius component of the combined velocity profile are used. However, neither of these scalings provide a sufficient collapse of the data. These neutral stability curves confirm that there are two separate modes which can become unstable, with widely varying properties. For the case of co-flow actuation, these two modes can be separated as being a (slow) TS wave and a (fast) outer mode, based on the real phase speed ($c_R = \frac{\omega_R}{\alpha}$). Examining the velocity profiles of these waves (Figure 3-20), it can be seen that the structure of the waves is different. The shape of TS mode is not independent of the plasma actuation, but it does retain its basic shape as the magnitude of the wall jet is varied. The faster mode shows a stronger dependence on the plasma actuation. As the momentum injection effects become more and more pronounced, the shape of this outer eigenmode also changes, indicating that this faster mode is strongly coupled to the momentum injection, and more sensitive to the magnitude of the wall jet.

This second mode does not become relevant until the wall jet effects in the boundary layer reach a certain level. From the computations of Fjørtoft's theorem this effect should occur at $\gamma = 0.153 \pm 0.003$. When the flow stability is examined in the inviscid limit ($Re \to \infty$) using the current eigenvalue method, the critical value is found to be $\gamma = .14375 \pm 0.006$. The viscid results (a sampling of which are shown in Figure 3-19) indicate that the inviscid instabilities become relevant near $\gamma = 0.156 \pm 0.006$. In all, there is reasonably good agreement at what point this mode should become important between these different methods and that this mode is inviscidly unstable.

Examining the structure of the outer mode as the wall jet component of the model becomes increasingly larger (i.e. increasing γ), the shape of the perturbation takes on a three maxima structure (Figure 3-20B) comparable to the three maxima structure of wall

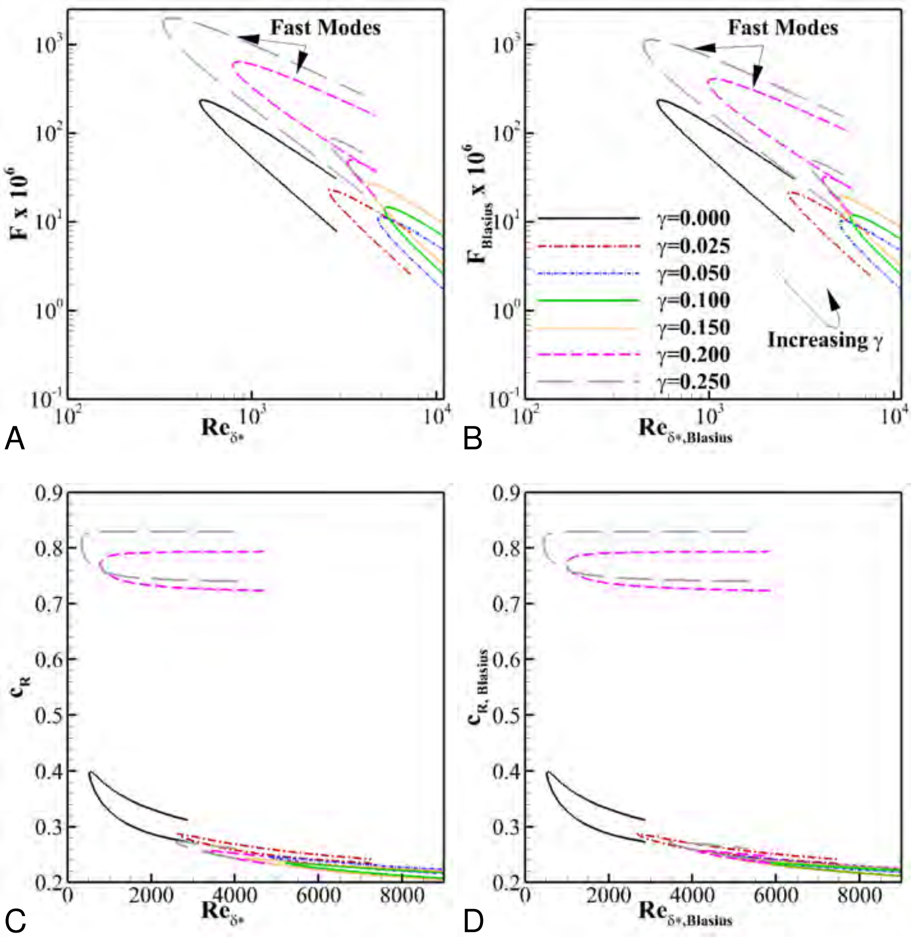

Figure 3-19. Neutral stability curves in terms of the A,B) reduced frequency, $F = \omega_R/Re$, and the C,D) phase velocity, $c_R = \omega_R/\alpha$ scaled by the displacement boundary layer heights of the A,C) combined velocity profile and the B,D) Blasius component of the velocity component. The TS waves are indicated by the solid lines. The outer mode is indicated by the grey lines.

jet instabilities (Amitay & Cohen, 1997; Mele *et al.*, 1985). Mele *et al.* (1985) and Amitay & Cohen (1997) also calculated neutral stability curves for the two instabilities present in wall jets (both of which have a three maxima structure), the results of which suggest that the growth mechanisms for the wall jet instabilities are inherently inviscid in nature, just like the outer mode instability. These two similarities suggest that this instability has more to do with wall jet component of the velocity profile than the combined boundary layer velocity profile, though there are modifications due to the addition of the boundary layer flow.

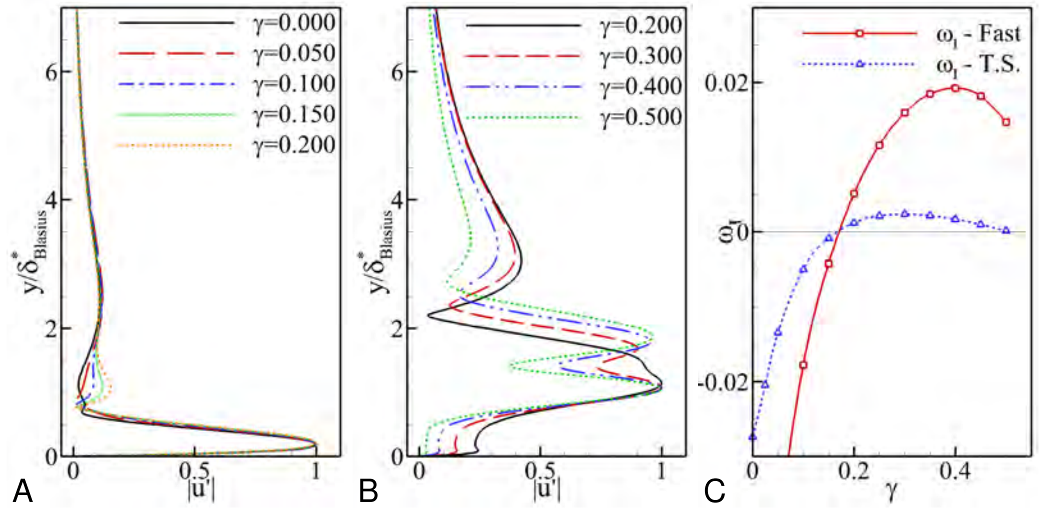

Figure 3-20. Eigenmodes of the A) TS and B) outer instabilities for the conditions of $Re_{delta*,\ Blasius} = 4000$ and $\alpha = 0.5$. C) The stability of the modes is also shown for reference.

3.3.5 Counter Flow Actuation ($\gamma < 0$)

If the plasma actuator is oriented in the opposite direction such that momentum is removed from the flow, it is expected that the boundary layer will be destabilized relative to the Blasius boundary layer profile. Neutral stability curves have been calculated for the case of counter flow operation (Figure 3-21). These calculations show that this method of operation is highly destabilizing, reducing the critical Reynolds number more than an order of magnitude from $Re_{\delta *} \approx 520$ for the Blasius boundary layer ($\gamma = 0$) $Re_{\delta *} < 30$ ($\gamma = -1$).

It was noted in Section 3.3.1, that the velocity profiles for counter flow operated plasma actuation may cause flow reversal. With this flow reversal, there is the implication that some eigenmodes of the flow may travel upstream or remain stationary. Within this subset of modes which remain stationary, the possibility of an absolute instability exists. Furthermore, the neutral stability curves (Figure 3-21) indicate that for sufficiently large, negative values of γ, there are unstable modes with zero real phase velocity (as $c_R = \omega_R/\alpha$). However, this observation does not satisfy the more rigorous

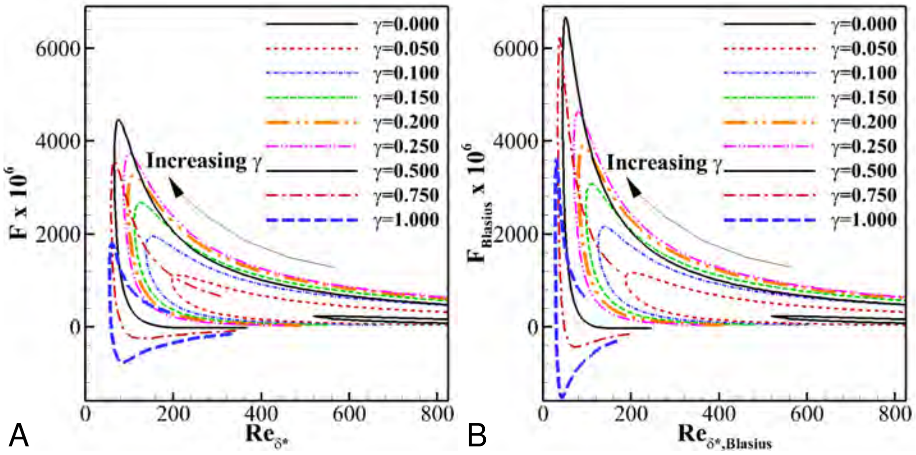

Figure 3-21. Neutral stability curves of the counter-flow modified boundary layers where $\eta = 1.0$. A)scaled by δ^* and B) $\delta^*_{Blasius}$.

requirements of an absolute instability as defined by Briggs (1964) and Bers (1972). These requirements for an absolute instability are that:

1. There exists a dispersion relationship connecting ω and α, defined as $\mathcal{D}(\omega, \alpha) = 0$. In the complex domains of ω and α, there must be saddle points where $\partial\omega/\partial\alpha = 0$, i.e. the group velocity equals zero.
2. The saddle points must be pinch points of an upstream and downstream traveling mode.
3. The saddle point must also be unstable. That is, $\omega_I > 0$ at the saddle point.

Constructing a "net map" allows for the visualization of the dispersion relationship (which is a function of the velocity profile and Reynolds number) in terms of the complex values of α and ω (Figure 3-22). A saddle point is immediately visible in each of these plots. It can be seen that as the Reynolds number is increased, the value of ω_I at this point increases from negative to positive, which satisfies the third requirement for an absolutely instability. It can be seen that above a critical Reynolds number, $Re_{\delta^*,abs.crit}$, the previously convective instability becomes an absolute instability.

This absolute instability presents a conflicting view of the viscous convection instability. Measurements of the eigenvalues as shown in Figure3-18 indicate that instabilities seen with counter flow actuation are direct modifications of the Tollmien-Schlichting

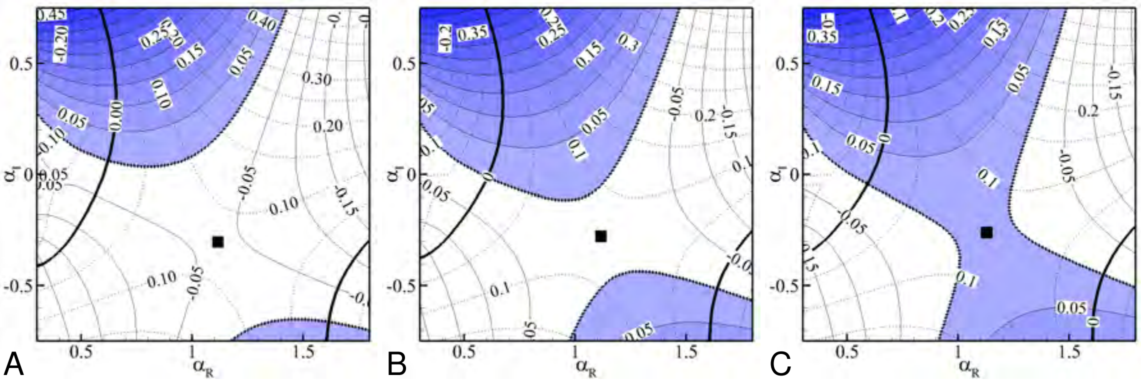

Figure 3-22. Net maps for low Reynolds number counter-flow modified boundary layers. A) $Re_{\delta^*,Blasius} = 26$, which is absolutely stable , B) $Re_{\delta^*,Blasius} = 30$, which is convectively unstable, and C) $Re_{\delta^*,Blasius} = 32$, which is absolutely unstable for $\gamma = -1.0$ and $\eta = 1.0$. Solid lines indicate the contours of ω_R. Dashed lines indicate the contours of ω_I. The values of ω at the pinch points are $\omega = 0.0926214 - i0.046581$, $\omega = 0.0885969 - i0.010166$, and $\omega = 0.0867067 + i0.00496014$, which are marked by the black squares.

wave as momentum is injected in the direction opposing the free stream velocity. However, Fjørtoft's criterion (and the calculations of the flow instability in the inviscid limit) suggest that an inviscid instability should be present, even for small, negative values of γ. When one considers the growth rates of instabilities occurring from counter flow operation (shown in Figure 3-18), the evidence pushes more towards this instability being inviscid in its behavior. Large growth rates are normally associated with inviscid instability, and the calculated growth rates are significantly higher for counter flow actuation than they are for a normal Blasius boundary layer and other known viscid instabilities.

3.3.6 Comparison of the Onset of Different Stability Modes

Combining all of the stability results that have been garnered from this model of the flow, it can be seen that there exist a wide variety of phenomena that occur within the combined wall jet/boundary layer velocity profile. The different critical Reynolds numbers have been plotted as a function of γ in Figure 3-23. It can be seen that the TS wave remains present for all values of γ, though for larger levels of co-flow actuation, the

TS instability is stabilized relative to its importance in the Blasius boundary layer, only being present at significantly higher Reynolds numbers. The upper limit on improving the stability of the boundary layer appears to occur around $\gamma = 0.075$, with the critical Reynolds number being increased from $Re_{\delta^*,Blasius} = 520$ for the non-actuated flow to $Re_{\delta^*,Blasius} = 5818$. For the counter flow actuation, the TS wave is destabilized, and becomes unstable at Reynolds numbers a full order of magnitude lower than that of the Blasius boundary layer. Furthermore, for sufficiently strong counter flow actuation, an absolute instability becomes significant.

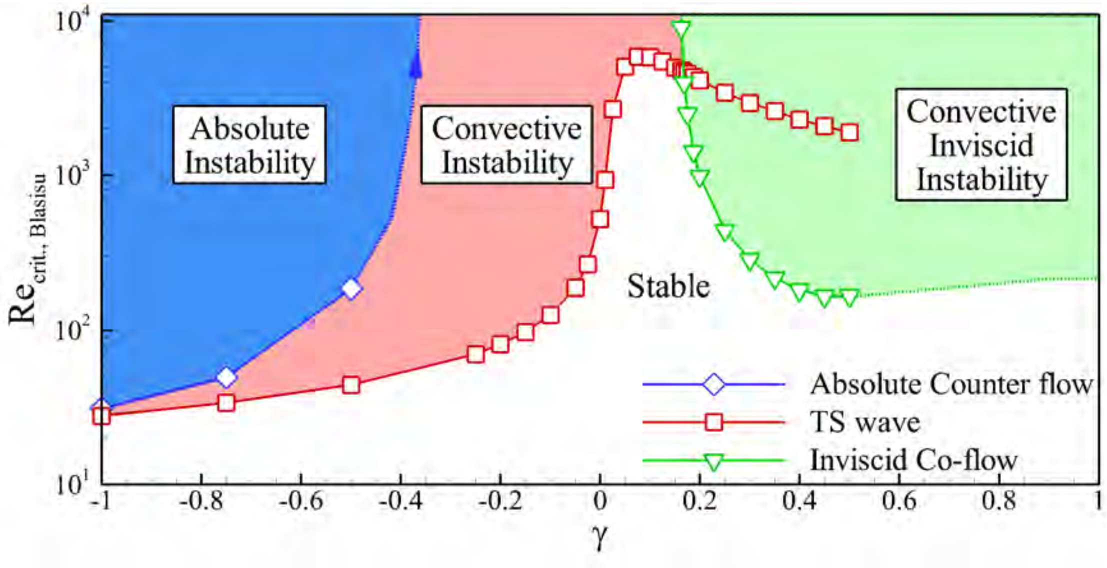

Figure 3-23. A comparison of the critical Reynolds numbers of the different instabilities compared to γ for $\eta = 1$.

3.3.7 Comparison to the Universal Correlation

It can be seen that both co-flow and counter flow operation of the plasma actuators have a profound effect on the boundary layer stability. However, other boundary layer profile modifications can have an equally strong effect on the flow stability. It is thought that there is a certain universal correlation between the flow stability and the shape factor (Wazzan *et al.*, 1979). It can be seen in Figure 3-24 that for the convective viscid instability, the critical Reynolds numbers reached as part of this study are in agreement with other boundary layers when compared via the shape factor, H.

For small levels of actuation, these stability limits are comparable to other boundary layer profiles. However, as larger levels of plasma actuation are examined, it can be seen that they deviate from the behavior seen in other boundary layer profiles. This effect is likely due to the wall jet component of the velocity profile becoming significant relative to the boundary layer component, and transforming the flow in such a way that it cannot be compared to other boundary layers. Data is presented for the critical Reynolds number scaled by both $\delta^*_{Blasius}$ and the calculated value of δ^* for the velocity profile. The choice of Reynolds number scaling does seem to make a difference in matching the current results to the universal correlation. However, once the velocity profile allows for significant wall jet like effects to develop, the critical Reynolds number diverges from that of more traditional boundary layers.

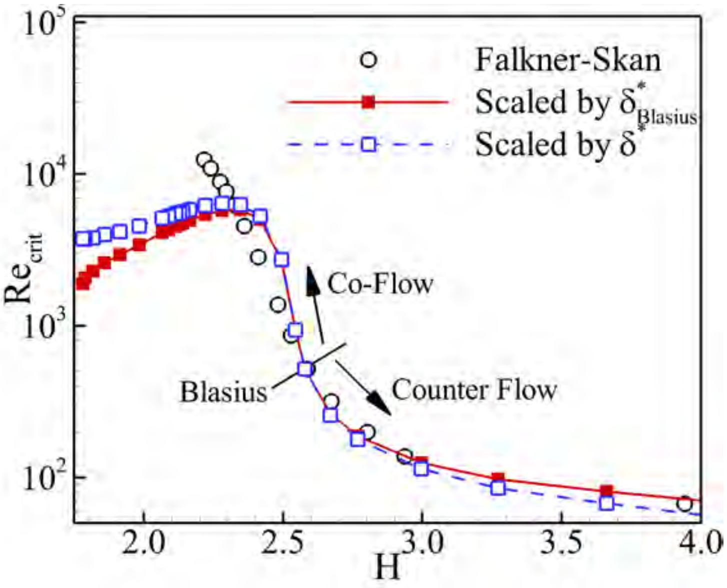

Figure 3-24. Comparison of current results to other boundary layer profiles. Falkner-Skan data taken from Wazzan *et al.* (1979).

3.3.8 Unsteady Effects

In all of these analysis, the body force generated by the plasma actuator has been treated as a steady source of momentum. However, this is a point of inaccuracy that is necessary for the existing stability formulations, which cannot handle unsteady flow.

In reality, the momentum addition provided by DBD actuation is inherently unsteady, as the devices are powered by a high frequency AC signal. Normally the time scales associated with plasma actuation are on the order of 10's of kHz, while those associated with a low speed flow are on the order of 100's of Hz. These two time scales are separated by two orders of magnitude, and it is often assumed that only the mean component of the momentum addition is relevant to the flow control. It should be noted that this order of magnitude approximation is still based around the use of a steady flow for the stability analysis. For a more accurate analysis, the unsteady effect of the plasma actuation on the boundary layer would need to be taken into account through a Floquet stability analysis.

The present analysis of instabilities relevant to the plasma actuated flow indicates that potential inviscid and absolute instabilities may occur at significantly higher frequencies than the TS wave. As such, assumptions based on the separation of time scales must be revisited in order to establish when they may or may not be valid. The non-dimensional frequency used to characterize the present instabilities can be defined using (dimensional) parameters as

$$F = \frac{2\pi f \nu}{u_\infty^2} \tag{3–11}$$

may be arranged to provide an upper limit on the speed where plasma actuation is able to be used without self-exciting the flow $(u_{\infty,NE})$. Performing this rearrangement, the upper limit is

$$u_{\infty,NE} < \sqrt{\frac{2\pi f_{plasma}\nu}{F_0}} \tag{3–12}$$

For each of the three instabilities, rough estimates of the baseline non-dimensional frequency, F_0, can be established in order to provide order of magnitude estimates as to when the plasma actuation will begin to excite these modes on its own, which are provided in Table 3-3. These frequencies are case specific, depending on the total level of momentum added into the flow, as well as the Reynolds number, so only approximate values are provided. For the other variables, dimensional parameters are $\nu = 1.5 \times 10^{-5} m^2/s$, and $f_{plasma} = 10kHz$. The results of this order of magnitude analysis indicate that even for relatively low speed flows, the inviscid and counter flow actuated TS instability mechanisms may be self excited by the plasma actuation. At moderately higher velocities (upwards of 68 m/s), the DBD actuation may even excite the TS mode when co-flow actuation is employed, at which point this type of actuation is actively causing the flow to transition, not stabilizing it.

Table 3-3. Approximate frequencies for different instability modes and the free stream velocity where the plasma actuation will begin to excite these modes.

Instability Mode	$F_0 \times 10^6$	$u_{\infty,NE}$ (m/s)
TS Wave - Co-Flow	200	68.4
TS Wave - Counter-Flow	2000	21.7
Inviscid Instability	1000	30.7

When it comes to stabilizing a flow using DBD plasma actuation, this result places an approximate upper limit on the free stream velocity where success may be found; that is $u_\infty < u_{\infty,NE}$. However, when attempting to accelerate the laminar to turbulent transition process at higher velocities (i.e. $u_\infty > u_{\infty,NE}$), it appears that the DBD actuation has the potential to simultaneously destabilize the flow and to generate the unstable perturbations. This self excitation may be one reason why these other instability modes have not yet been reported in the literature, and it may also provide some additional control authority at higher velocities when attempting to destabilize the boundary layer at higher velocities.

3.4 Conclusions

In this chapter, local stability analysis has been utilized to study the stability properties of boundary layer profiles downstream of a plasma actuator. Boundary layer profiles from CFD simulations, as well as a low order model have been examined, indicating that the addition or removal of momentum from the boundary layer can have wide ranging effects on the stability properties of the boundary layer.

In order to study specific boundary layer profiles, boundary layers have been simulated incorporating the effects of plasma actuation through a physics based approximation of a DBD plasma actuator, operated in a co-flow manner, continuously adding momentum into the boundary layer. Based on these flows, stability calculations suggest that the onset of instabilities (based on the critical Reynolds numbers with respect to x and δ^*) can be pushed much farther downstream as additional momentum is added into the boundary layer. In terms of the critical streamwise Reynolds number, the growth of instabilities can be pushed upwards of 50% farther downstream as compared to where they would normally occur.

Based on the boundary layer profiles collected from the CFD simulations, a low order model of the plasma modified boundary layer profiles has also been developed. This model allows for boundary layer profiles to be rapidly generated, allowing for much easier parametric studies. This model has been characterized with respect to the physics of boundary layer momentum addition as well as how accurately it predicts the stability properties of individual boundary layer profiles. Parametric studies have been performed using this model for co-flow and counter flow oriented plasma actuators.

Based on the parametric studies performed, evidence for a viscid absolute instability and an inviscid instability has been discovered. Considering the TS wave, dramatic increases and decreases in the critical Reynolds number are predicted to be possible based on this low order model of the boundary layer, extending an order of magnitude upwards and downwards of the critical stability of the Blasius boundary layer, depending on whether momentum is added or removed from the flow. Even as the boundary layer is stabilized or destabilized, the critical Reynolds number of boundary layer profile still correlates well with respect to the universal correlation of (Wazzan *et al.*, 1979), up to a certain point.

In all, these local stability analyses suggest that the addition of momentum into the boundary layer can have very dramatic effects on the boundary layer stability. The physics that can be examined using this type of analysis is limited, but these results suggest that further study using more sophisticated methods should be employed, specifically those that are able to handle the two dimensional nature of this flow, which is examined in Chapter 4.

The results and discussion in the present chapter have been presented and published in several documents (Riherd & Roy, 2013*b*; Riherd *et al.*, 2012, 2013).

CHAPTER 4
BI-GLOBAL STABILITY ANALYSIS OF A OF A PLASMA ACTUATED BOUNDARY LAYER

In Chapter 3, it was shown that local stability analysis methods predict flow stabilization of a boundary layer when plasma actuators are used to add momentum into the flow. However, in the region immediately around the plasma actuation, the assumptions required for a local stability analysis fail to hold (Figure 3-6). In this region, two-dimensional stability methods must be employed to study the stability properties.

In the last decade, matrix based bi-global stability methods have finally reached a level of maturity such that they can be applied to non-trivial research problems. In the past, parabolized stability equations (PSE) (Bertolotti *et al.*, 1992; Herbert & Bertolotti, 1987) or DNS (Bertolotti *et al.*, 1992; Fasel & Konzelmann, 1990) have been employed to study the stability of boundary layer flows. More recently, matrix based bi-global stability methods have been employed to study these flows (Åkervik *et al.*, 2008; Alizard & Robinet, 2007; Brandt *et al.*, 2011; Sipp & Marquet, 2012). As compared to DNS and PSE based methods, matrix based stability methods simplify the analysis of the results, as the required linear algebra operations often produce the desired information (temporal growth rates, maximum transient amplification, eigenmodes, singular modes, etc.). The two-dimensional implementation provides addition accuracy over local methods, as non-parallel and flow development effects can be taken into account.

It is known that the two primary instability mechanisms in a boundary layer are the TS wave and boundary layer streaks, which are exponential and algebraic instabilities, respectively. The present work aims to describe the response of a boundary layer flow modified by plasma actuation to these types of instabilities, as well as to quantify the growth and decay rates of these perturbations over the length of the boundary layer using a bi-global stability analysis. Parametric studies are performed with respect to the magnitude of the plasma actuation, as well as frequency and spanwise wave number.

4.1 Bi-Global Stability Analysis of the Tollmien-Schlichting Wave

In order to study the growth of the TS wave with greater accuracy and in the near actuator region, a bi-global stability method has been employed. This model, while more robust than a local stability analysis, focuses on only fluidic effects; there is no feedback mechanism between the fluid and plasma present in this analysis.

4.1.1 Numerical Method for Bi-Global Stability Analysis

In order to determine the response the plasma modified boundary layer to oncoming TS waves, a bi-global stability approach is employed. The velocity and pressure fields can be decomposed into the steady equilibrium and perturbation components, where $u_i = \bar{u}_i + u_i'$ and $p = \bar{p} + p'$. Using this decomposition, the incompressible Navier-Stokes equations can be linearized around this steady point such that

$$\frac{\partial u_i'}{\partial x_i} = 0 \tag{4–1a}$$

$$\frac{\partial u_i'}{\partial t} + \bar{u}_j \frac{\partial u_i'}{\partial x_j} + u_j' \frac{\partial \bar{u}_i}{\partial x_j} + \frac{\partial p'}{\partial x_i} - \frac{1}{Re} \frac{\partial^2 u_i'}{\partial x_j^2} = 0 \tag{4–1b}$$

Assuming that these perturbations are periodic in time, such that $u_i' = \tilde{u}_i \exp\left(-i\omega t\right)$, the problem can be put into matrix operator form such that

$$i\omega \mathbf{B}\mathbf{u} = \mathbf{A}\mathbf{u} + \mathbf{f} \tag{4–2}$$

where

$$\mathbf{u} = \begin{bmatrix} \tilde{u} \\ \tilde{v} \\ \tilde{w} \\ \tilde{p} \end{bmatrix}, \quad \mathbf{A} = \begin{bmatrix} \frac{\partial(\cdot)}{\partial x} & \frac{\partial(\cdot)}{\partial y} & i\beta & 0 \\ \mathcal{C} - \mathcal{D} + \frac{\partial \bar{u}}{\partial x} & \frac{\partial \bar{u}}{\partial y} & 0 & \frac{\partial(\cdot)}{\partial x} \\ \frac{\partial \bar{v}}{\partial x} & \mathcal{C} - \mathcal{D} + \frac{\partial \bar{v}}{\partial y} & 0 & \frac{\partial(\cdot)}{\partial y} \\ 0 & 0 & \mathcal{C} - \mathcal{D} & i\beta \end{bmatrix}, \quad \mathbf{B} = \begin{bmatrix} 0 & 0 & 0 & 0 \\ I & 0 & 0 & 0 \\ 0 & I & 0 & 0 \\ 0 & 0 & I & 0 \end{bmatrix} \tag{4–3}$$

The convection and viscous diffusion operators $\mathcal{C}$ and $\mathcal{D}$ are defined as $\mathcal{C} = \bar{u}\frac{\partial(\cdot)}{\partial x} + \bar{v}\frac{\partial(\cdot)}{\partial y}$ and $\mathcal{D} = \frac{1}{Re}\left(\frac{\partial^2(\cdot)}{\partial x^2} + \frac{\partial^2(\cdot)}{\partial y^2} - \beta^2\right)$. **f** indicates a complex periodic forcing to the system, and **u** is the response of the system to that forcing. The response of the system can be measured by solving the system of equations shown above such that

$$\mathbf{u} = [i\omega\mathbf{B} - \mathbf{A}]^{-1}\mathbf{f} \tag{4–4}$$

For the present study the periodic forcing term **f** represents a non-homogeneous boundary condition at the inlet of the domain.

4.1.1.1 Numerical discretization and boundary conditions

In order to perform these calculations, the matrix operations described in Equations 4–1a-4–3 are discretized on a semi-staggered mesh. The velocity fields and their gradients produced in Section 3.1.3 were interpolated onto this mesh. The meshes used to perform these stability calculations represention a portion of the domain used to calculate the base flows. Relative to the original domain, this subdomain is entirely downstream of the leading edge ($0.52 < x < 4.69$). The momentum equations are solved and velocity data is stored on a set of points coincident with the domain boundaries. The continuity equation is solved and pressure data is stored on the intermediate set of points. For the differencing, Chebyshev collocation methods are used in the y-direction. In the x-direction, 4th order accurate centered differencing is used for a majority of the domain. The exception to this is the streamwise convection term, $\bar{u}\frac{\partial(\cdot)}{\partial x}$. This term is up-winded using a 3rd order accurate finite difference stencil. Next to the boundaries, lower order stencils are used.

For boundary conditions, a TS wave is enforced at the inlet to the domain, examples of which are shown in Figure 4-1. Only two-dimensional TS waves are examined ($\beta = 0$), as those are known to be the most unstable (Squire, 1933). These TS waves are calculated using a local, spatial eigenvalue solver. The shape of the incoming TS wave is varied depending on the perturbation frequency. A sample of the inlet perturbations are shown in Figure 4-1. For the boundary layer wall and the free-stream, no slip conditions are employed. In the latter portion of the domain, a sponge region is implemented in order to damp the velocity perturbations as they approach the outlet. This sponge region effectively prevents the perturbations from reflecting off of the outlet and affecting the upstream flow.

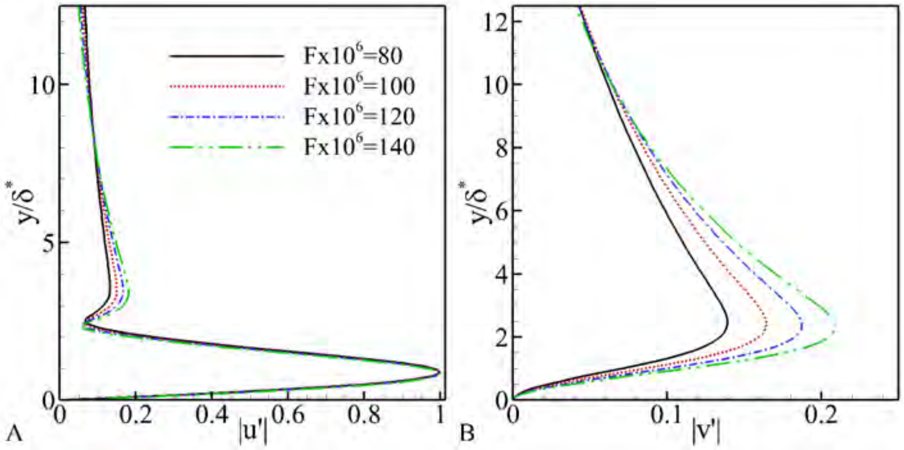

Figure 4-1. Perturbations enforced at the inlet of the domain at varying frequencies. A) u and B) v velocity components.

4.1.1.2 Grid resolution study

A grid resolution study has been performed in order to ensure that the problem is adequately resolved. The details of the domain and mesh parameters are indicated in Table 4-1. This study has been performed on the unforced boundary layer, but addition grid resolution studies for boundary layers where momentum addition was applied were also performed, indicating similar convergence.

In order to quantify the growth and decay of the TS wave as it propagates downstream, the magnitude of the perturbations along a line in the flow are measured, a sample of the results can be seen in Figure 4-2A. Examining the convergence of the results as a function of the streamwise grid density, it can be seen in Figure 4-2C that the results are approaching convergence as the mesh density increases.

Comparing the spatial exponential growth rates of these perturbations (Figure 4-2B), it can be seen that there is good agreement between the different meshes using

Table 4-1. Details of the grid resolution study performed for the linear TS wave calculations. The Very Fine-L, Fine-H, and Tall cases are identical.

Study	Case	n_x	n_y	L_x/δ_0^*	L_y/δ_0^*	$\Delta x/\delta_0^*$	$\Delta y_{wall}/\delta_0^*$
Streamwise resolution	Coarse-L	513	65	1061.7	40	2.0736	0.02409
	Medium-L	725	65	1061.7	40	1.4664	0.02409
	Fine-L	1025	65	1061.7	40	1.0368	0.02409
	Very Fine-L	1449	65	1061.7	40	0.7332	0.02409
Wall normal resolution	Coarse-H	1449	33	1061.7	40	0.7332	0.09631
	Medium-H	1449	49	1061.7	40	0.7332	0.04282
	Fine-H	1449	65	1061.7	40	0.7332	0.02409
Height	Short	1449	33	1061.7	20	0.7332	0.04815
	Medium	1449	49	1061.7	30	0.7332	0.03212
	Tall	1449	65	1061.7	40	0.7332	0.02409

this bi-global method. Comparisons can also be made with local stability methods, which predict similar behavior, though the exact values differ by a small amount. In order to make a good comparison with the bi-global stability analysis, the local growth rates have been normalized by the local boundary layer displacement height and multiplied by a factor of 2 to account for the energy (rather than velocity) perturbation growth. Convergence studies for the wall normal mesh density (Figure 4-2D) and domain height (Figure 4-2E) have also been examined, and show good convergence.

Based on this grid resolution study, all computations will be performed using the Very Fine-L mesh, and the magnitude of the boundary layer perturbations is assumed to be accurate to within a few percent.

4.1.2 Results

Comparing the perturbation flow fields in Figure 4-3, it can be seen that as the magnitude of the plasma actuation is increased, the perturbations are increasingly damped downstream of the plasma actuator.

The metric

$$A_0(x) = \frac{\int_0^\infty \left(|u'|^2 + |v'|^2\right) dy\Big|_x}{\int_0^\infty \left(|u'|^2 + |v'|^2\right) dy\Big|_{x=inlet}} \tag{4–5}$$

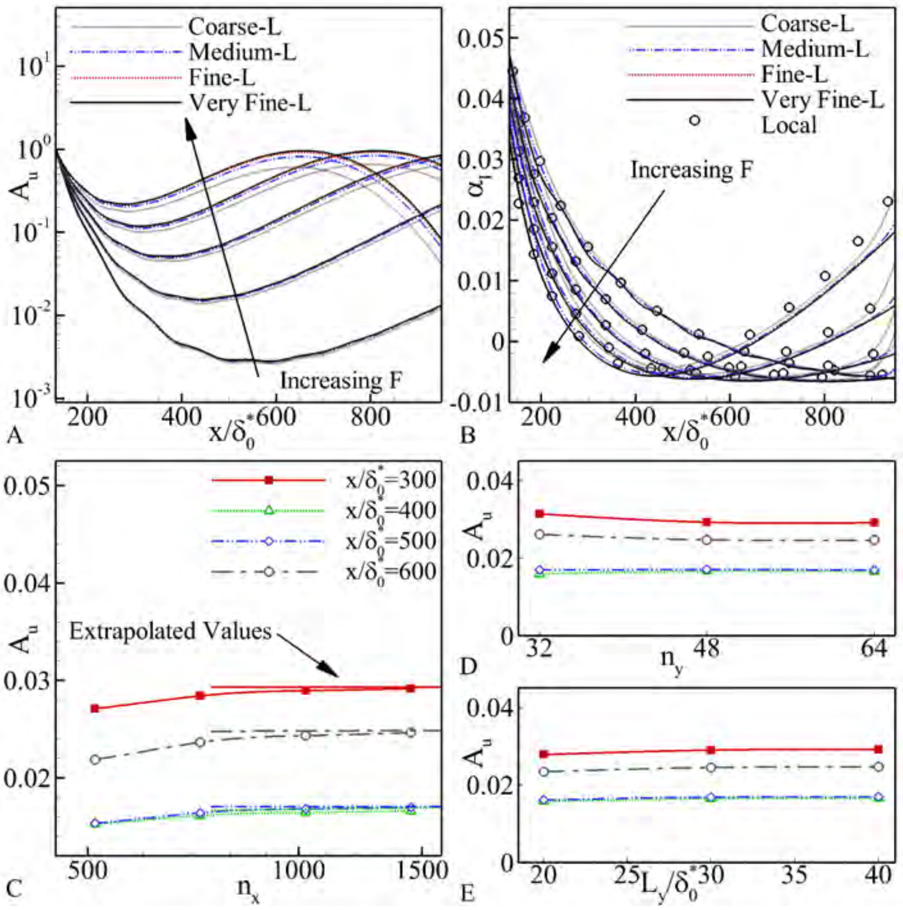

Figure 4-2. Convergence of amplitudes and spatial growth rates for the grid convergence study of the linear TS wave. A) amplitudes and B) spatial growth rates of the incoming TS waves for different mesh densities for 5 different frequencies. The convergence of the $F \times 10^6 = 150$ case can also be seen for the C) amplitudes D) spatial frequencies.

is used to quantify the magnitude of the boundary layer perturbation. This metric quantifies the amount of kinetic energy in the flow at a given point in x relative to the inlet.

Applying this metric, the magnitudes of the perturbations have been calculated, samples of which can be seen in Figure 4-4 for several different forcing frequencies. In examining the magnitudes of these perturbations, the amount of damping caused by the addition of flow wise momentum into the boundary layer is found to be significant. As the velocity ratio of the plasma actuation is increased, the magnitude of the energy perturbations are decreased by up to two orders of magnitude (only a single order of

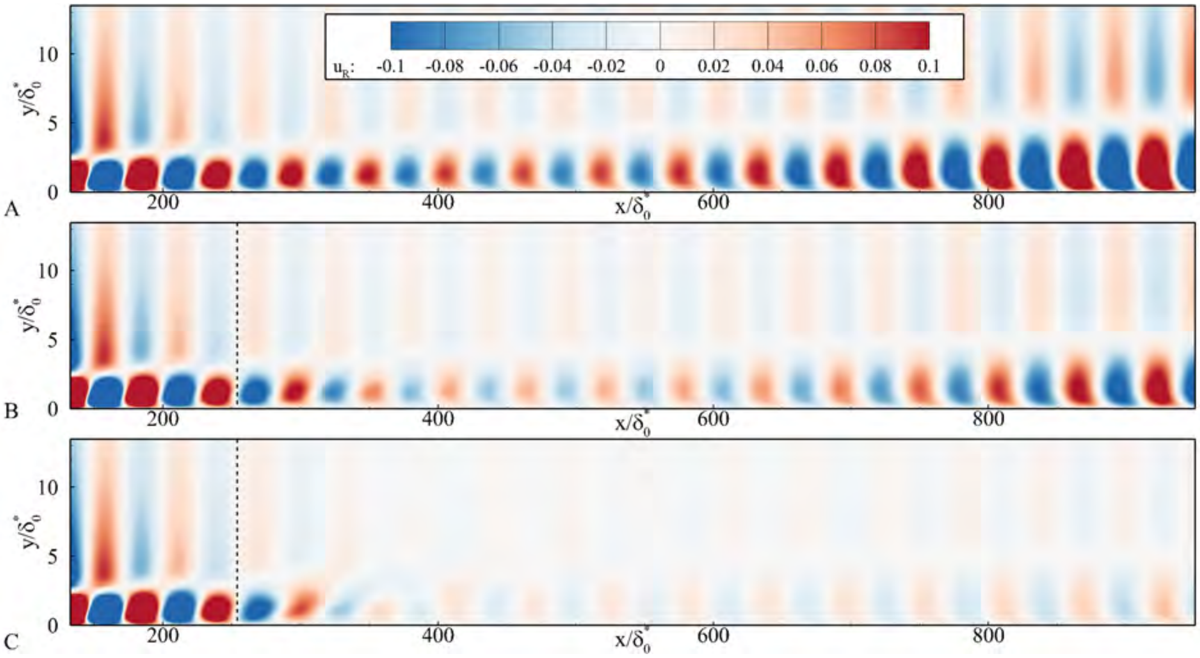

Figure 4-3. Real component of the u perturbation velocity for the non-dimensional frequency of $F \times 10^6 = 100$ and varying levels of plasma actuation. A) $\gamma_0 = 0.00$ (No plasma actuation), B) $\gamma_0 = 0.10$, and C) $\gamma_0 = 0.20$. The dashed line indicates the location of the plasma actuator. The contour values in this plot do saturate for $-0.1 < u_r$ and $0.1 > u_r$ in order to show greater detail for smaller values of the perturbation velocity.

magnitude for the velocity perturbations). In terms of N-factor (see Equations 2–22 & 2–23 and the related discussion), the damping of these perturbations is equivalent to a drop in the N-factor of approximately 2.3 relative to the non-actuated case. Considering that transition is normally assumed to occur in a boundary layer for an N-factor of 9 to 10 (van Ingen, 1956; Jaffe *et al.*, 1970), this damping of the perturbation could delay transition by a significant amount.

Based on this data, the growth rates of these perturbations can be calculated. The exponential growth rate is defined as

$$\alpha_I = -\frac{1}{A_u}\frac{dA_u}{dx} \tag{4–6}$$

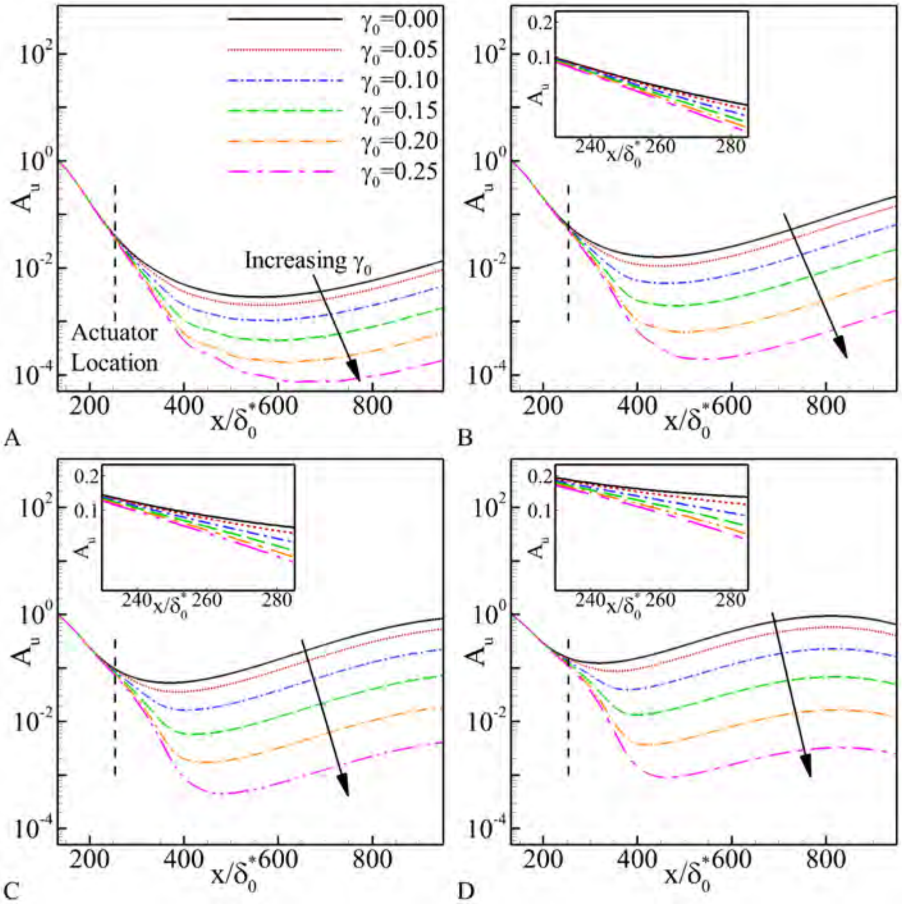

Figure 4-4. Magnitude of the TS perturbations at varying frequencies and as a function of the magnitude of the plasma actuation. A) $F \times 10^6 = 80$, B) $F \times 10^6 = 100$, C) $F \times 10^6 = 120$, and D) $F \times 10^6 = 140$. The vertical dashed line indicates the location of the actuator, and the inset figures are a close up of the near actuator region.

The growth rates for a number of cases are shown in Figure 4-5 for several different forcing frequencies. For these calculations, a negative value of α_I indicates instability (perturbation growth), while a positive value of α_I indicates stability (perturbation decay).

Examining the flow fields, perturbation magnitudes and exponential growth rates, it can be seen that the behavior of the TS wave is not homogeneous along the length of the boundary layer when plasma actuation is introduced into the boundary layer. Rather, there appear to be a number of distinct regions in the flow where this behavior changes. These regions can be described as the region upstream of the actuator, the regions immediately around and downstream of the actuator where the momentum addition

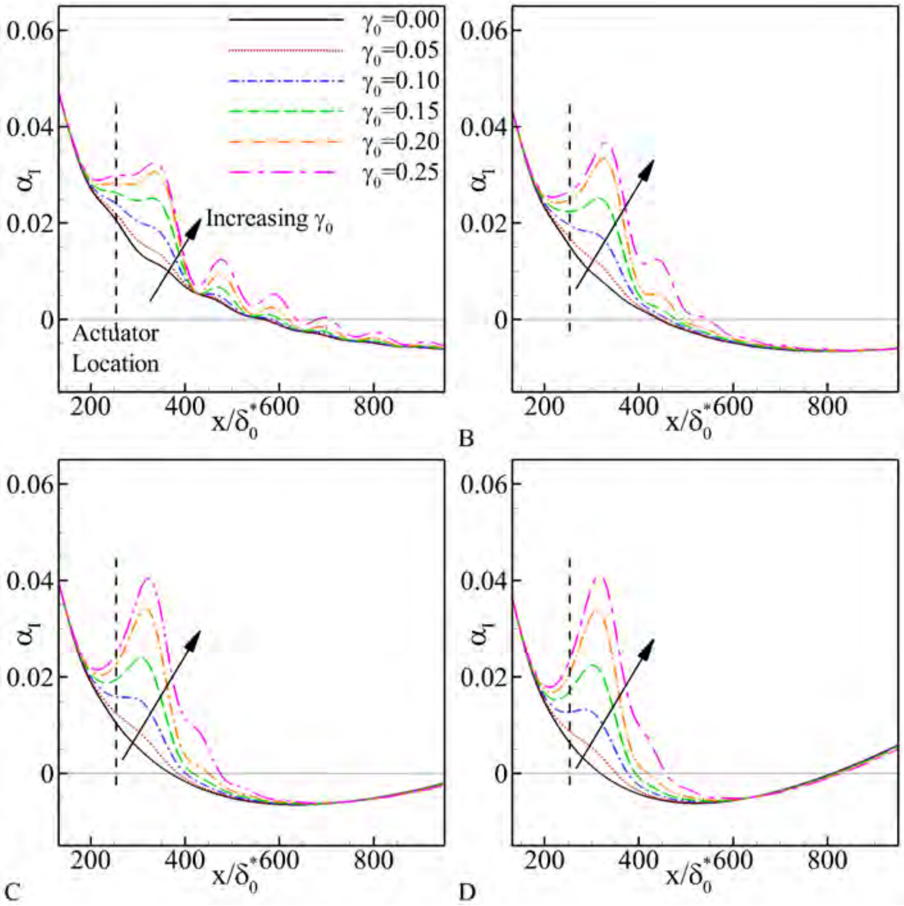

Figure 4-5. Spatial growth rates of the TS perturbations at varying frequencies and as a function of the magnitude of the plasma actuation. A) $F \times 10^6 = 80$, B) $F \times 10^6 = 100$,C) $F \times 10^6 = 120$, and D) $F \times 10^6 = 140$.

by the body force strongly modifies the flow field, and finally the region sufficiently far downstream such that the modifications to the boundary layer have relaxed enough to become negligible.

The first region in the flow is the region upstream of the actuator ($x/\delta_0^* < 240$), which exhibits only weak changes in its response to perturbations at the domain inlet. In this region, the behavior of the flow is slightly stabilized with the addition of plasma actuation relative to the non-actuated case, but there are no significant changes to the structure of the TS wave.

A second region in the flow can be defined as the region directly around the plasma actuator and its body force ($240 < x/\delta_0^* < 260$). Around the actuator, the TS wave rapidly begins to decay in magnitude (Figure 4-4, inset) to a lower value than it possessed upstream of the device. In order to evaluate the damping effects around the plasma actuator, a RANS based kinetic energy balance for these perturbations can be used.

$$\frac{D\left(TKE'\right)}{Dt} + \frac{\partial T_i}{\partial x_i} = P - \epsilon \tag{4–7}$$

where

$$TKE' = \frac{1}{2}\left(\overline{u'^{*}_{i} u'_{i}}\right) \tag{4–8a}$$

$$P = -\overline{u_i'^{*} u_j'}\frac{\partial \bar{u}_i}{\partial x_j} \tag{4–8b}$$

$$\epsilon = \frac{2}{Re}\left(\overline{s_{ij}'^{*} s_{ij}'}\right) \tag{4–8c}$$

and $\frac{\partial T_i}{\partial x_i}$ represent accelerative transport terms due to the perturbation's own pressure and strain fluctuations. The right hand side terms in Equation 4–7, P and ϵ, represent the production and dissipation of kinetic energy in the perturbation, respectively.

As the disturbance moves over the body force region, production of the wave's kinetic energy (here defined using the turbulent kinetic energy production) is reduced, and even becomes negative for large enough amounts of plasma actuation (Figure 4-6B, E, and H). Kinetic energy production is normally offset by dissipation (Figure 4-6C, F, and I). In the present scenario, the production of the TS wave's kinetic energy is reversed by the addition of the body force, which immediately begins to attenuate the perturbation magnitude, with dissipative effects compounding this attenuation. This near immediate drop in perturbation's growth around the plasma actuator indicates that the localized changes in the velocity field around the body force region are stabilizing. Again, there is no significant change in the structure of the TS wave at this point (Figure 4-8A), even though its magnitude does begin to drop at this point.

When the individual production terms are examined, several things become apparent (Figure 4-7). The $\overline{v'u'}\frac{\partial \bar{v}}{\partial x}$ and $\overline{v'v'}\frac{\partial \bar{v}}{\partial y}$ terms are found to be negligible when compared to the $\overline{u'v'}\frac{\partial \bar{u}}{\partial y}$ term. For the unforced flow, the streamwise flow development

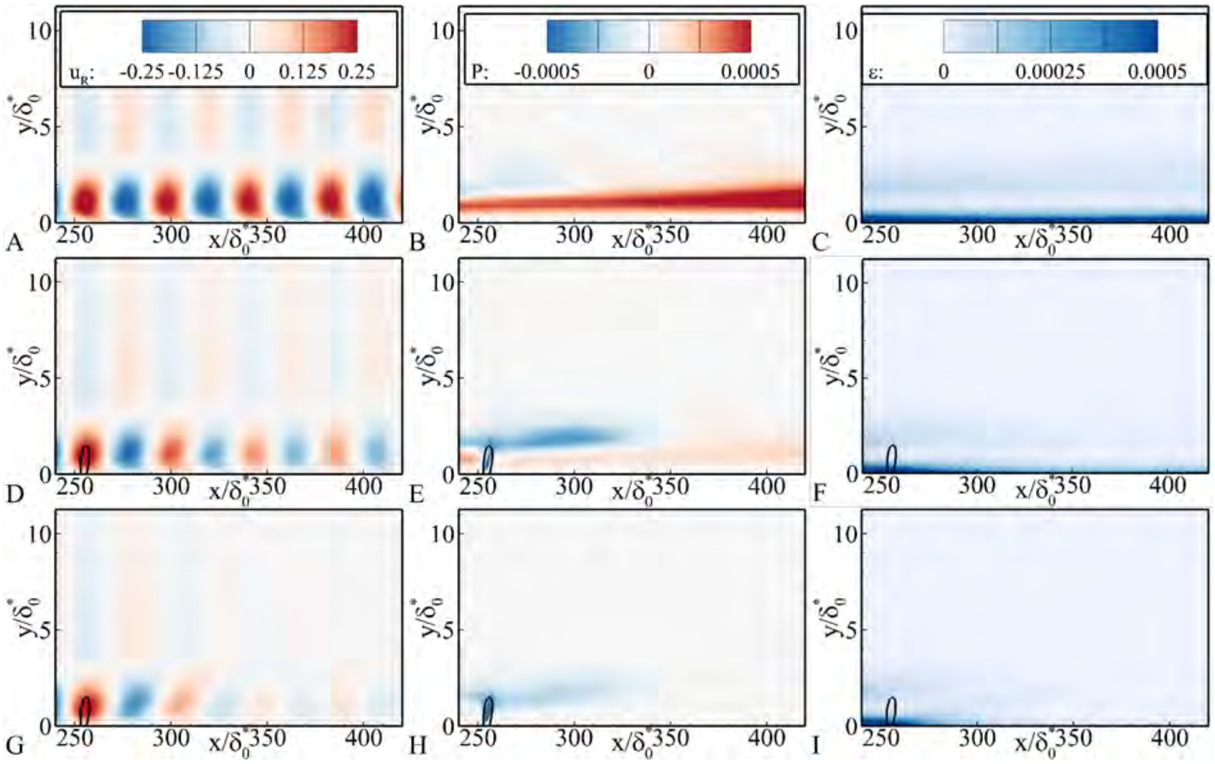

Figure 4-6. Comparison of u_R, kinetic energy production, and kinetic energy dissipation of TS waves in the near plasma region. A,D,G) Real component of the u perturbation velocity for the non-dimensional frequency of $F \times 10^6 = 140$, (B,E,H) perturbation kinetic energy production, and C,F,I) perturbation kinetic energy dissipation for plasma actuation levels of A-C) $\gamma_0 = 0.00$ (No plasma actuation), D-F) $\gamma_0 = 0.10$, and G-I) $\gamma_0 = 0.20$. The black line indicates a domain within which the body force is at least 10% of its maximum. The contour values in this plot saturate in order to show greater detail for smaller values of the perturbation velocity, perturbation kinetic energy production, and perturbation kinetic energy dissipation.

term $\left(\overline{u'u'}\frac{\partial \overline{u}}{\partial x}\right)$ also does very little to amplify or attenuate the perturbations. However, when plasma actuation is applied to the flow, there are some highly localized stabilization effects that occur. In the body force region, the rapid acceleration of the flow leads to significant flow acceleration, which implies negative production of kinetic energy. As the flow decelerates moving downstream, there is a gain in production offsetting this, but it does not account for the significant loss of perturbation kinetic energy that occurs in the near plasma region. Over a longer distance, it would seem that the production term associated with the wall normal gradient of the velocity profile has a greater role in stabilizing the flow. When plasma actuation is applied, the fuller velocity profiles that are generated lead to changes in the kinetic energy production. Overall, this term plays a greater role in stabilizing the flow than the streamwise development term.

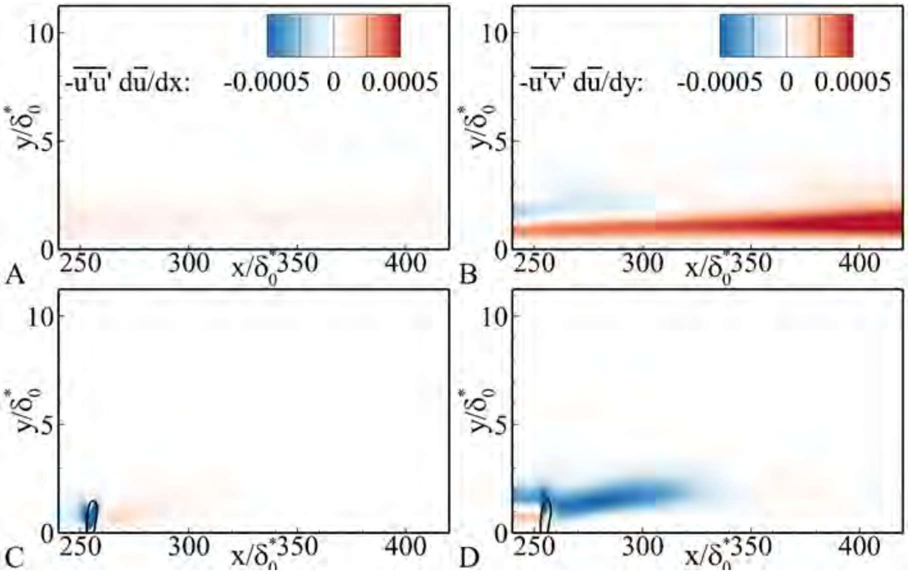

Figure 4-7. Comparison of different kinetic energy production terms for the TS waves in the near plasma region. A,C) streamwise kinetic energy and B,D) wall normal kinetic energy production terms A,B) without and C,D) with plasma actuation ($\gamma_0 = 0.20$) for the non-dimensional frequency of $F \times 10^6 = 140$.

Examining the flow fields downstream of the actuator ($260 < x/\delta_0^* < 600$, Figure 4-6), the effects of flow stabilization continue. The reduced production of perturbation kinetic energy leads to additional attenuation of the TS wave. The amount of perturbation energy production and dissipation are reduced in the flow farther downstream of the actuator, though this can likely be attributed to the reduced magnitude of the TS wave in this region. Furthermore, it seems that as soon as the wave convects over the actuator, it moves slightly away from the wall, before moving back down towards it. This effect is very slight for the weaker levels of plasma actuation, but can be more clearly seen for $\gamma_0 = 0.20$ and $\gamma_0 = 0.25$. This movement of the TS wave away from the wall can be more clearly seen through the perturbation velocity profiles, (Figure 4-8). It can be seen that the TS waves are modified by the changing boundary layer profiles, but in the near actuator region, the shape of the TS wave is preserved. However, as one examines the velocity profiles farther downstream where the perturbation has moved away from the wall, the shape of the perturbation changes greatly for the cases involving higher levels of plasma actuation, and more of the perturbation's energy is transferred away from the wall (i.e. for $\gamma_0 = 0.20$ and $\gamma_0 = 0.25$).

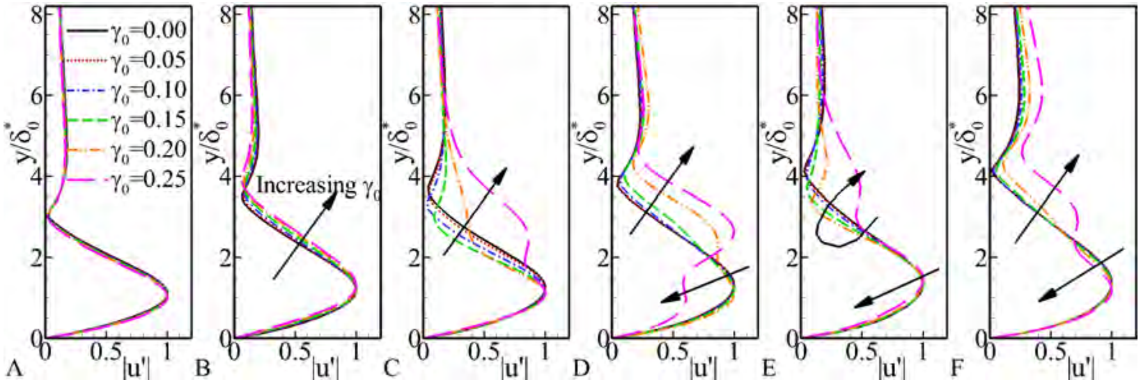

Figure 4-8. u-velocity profiles of the boundary layer disturbance downstream of the plasma actuator for varying levels of γ_0, normalized by each profile's maximum value for $F \times 10^6 = 100$. A) $x/\delta_0^* = 250$, B) $x/\delta_0^* = 300$, C) $x/\delta_0^* = 350$, D) $x/\delta_0^* = 400$, E) $x/\delta_0^* = 400$, and F) $x/\delta_0^* = 450$.

As the modifications to the boundary layer by the body force relax back to zero as one moves downstream, the TS wave eventually return to its original state. It can be seen in the perturbation growth rates (Figure 4-5), that the growth of the perturbations matches the baseline non-actuated case downstream of the plasma actuator, indicating that this final region begins at $x/\delta_0^* \approx 600$. Beyond this point, it would seem that the impact of the momentum addition is essentially zero.

4.1.3 Stabilization of the TS Wave

Understanding the localized behavior of the flow stabilization provides insight into the underlying physical mechanisms at play, but at the same time, it is also beneficial to reduce the entire TS wave stabilization process down to a single value, such that total effect of the stabilization can be understood. In order to understand this total effect of the addition of momentum into the boundary layer using DBD plasma actuation, the ratio of the perturbation magnitudes with and without plasma actuation can be used.

In Figure 4-9A, it can be seen that sufficiently far downstream of the plasma actuation (i.e. the region where the modifications to the stability properties have relaxed away), the ratio of the perturbation magnitudes is approximately constant. An average of the ratio of the perturbation magnitudes can be taken over a length of the boundary layer downstream of the actuation (B_u) in order to quantify this ratio in a more general manner. Defining this metric as

$$B_u = \frac{1}{x_e - x_s} \int_{x_s}^{x_e} \frac{A_u(x, \gamma_0)}{A_u(x, \gamma_0 = 0)} dx \tag{4–9}$$

where $x_s/\delta_0^* = 700$ and $x_e/\delta_0^* = 1000$.The averaged ratio of the magnitudes is weakly dependent on the frequency of the perturbations being examined (Figure 4-9B). It appears that the relative magnitude of these perturbations is much more dependent on the momentum addition into the boundary layer through plasma actuation.

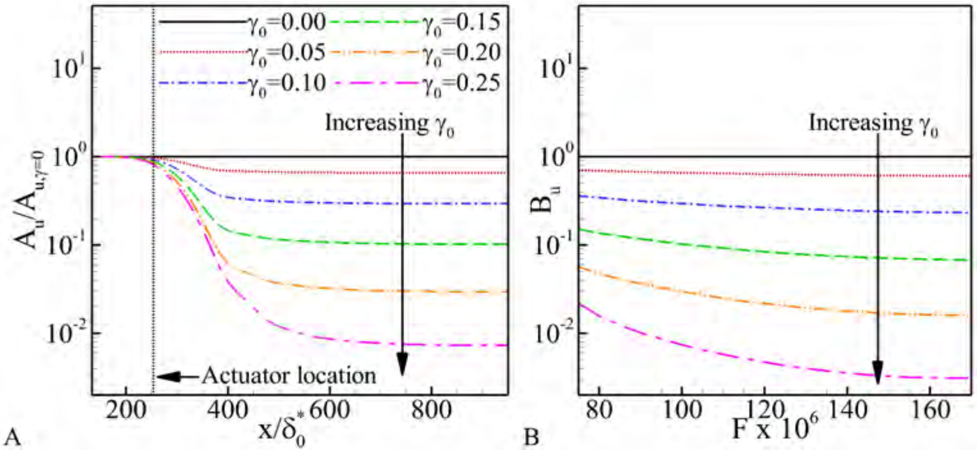

Figure 4-9. Comparison of relative TS wave magnitude as a function of velocity ratio. A) Comparison of the ratio of the perturbation magnitudes for varying values of the velocity ratio γ_0 for the non-dimensional frequency $F \times 10^6 = 100$. B) Average values of the velocity ratio along a length of the boundary layer downstream of the plasma actuation as a function of the non-dimensional frequency.

It can be seen in Figure 4-10A that for small values of the velocity ratio, the level of damping is proportional to the velocity ratio (that is, $1 - B_u \propto \gamma_0$). However, as the magnitude of the velocity ratio increases, this linear approximation of the damping breaks down. For larger levels of plasma actuation, it appears that the relative damping of the TS wave is more closely related to the amount of body force applied to the boundary layer by the plasma body force (Figure 4-10B) and that the relative magnitude of the perturbations decreases exponentially with respect to D_c (that is, $B_u \propto \exp(-kD_c)$, where k is a constant)

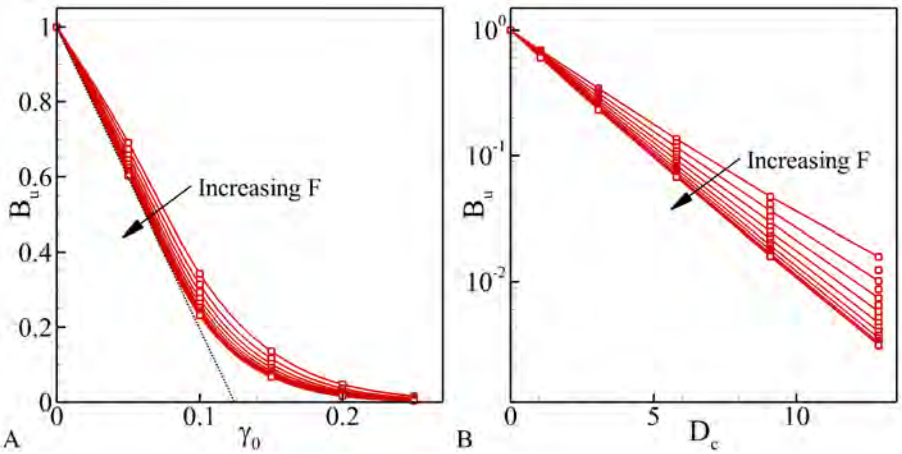

Figure 4-10. Damping ratio for TS waves downstream of the plasma actuator as a function of the A) velocity ratio, and B) proportional to the amount of momentum addition. The dashed lines indicate the A) linear ($1 - B_u \propto \gamma_0$) decrease in the relative magnitudes of the perturbations.

4.2 Stabilization of Boundary Layer Streaks

Stabilizing the TS path to turbulence does not imply that all of the remaining paths to turbulence are also stabilized. The transient growth of boundary layer streaks and transition due to free stream turbulence are areas where the use of plasma actuation for stabilization is still largely unknown. These two growth mechanisms are thought to be related to each other (Reshotko, 2001; Tumin & Reshotko, 2001). Furthermore, this type of disturbance is thought to be the one responsible for turbulent flow in the uncontrolled environments that air and ground vehicles experience. As such, this is the more relevant for practical flow applications. While the TS path to turbulence may still play a part in boundary layers becoming turblent, if the boundary layer streak path to turbulence cannot also stabilized with the use of plasma actuators, then their usefulness for flow stabilization will be severely limited.

4.2.1 Generation of Boundary Layer Streaks

Boundary layer streaks are algebraically growing disturbances, and have been identified as the most amplified perturbation over finite lengths of time and distance. Typically, the most amplified perturbations are generated using a superposition of the eigenmodes of the system (Butler & Farrell, 1992; Farrell, 1988), the computation of which is described in the previous subsection, such that

$$u' = \sum_{i}^{n_{eig}} c_i u'_i \tag{4–10a}$$

$$v' = \sum_{i}^{n_{eig}} c_i v'_i \tag{4–10b}$$

$$w' = \sum_{i}^{n_{eig}} c_i w'_i \tag{4–10c}$$

In order to study the growth of these disturbances, a quantifying metric must be employed. The metric

$$G(x) = \frac{\mathcal{K}(x)}{\mathcal{K}_0} \tag{4–11}$$

is selected, as it describes the amplification of the perturbation's kinetic energy as it develops in the streamwise direction, where

$$\mathcal{K}_0 = \int_0^{\infty} \frac{1}{2} \left(u'^* u' + v'^* v' + w'^* w' \right) dy \bigg|_{x=inlet} \tag{4–12a}$$

$$\mathcal{K}(x) = \int_0^{\infty} \frac{1}{2} \left(u'^* u' + v'^* v' + w'^* w' \right) dy \bigg|_{x} \tag{4–12b}$$

Furthermore, the most amplified perturbations are defined as those which maximize the growth in kinetic energy at some point along the streamwise direction, i.e.

$$G_{max}(x) = \max_{\mathcal{K}_0 \neq 0} \frac{\mathcal{K}(x)}{\mathcal{K}_0} \tag{4–13}$$

Farrell (1988) describes finding the most amplified modes by forming a second eigenvalue problem,

$$\mathbf{K}_0^{-1}\mathbf{K}_x\mathbf{c} = \lambda\mathbf{c} \tag{4–14}$$

where $\mathbf{K}_0$ and $\mathbf{K}_x$ are mass matrices representing the modal products of the different eigenmodes at the inlet and at downstream locations such that

$$K_{0,ij} = \int_0^\infty \frac{1}{2}\left(u_i'^* u_j' + v_i'^* v_j' + w_i'^* w_j'\right) dy\bigg|_{x=inlet} \tag{4–15a}$$

$$K_{x,ij} = \int_0^\infty \frac{1}{2}\left(u_i'^* u_j' + v_i'^* v_j' + w_i'^* w_j'\right) dy\bigg|_{x} \tag{4–15b}$$

The largest eigenvalue of the problem described in Equation 4–14 represents the amplification of the kinetic energy at a downstream point ($G_{max}(x)$). The initial conditions at the inlet can be extracted by the linear superposition of eigenvalue perturbations described in Equation 4–10. This eigenvalue problem is solved using the LAPACK subroutine ZGEEV (the details of which are described in Anderson *et al.* (1987)).

4.2.2 Grid Resolution Studies

A grid resolution study has been performed in order to ensure that the problem is adequately resolved. The details of the domain and mesh parameters are indicated in Table 4-2. This study has been performed primarily on the unforced boundary layer, but addition grid resolution studies for boundary layers where momentum addition was applied were also performed, indicating similar convergence.

For the grid resolution study, perturbations with spanwise wave numbers of $\beta = 0.45,\ 0.60\ \&\ 0.75$ and a temporal frequency of $\omega = 0$ are examined. The maximum amplification of perturbations at streamwise location of $x/\delta_0^* = 600$ is considered. It can be seen in Figure 4-11A and B, that the streamwise resolutions chosen converge very well in the absence of momentum injection in the boundary layer. Furthermore, the wall normal grid resolution appears to be sufficient (Figure 4-11C). A study of the domain height also shows convergence of the perturbation's magnitude (Figure 4-11D).

Table 4-2. Details of the grid resolution study performed for the linear boundary layer streak calculations. The Fine-L, Fine-H, and Tall cases are identical.

Study	Case	N_x	N_y	L_x/δ_0^*	L_y/δ_0^*	$\Delta x/\delta_0^*$	$\Delta y_{wall}/\delta_0^*$	n_{eig}
Streamwise resolution	Coarse-L	513	65	1061.7	40	2.0736	0.02409	64
	Medium-L	725	65	1061.7	40	1.4664	0.02409	64
	Fine-L	1025	65	1061.7	40	1.0368	0.02409	64
Wall normal resolution	Coarse-H	1025	33	1061.7	40	1.0368	0.09631	32
	Medium-H	1025	49	1061.7	40	1.0368	0.04282	48
	Fine-H	1025	65	1061.7	40	1.0368	0.02409	64
Height	Short	1025	33	1061.7	20	1.0368	0.04815	32
	Medium	1025	49	1061.7	30	1.0368	0.03212	48
	Tall	1025	65	1061.7	40	1.0368	0.02409	64

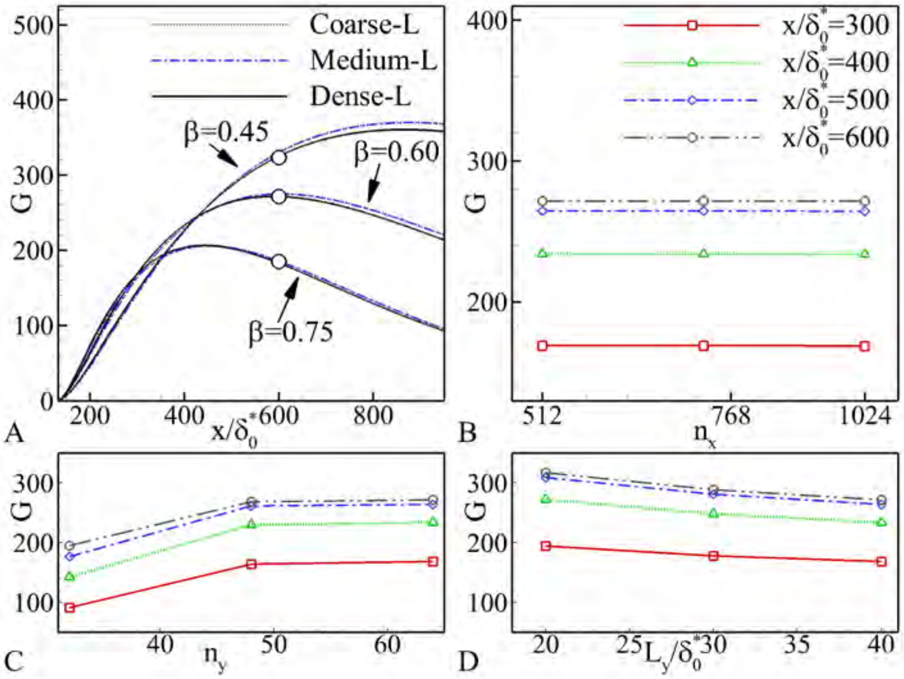

Figure 4-11. Convergence of boundary layer streak magnitudes for the grid resolution studies in an unforced boundary layer. A) Kinetic energy amplification for perturbations of spanwise wavenumber $\beta = 0.45,\ 0.60,\ 0.75$ that are most amplified at the location $x/\delta_0^* = 600$ as a function of the streamwise resolution, along with B) data collected at individual points along the streamwise direction for the $\beta = 0.60$ case. Convergence data for the C) wall normal resolution and D) domain height are also shown.

A case with a body force applied to the boundary layer is also considered. The streamwise resolution in the near actuator region may present itself as difficult to resolve due to the steep gradients in the streamwise direction. However, based on the grid resolution study performed (Figure 4-12), the Fine-L mesh should sufficiently resolve all of the important effects in the flow.

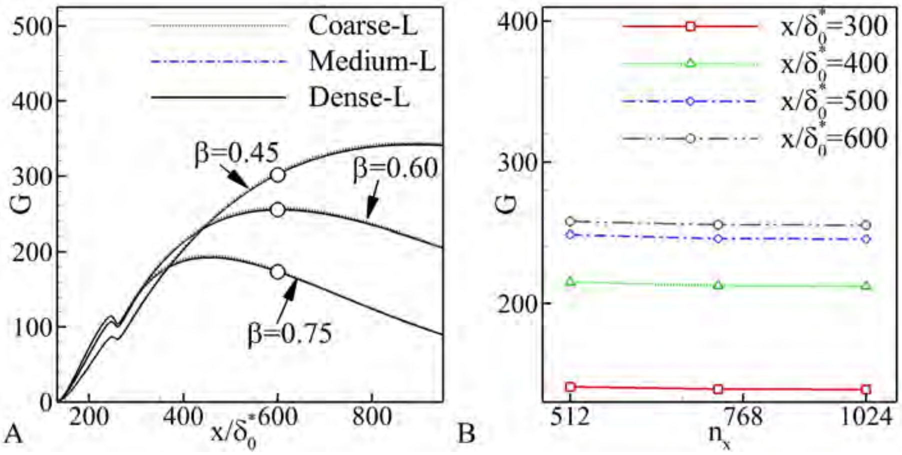

Figure 4-12. Convergence of boundary layer streak magnitudes for the grid resolution studies in a plasma modified boundary layer. A) Kinetic energy amplification for perturbations of spanwise wavenumber $\beta = 0.45,\ 0.60,\ 0.75$ that are most amplified at the location $x/\delta_0^* = 600$ case where body force is injected ($\gamma_0 = 0.20$) in the boundary layer as a function of the streamwise resolution, along with B) data collected at individual points along the streamwise direction for the $\beta = 0.60$.

4.3 Results

4.3.1 Baseline Case

Beginning with the unforced boundary layer, several things should be noted about the streaks that are generated using this method. First, the most amplified boundary layer streaks display similar trends in growth and structure regardless of where the optimization is performed in the streamwise direction, but there are quantitative variations in the growth depending on where along the streamwise direction the optimization takes place (Figure 4-13A). The growth of these streaks is driven by streamwise oriented vortices in the boundary layer (Figure 4-13B). These streaks start off as having a small, if not negligible streamwise velocity component. However, the streamwise oriented vortices transfer low momentum fluid upwards and away from the surface of the boundary layer on one side of the vortex, while simultaneously transporting high momentum fluid from the free stream downwards closer to the surface on the other. This results in localized high and low speed streaks in the surface (Figure 4-13C). As this process occurs, the magnitude of the streak grows as the vorticity continues to transport streamwise momentum into and out of the boundary layer, but after a certain length of boundary layer, viscous effects dissipate the streamwise vorticity, which limit the maximum growth, as well as the boundary layer streaks, which leads to their eventual decay in the absence of non-linear effects. This process is very well documented in the literature for both one-dimensional (Butler & Farrell, 1992; Ellingsen & Palm, 1975; Landahl, 1980) and two-dimensional flows (Luchini, 2000; White, 2002). The maximum level of growth for this type of perturbation is very strongly tied to the spanwise wavenumber of the perturbation. Wider perturbations grow more slowly at first, but ultimately reach larger magnitudes, but at points much farther downstream of narrower perturbations.

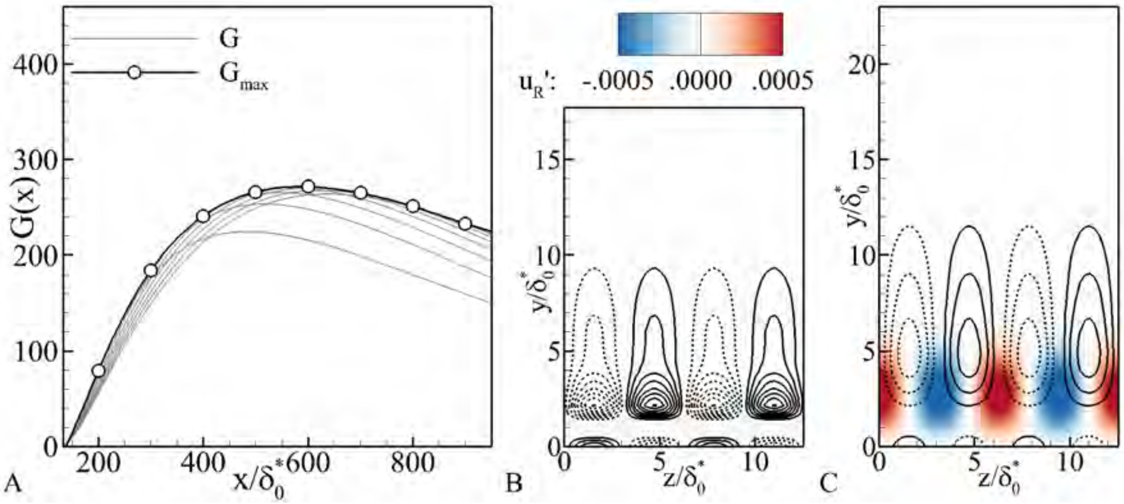

Figure 4-13. Growth and structure of a boundary layer streak for A) $\beta = 0.6$ (thin lines) as a function of where the most amplified perturbation is determined (circles). The thick line represents the envelope of maximum growth as a function of the streamwise location for $\beta = 0.6$. B) Spanwise slices of the flow field at the initial condition and C) flow at $x/\delta_0^* = 600$ are shown for the most amplified perturbation at $x/\delta_0^* = 600$ for $\beta = 0.6$. The contour lines indicate the streamwise vorticity, while the shading indicates the streamwise velocity.

4.3.2 With Plasma Actuation

When a plasma based body force is applied to the flow, adding momentum into the boundary layer, it appears that the boundary layer streaks are reduced in amplitude. Figure 4-14 shows that damping of the streaks downstream of the body force can occur, regardless of where they are considered to be the most amplified streak. Furthermore, depending on the magnitude of the body force and where the streak amplitude is considered, this damping appears be up to 20% of the overall streak magnitude.

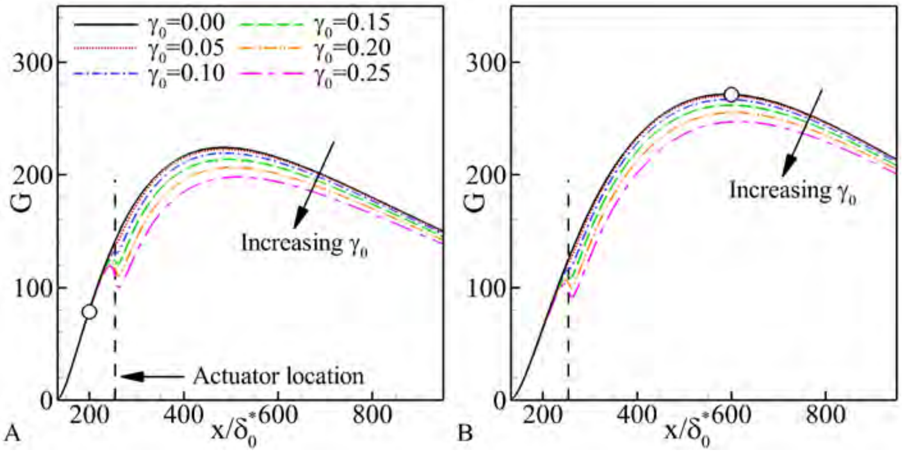

Figure 4-14. Growth of kinetic energy contained in boundary layer streaks for $\beta = 0.6$ with and without plasma actuation. The streaks shown are the most amplified perturbations at A) $x/\delta_0^* = 200$ and B) $x/\delta_0^* = 600$. The dashed vertical line indicates the location of the plasma actuator, and the circle indicates where this perturbation is the most amplified perturbation, as well as G_{max} for the unforced case.

Having observed that the kinetic energy contained in these streaks is reduced downstream of the plasma actuation, the next item of concern is to determine why this damping occurs. In order to identify the source of this damping, a RANS based kinetic energy balance for these perturbations is used. Evaluating the perturbation kinetic energy, production, and dissipation terms (Figure 4-15), it becomes apparent that the addition of a body force region in the boundary layer interferes with the production of the perturbation's kinetic energy. Inside of the body force region, it appears that not only is the production of kinetic energy attenuated, but if the amount of body force is high enough, it can even become negative. Examining the effects of viscous dissipation, it appears that this sink for the perturbation's energy is largely unaffected by the addition of plasma actuation, though there are some variations due to the decreased magnitude of the perturbation.

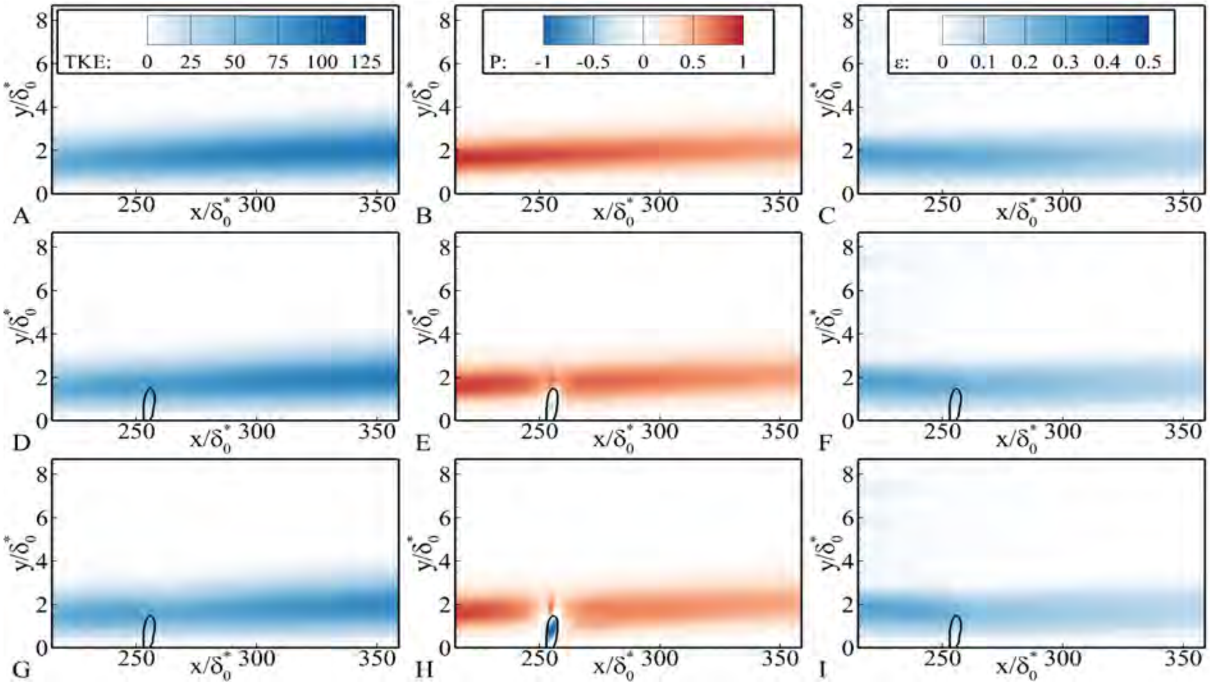

Figure 4-15. Comparison of streak tubulent kinetic energy, kinetic energy production, and viscous kinetic energy dissipation around the plasma actuator. A,D,G) Turbulent kinetic energy, B,E,H) kinetic energy production, and C,F,I) kinetic energy dissipation of boundary layer streaks for the A-C) unforced, D-F) $\gamma_0 = 0.10$ and G-I) $\gamma_0 = 0.20$ cases, for the most amplified perturbation at $x/\delta_0^* = 200$.

Decomposing the production of kinetic energy into its individual terms, the localized effects become even more apparent (Figure 4-16). The effects of the $\overline{v'u'}\frac{\partial \bar{v}}{\partial x}$ and $\overline{v'u'}\frac{\partial \bar{v}}{\partial x}$ on the energy production are negligible with or without the body force added to the flow, but the changes to the $\overline{u'u'}\frac{\partial \bar{u}}{\partial x}$ and $\overline{u'v'}\frac{\partial \bar{u}}{\partial y}$ terms and the changes to them are significant. It appears that the majority of the negative production in the body force region is due to the $\overline{u'u'}\frac{\partial \bar{u}}{\partial x}$ term. This term, which is the less dominant production term in the unforced boundary layer, is reliant on the streamwise development of the flow. As the addition of a very localized body force generates significant high gradients in the streamwise direction, it logically follows that this production term would be affected. As the flow is accelerated by the co-flow actuation, the streamwise velocity gradient $\frac{\partial \bar{u}}{\partial x}$ increases in magnitude, leading to a reduction in the perturbation's kinetic energy production by the $\overline{u'u'}\frac{\partial \bar{u}}{\partial x}$ term. The other term of significance is the $\overline{u'v'}\frac{\partial \bar{u}}{\partial y}$ term, which is responsible for a majority of the energy production. This term also shows a very localized attenuation in production, as well as a slight decrease in production downstream of the actuator. However, this effect does not seem to be as dominant to reducing the streak magnitude as the $\overline{u'u'}\frac{\partial \bar{u}}{\partial x}$ term.

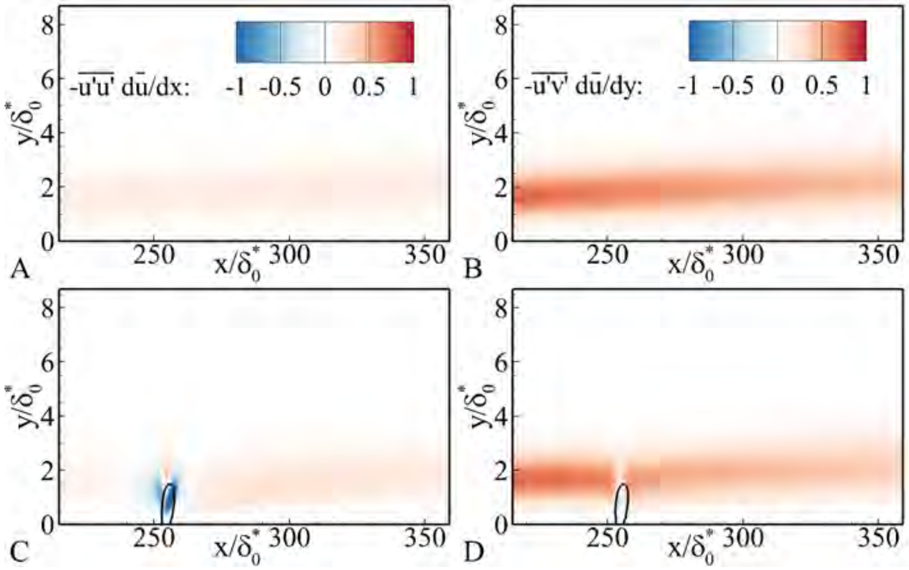

Figure 4-16. Comparison of boundary layer streak kinetic energy production terms around the plasma actuator. A,C) streamwise kinetic energy and B,D) wall normal kinetic energy production terms A,B) without and C,D) with plasma actuation ($\gamma_0 = 0.20$).

The change in perturbation kinetic energy production has also been noted in the stabilization of the TS wave. However in that scenario, the stabilization is primarily due to modification of the $\overline{u'v'}\frac{\partial \bar{u}}{\partial y}$ term, though local stabilization due to the $\overline{u'u'}\frac{\partial \bar{u}}{\partial x}$ term also plays a small part. For the TS wave, the streamwise and wall normal velocity components are of comparable magnitude. However, for boundary layer streaks, the streamwise velocity component is far greater in magnitude, and a large difference in magnitude of the $\overline{u'u'}$ and $\overline{u'v'}$ terms reflects this. As such, for boundary layer streaks, changes to $\frac{\partial \bar{u}}{\partial x}$ will have a greater impact on the production term than $\frac{\partial \bar{u}}{\partial y}$. Therefore, the localized acceleration of the flow by the co-flow oriented body force is stabilizing, but only in the region immediately around the plasma actuator. Downstream of the actuator, these effects reverse as the flow relaxes back to a zero pressure gradient boundary layer, and the normalized production due to the $\overline{u'u'}\frac{\partial \bar{u}}{\partial x}$ term will be increased relative to the baseline flow. This offsets most of the stabilization due to the fuller downstream boundary layer profile. Even so, the localized stabilization effects are sufficient enough to ensure a reduced magnitude of the streak in the downstream region. The extent of these stabilizing effects can be seen more clearly in Figure 4-17.

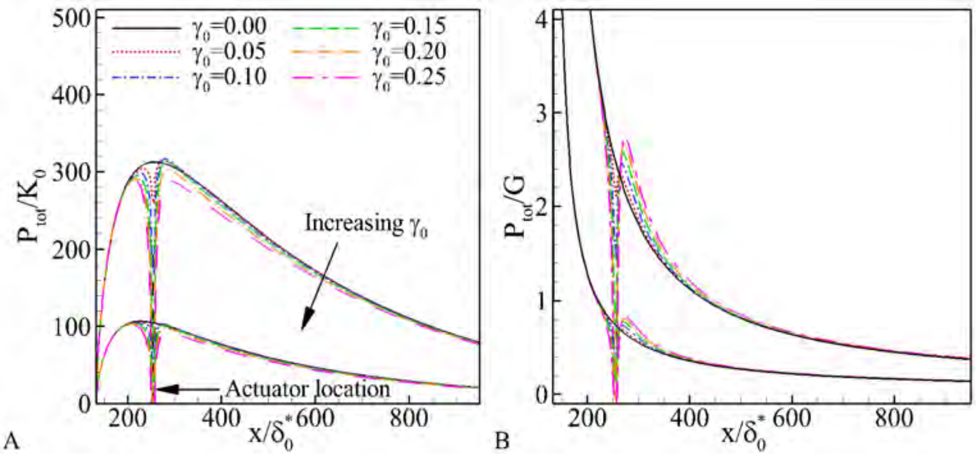

Figure 4-17. Total and normalized kinetic energy production in the boundary layer streaks. A) Total production of kinetic energy in the boundary layer ($P_{tot}(x) = \int_0^\infty P(x,y)dy$) for varying levels of plasma actuation. B) Total production of kinetic energy in the boundary layer normalized by the total kinetic energy contained in the perturbation ($\mathcal{K}(x)$).

4.3.3 Scaling of the Damping

The observation that the addition of a plasma based body force can reduce the amplitude of boundary layer streaks is interesting and suggests wider potential and applicability for flow stabilization, and it would be very beneficial to characterize the behavior of these devices over a broad range of parameters, as well as to reduce the scaling effects down to a single value for comparison, similarly to what has been done for the TS wave earlier in this chapter.

Parametric studies have been performed determining the value of G_{max} as a function of the spanwise wavenumber, as well as the velocity ratio along the streamwise direction (Figure 4-18). This approach, while it does not focus on the growth and decay of individual streaks, does provide information about what the maximum possible growth will be. As such, this approach describes the growth of the most amplified perturbation with or without the effects of the plasma actuator.

In Figure 4-18A, the values of G_{max} are shown across a spectrum of spanwise wavenumbers for the unforced boundary layer, indicating that wider perturbations grow more slowly initially, but eventually grow to larger magnitudes. With the addition of plasma control ($\gamma_0 = 0.20$, Figure 4-18B), this trend continues to hold, but there is a noticeable dip in the perturbation's energy located around the plasma actuator for all of the wavenumbers examined. Further examining this data, the maximum of G_{max} for all of the wavenumbers examined is shown in 4-18C. It can be seen in that figure that the addition of the body force damps the the entire envelope of most amplified potential perturbations.

In order to quantify the damping of these perturbations, the metric

$$H_{max} = \frac{G_{max}\left(x, \beta, \gamma_0\right)}{G_{max}\left(x, \beta, \gamma_0 = 0\right)} \tag{4–16}$$

is used, which compares the ratio of the maximum disturbance amplification with and without plasma actuation. Evaluating this metric at a point downstream of the plasma actuator ($x/\delta_0^* = 300$), it can be seen that there is damping of the perturbations, and that this damping can be significant, up to 25% of the overall magnitude of the perturbation, depending on the magnitude of the plasma actuation is examined. While the amplification of these perturbations is obviously wavenumber dependent (Figure 4-19A), the damping effects are not as sensitive to the spanwise wavenumber (Figure 4-19B). It would appear that while there is a slight spanwise wavenumber

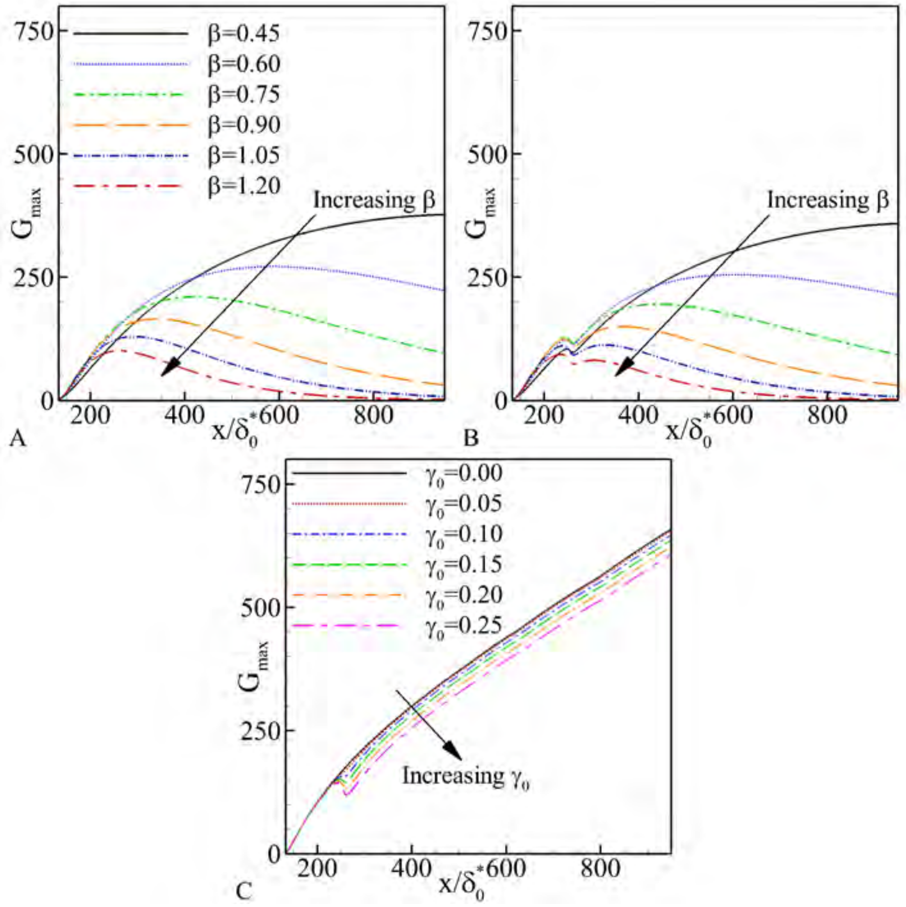

Figure 4-18. Effect of plasma actuation on individual streak amplitude and the envelope of streak energy with and without plasma actuation. Amplitude of the most amplified perturbations (G_{max}) A) without and B) with ($\gamma_0 = 0.2$) a plasma actuator as a function of the spanwise wavenumber and location. C) The maximum of G_{max} taken over all of the spanwise wavenumbers examined for varying levels of plasma actuation.

dependence, the damping is much more strongly dependent on the magnitude of the plasma actuation.

Comparing the damping of the streaks across a the velocity ratio and total amount of body force added to the flow (which is proportional to the parameter D_c), several trends become apparent. The magnitude of the damping increases monotonically with respect to both parameters. While the damping is very low ($\approx 5\%$) for the weaker levels of plasma actuation ($\gamma_0 < 0.1$), once the plasma actuation reaches a high enough level, a linear trend in the damping appears with respect to the total amount of body force

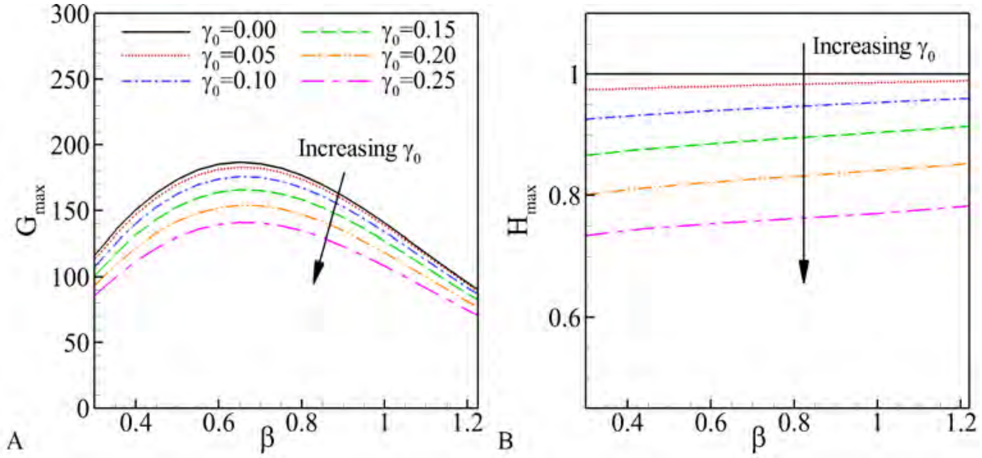

Figure 4-19. Overall comparison of streak magnitude with and with plasma actuation applied to the flow. A) G_{max} and B) H_{max} at the location $x/\delta_0^* = 300$ as a function of the spanwise wavenumber and the magnitude of the plasma actuation.

added to the flow. As such, it follows that the damping follows a power law trend for the velocity ratio as u_p is proportional to D_c.

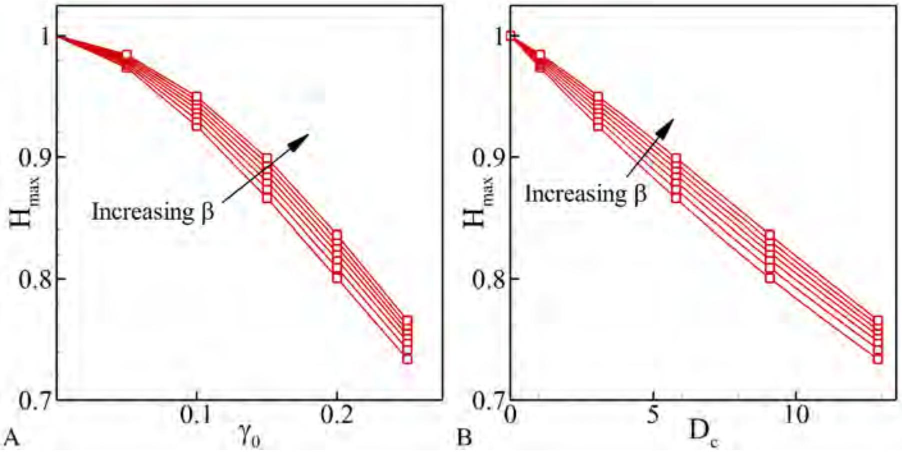

Figure 4-20. [Damping of the boundary layer streaks by the plasma actuators as a function of γ_0 and D_c. H_{max} in terms of the A) wall jet velocity ratio and B) total amount of body force added to the flow. H_{max} is shown for spanwise wavenumbers, β, between 0.3 and 0.9

4.4 Conclusions

The present bi-global stability analysis has examined how continuous momentum addition into a zero pressure gradient boundary layer through a plasma based body force can be used to stabilize the TS and boundary layer streak paths to transition.

Parametric studies have been performed varying the frequency of the oncoming TS wave and spanwise wave number of the boundary layer streak, as well as the magnitude of the body force injected into the flow. As multiple paths to transition have been examined, it is apparent that the effects of co-flow oriented plasma actuation has a broad effect on stabilizing the flow against generic perturbations. This is very promising, as it cannot always be predicted what type of perturbations a flow will experience, especially if those conditions depend on external factors, such as local atmospheric conditions.

The results contained in this chapter have been distributed through several different conference proceedings (Riherd & Roy, 2013*b*) and journal publications (Riherd & Roy, 2013*a*,*d*).

4.4.1 Conclusions on the Stabilization of the TS Wave

Examining the local flow physics around and downstream of the momentum injection point, a number of different effects are seen to occur. There is a sudden stabilization of the flow around the actuator. Immediately downstream of the actuator, where the displacement boundary layer heights and shape factor are reduced, the TS perturbation is further stabilized, leading to a significant decrease in its magnitude. Sufficiently far downstream of the point of momentum addition, the effects of flow control become minimal, and the flow returns to its uncontrolled state.

Based on the parametric studies, the relative magnitude of the oncoming TS waves can be monotonically decreased as the body force injecting momentum into the flow is increased. The magnitude of the perturbation can be decreased by up to two orders of magnitude across a wide range of frequencies, though more modest reductions in perturbation magnitude are seen for smaller levels of plasma actuation. For smaller amounts of plasma actuation, the stabilization effects are proportional to the velocity ratio between the freestream velocity and the induced velocity of the body force under quiescent conditions. For larger magnitudes of plasma actuations, the stabilization of the

TS wave appears to be exponential with respect to the amount of momentum added to the boundary layer.

4.4.2 Conclusions on the Stabilization of Boundary Layer Streaks

Using a bi-global stability analysis, it has been shown that DBD plasma actuators may be used to stabilize boundary layer streaks, filling a gap in the understanding of how these actuators can be used to delay the onset of turbulent flow in boundary layers with respect to algebraic and by-pass transition scenarios. The physical mechanisms responsible for flow stabilization been examined using a RANS approach to the perturbation growth. Parametric studies examining these streaks over a broad range of wavenumbers and levels of plasma actuation have also been performed. The damping of these streaks is predicted to be on the order of $5-25\%$ of the total streak magnitude, and occurs over a broad range of spanwise wavenumbers.

The stabilization of these streaks can be attributed to highly localized effects around the plasma induced body force. The addition of the body force locally deforms the flow field. In turn, the localized variations in the flow field attenuate the linearized production of the streak's kinetic energy, and for sufficiently high levels of actuation, these flow field variations can induce negative kinetic energy production, similar to the localized stabilization of the TS wave, but lacking the continued stabilization of the flow downstream due to the lower value magnitude of v'.

Based on the parametric studies performed, the overall effect of stabilization scales linearly with the magnitude of the body force applied to the flow by the plasma actuators. There is some wavenumber dependence to the stabilization, but the attenuation of the streaky structures in the flow is more strongly tied to the magnitude of the plasma actuation.

4.4.3 Future Work

Future work on this topic should focus on extending the use of these actuators over a broader range of conditions and under more realistic flow and application conditions and disturbance environments, particularly those that are experienced regularly by air and ground vehicles. Experimental validation will also be necessary in the future before these actuators can be widely adopted for stabilization, an area that has not been ignored, but has not received adequate attention at this point.

Very little attention has been given to the effects of using arrays of these actuators, rather than a single actuator (aside from the study of Duchmann *et al.* (2013*a*), who used a very loose description of the plasma modified flow field, but suggested that enormous gains in stability are possible). The use of multiple actuators could be extremely beneficial, as it would allow for perturbations to be damped beyond the limited effects of a single actuator. It would also allow for stabilization effects to be realized at very high Reynolds numbers where the velocity ratio of the plasma actuation is on the order of 0.01.

There may also be edge effects when these actuators are applied. Visbal *et al.* (1998) predicted that the edge effects for wall jet flows have a significant impact on the downstream flow and on the stability of the flow. In that study, it was found that there is a contraction in the width of the wall jet as it developed downstream, which led to the generation of cross-flow effects and a resulting instability at the spanwise edges of the wall jet. As the momentum addition to a boundary layer by DBD plasma actuators can be compared to adding a wall jet component to the flow, these effects would also be likely to occur if finite width plasma actuators were employed to stabilize the a real flow. However, they would likely occur at a slower rate along the length of the flow due to the added convective effects of the free stream (rather than quiescent) flow. Going forward, the impact of these edge effect will need to be quantified and understood, as they may become a limiting factor in the effectiveness of the control.

Should the effectiveness of these actuators still hold as they're implemented in a more rigorous environment, it would indicate that these devices can be used to reduce turbulent skin friction and potentially incur reduced fuel usage for a range of everyday transportation applications.

CHAPTER 5
FLOW STRUCTURE IN A BOUNDARY LAYER WITH SERPENTINE GEOMETRY PLASMA ACTUATION

In addition to the simple geometries first explored by Roth and his co-workers (Roth *et al.*, 1998, 2000), other geometric configurations for DBD plasma actuators have also been explored in the research literature. The concept of a plasma synthetic jet, where actuators are placed facing each other, and generate a plane or circular jet flowing normal to the surface has been explored (Santhanakrishnan & Jacob, 2007). Other geometries, such as the serpentine geometry (Durscher & Roy, 2012; Roy & Wang, 2009; Wang *et al.*, 2011) are able to produce three-dimensional effects due to their more complex, periodically varying electrode geometries. Many of the different actuator geometries can be generalized into what is referred to as a periodic serpentine geometry, examples of which are shown in Figure 5-1, and can be characterized by their periodic electrode shape, as well as the periodic length (λ) and the length of the electrode geometry from it's median position (A).

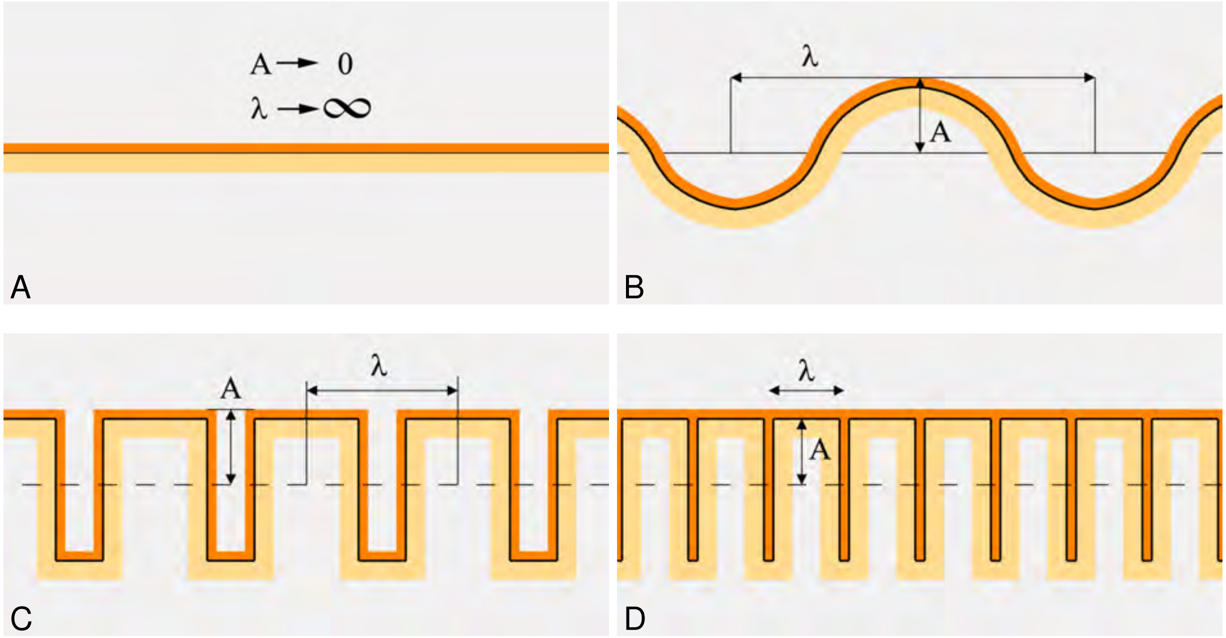

Figure 5-1. Schematic of various plasma actuator geometries. A) linear B) arc, C) rectangle, and D) comb geometries are shown.

The primary aim of using this type of actuator geometries is that they should allow for plasma actuators to tap into a wider set of flow physics than the standard geometry actuator would be able to do. The modification to the electrode geometry provides additional degrees of freedom for these actuators to be used for flow control. In particular, the spanwise wavelength λ is of the most importance, as this allows for perturbations of a specific spanwise length to be added to the flow. With this additional spanwise length scale, it is possible that steady (boundary layer streaks) and unsteady (oblique modal and secondary) instabilities could be excited by the actuator, something that is not possible with a single standard geometry plasma actuator.

Previous application of this type of actuator geometry have focused on separation control over airfoils (Riherd & Roy, 2012*a*; Rizzetta & Visbal, 2011) and control of swirl in combustion chambers (Wang & Roy, 2011). The current work aims to use this class of actuators to excite boundary layer streaks in a laminar boundary layer for transition control.

At low magnitudes, boundary layer streaks have been shown to be useful for damping TS waves and random background noise affecting a boundary layer. Fransson *et al.* (2006) found that with the addition of streaks into the boundary layer, the velocity profile could be sufficiently modified such that the stability properties of the boundary layer are also modified. It was found that for streaks of sufficient magnitude, transition of the flow can be delayed, if not avoided entirely.

When these boundary layer streaks are generated at or amplified to a sufficiently high magnitude, they possess their own instability properties (Andersson *et al.*, 2001), of which four similar but distinct instability modes have been identified (Figure 5-3). The secondary instability results of Andersson *et al.* (2001) indicate that the secondary instability is sensitive to slight changes in the mean field (which may present itself as a challenge when examining the flow generated by a realistic plasma device). Depending on the manner of the secondary instability, these instabilities may not become critical

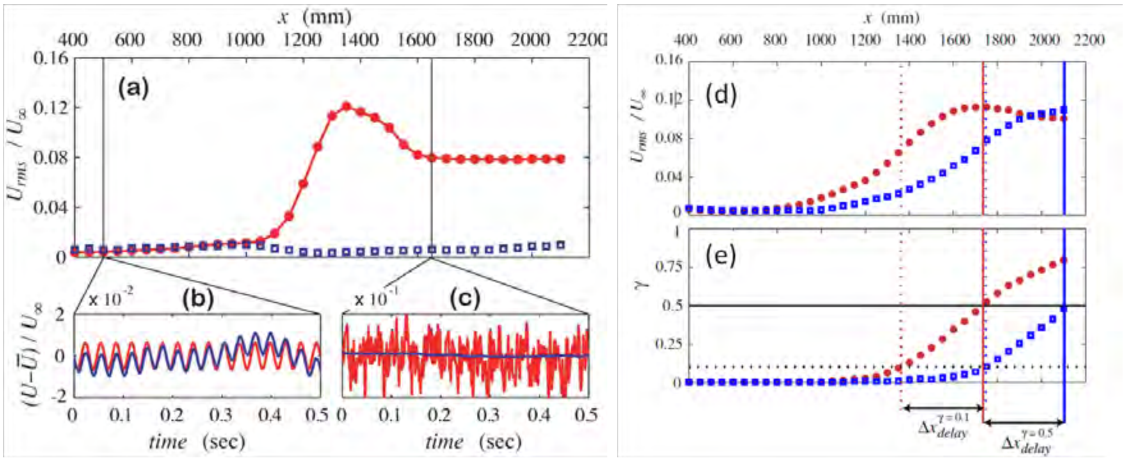

Figure 5-2. Comparison of unsteady flow measurements in a boundary layer with and without boundary layer streaks applied. A) Measurements of the RMS streamwise velocity magnitude of a TS wave in a 5m/s boundary layer with (blue squares) and without (red dots) boundary layer streaks generated by upstream roughness elements. Temporal measurements made using hot-wire anemometry show that the flow is laminar for both cases at B) $x = 400mm$, but has become turbulent in the absence of control downstream at C) $x = 1650mm$. The response to background noise in terms of the D) RMS streamwise velocity and E) intermittancy factor also indicate flow stabilization. From Fransson *et al.* (2006).

until the streak amplitude is upwards of 25% of the free stream velocity. Furthermore, the perturbations tend to be largest in the region of the highest shear stress in the streak. Researchers have also examined the transient breakdown of the boundary layer streaks, identifying that non-modal growth of perturbations on the streaks can occur even when the streaky boundary layer flow is stable with respect to exponential instabilities (Hœpffner *et al.*, 2005), which suggests that these streaks may be used to rapidly transition a laminar boundary layer even for modest levels of flow control.

As these boundary layer streaks possess both stabilizing and destabilizing effects depending on their magnitude, they may be extremely useful and versatile for transition control. As DBD actuators can be used as active flow control actuators, one actuator could be used to generate low magnitude streaks in order to stabilize the flow field when operated at one voltage and to destabilize the flow field using higher magnitude streaks

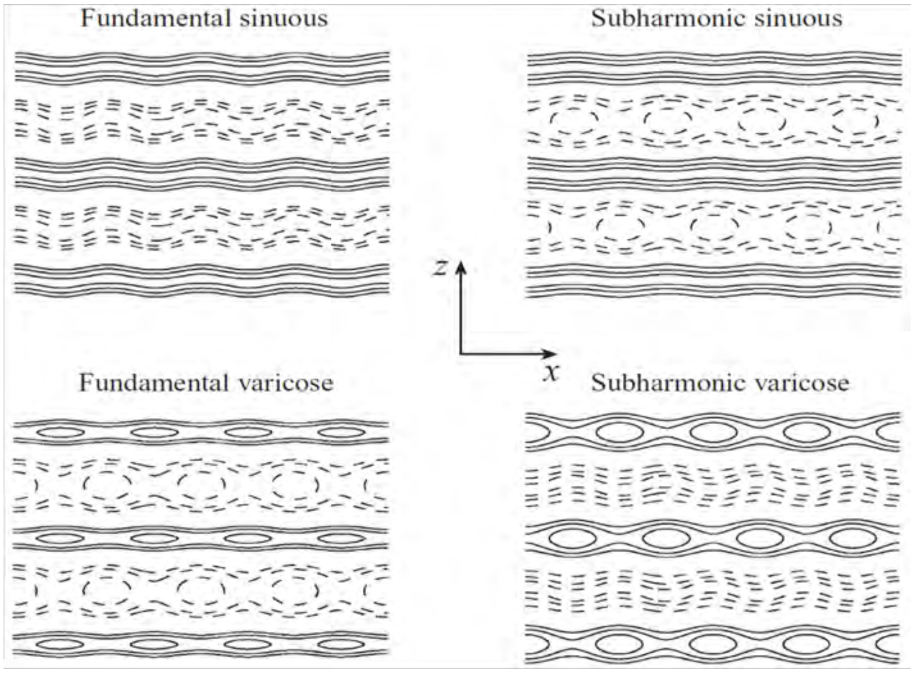

Figure 5-3. Different boundary layer streak breakdown modes as seen from above the boundary layer. Solid lines indicate the low speed streak regions and dashed lines indicate high speed streak regions. From Andersson *et al.* (2001).

when operated at a higher voltage. As many types of land and air vehicles undergo a variety of operating conditions over a single trip, this versatility may be highly beneficial, as it would allow for one actuator to operate for several different purposes.

In this chapter, numerical simulations of a serpentine geometry plasma actuator under quiescent are presented, which show good qualitative and quantitative agreement with comparable experiments (Durscher & Roy, 2012). Numerical simulations of serpentine geometry plasma actuators in a laminar boundary layer are then presented, the results of which are characterized. The results of these simulations indicate that boundary layer streaks are formed when serpentine geometry plasma actuators are applied in a co-flow manner to a laminar boundary layer.

5.1 Serpentine Geometry Actuator Under Quiescent Conditions

Under quiescent conditions, these plasma actuators have been shown to induce a very complex flow. In particular, this class of actuators has been shown to generate streamwise vortical structures downstream of the actuator (Durscher & Roy, 2012; Roy

& Wang, 2009; Wang *et al.*, 2011), an effect that is not seen for the standard geometry of plasma actuators. Slices of data from a stereoscopic PIV study are shown in Figure 5-4, illustrating this effect.

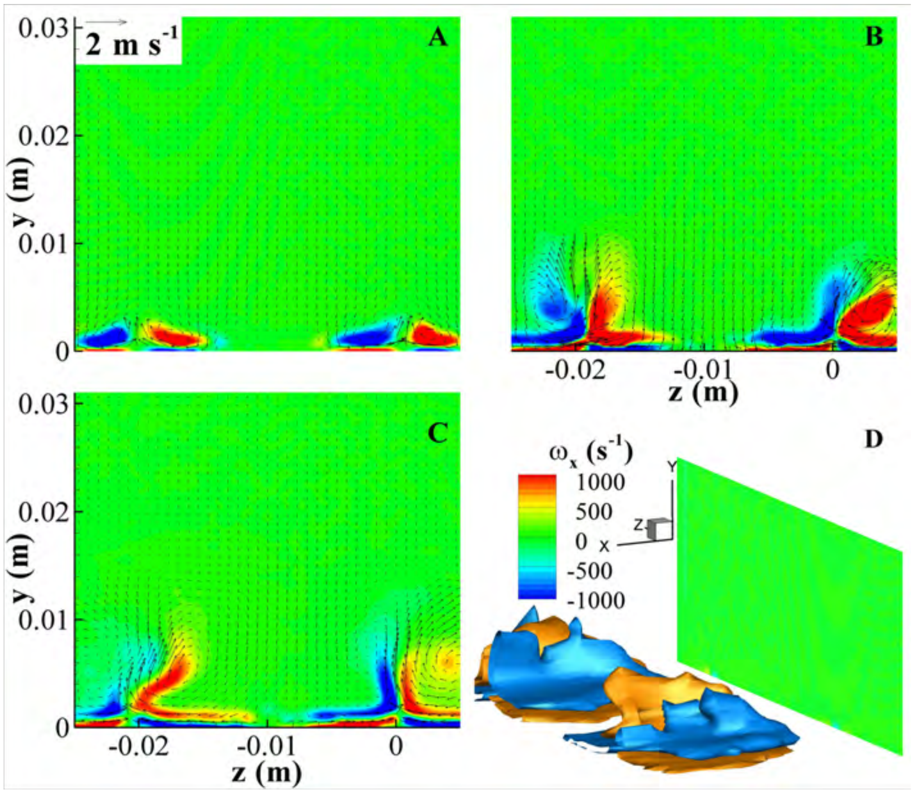

Figure 5-4. Spanwise slices of the streamwise voriticity generated by a serpentine geometry plasma actuator under quiescent conditions at A) 7.5mm, B) 12.5mm, and C) 17.5 mm downstream of a the leading edge of a curved geometry plasma actuator with spanwise wavelength of 20mm and an amplitude of 5 mm. The slice shown in (A) is taken in a region where the plasma body force is non-zero. In D) iso-surfaces of the streamwise vorticity are also shown. From Durscher & Roy (2012).

These actuators have also been shown to eject fluid away from the surface at the "pinch" points of the actuator (Durscher & Roy, 2012; Roy & Wang, 2009; Wang *et al.*, 2011). Flow visualization of this effect is shown in Figure 5-5.

Between these two effects, it is expected that the serpentine geometry actuators are able to generate a sufficient perturbation to the flow in order to excite the streamwise vortical structures intended to be used for flow control.

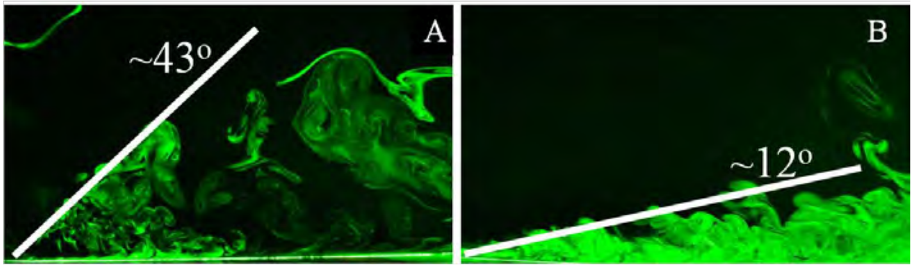

Figure 5-5. [Flow visualization of serpentine and standard geometry plasma actuators at A) the pinch point of a serpentine geometry actuator and B) by a standard geometry actuator under quiescent conditions. From Durscher & Roy (2012).

Before moving onto the effects of these actuators in a boundary layer, simulations of these actuators in a quiescent flow are performed in order to compare with these experimental results.

5.1.1 Numerical Details

In order to simulate these flows, the Implicit Large Eddy Simulation (ILES) Navier-Stokes solver, FDL3DI (Rizzetta *et al.*, 2008) is employed. This code solves the compressible, three-dimensional Navier-Stokes equations, and is described in more detail in Appendix C. For these simulations, the flow was simulated in a three dimensional box of size $[0.3, 8.0] \times [0, 1.5] \times [0.0, 0.1]$ in the $x \times y \times z$ directions. The grid used to resolve the mesh contains ≈7.5 million grid points. The mesh is highly refined at the inlet and around the actuator $1 < x < 1.1$, as well as near the surface where the actuator is placed. Far away from the wall and downstream of the actuator, the mesh is geometrically stretched. This stretching is done to minimize the number of grid points necessary, as well as to prevent reflections off of these boundaries. For boundary conditions, no slip conditions are applied at the inlet $(x = 0.3)$ and the wall surface $(y = 0.0)$, while a low order interpolation boundary condition is applied for the far field $(y = 1.5)$ and outlet $(x = 8.0)$ boundaries. The mesh and its boundary conditions are shown in Figure 5-6A. For treatment of the pressure and density boundary conditions, please refer to Section 3.1.1.

The serpentine geometry plasma actuator is located at the point $x = 1.025$. The streamwise amplitude of the serpentine geometry is $A = 0.025$, so the leading edge of the body force is located at the point $x = 1$. The trailing edge of the actuator geometry is centered at $x = 1.05$. The spanwise wave length of the actuator geometry is $\lambda = 0.1$. This geometry is equivalent to that shown in Figure 5-6C. To model the effects of the plasma, an approximate body force distribution is employed (Singh & Roy, 2008), a slice of which is shown in Figure 5-6B. This body force distribution is applied along the length of serpentine geometry electrodes, and the body force is rotated so that it is always oriented normal to the electrode edge.

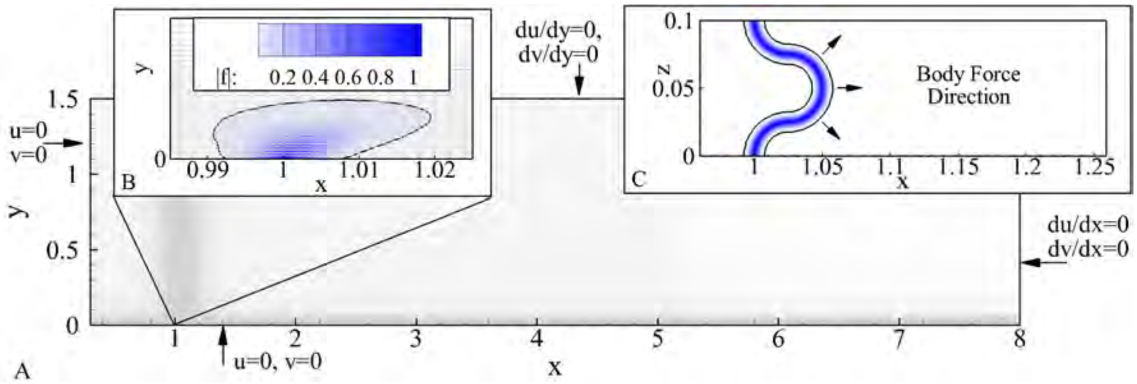

Figure 5-6. Computational mesh used to perform serpentine plasma actuator flow simulations. A) Mesh, B) two-dimensional slice of the body force, and C) geometry used to simulate the serpentine geometry plasma actuation. Every other point is shown.

As in the previous simulations, the magnitude of the plasma actuator is characterized by the velocity ratio (Equation 3–1). Details of the dimensional and non-dimensional parameters used are in Table 5-1.

5.1.2 Flow Characterization

Examining the flow fields around the serpentine geometry actuators operated under quiescent conditions, it can be seen that several interesting flow features are present (Figure 5-7). These results are shown alongside stereographic PIV results of a comparable experiment performed by Durscher & Roy (2012) for a comparable

Table 5-1. Dimensional and non-dimensional values used to compute the flow with a serpentine geometry plasma actuator.

Reference Parameter	Value
Dimensional values	
u_∞	$5.0 m/s$
L	$0.30 m$
ρ_∞	$1.20 kg/m^3$
ν	$1.5 \times 10^{-5} m^2/s$
Non-dimensional values	
Re	$100,000$
Pr	0.72
Ma	0.1
D_c	varies, see Figure 3-2a

experiment (Figures 8A and B of Durscher & Roy (2012)), and show good qualitative agreement. At the pinch point, a vectored jet is produced (Figure 5-7A). This contrasts with the much simpler behavior at the spreading point of the actuator geometry, where a simple wall jet has formed (Figure 5-7B). A twisted vectored jet is visualized using streamlines in Figure 5-8A, which compared favorably to experimental results in Figure 5-8b. In these streamlines, the effects of a streamwise oriented vortex can be seen downstream of the actuator (identified by the twisting braid of streamlines). The streamwise oriented vorticity in the flow field can be more clearly seen in Figure 5-9. As these flows have been discussed by Wang *et al.* (2011) and Durscher & Roy (2012), and are in qualitative agreement with those studies, they will not be discussed in further length here.

5.2 Boundary Layer Modification Using Serpentine Geometry Plasma Actuation

Having confirmed that the effects of serpentine geometry plasma actuation are comparable in simulations and experiments under quiescent conditions, a number of simulations have been performed in order to examine the effects of a serpentine geometry actuator in a laminar boundary layer. These simulations are based around flow conditions at relatively low Reynolds numbers, where the actuator is placed at a streamwise Reynolds number of $Re_x = 100,000$. These simulations are not perturbed in

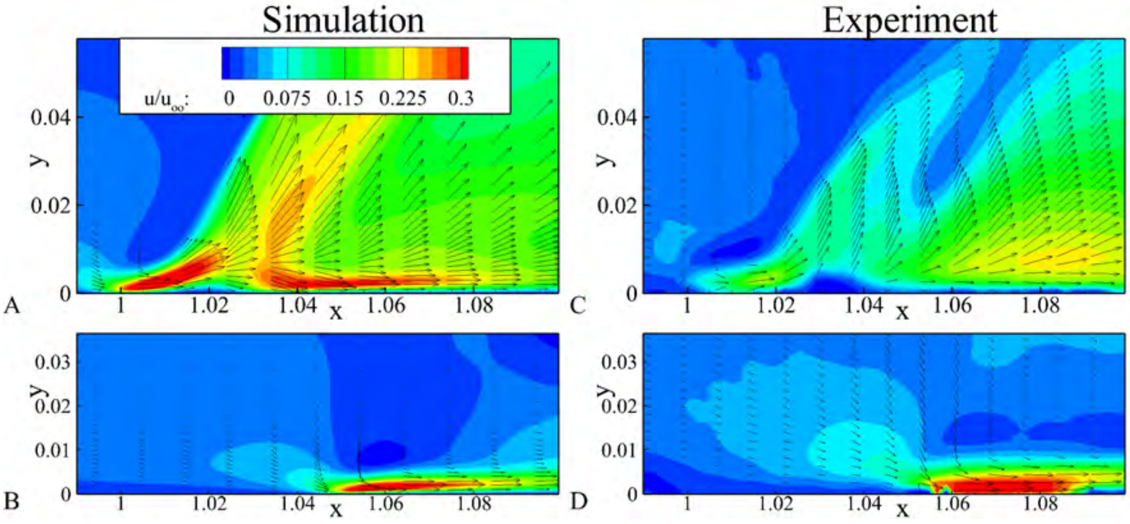

Figure 5-7. Comparison of simulated and experimental velocity fields induced by a serpentine geometry plasma actuator under quiescent conditions.. Velocity fields at the A,C) pinch point ($z = 0$), B,D) spreading point ($z = 0.05$) of the serpentine geometry actuator operated under quiescent conditions for A,B) simulations with a prescribed induced velocity of $u_p/u_\infty = 0.1$ and C,D) experiments performed by Durscher & Roy (2012). The experimental results have been non-dimensionalized so that the relative sizes of the actuators match.

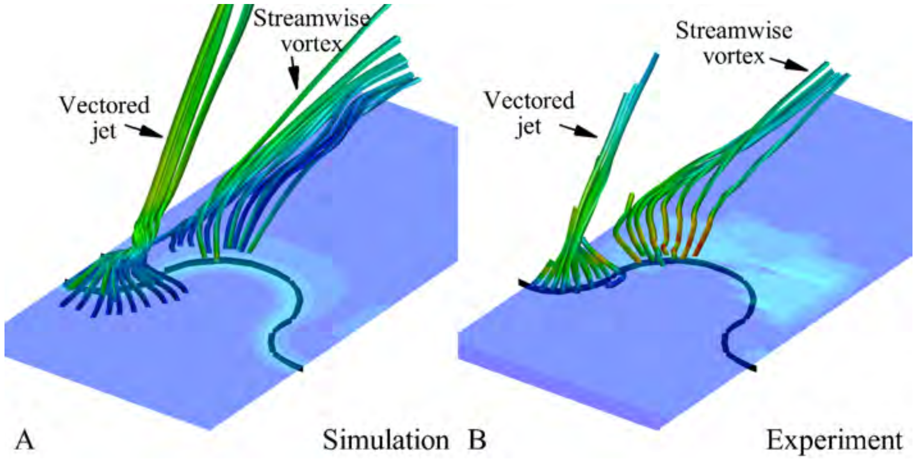

Figure 5-8. Comparison of simulated and experimental velocity streamlines induced by a serpentine geometry plasma actuator under quiescent conditions.. Streamlines in the flow fields from the A) simulation of a $u_p/u_\infty = 0.1$ serpentine actuator and B) experiments for a curved serpentine actuator. A black line is used to indicate the location of the actuator. Experimental data from Durscher & Roy (2012).

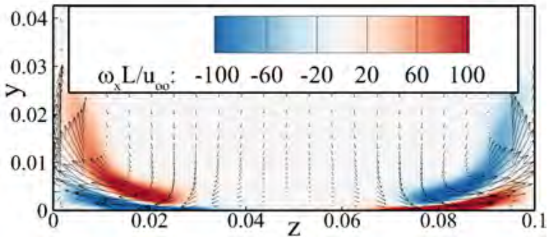

Figure 5-9. Streamwise vorticity at $x = 1.025$ of the serpentine geometry actuator operated under quiescent conditions for simulation with a prescribed induced velocity of $u_p/u_\infty = 0.1$

any active manner, other than the steady addition of momentum to the flow through the plasma body force.

5.2.1 Flow Characterization

There are two primary flow features in the flow that has been modified with the use of a serpentine geometry plasma actuator. The first of these is the forcing of fluid away from the surface in the region immediately downstream of the actuator in a vectored jet, comparable to the effects of a plasma synthetic jet (Santhanakrishnan & Jacob, 2007). Evidence of this effect can be found in Figure 5-10A and B. The second of these, is the counter rotating streamwise oriented vortices that propagate downstream (Durscher & Roy, 2012; Roy & Wang, 2009), evidence of which are given in Figure 5-10E and F, as well Figures 5-15 through 5-17. It is also expected that the streamwise vortical structures generate boundary layer streaks, which are the primary aim of implementing this device in a boundary layer.

Examining the flow field at the pinch point of the actuator (Figure 5-10A and B), it can be seen that the vectored jet produced in the presence of a mean flow is of much shallower angle than that produced under quiescent conditions. The angle of the jet is strongly dependent on the magnitude of the plasma actuation, where a larger velocity ratio produces a steeper jet. At the spreading point (Figure 5-10C and D), fluid is pulled down, towards the surface, an effect that has been seen for standard geometry plasma actuators in boundary layers previously. Overall, based on the spanwise averaged velocity field, the effect of the vectored jet is minimal, indicating that it is a localized effect.

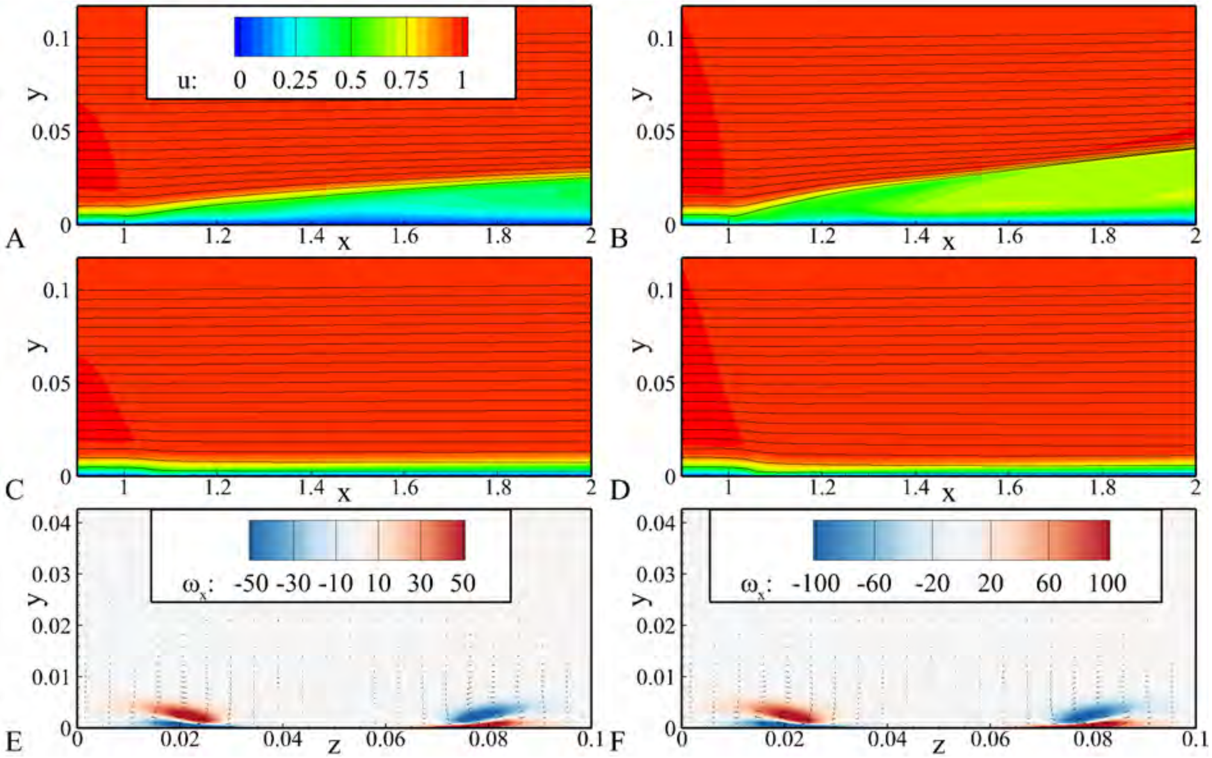

Figure 5-10. Slices of the boundary layer flow fields taken at the pinching and spreading points and streamwise vorticity when a serpentine plasma actuator is applied. A,C,E) $\gamma_0 = 0.05$ and B,D,F) $\gamma_0 = 0.10$. The streamwise velocities are shown for the A,B) pinching and C,D) spreading points. E,F) Streamwise vorticity at the center of the seprentine actuator ($x = 1.025$).

The presence of the streamwise vortices can be seen in Figures 5-10C,D and 5-12B, D and F. The strength of these vortices increases as the magnitude of the plasma actuation is increased. However, it can also be seen that as the strength of the actuation is increased beyond $\gamma_0 = 0.05$, the vortices are ejected from the boundary layer. This may be detrimental for applications of flow control, as these vortices will likely have less of an effect on the boundary layer as they move farther and farther away.

Examining the velocity profiles of the flow (Figure 5-13, it can be seen that there are several effects occurring simultaneously. At $x = 1$, it can be seen in the mean boundary layer profiles that the flow profile is being made fuller by the entrainment of additional

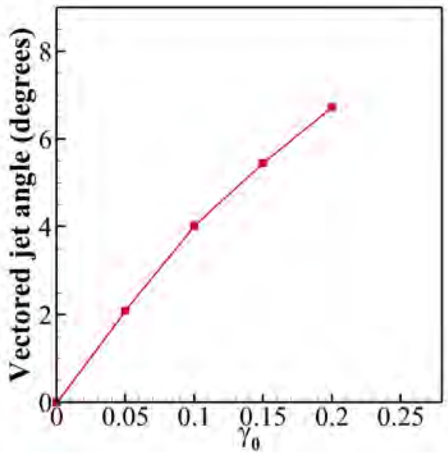

Figure 5-11. Angle of the vectored jet as the velocity ratio is varied. This angle was measured as the maximum flow angle at the height of $y = \delta_0^* = 0.0079$ along the impingement plane.

momentum into the boundary layer by the plasma actuator. Examining the streamwise velocity variations in Figure 5-13D,H,L, it can be seen that there are significant spanwise variations in the streamwise velocity, and for the lower levels of plasma actuation, the shape of the variations appears to be very similar. However, as the magnitude of the actuation is increased, non-linear effects become important, and the effect of the body force on the boundary layer no longer resembles the intended boundary layer streaks.

Defining the streak velocity magnitude as half the difference between the velocity at the center of the high (i.e. the spreading point, z=0.05) and low speed streak (i.e. the pinch point, z=0.00) regions,

$$A_u(x) = \max_{y\in[0,\infty)} \frac{|u_{pinch}(x,y) - u_{spread}(x,y)|}{2u_\infty} \tag{5–1}$$

and the streamwise vortex magnitude as the total amount of vorticity along the length of the boundary layer,

$$A_{\omega_x} = \int_{z=0}^{\lambda} \int_{y=0}^{\infty} |\omega_x| \, dydz \tag{5–2}$$

the magnitude of the streaks can also be quantified (Figure 5-14). In applying these metrics, it can be seen that magnitude of the vortex streak scales nicely with respect

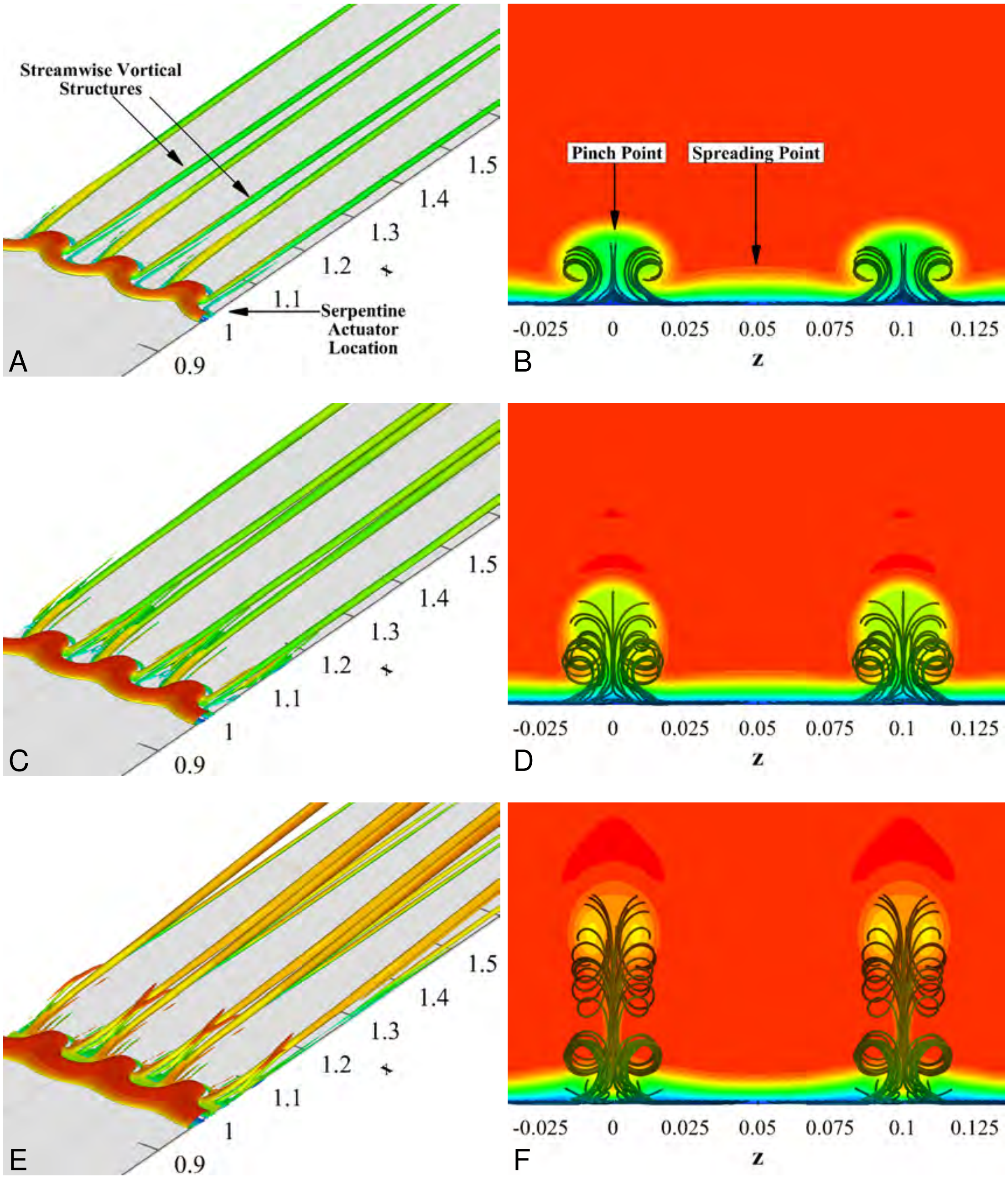

Figure 5-12. Visualization of the flow structure around and downstream of the serpentine plasma actuator in a laminar boundary layer. A,C,E) Q-criteria (colored by velocity magnitude) and B,D,F) streamtraces for the cases of A,B) $\gamma_0 = 0.05$, C,D) $\gamma_0 = 0.10$, and E,F) $\gamma_0 = 0.20$. In the background of B,D,F), a slice of the streamwise velocity component taken in the (y,z) plane at x=2 is shown. The data set is repeated twice in the z-direction, only a single wavelength was simulated.

to the velocity ratio γ_0 until non-linear effects become important. It appears that streak velocity magnitude can be amplified an order of magnitude larger the induced velocity of the plasma actuation. This amplification should also be a function of the spanwise wave number and the Reynolds number of the flow, effects not examined in the present study. The magnitude of the streamwise oriented vorticity seems to be more robust against non-linear effects, and appears to scale nicely with respect to $\gamma_0^{1/2}$ even after non-linear effects set in.

Examining the effects for larger levels of plasma actuation, it appears that the application of flow control may be too large in magnitude to excite the desired boundary layer streaks. That the variations in the flow field do not display similar profiles indicates that the magnitude of the perturbations is not behaving in a linear manner. For the linear behavior of the boundary layer streaks to occur, the magnitude of the actuation must be reduced.

As the flow control is applied, the boundary layer streaks separate from the surface. While this may still lead to the desired effect of accelerating the transition of the flow (as it appears that the streaks display multiple inflection points above the boundary layer, suggesting an inviscid instability), it will not necessarily be due to the same physics as the boundary layer streaks that are hoped to be excited. Even for the more moderate magnitudes of the plasma actuation, it can be seen that the boundary layer streaks are being transported out of the boundary layer, which may reduce the effectiveness of these actuators for flow control.

5.3 Conclusions

Simulations of a serpentine geometry plasma actuator have been performed under quiescent conditions, as well as in a boundary layer. Under quiescent conditions, comparisons were made to existing results in the literature (Durscher & Roy, 2012), indicating similar flow features. When applied to a boundary layer, it was confirmed that these actuators are able to generate boundary layer streaks.

The effects of using serpentine plasma actuators in a boundary layer were characterized. When plasma actuation was applied at a sufficiently low magnitude, the streaks generated were similar to the optimally generated streaks. These streaks could be used to control the laminar to turbulent transition mechanisms as currently understood, whether to accelerate (Andersson *et al.*, 2001; Hœpffner *et al.*, 2005) or delay (Fransson *et al.*, 2006) the onset of a turbulent flow.

When larger levels of plasma actuation were applied, the streaks deviated from the expected behavior, due to non-linear effects. In particular, it should be noted that the serpentine geometry plasma actuators generated vortical structures in the boundary layer that may be too large to be of use, as they lifted themselved out of the boundary layer. However, if the free stream velocity were to be increased, this effect would become a less likely scenario, due to the limitations of this class of actuators.

The present simulations indicate that the use of serpentine geometry plasma actuators may be very beneficial for higher speed applications. The natural amplification of the boundary layer streaks can be used to increase the magnitude of the perturbations generated by the plasma actuator.

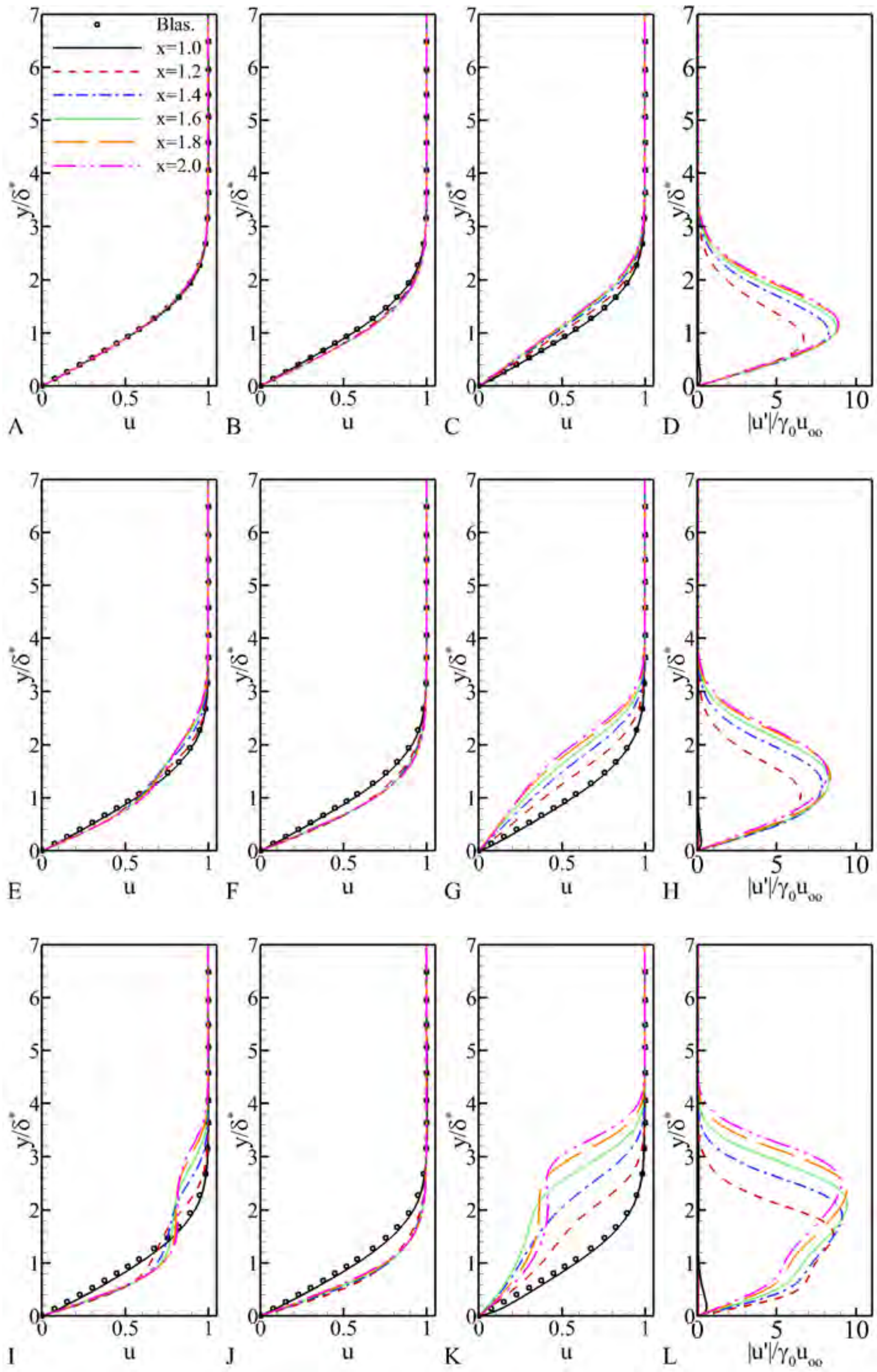

Figure 5-13. Various velocity profiles taken downstream of a serpentine plasma modified boundary layer as a function of the velocity ratio. A,E,I) Mean boundary layer profiles, B,F,J) boundary layer profiles at the spreading point, C,G,K) boundary layer profiles at the pinch point, and D,H,L) spanwise spandard deviation in the boundary layer profiles at various points along the length of the boundary layer for A-D) $\gamma_0 = 0.01$, E-H) $\gamma_0 = 0.025$, and I-L) $\gamma_0 = 0.05$.

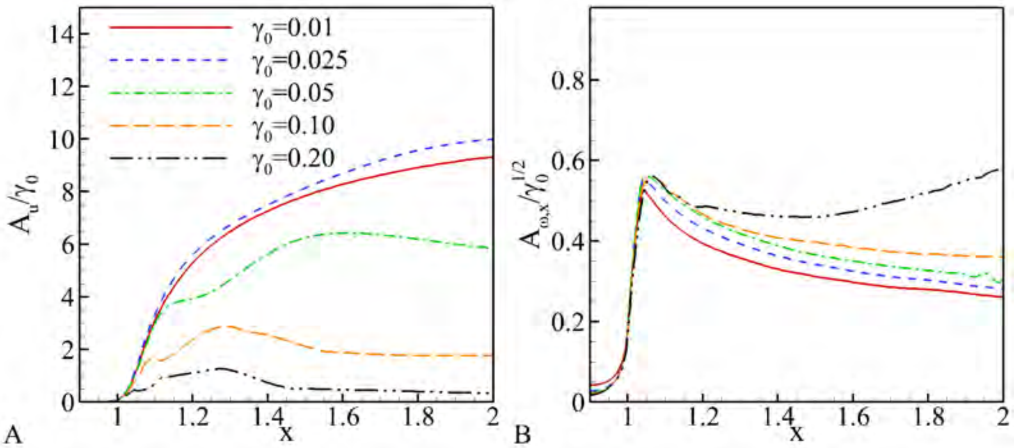

Figure 5-14. Normalized boundary layer streak A) velocity magnitude and B) streamwise vortex magnitude.

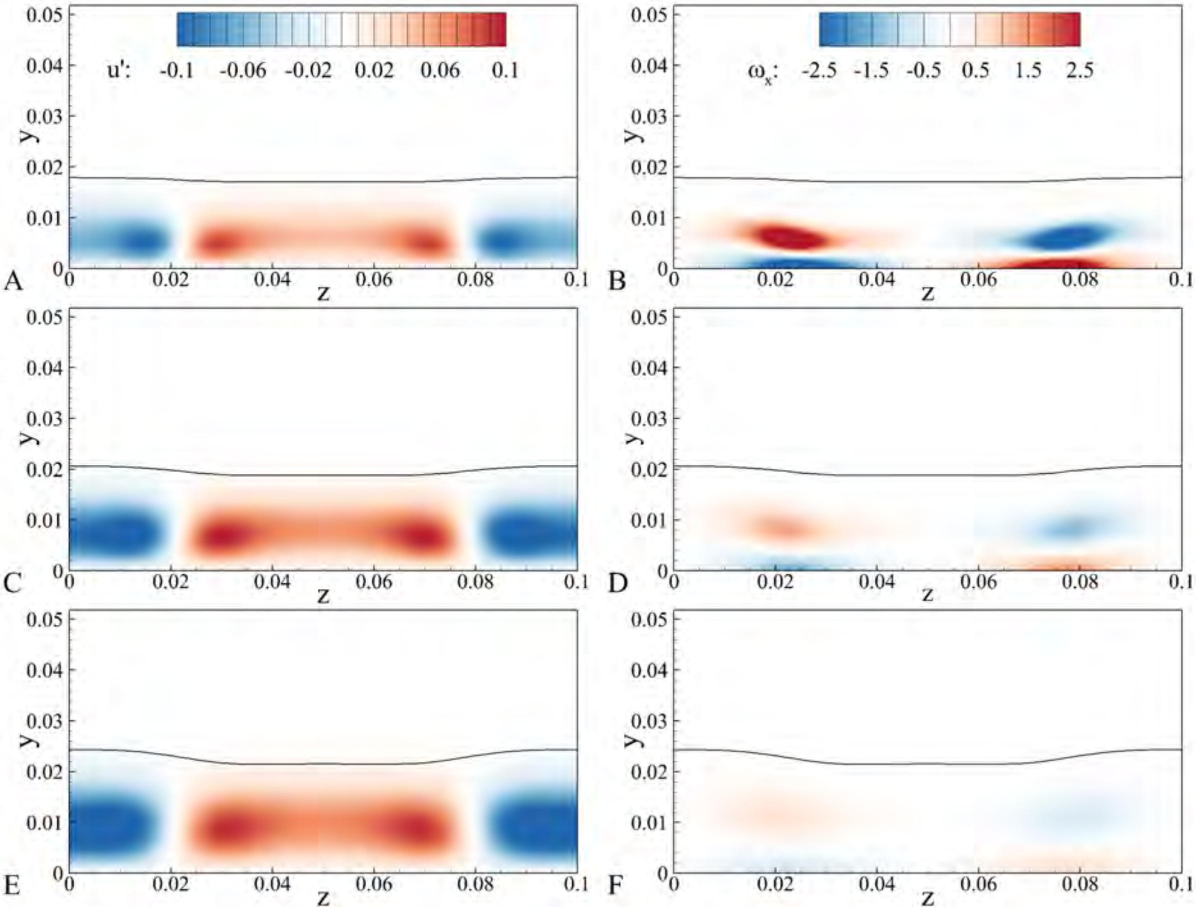

Figure 5-15. Boundary layer streaks in a serpentine plasma actuator modified boundary layer ($\gamma_0 = 0.01$). A,C,E) Streamwise variations in the velocity magnitudes and B,D,F) streamwise vorticity and velocity vectors at A,B) x=1.2 , C,D) x=1.5 , and E,F) x=2.0. The 99% boundary layer height ($\delta_{99\%}$) is marked by the thick solid line.

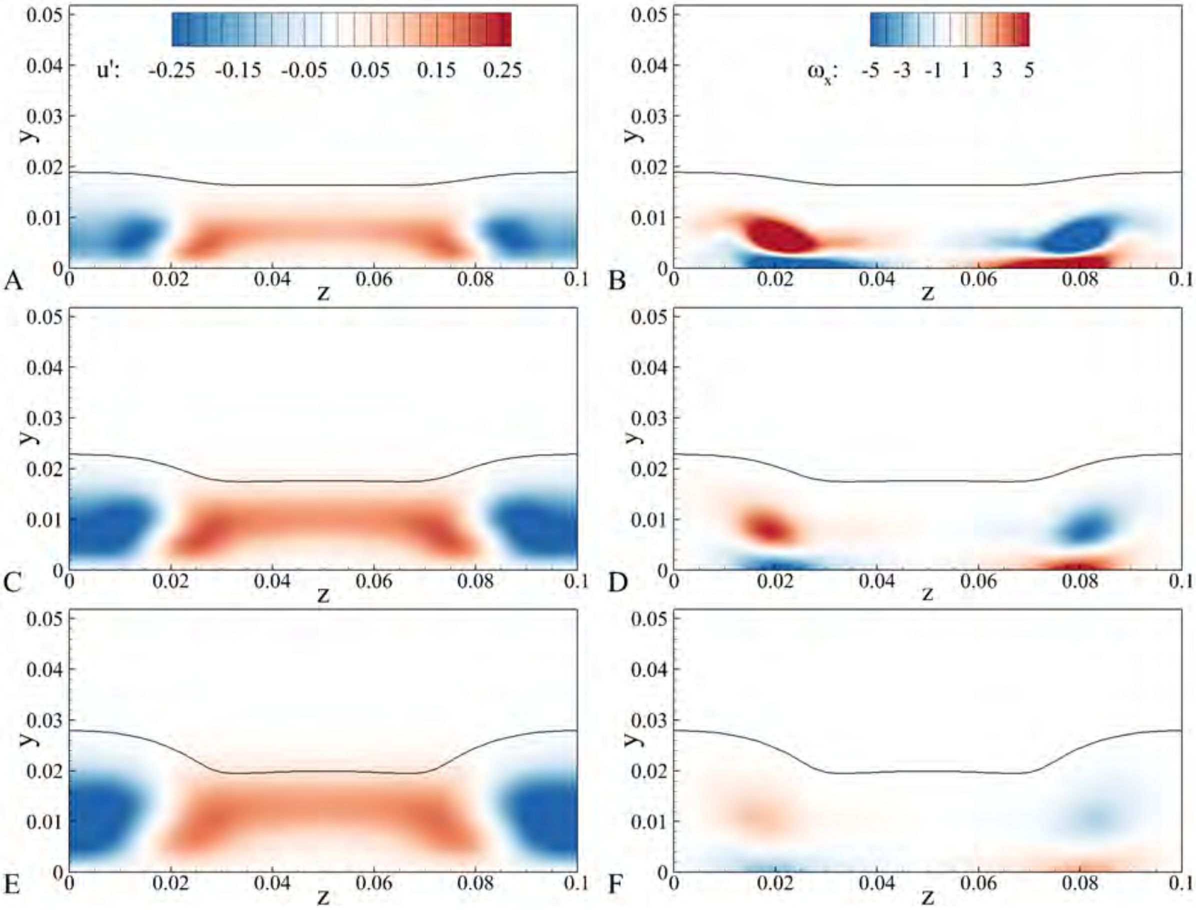

Figure 5-16. Boundary layer streaks in a serpentine plasma actuator modified boundary layer ($\gamma_0 = 0.025$). A,C,E) Streamwise variations in the velocity magnitudes and B,D,F) streamwise vorticity and velocity vectors at A,B) x=1.2 , C,D) x=1.5 , and E,F) x=2.0. The 99% boundary layer height ($\delta_{99\%}$) is marked by the thick solid line.

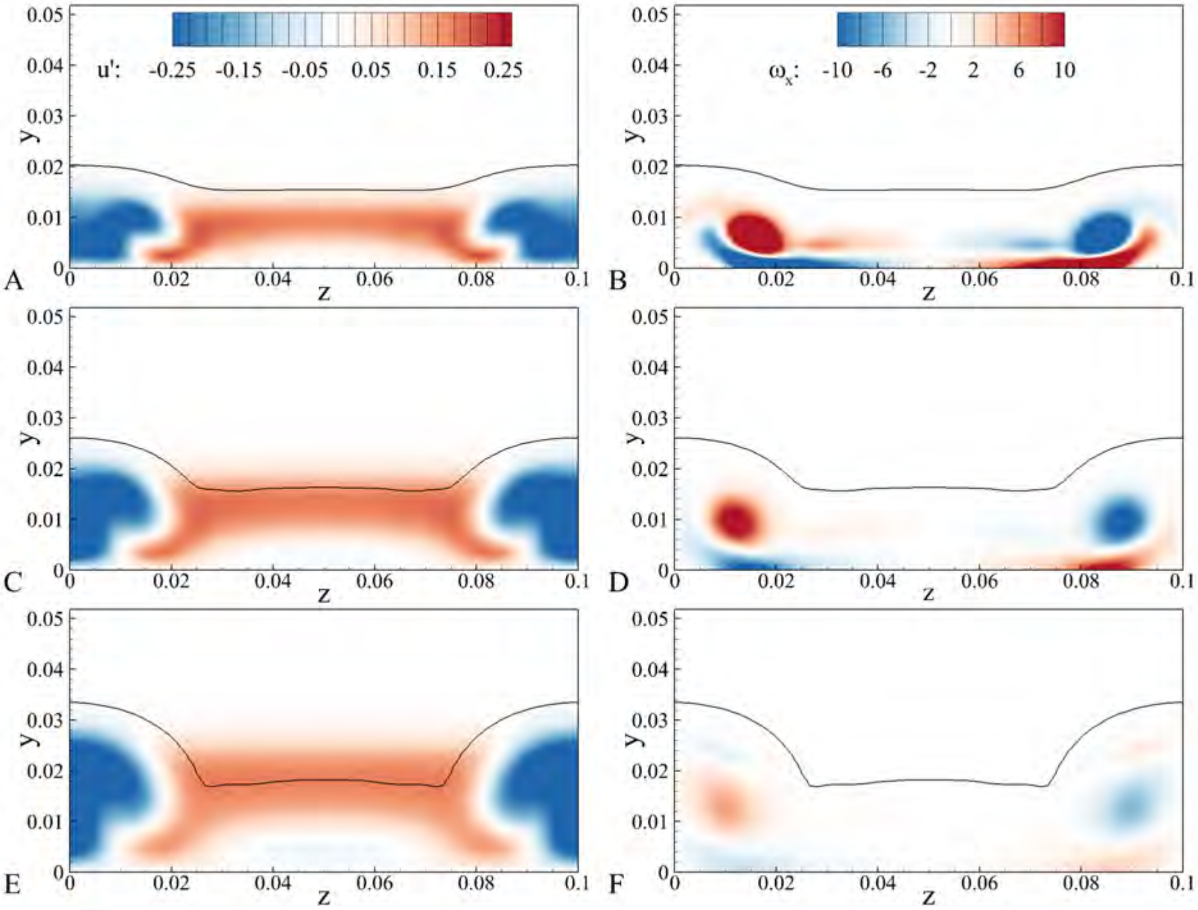

Figure 5-17. Boundary layer streaks in a serpentine plasma actuator modified boundary layer ($\gamma_0 = 0.05$). A,C,E) Streamwise variations in the velocity magnitudes and B,D,F) streamwise vorticity and velocity vectors at A,B) x=1.2 , C,D) x=1.5 , and E,F) x=2.0. The 99% boundary layer height ($\delta_{99\%}$) is marked by the thick solid line.

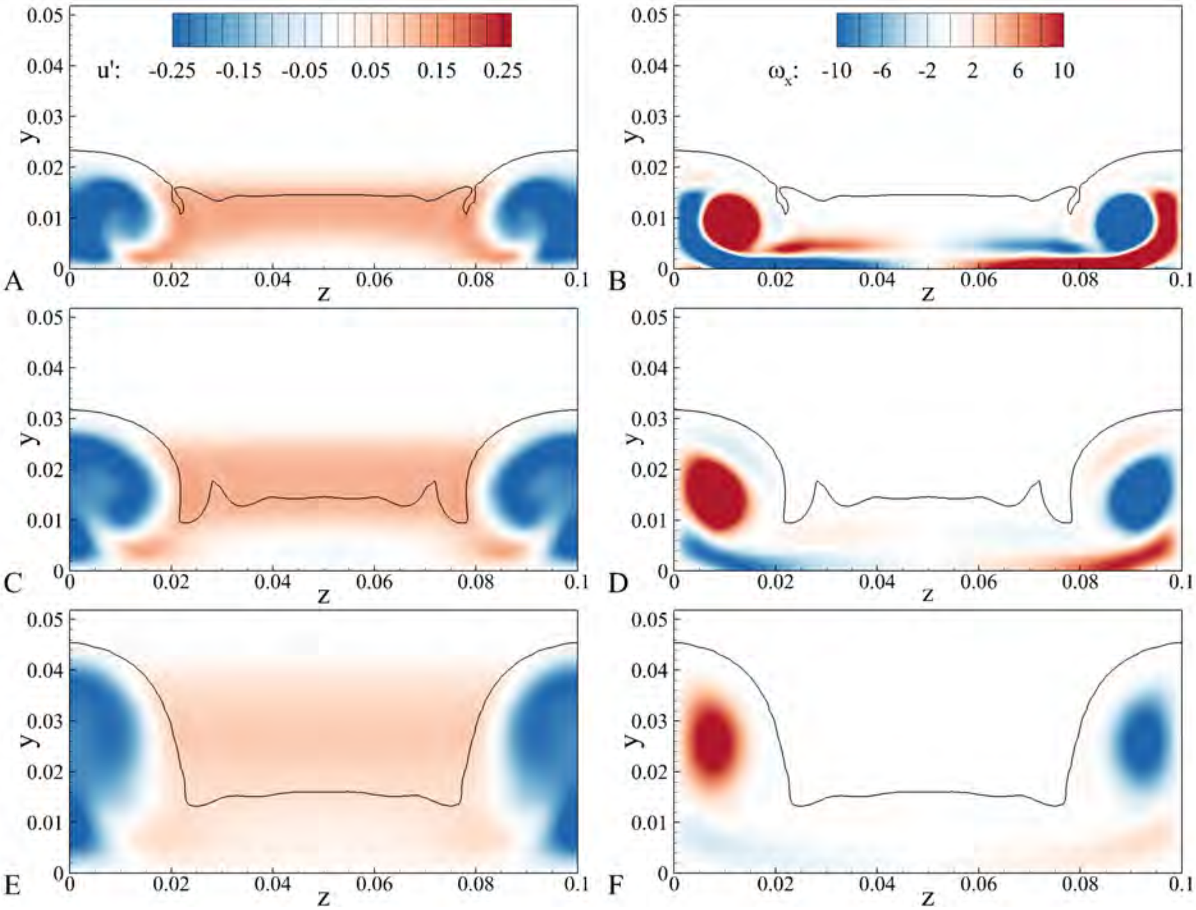

Figure 5-18. Boundary layer streaks in a serpentine plasma actuator modified boundary layer ($\gamma_0 = 0.10$). A,C,E) Streamwise variations in the velocity magnitudes and B,D,F) streamwise vorticity and velocity vectors at A,B) x=1.2 , C,D) x=1.5 , and E,F) x=2.0. The 99% boundary layer height ($\delta_{99\%}$) is marked by the thick solid line.

CHAPTER 6
USING PLASMA TO DRIVE A CHANNEL FLOW

There exist many types of channel flows, which can be powered by any number of different mechanisms. Once fully developed along the length of the channel, these simple flows can be considered to driven by a uniform body force, where the time mean pressure gradient or gravity mimics the effects of a body force (i.e. $f_x = \frac{\partial \bar{p}}{\partial x}$ or $f_x = \rho g$). That these channel flows are essentially driven by a body force leads to the concept of driving a channel flow using a plasma based body force.

There are obviously some distinct differences between the approximation of pressure gradients and gravity as a uniform body force and a plasma based body force. The most obvious of these is that the plasma body force is an unsteady, localized force, while the pressure/gravity force is usually steady and localized. However, comparisons on the plasma driven channel as a whole should be made with other types of pumps, as the plasma channel is actually driving the flow, whereas the pressure drop associated with channel flows is actually an impediment to whatever pump is driving the flow.

Before going into extensive detail exploring the internal flow structure as it is driven by a plasma channel (which is presented in Chapter 7), a proof of concept and an exploration of general system characterization would be very beneficial. Knowledge of the system as a whole would help to guide any numerical simulations, as it would provide a general range of flow conditions that could be expected under normal operation. These parameters would also be beneficial in understanding where a pump of this type could be useful in applications, where system parameters such as the maximum pressure differential or volume flow rate can be of greater importance than measurements of the Reynolds stress or turbulent kinetic energy. Studies of the flow physics will be performed in Chapter 7.

A schematic of a finite length plasma driven channel is shown in Figure 6-1A. The length scales shown are the channel height (h), the distance between the leading edges

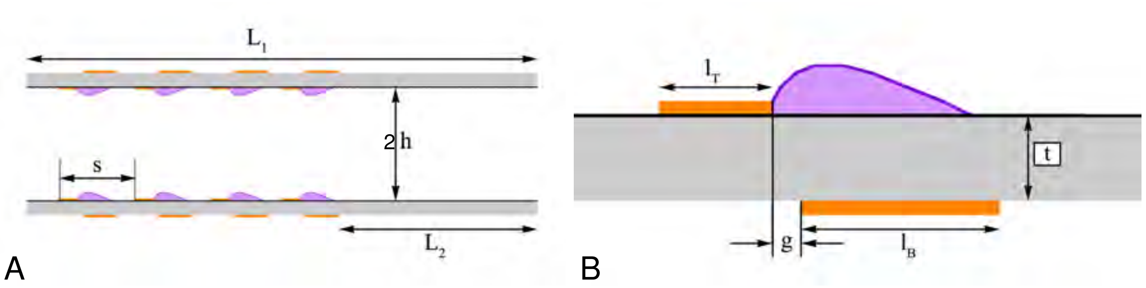

Figure 6-1. Schematic of the plasma channel and of a plasma actuator. A) the plasma channel and B) the plasma actuator.

of two consecutive actuators (s), the total length of the device (L_1) and the length for the flow to develop downstream of the devices (L_2). For each plasma actuator, there are also several important length scales (Figure 6-1B). There are the upper and lower electrode widths (l_U and l_L), as well as the electrode gap (g) and the dielectric thickness (t).

6.1 Experimental Measurements of a Finite Length Channel Flow

As a first step into understanding these flows, experiments have been performed in which the system characteristics are measured.

In the experiments performed as part of this study, each plasma actuator is powered by the same high voltage, high frequency signal, and connected to the same ground. All of the plasma actuators have also been built with uniform electrode geometries, so that they all produce a similar body force. This signal originates in a Tektronics AFG3022B function generator as 14kHz sinusoidal signal. The signal is then amplified to a higher current using a QSC RMX2450 audio amplifier. A Corona Magnetics high voltage transformer is used to convert the low voltage, high current signal to a high voltage, low current signal, which is then connected to the powered (upper) electrode. A high voltage probe and oscilloscope are used to measure the signal and ensure that an accurate voltage is applied to the plasma actuators. When a larger number of plasma actuators are operated simultaneously (i.e. when the current necessary to power the devices exceeds the rating of the transformers), this system is doubled, such that two identical

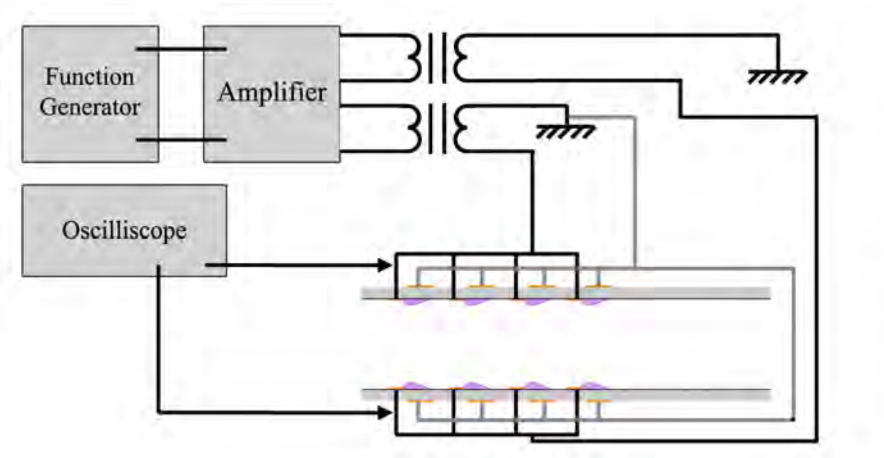

Figure 6-2. Circuit diagram of the plasma channel.

signals originating from the function generator, which are then amplified, transformed, and connected to the plasma actuators. A diagram of this system is shown in Figure 6-2.

The plasma channel was constructed out of PMMA (plexiglass), which also served as the dielectric for the plasma actuators. Four pairs of actuators were installed in the channel, for a total of 8 actuators inside of the channel. The grounded electrodes were sandwiched between two layers of PMMA, which were epoxied together. This two layer approach was effective at controlling thermal deformation, which had been significant in earlier experiments where only electrical tape had been used to encapsulate the grounded electrodes. While the DBD actuator creates a “non-thermal” plasma, the devices still became hot enough to create significant deformations when the channel was not stiffened. Four DBD actuators were installed on the upper surface of the channel and four more on the lower actuators were installed on the lower surface of the channel, for a total of eight DBD actuators in the channel. Super glue was used to attach side walls to the channel, allowing for a channel width of $10cm$. The electrodes for the plasma actuators extended all the full width of the channel. While this finite channel width implies that the flow inside the channel is not two dimensional, but is three dimensional instead, with an aspect ratio of 5, this channel should provide a relatively two dimensional flow at the center of the channel’s span. Furthermore, measurements were primarily taken at the channel centerline, where the mean flow should be symmetric. For the measurements and simulations performed, a channel of the following dimensions was examined.

Table 6-1. Dimensions of the plasma channel used for velocity measurements.

	Parameter	Value
Channel	L_l	2.1 cm
	L_{tot}	30.0 cm
	L_{dev}	20.0 cm
	s	2.5 cm
	$2h$	2.0 cm
	w	10.0 cm
	N	1-4
Actuators	L_U	0.4 cm
	L_L	0.4 cm
	g	0 cm
	t	0.25 cm

Before any data was collected, the plasma was operated for 30 seconds to remove any transient effects. After each set of samples was collected, the device was allowed to cool down for 180 seconds. Measurements were performed for a varying number of actuators operated at a single time, and varying the applied voltage for each actuator. As part of this study, the denotation of n actuators implies that n actuators were operated on the upper surface of the plasma channel and n more actuators were operated on the lower surface in order to promote a symmetric channel flow. These experiments were performed in a $0.6m \times 1.2m \times 1.2m$ quiescent chamber. No mean flow was present, except for the flow induced in and around the plasma channel by the DBD actuators.

While voltage and current data was only observed and not recorded during the collection of velocity and pressure data, electrical data has been collected in order to quantify the amount of power consumption of these devices during operation. A single actuator, of the same dimensions used in the experiments was operated under the same operating conditions as in the experiments. The power data collected shows a similar power law relationship as describe in recent reviews (Corke *et al.*, 2010; Moreau, 2007), where $Power \propto V^{3.5}$.

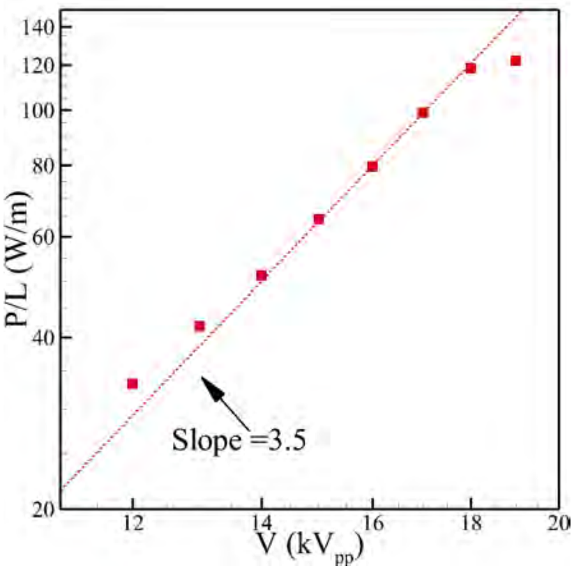

Figure 6-3. Power consumption by a single DBD actuator with the same dimensions and dielectric as used in the channel.

6.1.1 Velocity Measurements and Simulations of the Finite Length Channel Flow

A LaVision PIV system was used to make measurements of the flow exiting the channel. A 532 nm Nd:YAG laser was used to illuminate the Ondina seeded fluid. 250 samples were taken at a rate of 15 samples per second using a Phantom 7.3 high speed camera, which has a 600×800 pixel resolution focused on a $4cm \times 5cm$ region near the exit of the plasma channel. Measurements inside of the channel were attempted, but an opaque residue from the use of super glue on the channel sidewalls and reflections of the laser bouncing off of the upper and lower channel walls and electrodes prevented high quality from being captured. These samples were then analyzed using LaVision's DaVis software. The velocity field was calculated using a 16×16 pixel integration window with 50% overlap. A 32×32 pixel integration window was also used with 50% overlap in order to verify that the results were insensitive to the PIV processing.

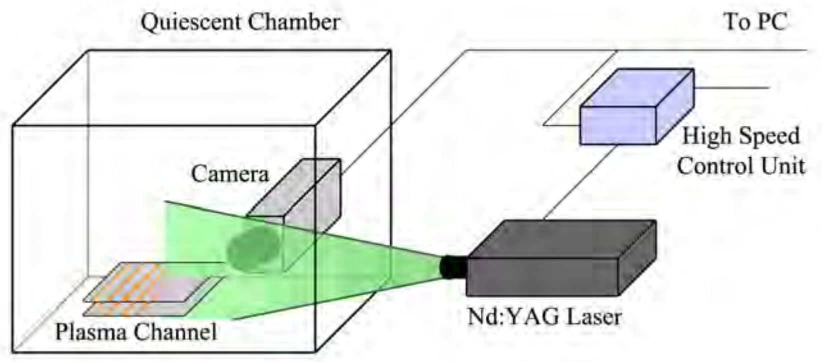

Figure 6-4. PIV Setup for examining the plasma driven channel flow.

It can be seen in Figure 6-5A, that upon it's exit, the flow produced by the plasma channel produces unsteady jet-like effects. However, when time averaged over the available samples, the flow can be seen to be nearly symmetric in nature (Figure 6-5B). These large scale unsteady effects can largely be attributed to instabilities in the jet (Bickley, 1937), rather than large flow perturbations in the channel flow. Based on the exit velocity, the Reynolds number of the channel flows ranges from approximately 1500 to 4000 (for a single set of actuators operated at $16kV_{pp}$ to 4 sets of actuators operated at $19kV_{pp}$) in these experiments, which is a range where unsteady effects and hydrodynamic instabilities can become important. While this may lead to a relatively low Reynolds number turbulent channel flow, it does not preclude the channel flow from eventual turbulent flow effects in longer channels with higher Reynolds numbers due to increased flow velocity or channel height.

Exploring the effects of voltage and operating different numbers of plasma actuators simultaneously, it can be seen that the maximum velocity and the total mass flow per unit width ($Q\rho/w$) contained in the channel flow as it exits increases with respect to both the applied voltage and the number of actuators run for a specific case (Figure 6-6). This is a logical conclusion to arrive at, as the total amount of body force pushing the fluid downstream increases with respect to both of these variables. As the total amount of

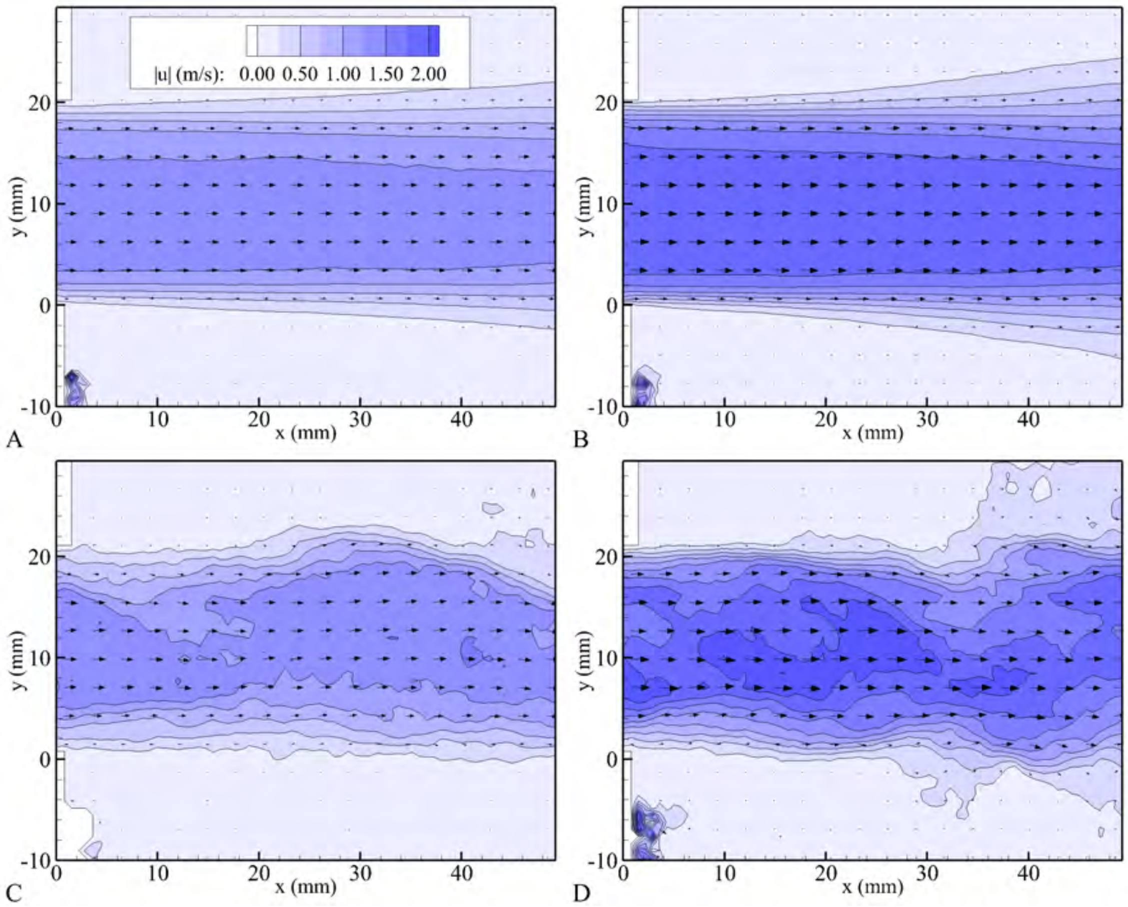

Figure 6-5. Velocity magnitudes measurements at the exit of the plasma driven channel. A,B) Instantaneous and C,D) time averaged velocity magnitudes measurements at the exit of the channel with an applied voltage of 18 kVpp for A,C) 1 and B,D) 3 actuators powered on the top and bottom of the channel.

body force inside of the channel increases, the momentum addition similarly increases, which will in turn lead to higher velocity flow in the channel. Assuming that a power law relationship can also be applied to the maximum velocity exiting the channel,

$$u_{max} \approx \alpha n_{act}^{\gamma} V^{\beta} \tag{6–1}$$

where α, β, and γ are the empirically derived constants $\alpha = 3.98 \times 10^{-3}$, $\gamma = 0.307$ and $\beta = 2.02$ from a power law curve fit. In this relationship, the voltage V must be in kV_{pp}, the maximum velocity in m/s. Performing the same power law curve fit for the mass flow per unit width, the constants are $\alpha = 1.87 \times 10^{-5}$, $\gamma = 0.352$ and $\beta = 2.29$.

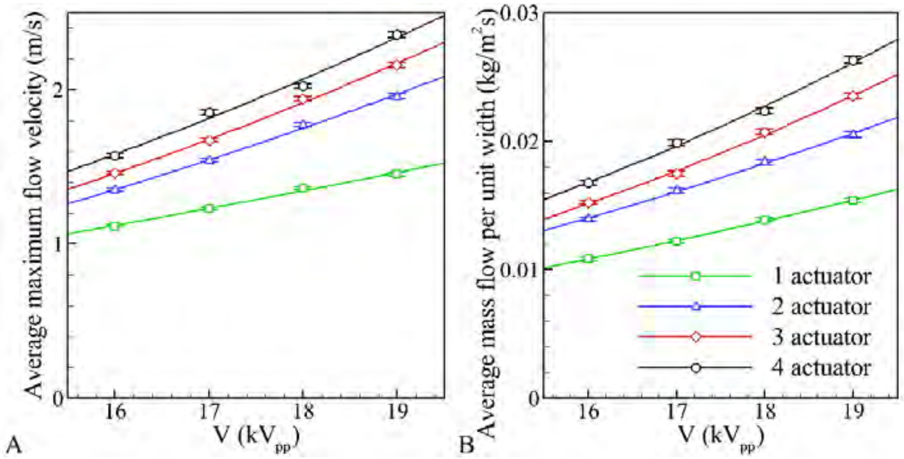

Figure 6-6. Velocity and mass flow measurements at the channel exit. A) Maximum velocity and B) total mass flow per unit width ($Q\rho/w$) of the flow 0.5cm downstream of the channel exit.

6.1.2 Pressure Measurements

A longer channel was also examined ($L_1 = 45cm$) in order to better gage how the pressure varies within the channel around and downstream of the actuators. Pressure taps were installed at numerous locations in the channel. Near the actuators, taps were installed on the side of the channel at the centerline in order to measure the pressure. The centerline location was selected in order to avoid any effects of the wall normal velocity impinging down on the surface of the channel, which could create lead to greater uncertainty in the pressure measurements. Downstream of the actuators, where the surface normal velocity induced by the actuators is not of significant concern, pressure taps were installed on the surface of the channel. A Furness Controls Model 332 Differential pressure transmitter was used to take measurements. 512 samples were taken at each location shown at a rate of 20 samples per second. Again, a 30 second warm up period was allowed between the start of plasma actuation and the start of data collection, and a 180 second cool down period after each pressure sampling. The differential pressure was measured against the pressure in the quiescent chamber located approximately one meter away from the plasma channel. The Thompson-Tau outlier removal method was applied to remove spurious results.

Samples are shown for 1, 2, and 3 plasma actuators running simultaneously. These plasma actuators are located between the first and second, second and third, and third and fourth pressure taps. It can be seen in Figure 6-7 that there is an initial rise in pressure at the inlet of the channel, corresponding to both the first plasma actuator and any potential inlet effects. With the addition of a second (Figure 6-7B) and third (Figure 6-7C) plasma actuator downstream of the initial actuator, further increases in pressure effects can be seen to occur. As one moves downstream of the plasma actuators, the pressure can be seen to continue to increase as the flow develops in the channel. Farther downstream, the pressure is finally seen to slowly drop, indicating that the viscous effects of skin friction with the channel walls create a negative pressure gradient.

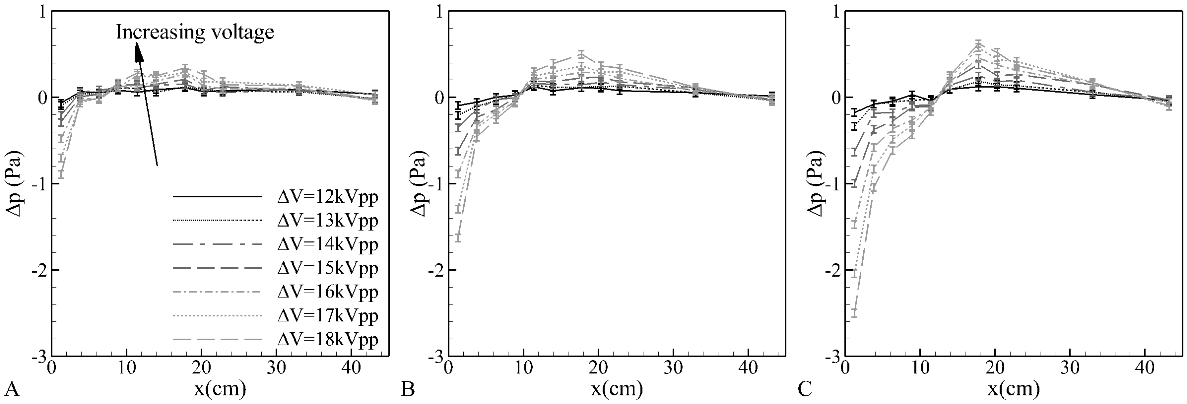

Figure 6-7. [Pressure measurements along the centerline and surface of the plasma channel for a varying number of actuators. A) 1, B) 2, and C) 3 actuators.

Experiments were also performed with a screen impeding the flow of air through the channel downstream of the actuators, with the screen located at $x = 15\ cm$. The screen was hexagonal in nature and approximately 2.5 cm thick, with 3 mm holes arranges in a hexagonal pattern. This screen was intended to steady the flow, and remove any vortices in the flow , but the result was a near blockage of flow through the channel. However, pressure measurements were still recorded with the same sampling rate as the unimpeded plasma channel. With this impedance, the pressure builds up at the mesh, and the pressure drop primarily occurs across the mesh, with no significant changes occurring downstream of the mesh (Figure 6-8).

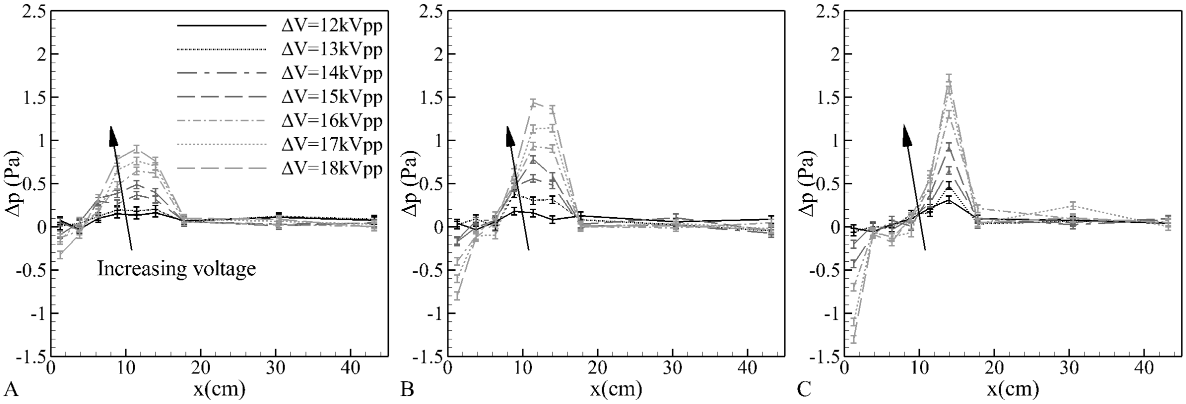

Figure 6-8. Pressure measurements along the centerline and surface of the plasma channel with the addition of an screen impeding the channel flow. A) 1, B) 2, and C) 3 actuators.

While these two channel flow experiments show significant differences in the differential pressure along the length of the channel, when the maximum pressure differential within the interior of the channel (that is $max(\Delta p) - min(\Delta p)$) is examined, a striking result is found (Figure 6-9). The maximum pressure differential for the number and applied voltage of the plasma actuators is seen to match up fairly well. This indicates that the plasma actuators are generating the same pressure differential across each actuator, independently of whether the flow is moving downstream or not under these low velocity conditions.

Considering the well behaved nature of these relationships, an empirical model of the expected pressure rise can be developed. A proportional increase in the pressure with respect to the number of plasma actuators employed is expected. Power law relationships have been drawn between the thrust production, power consumption and operating voltage of the plasma actuator. As such, a power law relationship is expected with the voltage. This leads to the approximate correlation

$$\Delta p_{max} \approx \alpha n_{act} V^{\beta} \tag{6–2}$$

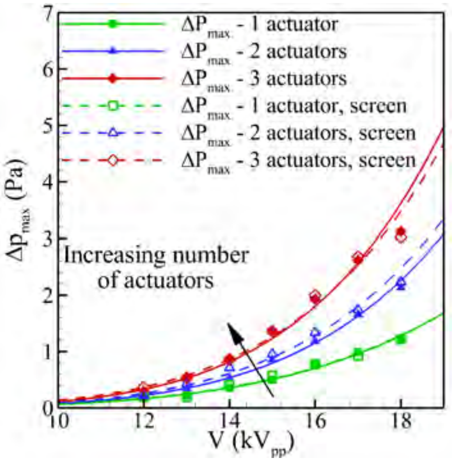

Figure 6-9. Maximum pressure differential measured within the plasma channel. Lines denote power law curve fits to the data.

where α and β are the empirically derived constants $\alpha = 1.21 \times 10^{-7}$ and $\beta = 5.57$. In this relationship, the voltage V must be in kV_{pp}, the resulting pressure differential will be in Pascals.

6.1.3 Device Efficiency

Implementing these plasma actuators in a closed environment provides an opportunity to evaluate the efficiency of plasma actuators in imparting momentum to fluid in the channel. Defining this efficiency as the ratio of hydrodynamic power to the input electrical power

$$\eta = \frac{P_{flow}}{P_{in}} = \frac{\int_0^h (u\Delta p)\, dA}{P_{in}} \tag{6–3}$$

which can be approximated in two different ways. If the average flow is assumed to be plug-like, $u \approx u_{max}$, then the approximation

$$\eta_u \approx \frac{u_{max} h \Delta p_{max}}{P_{in}/L} \tag{6–4}$$

arises, which can also be considered an upper bound on the device efficiency. For a more accurate approximation using the power and mass flow rate per unit width, the efficiency can be approximated as

$$\eta_Q \approx \frac{Q/L\Delta p_{max}}{P_{in}/L} \tag{6–5}$$

Computing these efficiencies from the experimental data (and using approximated data based on the power law curve fits when necessary), the efficiency of the plasma channel can be seen to be less that 0.1% (Figure 6-10). The channel efficiency appears to be highly dependent on the operating voltage and increases an order of magnitude as the operating voltage is increased from a low to moderate value.

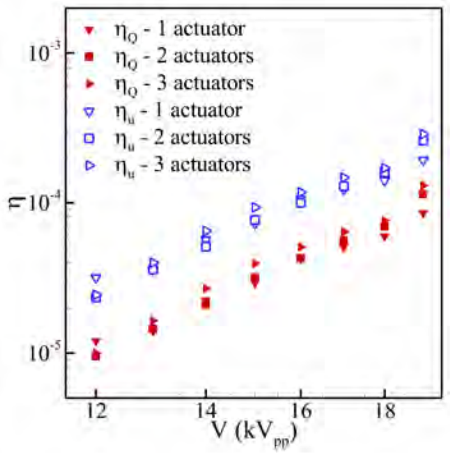

Figure 6-10. Efficiency of the plasma actuation.

Using the different empirical power law relationships developed for u_{max}, Δp_{max} and P_{in}, the efficiency of the channel can also be put in terms of a power law relationship with respect to the input voltage, such that

$$\eta_Q \approx \frac{\left(\alpha_Q n_{act}^{\gamma_Q} V^{\beta_Q}\right)\left(\alpha_p n_{act} V^{\beta_p}\right)}{\alpha_e n_{act} V^{\beta_e}} \tag{6–6}$$

$$\eta_u \approx \frac{\left(\alpha_u n_{act}^{\gamma_u} V^{\beta_u}\right)\left(\alpha_p n_{act} V^{\beta_p}\right)}{\alpha_e n_{act} V^{\beta_e}} \tag{6–7}$$

where the various coefficients are denoted by Q for the mass flow rate per unit width, u for the maximum velocity, p for the maximum pressure and e for the electrical input. Ignoring the constants, there is an important propotionality to these efficiency calculations.

$$\eta \approx \eta_{Q,u} \propto V^{\beta_{Q,u}+\beta_p-\beta_e} \tag{6–8}$$

Computing this exponent based on the empirical curve fits, $\beta_Q + \beta_p - \beta_e = 4.35$ and $\beta_u + \beta_p - \beta_e = 4.09$, indicating that these plasma devices become increasingly more efficient at imparting momentum to the flow as the operating voltage is increased. However, the upper range of operating voltages is limited by the effects of plasma streamer formation and dielectric breakdown (Thomas *et al.*, 2009).

6.2 Conclusions

The results of these experiments and simulations show that with the application of dielectric barrier discharge actuators, channel flows of up to several meters per second can be generated. In using DBD actuation to drive this flow, the actuation is effectively working as a low speed pump for small flows. A distinct difference exists, as this type of pump is inherently two-dimensional in nature and can be extended to a very large width, something which traditional centrifugal and axial pumps cannot do.

Results of parametric studies varying the number of DBD actuators operated in a channel, as well as the operating voltage applied to these actuators, have been discussed. These experiments indicate several conclusions.

The exit velocities, maximum pressure, mass flux, and differential across an array of actuators fit well to a power law relationship with respect to the operating voltage. These relationships indicate that there is an increasing margin of return for the maximum velocities, mass flux, and pressure rise due to the actuators with respect to voltage. However, only the pressure differential continues to rise with respect to input electrical power as the voltage is increased. The maximum velocities and mass flux per unit power input decrease as the voltage is increased.

Each plasma actuator generates the same pressure increase across its surface, independently of the bulk flow in the channel. While there may be some upper bound on the total pressure differential than can be created in the channel, the maximum pressure increase appears to have a linear relationship with the total number of actuators in the channel.

The efficiency of the DBD plasma channel can easily be inferred from the mass flow and maximum pressure differential in the channel. Using the previously developed power law relationships for the mass flow, maximum pressure differential, and electrical power input, the channel efficiency also appears to display a power law relationship with respect to the operating voltage, with an exponent on the order of 4.09 to 4.35. While the efficiency of the devices is low, this exponent suggests that large increases in efficiency may be possible.

These results have been published in the research literature (Riherd & Roy, 2012*b*).

CHAPTER 7
FLOW STRUCTURE OF PLASMA DRIVEN CHANNEL FLOWS

While the general characteristics of a plasma driven channel are useful for certain applications and in order to define a range of operating parameters for a device of this type, there are a number of outstanding questions regarding the characterization and physical understanding of this flow itself, how manipulating the flow physics can be used to improve the efficiency of the channel, and how it compares to more canonical channel flows. With the localization of the body force, the assumptions of a one-dimensional flow are no longer valid, and issues that can normally be neglected become important.

Several studies have been performed examining the internal structure of these flows in the past (Debiasi & Jiun-Ming, 2011; Morgan & Visbal, 2013; Riherd & Roy, 2012*b*), but these have primarily been computational in nature, and there has been little in the way of experimental validation of the flow structure inside of the channel. The only experimental study that did look inside the channel is of questionable accuracy and does not provide much in the way of data or explanation of the flow's effects around the actuator (Debiasi & Jiun-Ming, 2011). More in depth descriptions of the flow field are presented in Morgan & Visbal (2013).

As described in Chapter 6, under quiescent conditions and in a semi-bounded domain, DBD actuators are known to produce wall jets. These wall jets have been shown to mimic the Glauert wall jet similarity solution sufficiently far downstream of the plasma actuator (Opaits *et al.*, 2010). The body force created by the plasma actuator entrains fluid from upstream of and above the actuator relative to the wall jet (Figure 7-1A). This fluid is then convected by the wall jet, which gradually decreases in magnitude while increasing in its height normal to the surface.

However, when the domain of the plasma actuation is bounded, such as in a channel flow, the regions from which fluid is entrained changes (Figure 7-1B). In the bounded domain, the fluid entrained by the wall jet is largely drawn from upstream of

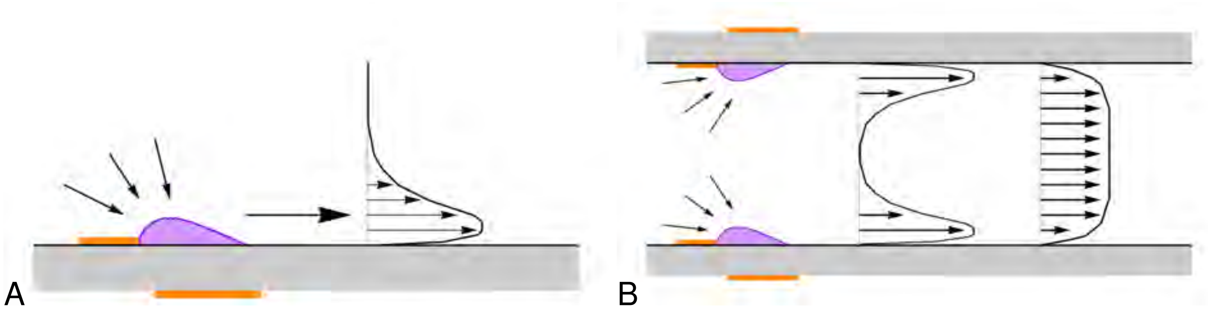

Figure 7-1. Comparison of the flow effects for plasma actuators in different domains. A) Plasma actuator in an semi-unbounded domain. B) Pair of oppositely placed plasma actuators in a channel.

the wall jet, though some is still pulled downwards toward the surface. For a pair of plasma actuators placed on opposite sides of a channel, a wall jet will form near both of the actuators. However, as the wall jets expand and decelerate, they will coalesce with each other, eventually forming a channel flow sufficiently far downstream of the plasma actuators. As flow is pushed through the channel, the plasma actuators are effectively acting as a pump or a fan, with the body force replacing the effects of any moving parts.

7.1 Problem Description

There are two geometries of plasma driven channels that are currently under investigation. In one configuration, plasma actuators are located on the bottom of the channel at a periodic distance, L_x. This geometry will be referred to as a “single” configuration. In the second configuration, there are symmetrically placed pairs of plasma actuators located periodically along the length of the channel at a distance of L_x. This geometry will be referred to as a “double” configuration. These two configurations are shown in Figure 7-2.

In Chapter 6, it was shown that across each plasma actuator, there is an increase in the pressure across each plasma actuator, a result also indicated in the simulations of Morgan & Visbal (2013). This pressure increase is due to the flow resisting the applied body force generated by each of the sets of plasma actuators. As such, it would appear that as the number of actuators increases and the flow reaches a periodic mean state,

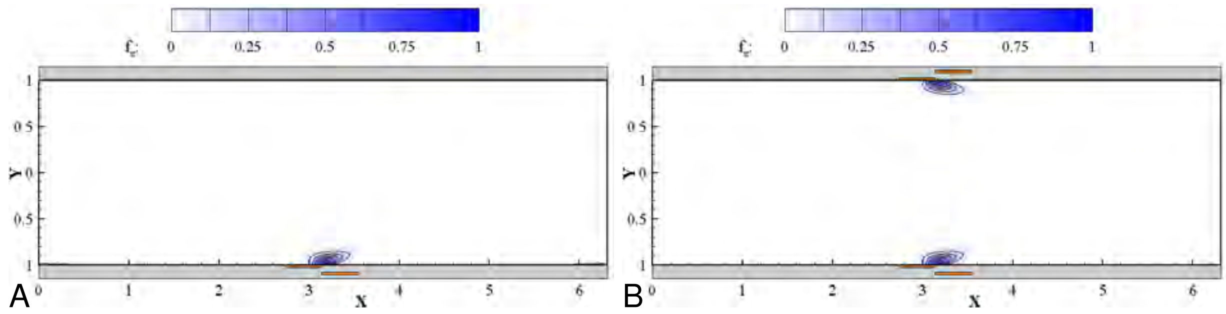

Figure 7-2. Comparison of plasma channel geometries. Streamwise body force (f_x) for A) single and B) double' geometry plasma driven channel flows for $L_x = 2\pi$.

the pressure in the flow does not reach a periodic state, rather the pressure gradient becomes periodic. Because of this, any simulations of a plasma driven channel flow with periodic boundary conditions would necessarily require a mean pressure gradient to be applied in order to account for this induced pressure gradient. While this mean pressure gradient could be estimated, based on previous experiments or simulations, it cannot be determined exactly a priori. Due to this constraint, any simulation would be speculative with respect to the actual pressure gradient applied to the channel and the induced pressure gradient.

Based on the need to have a clearly defined pressure gradient applied to the channel flow, the present work focuses on finite length channel flows with inlets and outlets, though it is hoped that the flow reaches a nearly periodic state inside of the channel as it develops.

7.2 2D Laminar Flow Characterization

At sufficiently low Reynolds numbers, it is expected that these flows remain laminar. In order to examine the behavior of these flows under laminar conditions, two-dimensional simulations of these flows have been performed using the two-dimensional variant of the code FDL3DI (Appendix C).

7.2.1 Numerical Details

In simulating these plasma driven channel flows, channels of fixed length and height have been discretized on a body fitted mesh. At the inlet and outlet, the surface of the channel is rounded in order to produce smooth mesh. Outside of the inlet and outlet of the channel flow, the mesh is extended for a further distance in order to allow for the appropriate level of inflow and outflow from the channel. A schematic of the domain used can be seen in Figure 7-3.

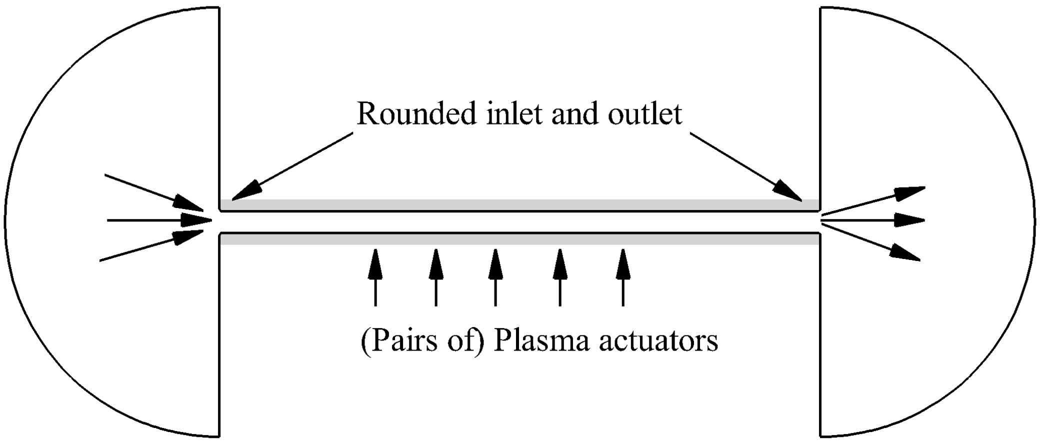

Figure 7-3. Basic schematic of the flow domain used for simulations of the plasma driven channel flow.

A Reynolds number of 3300 was used for these simulations, which corresponds to a characteristic velocity of 5 m/s and a channel half height of 1cm using air as the fluid (ρ=1.2 kg/m^3, ν =1.5$\times$10^{-5}). Based on the plasma model used, the integrated body force per unit length from each plasma actuator is equal to D_c 39.3 mN/m.

For a majority of the simulations, a time step of $\Delta t = 0.005$ was used (though temporal resolution studies were performed in order to establish that this was a sufficiently low time step). Several different mesh densities were tested as part of a grid resolution study, the details of which are in Table 7-1. For the streamwise mesh resolution study, the time step was altered so that the CFL number remains the same.

Table 7-1. Meshes used for grid resolution studies of the channel geometry.

Study	Mesh	L_x	L_y	$N_{x,tot}$	$N_{x,channel}$	N_y	$\Delta x_{channel}$	Δy_{wall}
Streamwise resolution	Fine-L	56	2	6910	6351	101	0.01	0.00505
	Baseline	56	2	3455	3175	101	0.02	0.00505
	Coarse-L	56	2	1867	1727	101	0.04	0.00505
Wall normal resolution	Fine-H	56	2	3455	3175	201	0.02	0.00252
	Baseline	56	2	3455	3175	101	0.02	0.00505
	Coarse-H	56	2	3455	3175	51	0.02	0.01012

Based on the simulations of a single geometry channel, velocity profiles after 750 units of time are shown in Figures 7-4 and 7-5. It should be stated that at this time, the flow is unsteady, but that there is still relatively good agreement between the different mesh resolutions examined. As such, it appears that the Baseline grid resolution is sufficient for these simulations.

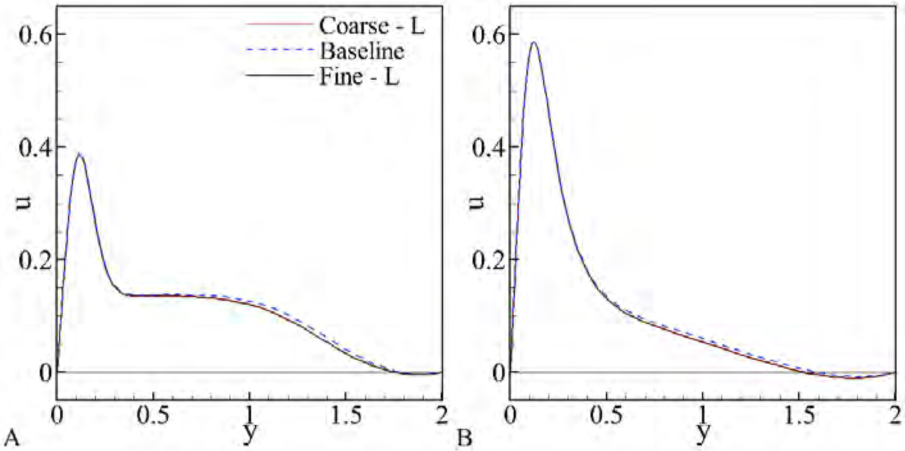

Figure 7-4. Velocity profiles from the streamwise grid resolution study at A) $x/h = 19.0$ and B) $x/h = 44.2$ units downstream from the channel inlet.

In order to properly capture the far field behavior of the plasma driven channel flow, adaptive sponge regions have been applied at a distance from the channel inlet and outlets. These sponge regions have been implemented in order to damp out any acoustic waves that are generated by the channel and prevent them from reflecting off

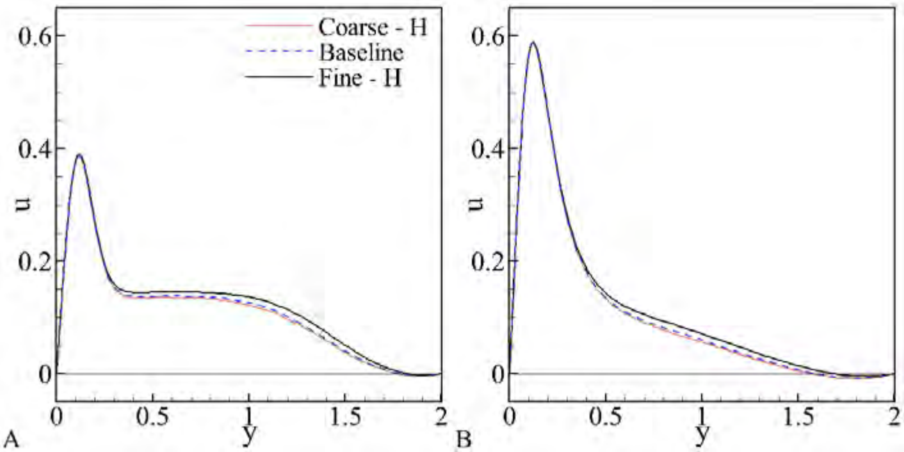

Figure 7-5. Velocity profiles from the wall normal grid resolution study at A) $x/h = 19.0$ and B) $x/h = 44.2$ units downstream from the channel inlet.

the boundary conditions, which could interfere with the flow inside of the channel in a non-physical manner. However, as the upstream and downstream conditions on the flow are unknown, the base state for the sponge region is determined using a temporal filter, as described in Åkervik *et al.* (2006). The mesh was extended radially from the inlet and outlet, along with the start and end of the sponge region has also been varied. Based on the average velocity in the channel, it appears that the distance between the inlet/outlet and the boundary conditions does play a role in the velocity of the flow inside of the channel (Figure 7-6), but so long as the domain is extended more than 30 units of length from the channel inlet/outlet, it would seem that the flow's dependence on the boundary conditions is limited.

7.2.2 Description of the Resulting Flow Fields

In order to examine these flows, a number of different parametric studies have been performed, varying the magnitude of the plasma body force and the height of the channel. Simulations performed of these flows show an interesting, but predictable flow field. Near the plasma actuators, fluid is entrained towards the actuator. The highest velocities are found near the actuator. Between the two geometries, there are some distinct differences, affecting the structure of the flow fields.

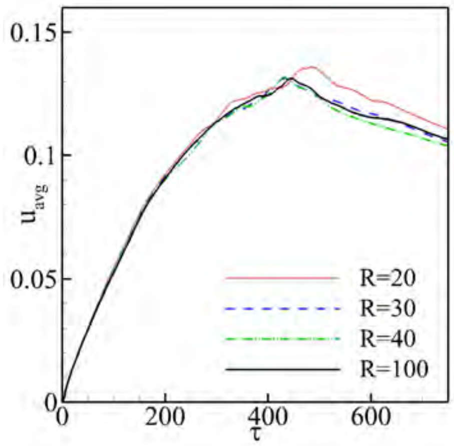

Figure 7-6. Average velocity in the channel as a function of time and the distance between the channel inlet/outlet and boundaries. The single channel geometry and $D_c = 1.0$ are used.

First, the single geometry flow field is examined. Instantaneous flow fields can be seen in Figures 7-7 and 7-8. For this flow, it can be seen that at the leading edge, flow separation can occur, in the form of a laminar separation bubble. For sufficiently large levels of plasma actuation, the velocity in the channel becomes high enough that these laminar separation bubbles can become unstable, periodically releasing vortices into the channel, which ensures that the flow becomes and remains unsteady. Between the leading edge of the channel and the plasma actuators, the flow develops in a predictable manner, with the boundary layers thickening as it develops. As the flow approaches the first plasma actuator, fluid is entrained from the center of the channel and a majority of the momentum becomes concentrated on the side of the channel where the plasma actuators are located, forming what is essentially a wall jet. For lower levels of plasma actuation, the flow on the unactuated side of the channel can separate, forming a massive flow separation in the channel. As one examines the flow farther and farther downstream in the channel, the amount of momentum contained in the wall jets increases as more and more fluid is entrained into the wall jet with each additional plasma actuator, and the negative velocities in the flow separation region increase in magnitude. This is caused by the confluence of an induced pressure gradient by the plasma actuator, resisting the movement of fluid travelling in the downstream direction, with the concentration of the momentum on a single side of the channel. In the high momentum region, near the plasma actuators, the flow is able to overcome the pressure gradient, but away from the plasma actuators, where the flow velocity is reduced, the pressure gradient is too strong for the flow to continue to move downstream. As such, the flow is forced to move upstream. For higher levels of actuation, this effect is much less significant, and while there are small flow separations, they do not generate a negative mean flow velocity.

Another important feature of these flow fields at higher velocities is the onset of instabilities in the wall jets. These instabilities grow as they are convected downstream. They also reach a sufficiently high magnitude such that secondary instabilities may become important, which cannot be captured in these two-dimensional simulations.

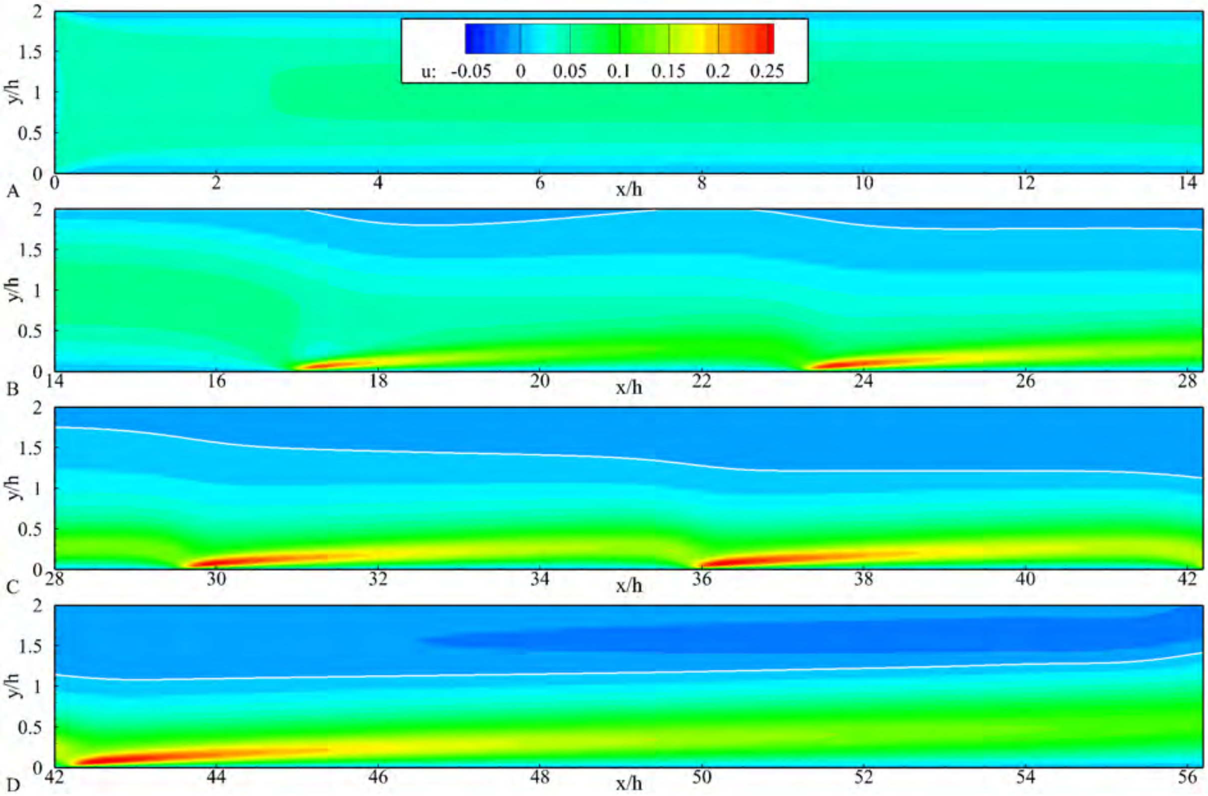

Figure 7-7. Instantaneous view of the two-dimensional channel flow for $D_c = 0.5$ in the single geometry.

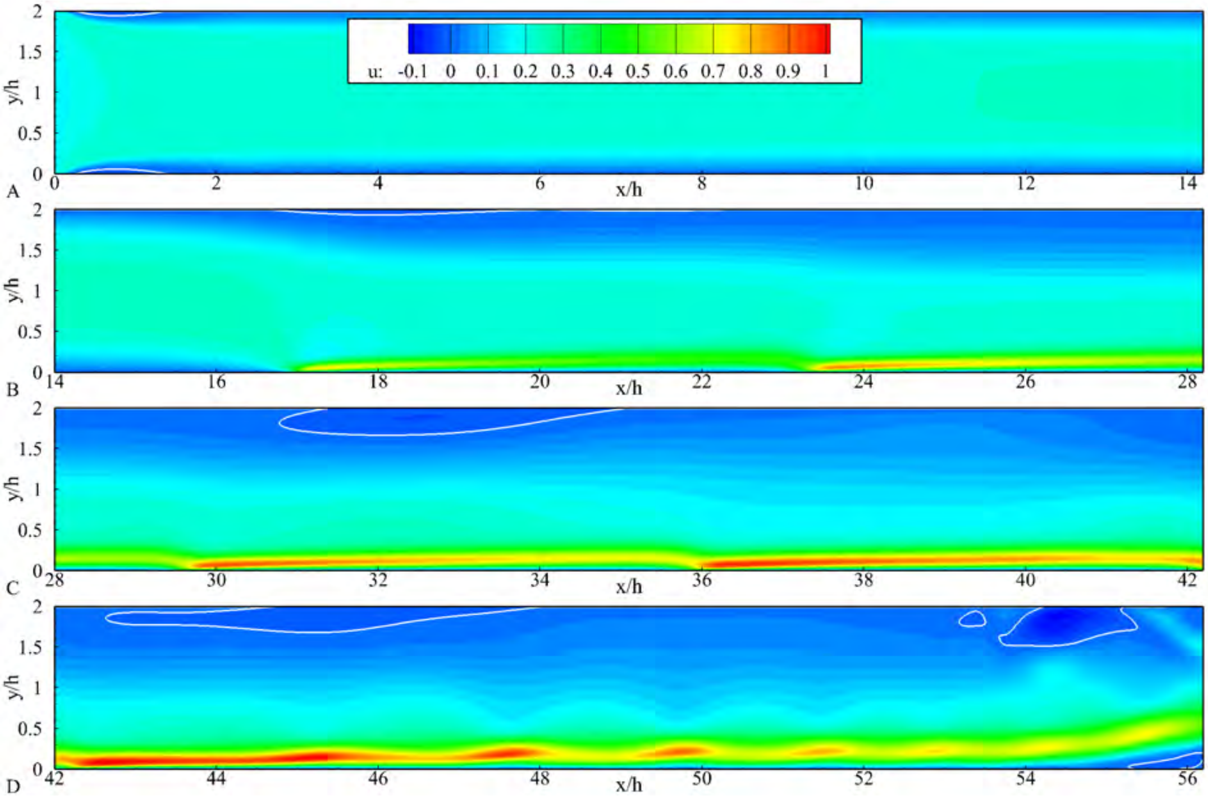

Figure 7-8. Instantaneous view of the two-dimensional channel flow for $D_c = 2.0$ in the single geometry.

In examining the channel velocity profiles, the unsteady nature of the flow becomes more apparent (Figure 7-9). For the highest and the lowest levels of plasma actuation, the wide extent of the separation bubble becomes more apparent. While this bubble can take up a large span of the channel height, the velocity of the flow in the reversal is only a few percent of the velocity in the wall jet. These velocity profiles also indicate that for lower levels of actuation, the bubble should be steadier than at higher levels, though this will only be able to be confirmed with the use of three-dimensional simulations and experimental validation.

Examining these flows over an extended length of time, the average velocity in the channel suggests that there is a very low frequency, quasi-periodic effect occuring in these channels when the velocity becomes high enough, and that this has an enormous impact on the mass flux through the channel (Figure 7-10).

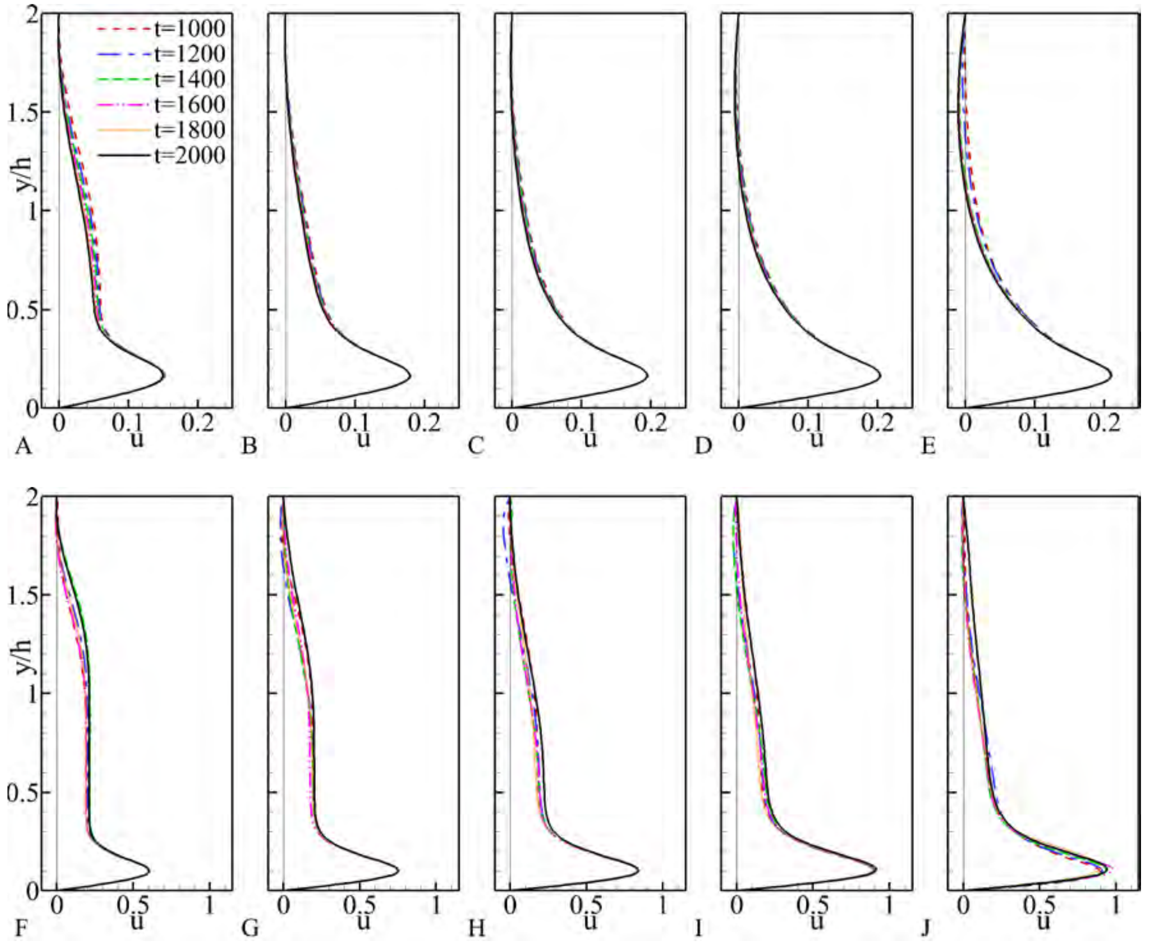

Figure 7-9. Velocity profiles from the single channel geometry for A-E) $D_c = 0.25$ and F-J) $D_c = 2.0$. These velocity profiles are taken two units of length (2h=2 cm) downstream of each plasma actuator, i.e. A,F) x/h=19.0, B,G) x/h=25.3, C,H) x/h=31.6, D,I) x/h=37.9, and E,J) x/h=44.2.

Examining the size and shape of the flow reversal more carefully, it comes to seem that the size and shape of the flow's reversal approach a steady state for all but the highest level of actuation that was simulated (and perhaps the second highest level on a must longer time scale). For the highest level of actuation, the flow separation starts off as several small flow separations, which extend in length as they are slowly convected downstream (Figure 7-12). The rate that these separations are transported downstream is less than the rate that they grow at, allowing for the separation bubbles to join each other, forming larger flow separations. These eventually form one enourmous separation bubble, choking the rate of flow in the channel. However, once the separation bubble

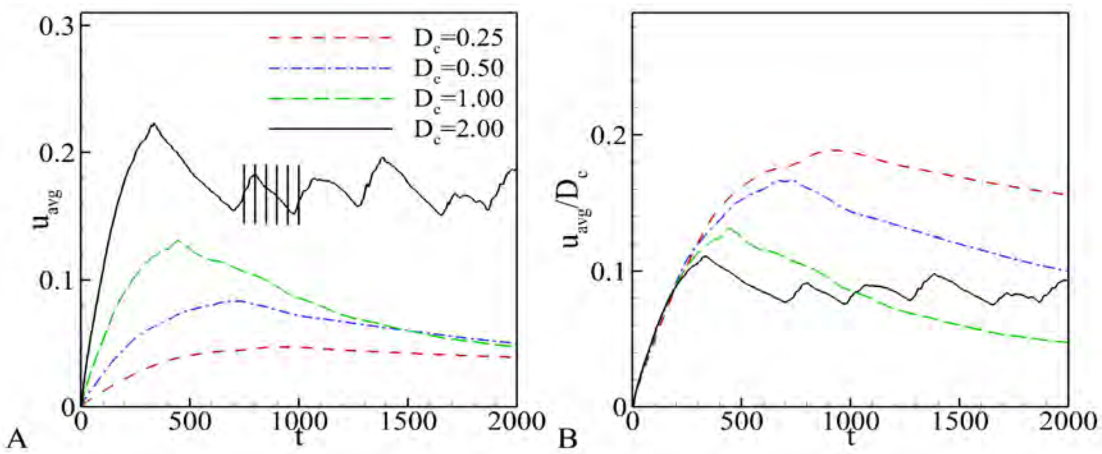

Figure 7-10. Average velocity in the channel with a single geometry plasma actuator A) as a function of time and B) Average velocity in the channel normalized by D_c. The vertical dashed lines indicate the times sampled for Figure 7-12.

reaches a certain size, it bursts and is rapidly transported downstream and passed through the outlet, allowing for an increased rate of flow in the channel. It logically follows that the formation and bursting of the massive separation bubble in the channel is the root of the quasi-periodic pulsing in the channel flow.

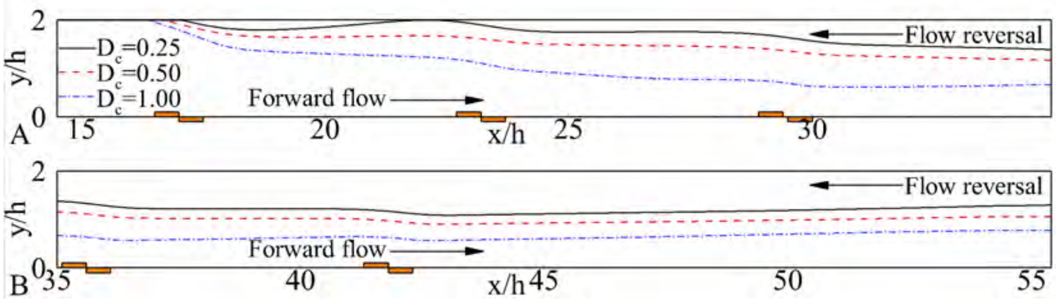

Figure 7-11. Bounds on the flow separation for lower levels of plasma actuation with the single geometry and $D_c = 0.25,\ 0.50,\ 1.00$.

For the double geometry channels, the flow appears to be much simpler. Instantaneous flow field can be seen in Figures 7-13 and 7-14. The mean velocities in the channel are roughly double what they are for the single geometry channels, and the effects of the leading edge separation bubble are more significant because of that. The velocity of the flow in the wall jets is also of comparable magnitude for a fixed value of D_c with the single geometry channel flow cases, even though the mean velocity in the channel

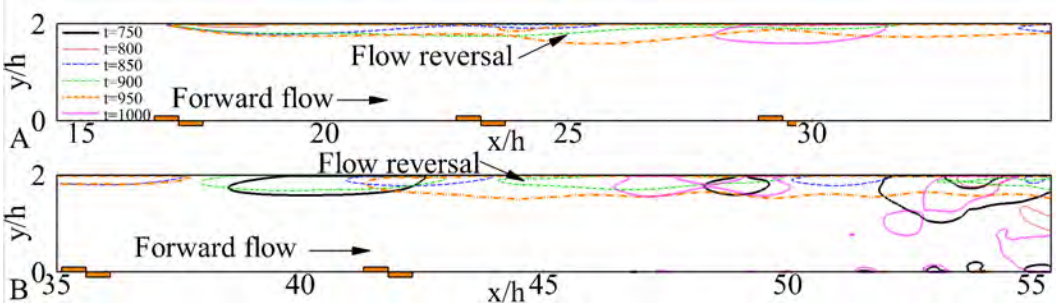

Figure 7-12. Instantaneous bounds on the flow separation for the channel with the single geometry and $D_c = 2.0$.

is roughly double when actuators are placed on both sides of the channel. As fluid approaches the region where plasma actuators are placed on both sides of the channel, instead of being entrained to a single side of the channel, fluid is now entrained to both sides of the channel. Thus, on each wall, there exists a high momentum region, while the flow at the center of the channel is of lesser velocity. However, while the velocity at the centerline of the channel is reduced, it does not become negative and form a flow separation in the center of the channel.

These effects of the wall jet development and entrainment of momentum can be more clearly seen in the channel velocity profiles (Figure 7-15). These profiles show that as one follows the flow past additional plasma actuators, more and more fluid and momentum is entrained in the wall jets, which are growing in height and velocity with each additional plasma actuator. The end result of this is that very litttle momentum exists at the center of the channel around the actuators.

Examining the average velocity in the channel flow with actuators on both sides of the flow (Figure 7-16), it can be seen that once the flow reaches its maximum, there are no significant oscillations in the average velocity in the channel. While small scale oscillations persist, there is no generation and ejection of a massive flow separation as there is for the single geometry channel (Figures 7-10 and 7-12).

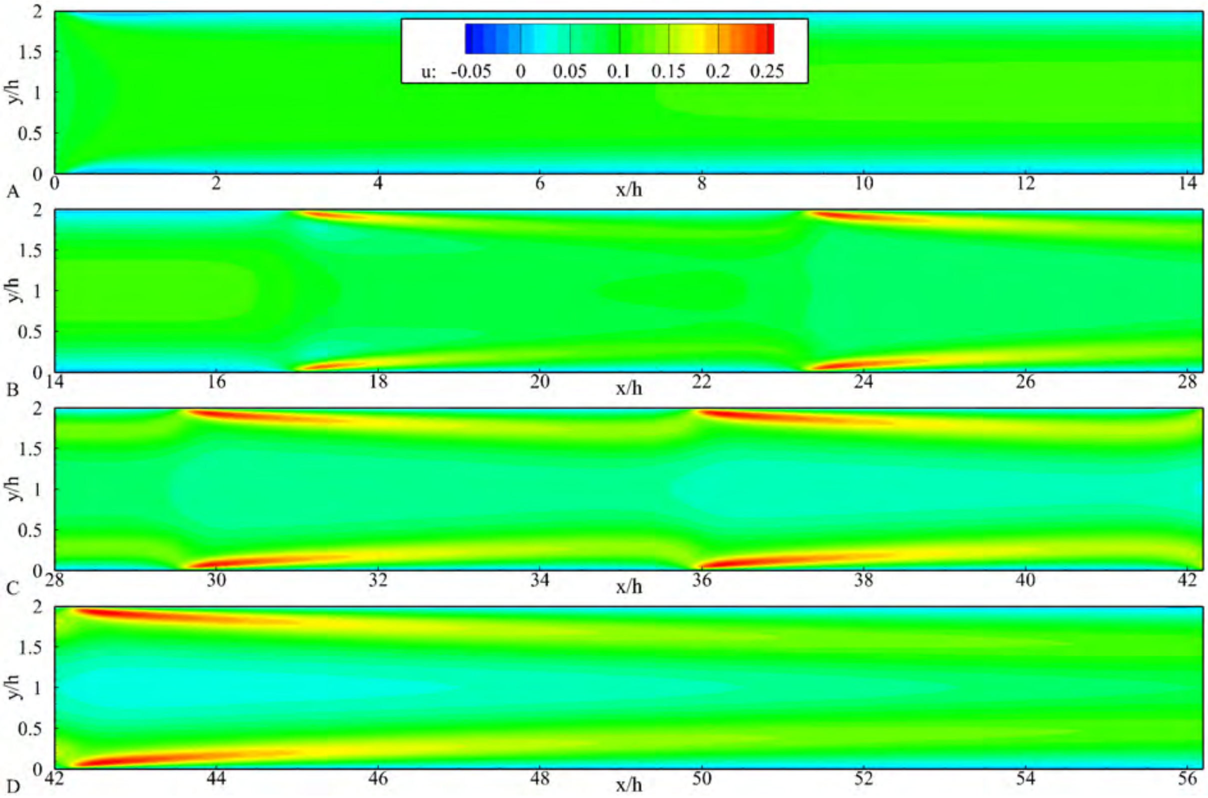

Figure 7-13. Instantaneous view of the two-dimensional channel flow for $D_c = 0.5$ in the double geometry.

7.2.2.1 Effects of height in the channel

Channels with a height of 1.0 cm have also been examined. The emphasis here is on examining what happens as these plasma actuators are pushed more towards smaller scale pumping applications.

One result of reducing the channel height is that the velocities and unsteadiness in the channel decreases (Figure 7-17A and C). This can largely be attributed to the flow becoming relatively more viscous with the reduction in the channel height. As the channel height is decreased, viscous effects become increasingly more important and act to restrict the movement of fluid in the channel and damp out any perturbations. With the reduced channel velocities, the effective Reynolds number is less that 1500 at most, and in the hundreds in for some of the cases. This would suggest a very low speed, laminar flow, which wouldn't necessarily require further three-dimensional modeling to

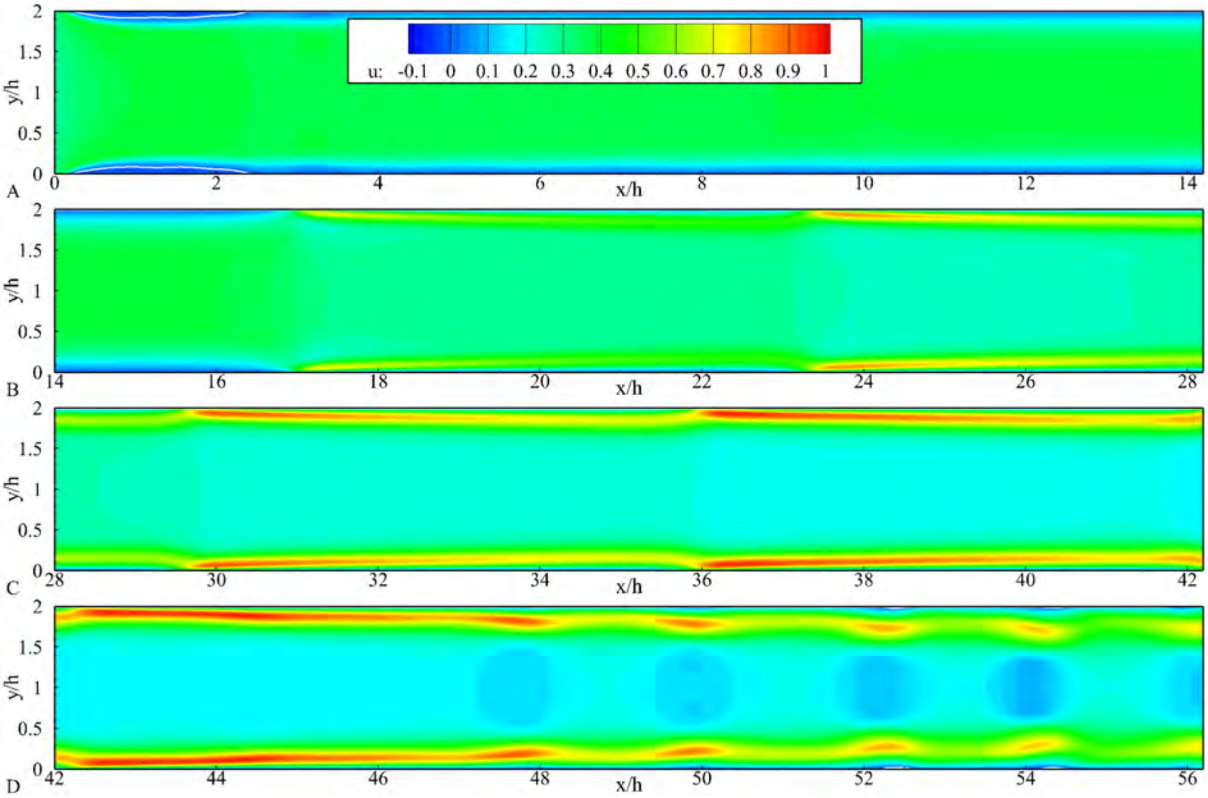

Figure 7-14. Instantaneous view of the two-dimensional channel flow for $D_c = 2.0$ in the double geometry.

accurately describe the behavior inside of the channel. The reduced marginal gains in velocity can also be seen in Figure 7-17B and D, indicating that just as with the taller channel, as more body force is applied to the channel, the velocities do not increase proportionally.

The general behavior of the flow inside of the channel largely remains comparable. Large scale flow reversal occurs for geometries where plasma actuators are only located on one side of the channel but doesn't occur when plasma actuators are located on both sides of the channel. One significant difference is that the geometries with reduced channel heights do no see the formation of a laminar separation bubble at the channel inlet. This flow feature is a significant contributor to high frequency unsteadiness in the channel. Another big difference between the shorter and taller single channel geometries is the size and stability of the separation bubbles around the actuators. For

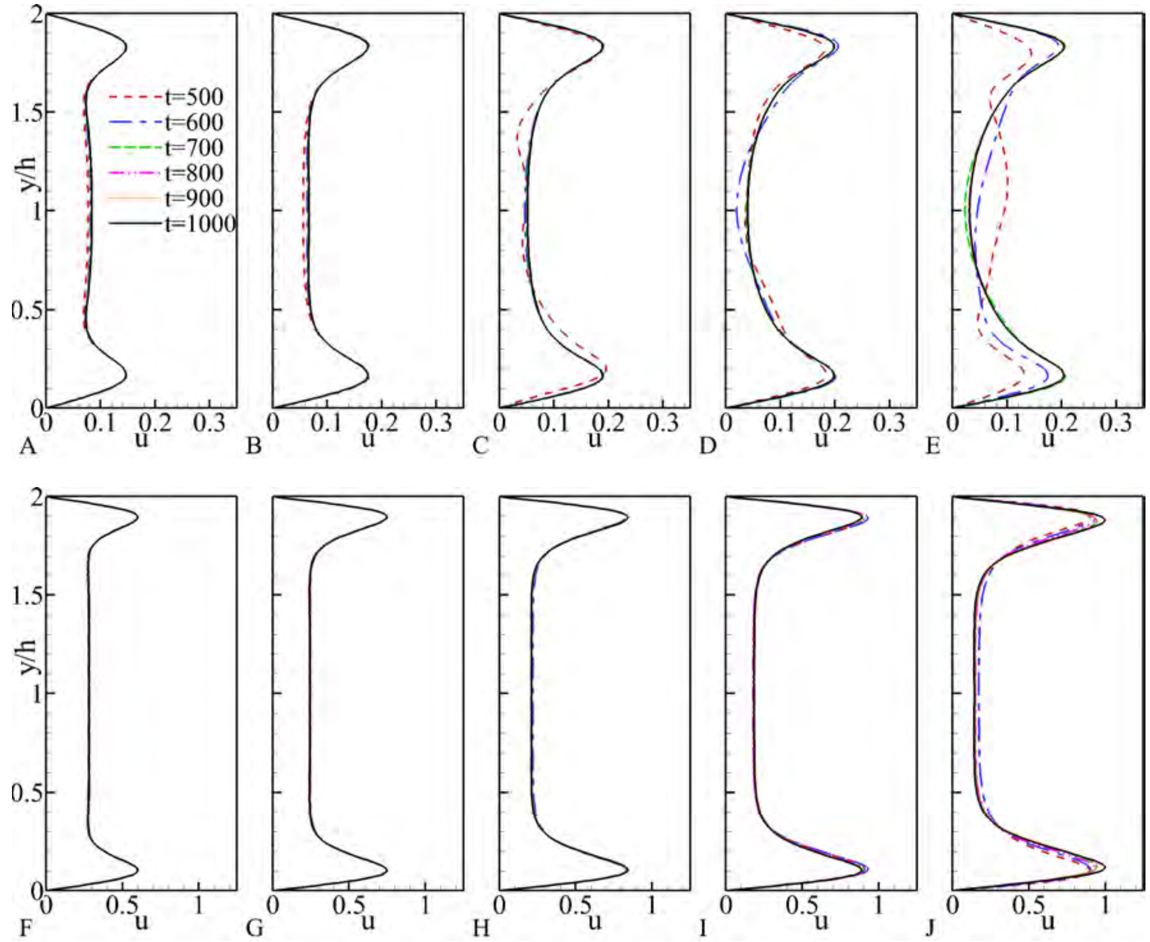

Figure 7-15. Velocity profiles from the double channel geometry for A-E) $D_c = 0.25$ and F-J) $D_c = 2.0$. These velocity profiles are taken two units of length (2h=2 cm) downstream of each plasma actuator, i.e. A,F) x/h=19.0, B,G) x/h=25.3, C,H) x/h=31.6, D,I) x/h=37.9, and E,J) x/h=44.2.

the shorter channel geometries, the development length between and downstream of the actuators is double that of taller channels. As such, the viscous effects in the flow are given additional space to take effect, and instead of relying on unsteadiness and instabilities to reattach the flow, viscous effects can accomplish that task instead. The end result is that the separation bubbles don't extend as far down the length of the channel when the channel height is reduced.

7.3 Experimental Validation

In order to ensure that accurate flow physics is being captured by the simulations described in this chapter, experimental validation is also necessary. As in Chapter 6, PIV

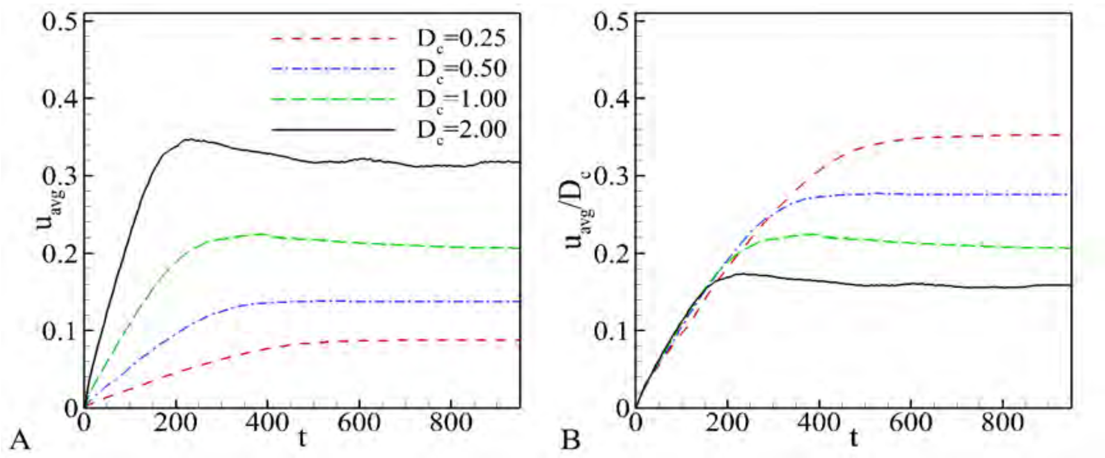

Figure 7-16. Average velocity in the channel with a double geometry plasma actuator A) as a function of time and B) Average velocity in the channel normalized by D_c.

was used to examine the flow fields generated by the plasma actuators. The present emphasis is placed on the flow inside of the channels, though.

7.3.1 Characterization of the DBD Plasma Actuators

Before moving onto the entire channel flow, the performance of the plasma actuator itself should be characterized. A plasma actuator constructed out of 3mm thick PMMA and two 10mm wide electrodes was made. Zero gap was used between the electrodes in the streamwise direction. A high voltage, high frequency (14kHz), AC signal was applied to the actuator, and the resulting flow fields were collected using PIV (Figure 7-18).

In the experiments, voltages between 14 and 20 kVpp are tested. The same voltage range was tested for the characterization of the plasma actuators. The resulting flows produce wall jets with velocities between 1 and 5 m/s.

7.3.2 Construction of the Channel Experiment

For the present experiments, an experimental setup has been constructed (Figure 7-19), which is different from the one for used in Chapter 6. All of the parts of the experimental setup are made of 6.35 mm thick (1/4”) PMMA and are designed to be removable and interchangeable. The sidewalls connect all of the pieces, and sidewalls

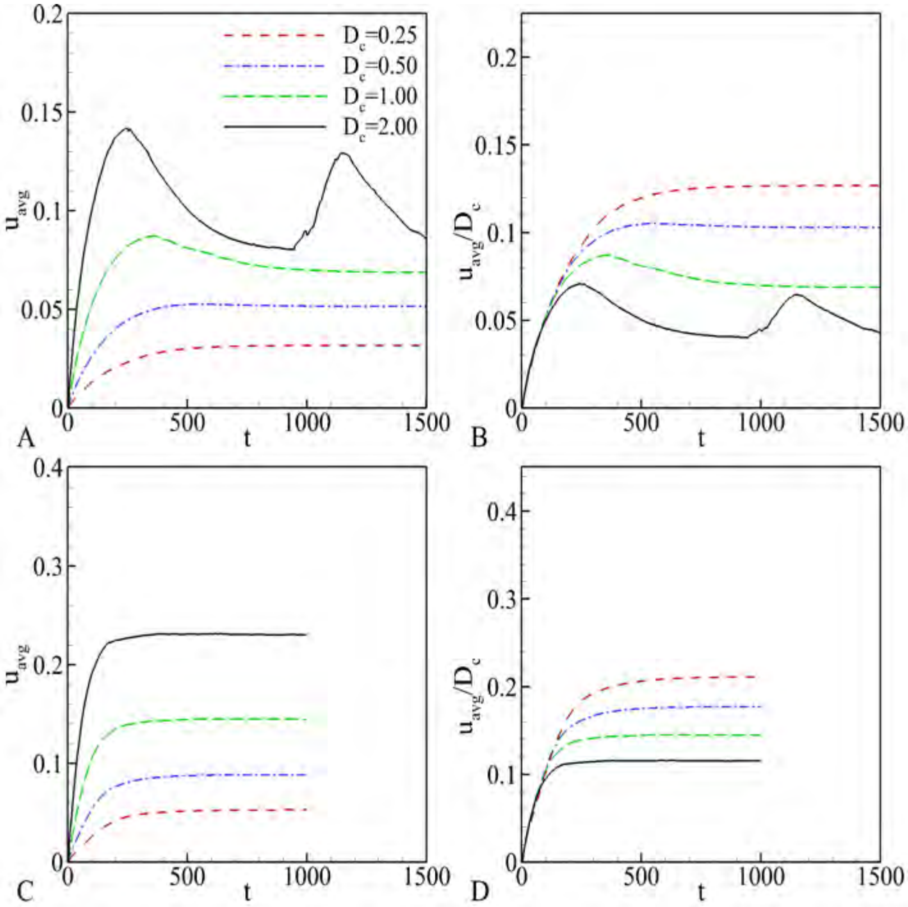

Figure 7-17. Average velocities in the shortened channel as a function of time. u_{avg} in the A) single and C) double geometries channels. u_{avg}/D_c in the B) single and D) double geometry channels.

of various heights have been manufactured in order to vary the channel height. The inlet and outlet segments are separate from the portion of the channel where the actuators are located. In order to drive the flow, the actuators are installed on a 30 cm plate, which lies between the inlet and outlet segments. All of these pieces are attached to the sidewalls using hot glue, which does not generate an optical impedance along the entire the sidewalls, only in local regions, allowing for PIV data to be taken inside of the channel. The experiments are performed in the same chamber as described in Chapter 6.

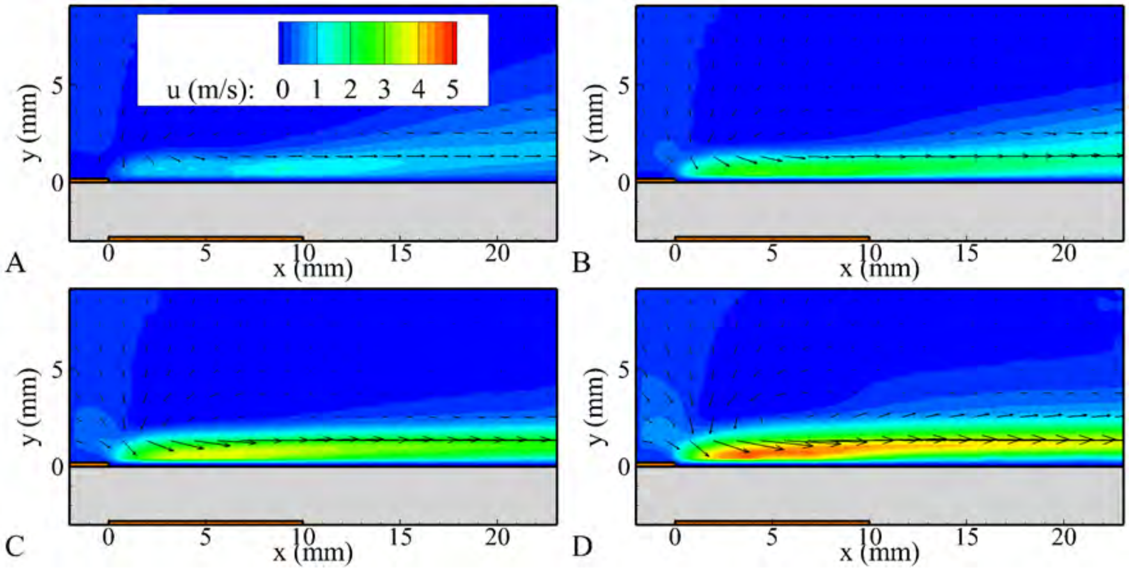

Figure 7-18. Wall jets formed by the DBD plasma actuator under quiescent conditions at varying voltages. A) $14\ kV_{pp}$, B) $16\ kV_{pp}$, C) $18\ kV_{pp}$, and D) $20\ kV_{pp}$.

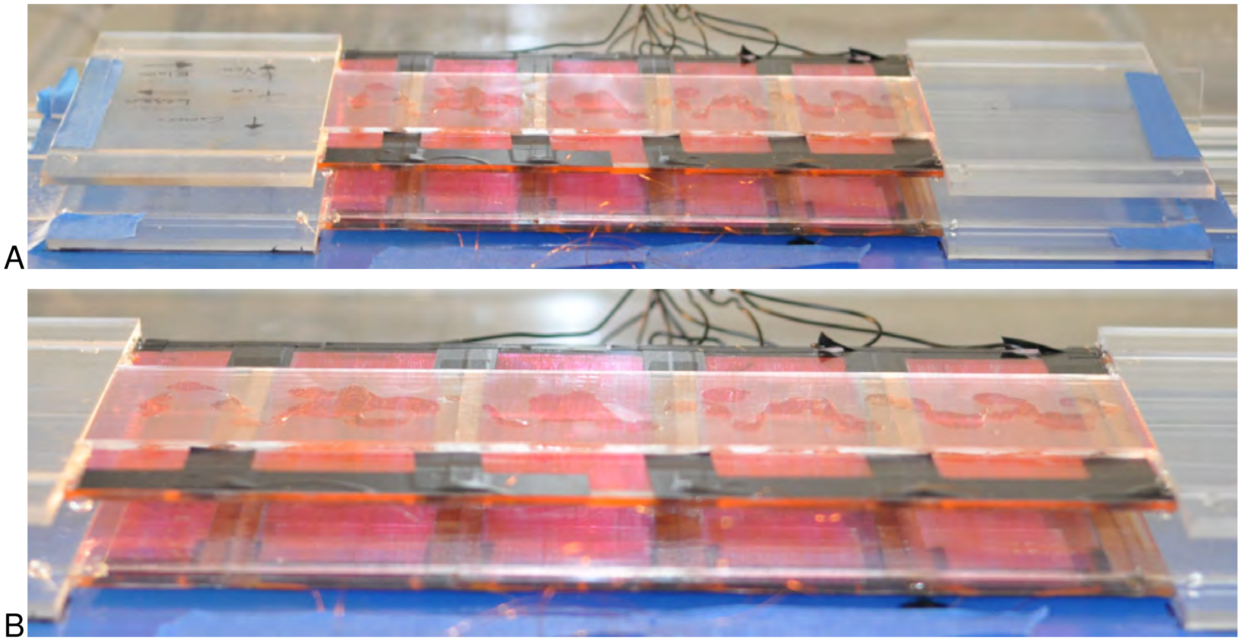

Figure 7-19. Photographs of the plasma channel. A) Assembled plasma channel experiment. B) Close-up of the segment of the plasma channel where the actuators are located.

7.3.3 Details of the Experimental Method

These experiments were conducted multiple times due to unforeseen difficulties, but with each additional iteration, improvements were made in the design and construction of the channels and the execution of the experiments. Among the difficulties encountered in constructing and testing these channels were

1. Over the course of repeated experiments, the sidewalls of the channels can be degraded due to interactions with the plasma actuators. This deformation prevents the collection of quality data inside around the plasma region, which is of primary interest. In order to correct this, the plasma actuators were moved away from the walls so that there are 2 to 3 mm of space between the end of the plasma and the sidewalls, which lessened the degree of optical degradation.
2. While moving the plasma actuators slightly away from the sidewalls prevented the prevented some physical and optical degradation, the plasma actuators were still able to degrade the optical quality of the PMMA sidewalls by causing a residue to form around the actuator. It was found through experimentation that wiping down the sidewalls with a damp rag between tests could remove much, but not all of the reside and allow for improved, but not perfect data collection.
3. Over extended periods of testing, the Ondina seed material used for the PIV data collection would build up on the surface of the plasma channel, particularly on the bottom surface of the channel. The build up of the seed material can lead to increased reflections off of the channel surfaces and reduced actuator performance. In order to minimize these effects, the channel surfaces were wiped down with a damp rag between tests. In order to do this, the top of the channel was made removable and not attached with any type of semi-permanent adhesive. Instead, the ends of the channel were taped on, and a heavy object used to hold it in place.
4. These devices are hand made and there is some error associated with the construction in the plasma actuators. Furthermore, the applied voltage does vary from sample to sample and even within each sample. The error associated with these voltage variations is approximately ± 0.2 kVpp, which is approximately 1-2% of the applied voltage. These two factors lead to a certain degree of inconsistency in operating the actuators.

In performing these experiments, the plasma actuators were run for 30 seconds in order to warm up and establish a statistically steady flow in the channel. 500 image pairs were collected over a time of 33 seconds at a rate of 15 Hz. The plasma actuators were then turned off for a minimum of 90 seconds before moving on to the next test. Often, the plasma actuators were allowed to cool off for a greater amount of time in order for the amplifier powering the circuit to cool down as well.

Diagrams of the circuit powering the system (Figure 6-2) and the setup of the PIV system (Figure 6-4) can be found in Chapter 6. Data was only collected along a partial length of the channel, in the region of the plasma actuators ($13.5cm \leq x \leq 41.5cm$), but not around the inlet or outlet. In order to accurately capture data along this length, the channel was placed on a movable horizontal rail, while the laser and camera were put in stationary positions, allowing for the channel to move without having to recalibrate and re-focus the laser/camera setup for PIV.

7.3.4 PIV Results

7.3.4.1 Single geometry channels

From the numerical simulations discussed earlier in this chapter, the two most important flow features in the single geometry channel are the generation of a wall jet that increases in height and velocity as it develops downstream with additional plasma actuators and the existence of a flow separation on the opposite side of the channel. In examining the time mean flow fields captured using PIV (Figures 7-24, 7-25, and 7-26), it can be seen that there is some qualitative agreement with the simulations that have been performed.

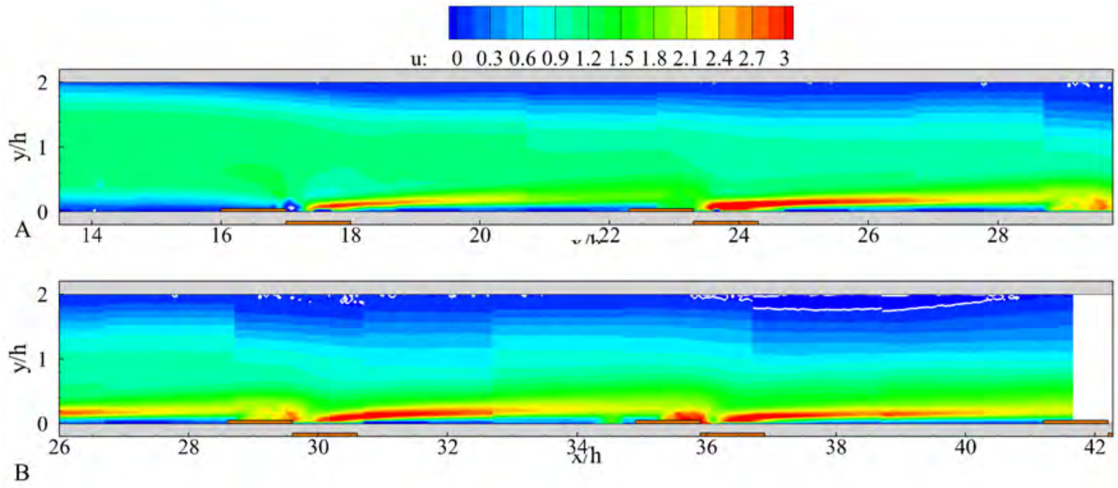

Figure 7-20. Time mean streamwise velocity for the single geometry plasma actuators at 16 kVpp. The white line in A) and B) represents where the flow separation occurs.

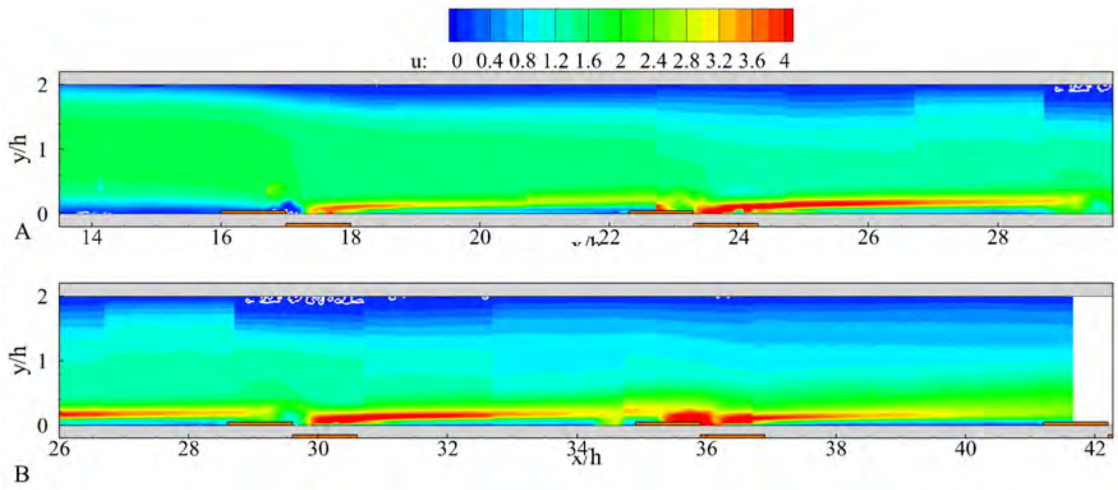

Figure 7-21. Time mean streamwise velocity for the single geometry plasma actuators at 18 kVpp.

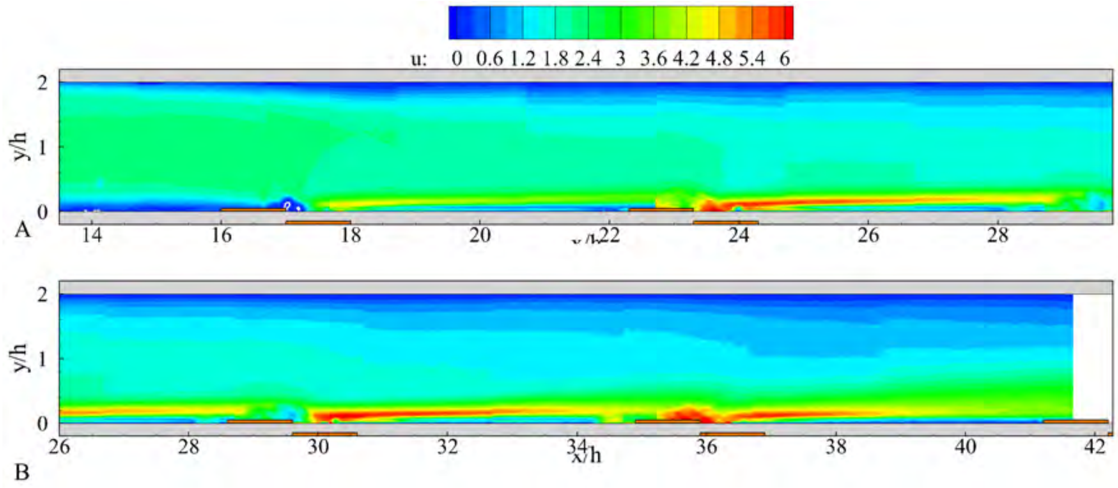

Figure 7-22. Time mean streamwise velocity for the single geometry plasma actuators at 20 kVpp.

It can be seen that the wall jets form in the vicinity of the plasma actuators, and that the size and magnitude of these wall jets increases as they develop over each additional actuator. The effects of fluid entrainment are also visible due to this increasingly significant wall jet, which leads to lower velocities on the opposite side of the channel, consistent with the CFD simulations.

One significant difference between the simulations is the existence of the massive separation bubbles. In Figure 7-20, it can be seen that there is a small separation bubble in the time mean flow. However, this is in contrast with the simulations, which predict much more robust separation bubbles, and bubbles that exist at higher and lower velocities. The $D_c = 1.0$ generates wall jet velocities comparable to experiments with an applied voltage of 16 kVpp. In those simulations, there is a relatively steady, very large, separation bubble. In the experiment, there is much more unsteadiness, and there may be several different reasons for this. It can be seen in the time mean PIV data (Figure 7-20A) from around an actuator, that the flow is on average not reversed. When the instantaneous PIV data is examined (Figure 7-20C-F), there is a very unsteady flow reversal near the surface away from the plasma actuators. However, because of these oscillations, the separation doesn't seem to remain constant, and once averaged, lead to a forward flow, rather than a reversed one.

7.3.4.2 Double geometry channels

The numerical simulations presented earlier in this chapter suggest tha the double geometry channel configuration should be comprised of two symmetric wall jets that grow in height and velocity as they develop downstream with additional plasma actuators.

In examining the time mean flow fields captured using PIV (Figures 7-24, 7-25, and 7-26), it can be seen that there is reasonable qualitative agreement with the simulations that have been performed. For all of these simulations, wall jets of comparable magnitude form on each side of the channel. The size and magnitude of the wall jets also increases as they develop downstream. It can also be seen that fluid is entrained on both sides from the center of the channel into the wall jets, by the reduction of velocities in the center of the channel.

7.4 Conclusions

The internal structure of plasma driven channel flows with two actuator geometries has been investigated using numerically and experimentally using PIV. The different

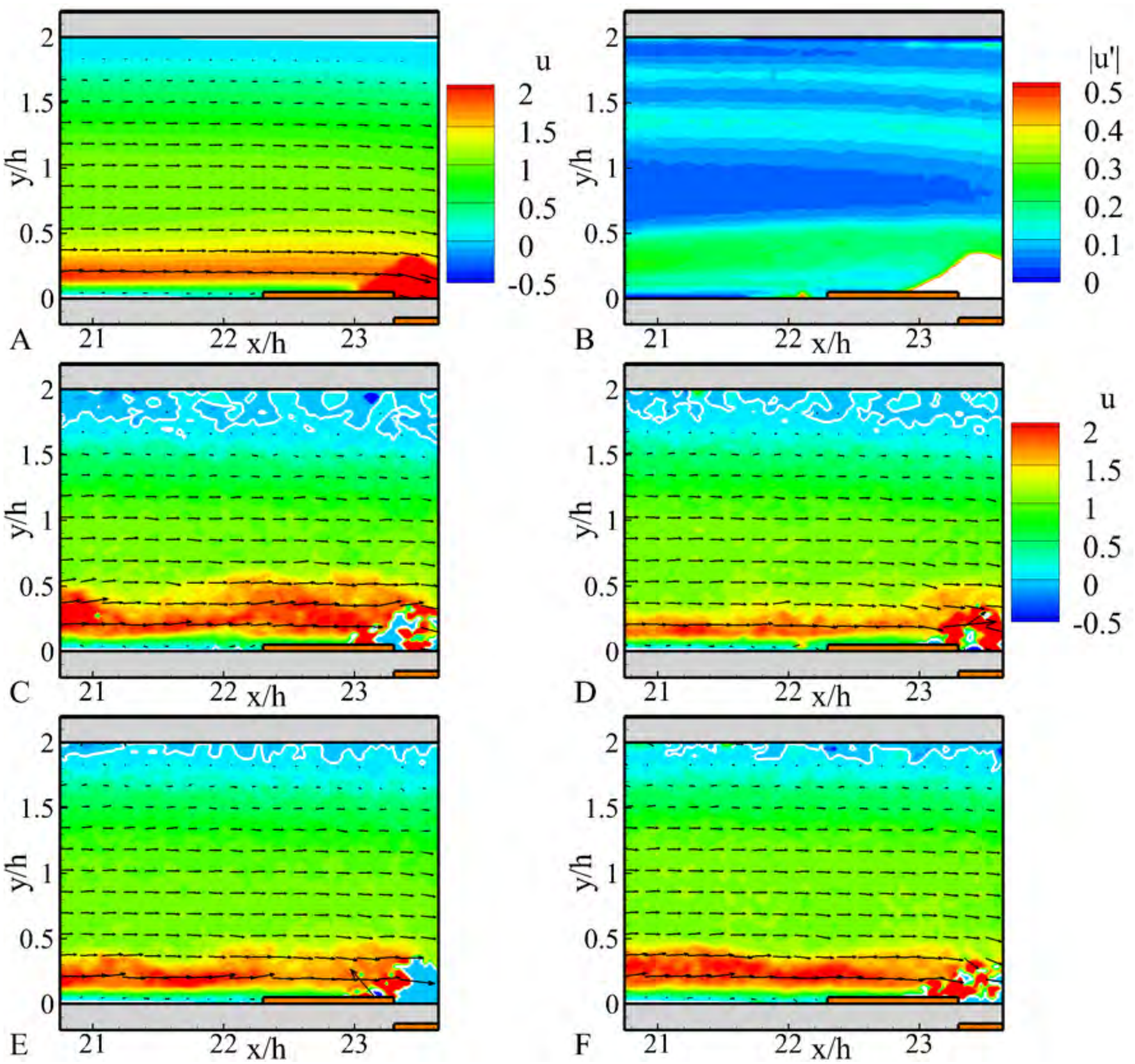

Figure 7-23. Behavior of the flow near the a plasma actuator at 16 kVpp. A) Time mean streamwise velocity. B) RMS values of the streamwise velocity. C-F) Instantaneous velocities taken at different instances in time.

approaches yield varying results, but there is a degree of commonality between the resulting flow fields.

Two-dimensional simulations predict that the flows generated by the channels should be relatively steady, except for at higher levels of plasma forcing. When actuators are placed on one side of the channel, the flow on that side forms a single, long wall jet. This wall jet grows in height and velocity as it develops along each additional plasma actuator, such that a majority of the momentum in the channel ends up being in the wall

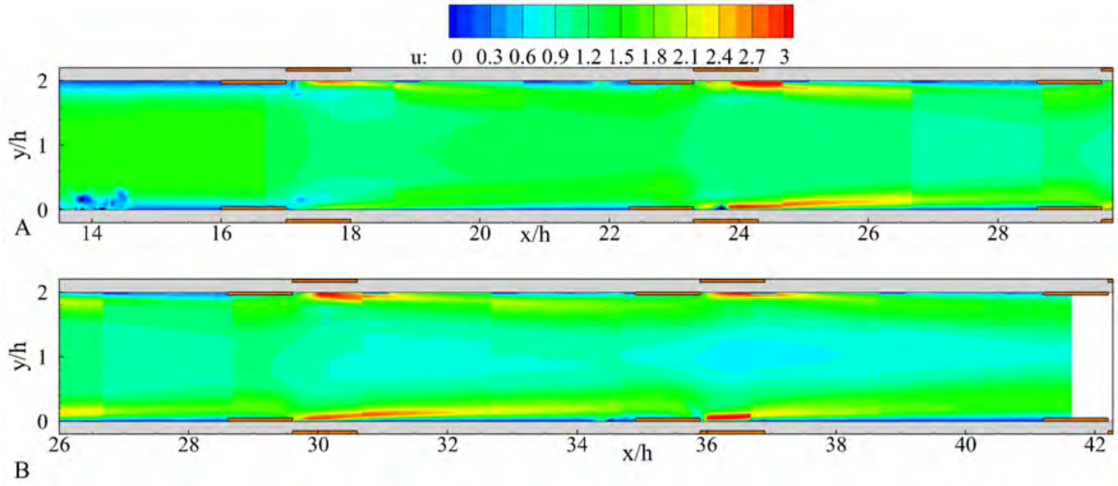

Figure 7-24. Time mean streamwise velocity for the double geometry plasma actuators at 16 kVpp.

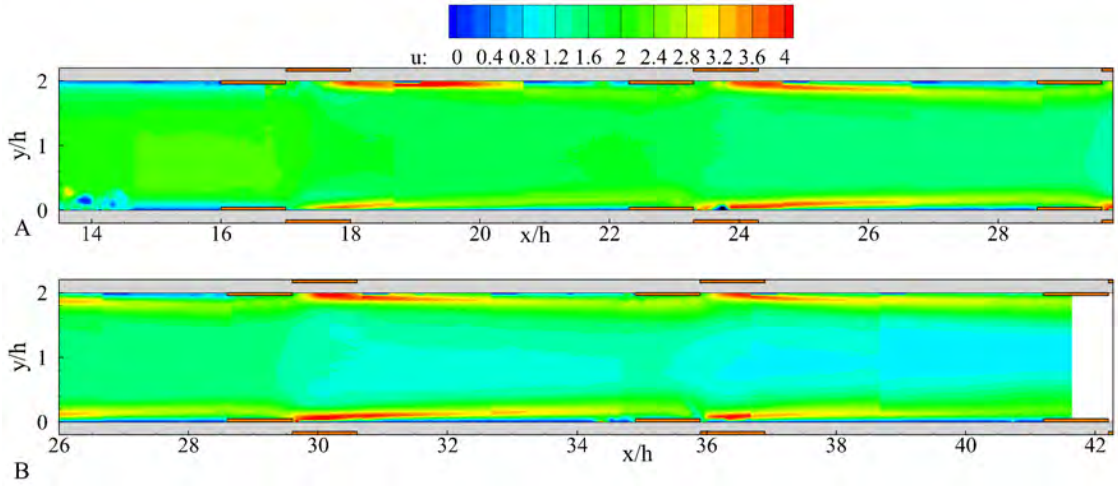

Figure 7-25. Time mean streamwise velocity for the double geometry plasma actuators at 18 kVpp.

jet. In these simulations, the flow on the opposite side of the channel usually separates, so that a very long, vortical separation bubble forms in the channel, which may or may not be steady or stable. This flow separation is due to the pressure gradient induced by the plasma actuators. As the plasma body force pushes flow downstream, the downstream pressure is increased relative to the upstream pressure. While this effect has been noted for plasma actuators in semi-bounded domains before, its impact in boundary domains has only been examined recently (Morgan & Visbal, 2013; Riherd

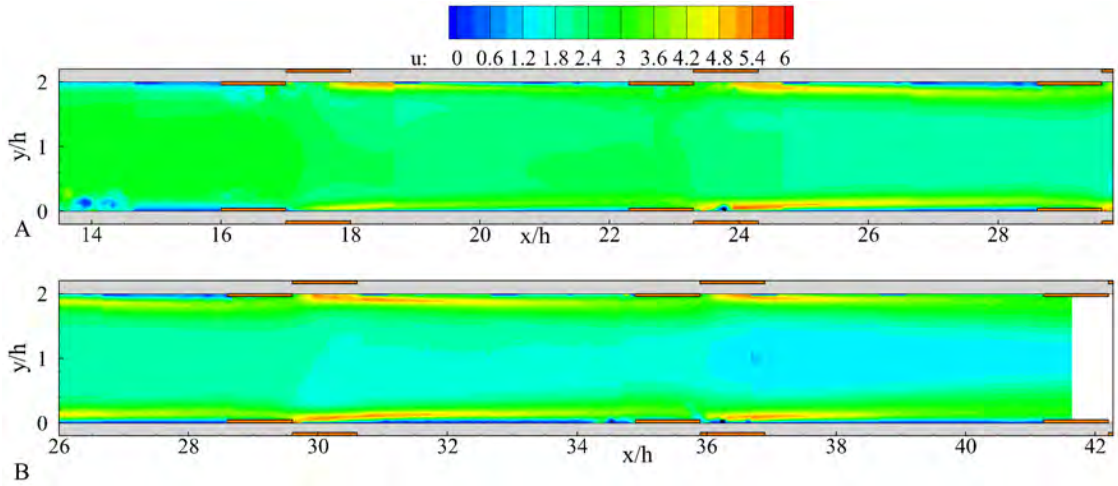

Figure 7-26. Time mean streamwise velocity for the double geometry plasma actuators at 20 kVpp.

& Roy, 2012*b*). This induced pressure gradient pushes the flow backwards, and in the configuration where plasma actuators are only placed on one side of the channel, this backwards push may be able to cause flow separation. Further experimental efforts to validate these effects have suggest that the flow separation is less important when the operating environment is more unsteady. The unsteadiness in these additional examinations appears to lessen the effects of the flow separation, and while there appears to be instantaneous amounts of flow separation, the large scale flow separation seen in the two-dimensional simulations does not appear to be valid.

When plasma actuators are placed on both sides of the channel, a much more favorable flow structure results. Wall jets form on both sides of the channel, which entrain a majority of the momentum contained in the flow. For this configuration, no instantaneous or mean flow separations are encountered in the region of the plasma actuators. With this increased predictability in the flow structure, this configuration will likely be preferred for any future studies or applications.

Continued work on this topic should focus on increasingly small channels and in the development of additional applications for these channels. The boundary layer control application developed by Morgan & Visbal (2013) seems promising, but further development of this application will be necessary in low speed and laboratory settings before more realistic applications can be approached. However, it is likely that this type of application can be extended to mimic the behavior of other, more traditional flow control actuators as well. As these devices are developed at smaller and smaller length scales, the effects of unsteadiness should become lessened due to a reduced Reynolds number for the channel.

CHAPTER 8
SUMMARY AND RECOMMENDATIONS FOR FUTURE WORK

Several aspects of using DBD plasma actuators to control boundary layer and channel flows have been investigated. The intended impact of these studies has been to expand the versatility of these devices across a range of potential applications as well as to quantify the impact of the plasma actuators for these applications.

8.1 Control of Boundary Layer Stability

Local and bi-global hydrodynamic stability codes have been written to quantify the stability of incompressible flows. For the bi-global stability code, a parallel implementation of the code has been performed, allowing for much larger domains to be examined than could be on a single processor. These codes have been benchmarked and found to be accurate relative to other hydrodynamic stability codes.

Parametric studies of the local stability analysis of a plasma modified boundary layer have been performed. From simulations of the boundary layer with plasma actuators operating in a flow-wise (co-flow) manner, it has been determined that the addition of momentum into the boundary layer leads to changes in the boundary layer profiles. The local stability analysis performed indicates that the changes to the shape of the boundary layer profiles are the primary stabilizing effect, though there may be some small impact due to boundary layer height reduction.

Furthermore, a low order model of the boundary layer profiles has been constructed and validated in comparison to the computational results. This model allows for the examination of flows where the plasma actuator is operated in a co-flow or a counter flow manner. The evidence suggests that there are additional instability mechanisms present, including previously undocumented inviscid and absolute instability processes.

Bi-global stability analyses have been performed examining the effects of using continuously operated co-flow oriented plasma actuators to stabilize TS waves and boundary layer streaks. Flow stabilization is indicated using this manner of stability analysis over a broad range of the frequency spectra for the TS waves and over a significant range of the spanwise wavenumber spectra for the boundary layer streaks. A RANS-type analysis of the perturbation's kinetic energy indicates that the flow is stabilized in the near plasma region. Interestingly, as the magnitude of the plasma actuation is increased, the application of a plasma body force leads to negative kinetic energy production term.

Linear stability analysis suggest that TS waves can be damped by upwards of 90% of their kinetic energy, but boundary layer streaks can likely only be damped by up to 25% of their kinetic energy. While the stabilization of the TS waves is much more pronounced that of the boundary layer streaks, the stabilization for both of these instabilities is significant.

Future work on this topic should place emphasis on how this problem scales up at higher Reynolds numbers. A concerted focus on experimental validation would also be very beneficial, as the existing literature is limited with respect to studies focusing on the individual instabilities. If these actuators can be demonstrated to be effective at controlling all of the different paths to turbulence in boundary layers (along with the additional requirements of being robust against environmental concerns, reliability, power consumption, etc.), then they could have a significant impact for reducing turbulent skin friction for those applications. There should also be a push into the implementation of these devices for real applications, and the understandings of the limits in implementation. The present analyses have focused on the effects of a single, infinitely long actuator, but in practice, arrays of finite width actuators are more likely to be used. The limitations of such implementation will need to be understood for practical applications.

Another potential avenue for applications is in the modification of unsteady flow features in turbulent boundary layers. As plasma actuators have been shown to modify what is essentially a turbulence production term for different linearized perturbations, its possible that DBD actuators could do the same in a highly non-linear, turbulent boundary layer. A reduction in the unsteady flow features would impact the $\overline{u'v'}$ Reynolds stress in turbulent flows, which could directly impact the boundary layer profiles and the viscous skin friction.

In order for this type of technology to move from the laboratory setting to more impactful applications, more work in experimental testing will be necessary, in order to address the concerns of reliability, robustness, and power consumption that face these devices.

8.2 Serpentine Geometry Plasma Actuators

Simulations of serpentine geometry plasma actuators in a laminar boundary layer have also been performed. Characterization of these flows indicates that they are able to generate boundary layer streaks and could be used for transition control. Depending on the magnitude of the actuation, these actuators may be used to either delay or accelerate the transition of the flow.

While the application of using boundary layer streaks for flow control applications is by no means a new contribution, that this could be done using DBD plasma actuators allows for greater ease and in constructing flow control systems. Normally these streaks are generated by fixed structures on an airfoil or the roof of a car. As such, these fixed devices can be optimized for a single condition, offering reduced performance over the wider range of conditions where control is (or is not) desired. Plasma actuators allow for greater flexibility in their operation, as they can be turned off when not needed for control, and their performance can be modulated when they are desired. This flexibility indicates that these actuators have greater versatility than more traditional means of generating boundary layer streaks.

The present work has only examined the impact of using these actuators to generate boundary layer streaks in a laminar boundary layer, but boundary layer streaks are also very common in turbulent boundary layers, particularly in the viscous sublayer.

The introduction of streaks by a serpentine geometry actuator into the viscous sublayer could be used to modify the structure of the flow in the near wall region. Furthermore, if these actuators were operated in a pulsed manner, it may be possible to generate organized arrays of hairpin vortices for the purposes of flow control and modulating the mixing properties in a boundary layer. Both of these approaches could be modified to take advantage of linear and non-linear amplification of these perturbations by the flow, allowing for increased control authority for each unit of power delivered to the actuators.

Going forward, this actuator geometry should be used to extend the control authority DBD actuators to increasingly more difficult flow control problems, but for the most difficult goals to be met, these actuators must be used in deliberate and intentional ways to optimize the effects that they introduce to the flow. Sloppy implementation of these devices may be more detrimental than beneficial to control efforts. The impact of three-dimensional perturbations has not yet been fully realized, and serpentine geometry plasma actuators are a flexible and versatile tool for future applications.

8.3 Plasma Driven Channel Flows

Experiments using plasma actuators to drive a channel flow have shown that it is possible to drive a low speed channel flow up to several meters per second using plasma actuators. Functional relationships between the operating voltage, flow velocity, and pressure differential in the channel have all been developed. These functional relationships have been used to determine a similar relationship for the efficiency of the plasma actuator to drive the flow as a function of the voltage. Based on these results, the plasma actuators become more efficient as they are operated at a higher voltage.

Numerical simulations and experiments have also been performed examining the internal structure of these channel flows. It is found that the plasma actuators cause a majority of the momentum in the channel to be entrained into wall-jet features wherever the plasma actuators are located at in the flow field. If plasma actuators are only located on one side of the channel flow, it is possible that the flow separates in a massive way on the opposite side of the channel.

Future work on this topic should aim to implement these devices for flow control applications. Some research to this effect has been performed by Morgan & Visbal (2013). There are also ongoing efforts to use this type of plasma driven channel flow to reduce heat transfer effects in cold air curtains (such as those in open air refrigerators). There may also be applications at increasingly smaller scales (μm to cm) for fluid and heat transfer purposes, where traditional fans and blowers would not be as effective.

APPENDIX A
MODEL OF THE LOCAL TEMPORAL STABILITY ANALYSIS

Local linear stability theory can be used to predict the existence and growth rates of instabilities that may manifest in a the boundary layer or channel flow, supposing that certain assumptions regarding how parallel the flow is and how slowly the flow continues to develop. Though temporal instabilities are examined here, using the Gaster transformation spatial instabilities could be similarly approximated (Gaster, 1962), or by reducing the spatial order of the governing equations using auxillary equations as described in Schmid & Henningson (2000).

A.1 Eigenvalue Problem Formulation

The linearized Navier-Stokes equations (Equation 2–15) can be simplified using the assumptions of a fully developed, parallel flow, with wave like perturbations, such that it can be formulated as a generalized eigenvalue problem

$$i\alpha u' + \frac{\partial v'}{\partial y} + i\beta w' = 0 \tag{A–1a}$$

$$i\alpha\bar{u}u' + v'\frac{\partial \bar{u}}{\partial y} + i\alpha p' - \frac{1}{Re}\left(-\alpha^2 u' + \frac{\partial^2 u'}{\partial y^2} - \beta^2 u'\right) = i\omega u' \tag{A–1b}$$

$$i\alpha\bar{u}v' + \frac{\partial p'}{\partial y} - \frac{1}{Re}\left(-\alpha^2 v' + \frac{\partial^2 v'}{\partial y^2} - \beta^2 v\right) = i\omega v' \tag{A–1c}$$

$$i\alpha\bar{u}w' + i\beta p' - \frac{1}{Re}\left(-\alpha^2 w' + \frac{\partial^2 w'}{\partial y^2} - \beta^2 w\right) = i\omega w' \tag{A–1d}$$

This formulation only accommodates one-dimensional flow velocity profiles, which can be described at $\bar{u} = \bar{u}(y)$. The physics of more complex flows is entirely neglected by this formulation. Further simplification of these equations would result in the Orr-Sommerfeld-Squire equations (Equation 2–18). However, this more extended formulation is used, as it is simpler to implement due to the lower order derivatives and easier implementation of boundary conditions.

For the present computations, this set of equations (Equations A–1) was then discretized onto a uniform staggered mesh (Patankar, 1980). A 4^{th} order accurate,

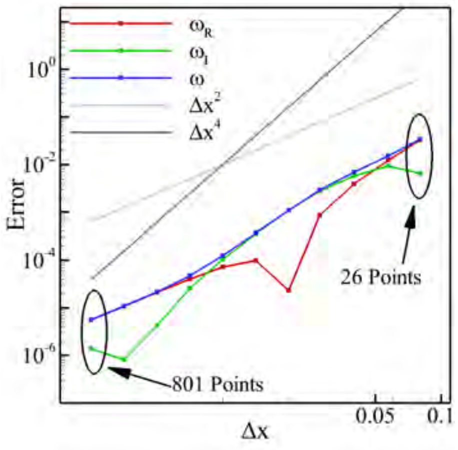

Figure A-1. Grid convergence of the numerical method as compared to Orszag (1971) for Poisseuille flow. $Re = 10,000$, $\alpha = 1$, $\beta = 0$, $\omega = 0.23752649 + i0.00373967$.

centered, finite difference stencil was used for the differencing over a majority of the domain. A 2nd order accurate, centered, finite difference scheme was used near the boundaries. The code was benchmarked against that of the Poisseuille flow as discussed by Orszag (1971). The Reynolds number of this case is $Re = 10,000$. The wave numbers are $\alpha = 1$ and $\beta = 0$. The single unstable eigenvalue is $\omega = 0.23752649 + i0.00373967$, and is considered accurate to within 8 significant digits. The calculated value of this eigenvalue was used to determine the order of accuracy of the present code. The order of accuracy of the code has been found to be somewhere between 2 and 4 (Figure A-1). The asymptotic region is reached relatively quickly for this problem.

A.2 Transient Stability Analysis

While the straightforward eigenvalue analysis allows for a clear understanding of the behavior of growth of infinitesimally small perturbations in the very long time scales, it is also beneficial to understand how perturbations grow on much shorter time scales. For these conditions, a transient analysis, examining the algebraic growth of perturbations must be performed. The origins of a transient analysis lie with Orr (1907), but the present formulation for a viscous flow is largely adapted from Farrell (1988).

In the transient analysis, we are most interested in the growth of the kinetic energy of the perturbations, that is $u'^*u' + v'^*v' + w'^*w'$. We can describe these perturbations as a sum of the eigenmodes such that

$$\begin{bmatrix} u' \\ v' \\ w' \end{bmatrix} = \sum_j c_j \begin{bmatrix} u' \\ v' \\ w' \end{bmatrix} \exp\left(-i\omega t\right) \tag{A–2a}$$

$$= \mathbf{Ec} \exp\left(-i\omega t\right) \tag{A–2b}$$

where the matrix $\mathbf{E}$ contains all of the eigenvectors, and the matrix $\mathbf{c}$ contains the values of the coefficients. The matrix $\mathbf{A}_0$ is defined as $\mathbf{A}_0 = \mathbf{E}^*\mathbf{E}$

At time $t = 0$, the kinetic energy has some value such that

$$\mathcal{K}\left(t = 0\right) = \left(\mathbf{Ec}\right)^* \left(\mathbf{Ec}\right) = \mathbf{c}^*\mathbf{E}^*\mathbf{Ec} = \mathbf{c}^*\mathbf{A}_0\mathbf{c} \tag{A–3}$$

and at time t, the kinetic energy has some value such that

$$\mathcal{K}\left(t\right) = \mathbf{c}^*\mathbf{A}_{\mathrm{t}}\mathbf{c} \tag{A–4}$$

where $\mathbf{A}_{\mathrm{t}}$ represents the multiplication of the eigenmodes as they've been progressed in time. More explicitly, $\mathbf{A}_t = \exp\left(-i\omega t\right)^* \mathbf{E}^*\mathbf{E} \exp\left(-i\omega t\right)$. From this, it can be shown using variational methods that

$$\mathbf{A}_{\mathrm{t}}\mathbf{c} + \lambda\mathbf{A}_0\mathbf{c} = 0 \tag{A–5}$$

where λ represents the factor of energy growth of a perturbation, defined as the sum of the modes with the coefficients in the vector $\mathbf{c}$. This problem is essentially an eigenvalue problem, where the largest value of λ represents the optimal energy growth, and the successively smaller values represent orthonormal modes of energy growth. This eigenvalue problem can be handled using standard techniques, as the size of this matrix is usually only $(O)(10^2) \times (O)(10^2)$.

Performing this calculation for a channel flow, it can be seen that, the transient growth mechanism produces a larger perturbation than the modal growth of the unstable eigenvalue, and that the results are comparable to those of Farrell (1988).

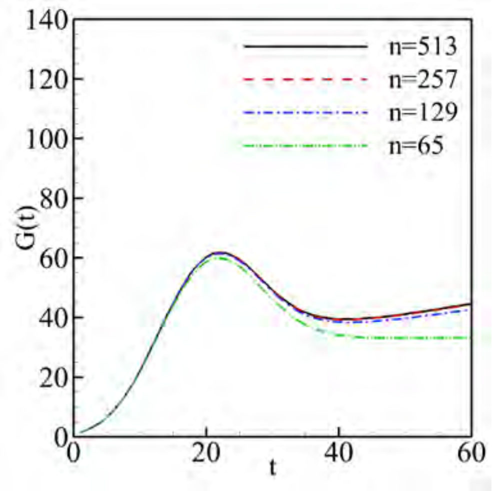

Figure A-2. Calculation of the transient growth for a perturbation in a channel flow of $\alpha = 1$, $\beta = 0$, $Re_h = 10,000$.

APPENDIX B
MODEL OF THE BI-GLOBAL STABILITY ANALYSIS

For flows that vary in two-dimensions, the assumptions necessary to for one-dimensional stability analysis are violated. Under some circumstances, these assumptions may be only weakly violated, and a one-dimesional analysis can still hold a certain level of accuracy (such as in slowly developing boundary layers). However, when these assumptions are more strongly violated, more computationally expensive methods, such as bi-global stability analysis become necessary tools.

Only in the past decade have matrix based bi-global stability methods reached a level of maturity such that they can be used for physically important problems. Before this time, bi-global stability analysis focused on geometrically simple lid driven cavity and pressure driven duct flows (Tatsumi & Yoshinmura, 1990; Theofilis *et al.*, 2004). More recently, bi-global stability methods have extended themselves from canonical flow problems such as simple duct and cavity flows to separated flows over plates (Merle *et al.*, 2010; Theofilis & Rodriguez, 2009) and cavities (Brès & Colonius, 2008) and two-dimensional channel flows (Chedevergne *et al.*, 2006). More complex geometries over airfoils (Theofilis & Rodriguez, 2009) and turbine blades (Abdessemed *et al.*, 2009; Sharma *et al.*, 2011) have also been examined, indicating that the present methods can finally be applied to industrially important flow fields.

In addition to the modal growth problems, bi-global stability methods have been extended to transient growth problems (Abdessemed *et al.*, 2009; Åkervik *et al.*, 2008; Alizard & Robinet, 2007; Sharma *et al.*, 2011), periodic Floquet stability analysis (Abdessemed *et al.*, 2009; Sharma *et al.*, 2011), and the optimal forcing problem (Brandt *et al.*, 2011; Sipp & Marquet, 2012). Tri-global stability methods have been implemented, but the computation cost of these methods remains exceedingly high, and only specialized methods have shown any success (Bagheri *et al.*, 2009; Natarajan & Acrivos, 1993).

Using the linearized incompressible Navier-Stokes equations (Equation 2–15) and only requiring that the flow be two-dimension, simplification of the governing equations leads to the system of equations

$$\frac{\partial u'}{\partial x}+\frac{\partial v'}{\partial y}+i\beta w'=0 \tag{B–1a}$$

$$\bar{u}\frac{\partial u'}{\partial x}+\bar{v}\frac{\partial u'}{\partial y}+\bar{w}i\beta u'+u'\frac{\partial \bar{u}}{\partial x}+v'\frac{\partial \bar{u}}{\partial y}+\frac{\partial p'}{\partial x}-\frac{1}{Re}\left(\frac{\partial^2 u'}{\partial x^2}+\frac{\partial^2 u'}{\partial y^2}-\beta^2 u'\right)=i\omega u' \tag{B–1b}$$

$$\bar{u}\frac{\partial v'}{\partial x}+\bar{v}\frac{\partial v'}{\partial y}+\bar{w}i\beta v'+u'\frac{\partial \bar{v}}{\partial x}+v'\frac{\partial \bar{v}}{\partial y}+\frac{\partial p'}{\partial y}-\frac{1}{Re}\left(\frac{\partial^2 v'}{\partial x^2}+\frac{\partial^2 v'}{\partial y^2}-\beta^2 v'\right)=i\omega v' \tag{B–1c}$$

$$\bar{u}\frac{\partial w'}{\partial x}+\bar{v}\frac{\partial w'}{\partial y}+\bar{w}i\beta w'+u'\frac{\partial \bar{w}}{\partial x}+v'\frac{\partial \bar{w}}{\partial y}+i\beta p'-\frac{1}{Re}\left(\frac{\partial^2 w'}{\partial x^2}+\frac{\partial^2 w'}{\partial y^2}-\beta^2 w'\right)=i\omega w' \tag{B–1d}$$

This system of equations can be put into a generalized eigenvalue problem form.

B.1 Numerical Concerns and Implementation

Due to the size of the necessary matrices for the bi-global hydrodynamic stability problem, the numerical differentiation becomes a very tricky problem to address. The matrices used must be storeable on the available memory resources, otherwise the problem cannot be solved. With the present use of the Arnoldi Algorithm and LAPACK subroutines for the eigenvalue computation, some of the memory requirements can be distributed, as in the case of the matrix $\tilde{\mathbf{A}} = \mathbf{A}^{-1}\mathbf{B}$, however, others cannot. In order to reduce the size of the matrices, there are two available options

1. Reduce the necessary number of degrees of freedom.
2. Reduce the number of elements stored via sparse and banded matrix methods.

The first of these options, reducing the number of degrees of freedom immediately suggests that higher order and spectral methods are appropriate for the bi-global stability problem, which have higher resolvability than lower order schemes. However, as high order methods are employed, the density of the matrices used increases.

Therefore, there is a trade off present between the accuracy and resolvability of a scheme and the density of the resulting differentiation matrices.

Sparse matrix methods were considered, but they are not optimal for use with the present LAPACK subroutines. Sparse matrix methods allow for the least memory storage, but they present difficulties in implementation, and the available libraries do not have extensive support for complex number arithmetic.

Banded matrix methods are well supported in the existing numerical linear algebra libraries, including LAPACK (Anderson *et al.*, 1987). Using banded matrices, the total number of elements stored can be greatly reduced, while still retaining numerical accuracy and resolvability.

Using a banded matrix method in conjunction with sparse finite difference or finite element differentiation is still sub-optimal however, as there are a large number of empty elements in the matrices. In order to take advantage of the available memory storage for a banded matrix method, a Chebyshev collocation differencing scheme can be applied in one direction, and a finite different scheme is applied in the other. This configuration provides the fewest possible empty elements in the matrix, hopefully reducing the necessary number of elements in the matrices to a near minimum while still retaining numerical accuracy.

Even if these types of methods are employed, this type of problem continues to be constrained in that it is a general eigenvalue method, that is

$$i\omega \mathbf{A}\mathbf{u} = \mathbf{B}\mathbf{u} \tag{B–2}$$

The normal method of approaching this problem is to employ the shift and invert or Cayley spectral transforms, which require the inversion of matrix (Theofilis, 2003, 2011). Even so, the inversion of this matrix (even if it is sparse), leads to a dense matrix, which will be referred to as $\tilde{\mathbf{A}}$. The relative size of the necessary matrices, is described in Table B-1. It can be seen that the largest constraint on memory is the storage of the matrix $\tilde{\mathbf{A}}$.

Table B-1. Memory requirements for the size of certain matrices involved in bi-global stability analysis

Matrix	Dense matrix storage	Banded matrix storage	Sparse matrix storage
A	$\mathcal{O}(n_x^2 n_y^2 n_{gov}^2)$	$\mathcal{O}(n_x n_y^2 n_{gov}^2(2n_{diff}+1))$	$\mathcal{O}(n_x n_y n_{gov}^2(4n_{diff}^2+1))$
B	$\mathcal{O}(n_x^2 n_y^2 n_{gov}^2)$	$\mathcal{O}(n_x n_y^2 n_{gov})$	$\mathcal{O}(n_x n_y n_{gov})$
$\tilde{\mathbf{A}}$	$\mathcal{O}(n_x^2 n_y^2 n_{gov}^2)$	$\mathcal{O}(n_x^2 n_y^2 n_{gov}^2)$	$\mathcal{O}(n_x^2 n_y^2 n_{gov}^2)$

B.1.1 Differencing Schemes Used

Implementing this bi-global stability analysis, a 4th order accurate finite difference scheme is applied in the x-direction. A Chebyshev collocation differencing scheme can be applied in the y-direction. A compact 10th order differentiation scheme has also been implemented into the code for differencing in the y-direction, based on the work of Lele (1992). This scheme uses a combination of staggered and non-staggered differentiation stencils of 10th order accuracy in the center of the domain, but of lesser accuracy near the boundaries. The continuity and momentum equations are solved on a semi-staggered mesh. The momentum equations are solved and the velocity data stored on points co-incident with the boundaries. The continuity equation is solved and the pressure data is stored on intermediate points.

B.1.2 Memory Distribution

As the memory can be distributed for the matrix $\tilde{\mathbf{A}}$, the matrix **B** is also distributed. However, in order to use the LAPACK subroutines ZGBSV and DGBSV to invert **A**, that matrix cannot be presently distributed across multiple processors. The memory distribution of $\tilde{\mathbf{A}}$ and **B** is done in such a way that a number of consecutive columns from the matrix are stored on each processor independently from each other.

This type of memory distribution is also very easy to implement with respect to the Arnoldi algorithm. The individual Arnoldi basis vectors (q_n) can also be distributed over the available processors. In doing this, the matrix-vector multiplication $\tilde{\mathbf{A}}\mathbf{q}_n$ is

$$\tilde{\mathbf{A}} = \left[\begin{array}{c|c|c|c} \tilde{\mathbf{A}}_1 & \tilde{\mathbf{A}}_2 & \cdots & \tilde{\mathbf{A}}_{n_{proc}} \end{array} \right]$$

$$\mathbf{B} = \left[\begin{array}{c|c|c|c} \mathbf{B}_1 & \mathbf{B}_2 & \cdots & \mathbf{B}_{n_{proc}} \end{array} \right]$$

$$\tilde{\mathbf{A}}_i = \left(\mathbf{A} + \sigma\mathbf{B}\right)^{-1}\mathbf{B}_i$$

Figure B-1. Distribution of memory for a shift and invert strategy (with a shift of σ).

reduced to only the components stored with each processor. In doing this, the need for communication between the processors is reduced, except for the summation required to form the upper Hessenberg matrix, $\mathbf{H}$, which approximates the eigenvalues of $\tilde{\mathbf{A}}$ ($\tilde{\mathbf{A}} \approx \mathbf{QHQ}^*$)

$$\mathbf{Q} = [\mathbf{q}_1, \ \mathbf{q}_2, \ \cdots \ , \ \mathbf{q}_n] = \left[\begin{array}{c} \mathbf{Q}_1 \\ \hline \mathbf{Q}_2 \\ \hline \vdots \\ \hline \mathbf{Q}_{n_{proc}} \end{array} \right]$$

Figure B-2. Distribution of memory for the Arnoldi algorithm.

B.1.3 Arnoldi Algorithm

In addition to the memory constraints, there is also the consideration of performing this type of large scale computation within a reasonable amount of time. Eigenvalue and SVD problems are solved using similar algorithms, as the SVD problems are usually modified eigenvalue methods, the computational cost of which are outlined in Table B-2

Table B-2. Operation counts for the size of certain algorithms involved in the EV and SVD problems for a dense matrix.

Arnoldi Algorithm	QR Algorithm
$\mathcal{O}(n_x^2 n_y^2 n_{gov}^2 n_{arno}^2)$	$\mathcal{O}(n_x^3 n_y^3 n_{gov}^3)$

The Arnoldi algorithm has been implemented as the present eigenvalue solver. This algorithm is easily adjustable for the memory distribution used at present. The Arnoldi algorithm is described in detail in Trefethen & Bau (1997).

In implementing a parallel Arnoldi algorithm, no vectors need to be passed using a parallel implementation. Instead, the necessary matrix vector products can be performed locally on each processor. The vector-vector products and vector norms can also be performed locally on each processor, only the partial sums need to be combined and passed at the end of the multiplication. The Arnoldi algorithm produces a matrix **H** and an incomplete basis set of vectors $\mathbf{Q}_n$, which can be used to approximate the eigenvalues and eigenvectors of $\tilde{\mathbf{A}}$. The eigenvalue problem of **H** is small enough that it can be computed on a single processor in a reasonable amount of time (on the order of 10-60 seconds).

B.2 Verification

In order to validate this case, two examples have been examined, the canonical case of channel flow as examined by Orszag (1971), and a duct flow case.

B.2.1 Channel Flow

The purpose of this example is to show that the results of the bi-global stability code agree with the single dimension results. The use of a bi-global stability code for a flow such as this is a vastly inefficient use of computational resources, but will provide assurance that the problem is being addressed correctly.

In order to apply periodic boundary conditions while maintaining a high order of accuracy, the channel flow is rotated 90 degrees, such that $v = v(x) = 1 - x^2$ and $u = w = 0$. Three grid resolutions were tested for this case. 800 Arnoldi iterations are used to evaluate the eigenvalue problem. The results are shown in Table. B-3. With the course grid resolution, the eigenvalue is accurate to approximately 1%, which is comparable to the error from a local stability analysis with the same grid resolution and similar 4th order accurate, semi-staggered, finite difference scheme (described in Appendix 8.3). As the resolution is increased, the accuracy of the result also increases. Based on these eigenvalue calculations, this channel flow can be accurately analyzed using the present bi-global stability method.

Considering the transient instability analysis, a similar grid resolution study has been performed. Comparing the non-modal growth of perturbations over a finite amount

Table B-3. Grid resolutions and most unstable eigenmodes for the channel flow.

Case	n_x	n_y	Δx	Δy_{wall}	ω
Bi-Global - Coarse	65	32	0.03125	0.1963495	0.240163-i0.000284
Bi-Global - Medium	129	32	0.015625	0.1963495	0.237686+i0.003064
Bi-Global - Fine	257	32	0.0078125	0.1963495	0.237532+i0.003660
Local - Coarse	65	n/a	0.03125	n/a	0.238947+i0.000203
Local - Medium	129	n/a	0.015625	n/a	0.237435+i0.003245
Local - Fine	257	n/a	0.0078125	n/a	0.237479+i0.003700
Orszag (1971)	"Exact"	n/a	n/a	n/a	0.23752649+i0.00373967

of time (Figure B-3, the local and bi-global stability analysis produce comparable results. The higher grid resolutions appear to converge for all of the times examined. The lower grid resolutions produce a good result for smaller amplification times (10-40), but eventually diverge from the more resolved times due to exponential amplification of error in the calculated eigenvalues.

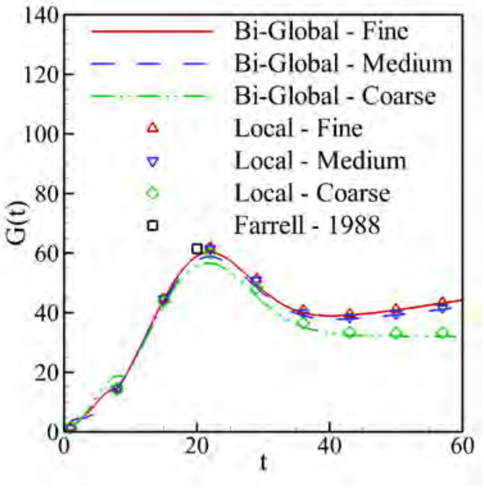

.

Figure B-3. Optimal transient growth in the channel as a function of the grid-resolution. Comparisons with local stability analysis and a past result are also shown.

B.2.2 Duct Flow

The purpose of this example is to validate the bi-global stability code for a flow that has gradients in two directions. Whereas the channel flow case is a two-dimensional extension of local stability theory, this case is something that can only be examined using bi-global stability analysis. The flow here represents a low Reynolds number pressure driven flow in a finite aspect ratio duct. The base flow can be found by solving the equation

$$\frac{1}{Re}\left(\frac{\partial^2 w}{\partial x^2}+\frac{\partial^2 w}{\partial y^2}\right)=\frac{\partial p}{\partial z} \tag{B–3}$$

which can be derived by assuming a steady, two-dimensional flow fully developed flow in the z-direction, and assuming that there are no standing streamwise vortices. The solution to this equation can be found using separation of variables and is

$$w=\sum_{n=0}^{\infty}\frac{4\left(-1\right)^n}{\left(2n+1\right)\pi}\frac{\sinh\left(\left(2n+1\right)\pi\left(y+A\right)/2\right)}{\sinh\left(\left(2n+1\right)\pi A\right)}\cos\left(\left(2n_1\right)\pi x/2\right) \tag{B–4}$$

For this flow, three grid resolutions were examined, which are indicated in Table B-4. The Reynolds number is chosen to be 100 and the streamwise wave number to be $\beta = 1$. Based on the most unstable eigenmode, all of these grid resolutions appear to resolve the most unstable dynamics. The eigenspectra computed for each of these conditions is shown in Figure B-4A.

Table B-4. Grid resolutions and most unstable eigenmodes for the duct flow of aspect ratio 1.

Grid	n_x	n_y	Δx	Δy_{wall}	ω
Coarse	17	17	0.125	0.0192147	0.325631-i0.115880
Medium	33	33	0.0625	0.0048153	0.325713-i0.115654
Fine	65	65	0.03125	0.0012045	0.325729-i0.115606

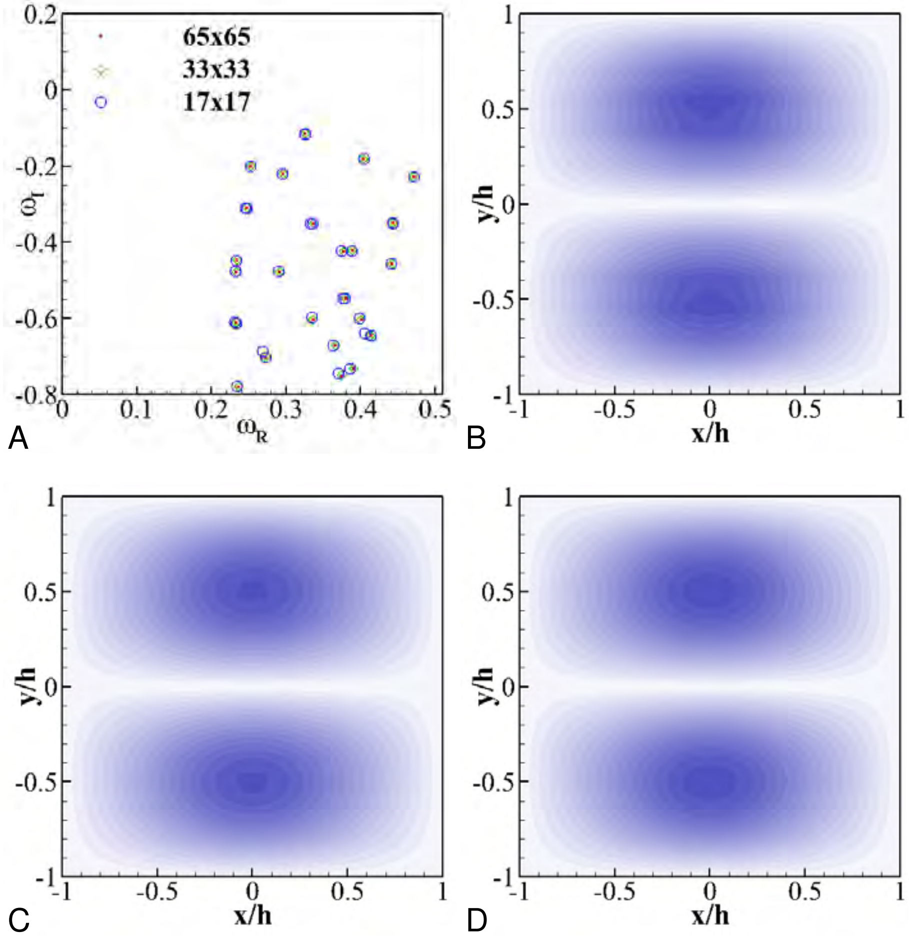

Figure B-4. A) Eigenvalues of the duct flow for $Re = 100$, $A = 1$, and $\beta = 1$ for the three grid resolutions tested. The absolute value of the streamwise velocity perturbation ($|w'|$) of the least stable eigenmode for the B) Coarse, C) Medium, and D) Fine grids is also shown.

APPENDIX C
DESCRIPTION OF FDL3DI

In order to simulate these flows, the Implicit Large Eddy Simulation (ILES) Navier-Stokes solver, FDL3DI (Rizzetta *et al.*, 2008) is employed. This code solves the compressible two-dimensional Navier-Stokes equations (Equation 2–1) in a body fitted, diagonalized, conservation form.

$$\frac{\partial}{\partial t}\left(\frac{1}{\mathcal{J}}\mathbf{Q}\right)+\frac{\partial}{\partial \xi}\left(\mathbf{F}-\frac{1}{Re}\mathbf{F}_v\right)+\frac{\partial}{\partial \eta}\left(\mathbf{G}-\frac{1}{Re}\mathbf{G}_v\right)+\frac{\partial}{\partial \zeta}\left(\mathbf{H}-\frac{1}{Re}\mathbf{H}_v\right)=D_c\mathbf{S} \tag{C–1}$$

The dependent variables are defined as

$$\mathbf{Q}=\begin{bmatrix}\rho, & \rho u, & \rho v, & \rho w, & \rho E\end{bmatrix}^T \tag{C–2}$$

with the inviscid and viscid fluxes are defined as

$$\mathbf{F}=\frac{1}{\mathcal{J}}\begin{bmatrix}\rho U\\ \rho uU+\xi_x p\\ \rho vU+\xi_y p\\ \rho wU+\xi_z p\\ \rho EU+\xi_{x_i}u_i p\end{bmatrix},\ \mathbf{G}=\frac{1}{\mathcal{J}}\begin{bmatrix}\rho V\\ \rho uV+\eta_x p\\ \rho vV+\eta_y p\\ \rho wV+\eta_z p\\ \rho EV+\eta_{x_i}u_i p\end{bmatrix},\ \mathbf{H}=\frac{1}{\mathcal{J}}\begin{bmatrix}\rho W\\ \rho uWV+\zeta_x p\\ \rho vW+\zeta_y p\\ \rho wW+\zeta_z p\\ \rho EW+\zeta_{x_i}u_i p\end{bmatrix} \tag{C–3}$$

$$\mathbf{F}_\text{v}=\frac{1}{\mathcal{J}}\begin{bmatrix}0\\ \xi_{x_i}\tau_{i1}\\ \xi_{x_i}\tau_{i2}\\ \xi_{x_i}\tau_{i3}\\ \xi_{x_i}(u_j\tau_{ij}-Q_i)\end{bmatrix},\ \mathbf{G}_\text{v}=\frac{1}{\mathcal{J}}\begin{bmatrix}0\\ \eta_{x_i}\tau_{i1}\\ \eta_{x_i}\tau_{i2}\\ \eta_{x_i}\tau_{i3}\\ \eta_{x_i}(u_j\tau_{ij}-Q_i)\end{bmatrix},\ \mathbf{H}_\text{v}=\frac{1}{\mathcal{J}}\begin{bmatrix}0\\ \zeta_{x_i}\tau_{i1}\\ \zeta_{x_i}\tau_{i2}\\ \zeta_{x_i}\tau_{i3}\\ \zeta_{x_i}(u_j\tau_{ij}-Q_i)\end{bmatrix}, \tag{C–4}$$

and the right hand side source term are defined as

$$\mathbf{S}=\frac{1}{\mathcal{J}}\begin{bmatrix}0, & f_x, & f_y, & f_z, & u_i f_{x_i}\end{bmatrix}^T \tag{C–5}$$

where

$$E = \frac{T}{\gamma(\gamma-1)M_\infty^2} + \frac{1}{2}(u^2 + v^2 + w^2) \tag{C–6}$$

$$Q_i = -\left(\frac{1}{(\gamma-1)M_\infty^2}\right)\left(\frac{\mu}{Pr}\right)\frac{\partial\xi_j}{\partial x_i}\frac{\partial T}{\partial\xi_j} \tag{C–7}$$

$$\tau_{ij} = \mu\left(\frac{\partial\xi_k}{\partial x_j}\frac{\partial u_i}{\partial\xi_k} + \frac{\partial\xi_k}{\partial x_i}\frac{\partial u_i}{\partial\xi_k} - \frac{2}{3}\delta_{ij}\frac{\partial\xi_l}{\partial x_k}\frac{\partial u_k}{\partial\xi_l}\right) \tag{C–8}$$

$$U = \frac{\partial\xi}{\partial x_i}u_i,\ \ V = \frac{\partial\eta}{\partial x_i}u_i, W = \frac{\partial\zeta}{\partial x_i}u_i \tag{C–9}$$

In this system of equations, ρ represents the fluid density, u and v are the flow velocities, p is pressure, and E is the specific energy. All of these variables are non-dimensionalized by their reference values. Pressure is the exception to this, as it has been non-dimensionalized by the dynamic head ($\rho_\infty u_\infty^2$). τ_{ij} represents the stress tensor and Q_i is the heat flux vector. f_x, f_y and f_z describe the normalized, spatially varying body force. The magnitude of this body force is modulated by the value of D_c. ξ, η, and ζ represent the body fitted coordinate system, $\mathcal{J}$ is the grid Jacobian, U,V and W are the body fitted velocities. The non-dimensional variables Re, Pr, and Ma_∞ represent the freestream Reynolds ($Re = \frac{u_\infty L}{\nu}$), Prandtl ($Pr = \frac{\nu c_p}{k}$), and Mach ($M_\infty = \frac{u_\infty}{\sqrt{\gamma R T_\infty}}$) numbers, respectively. Here, γ represents the ratio of specific heats and is equal to 1.4. The ideal gas law (Equation 2–4) is also used in order to close the system of equations. While this is the compressible form of the Navier-Stokes equations, and incompressible flow can be solved by setting the Mach number, M_∞, to an appropriately low value. It has been determined that a value of $M_\infty = 0.1$ provides a reasonable balance of incompressibility and numerical stability for this particular code.

In order to implement the plasma body force in the fluid system, the body force term **S** is employed. This term can be made to be steady or unsteady, depending on what manner of body force is desired.

For the finite differencing scheme, compact, high order schemes have been implemented into FDL3DI (Rizzetta *et al.*, 2008). These compact schemes allow for greater resolvability of the flow field using adjacent mesh points (Lele, 1992) than more traditional explicit differencing schemes. These stencils generally take the form of

$$\begin{gathered}\beta\left(\phi'_{i+2}+\phi'_{i-2}\right)+\alpha\left(\phi'_{i+1}+\phi'_{i-1}\right)+\phi' = \\ \frac{c}{6h}\left(\phi_{i+3}-\phi_{i-3}\right)+\frac{b}{4h}\left(\phi_{i+2}-\phi_{i-2}\right)+\frac{a}{2h}\left(\phi_{i+1}-\phi_{i-1}\right)\end{gathered} \tag{C–10}$$

where ϕ is the variable being differenced, the subscript i indicates the mesh index, and h is the mesh spacing, though the width of the stencil can be varied to be wider or narrower. The coefficients of α, β, a, b, and c can be varied in order to control the accuracy and resolvability of the differencing, subject to certain constraints. Near boundaries, this type of compact differencing scheme can be adapted to non-centered stencils (Visbal & Gaitonde, 1999). For FDL3DI, a sixth order accurate, tri-diagonal differencing scheme are employed over a majority of the domain. Non-centered, fourth and fifth order accurate, compact differencing schemes are employed near the boundaries of the flow(Rizzetta *et al.*, 2008).

The temporal integration employed in FDL3DI is the Beam-Warming approximate factorization method (Beam & Warming, 1978), which diagonalizes the Navier-Stokes equations as they're being solved. For the simulations performed, a three-point, backwards implicit scheme has been used, which has second order temporal accuracy (Rizzetta *et al.*, 2008). In order to address non-linear terms, three Newton like sub-iterations have been performed for each time step. The factorization of this system is solved in delta form (where δ_{xn} indicates the spatial differencing in the x direction with

n^{th} order accuracy) as

$$\begin{gathered}
\left(\frac{1}{\mathcal{J}}+\left(\frac{2\Delta t}{3}\right)\delta_{\xi 2}\left(\frac{\partial \mathbf{F}^p}{\partial \mathbf{Q}}-\frac{1}{Re}\frac{\partial \mathbf{F}_v^p}{\partial \mathbf{Q}}\right)\right)\mathcal{J} \\
\times\left(\frac{1}{\mathcal{J}}+\left(\frac{2\Delta t}{3}\right)\delta_{\eta 2}\left(\frac{\partial \mathbf{G}^p}{\partial \mathbf{Q}}-\frac{1}{Re}\frac{\partial \mathbf{G}_v^p}{\partial \mathbf{Q}}\right)\right)\mathcal{J} \\
\times\left(\frac{1}{\mathcal{J}}+\left(\frac{2\Delta t}{3}\right)\delta_{\zeta 2}\left(\frac{\partial \mathbf{H}^p}{\partial \mathbf{Q}}-\frac{1}{Re}\frac{\partial \mathbf{H}_v^p}{\partial \mathbf{Q}}\right)\right)\Delta\mathbf{Q} \\
=-\left(\frac{2\Delta t}{3}\right)\left(\left(\frac{1}{2\Delta t}\right)\left(\frac{3\mathbf{Q}^p-4\mathbf{Q}^n+\mathbf{Q}^{n-1}}{\mathcal{J}}\right)+\right. \\
\left.\delta_{\xi 6}\left(\mathbf{F}^p-\frac{1}{Re}\mathbf{F}_v^p\right)+\delta_{\eta 6}\left(\mathbf{G}^p-\frac{1}{Re}\mathbf{G}_v^p\right)+\delta_{\zeta 6}\left(\mathbf{H}^p-\frac{1}{Re}\mathbf{H}_v^p\right)-D_c\mathbf{S}^p\right)
\end{gathered} \tag{C–11}$$

where the superscript n indicates the time step, and the superscript p indicates the sub-iteration being solved for at time step $n+1$. $\Delta\mathbf{Q} = \mathbf{Q}^{p+1} - \mathbf{Q}^p$. For the first sub-iteration of each time step, the first sub-iteration is equal to the solution at the previous time step (i.e.$\mathbf{Q}^p = \mathbf{Q}^n$). For the implicit, spatial discretization terms in this scheme, FDL3DI uses an explicit second order accurate scheme. For the explicit, spatial differencing terms, the high order, compact schemes are used.

This method of solving the equations does not employed a subgrid stress (SGS) model, common in most LES methods (Lesieur *et al.*, 2005). Instead, the diffusion of smaller eddies at the unresolved scales are modeled by the LES filter (Grinstein *et al.*, 2007). So long as enough of the length scales are resolved, the ILES method is able to resolve turbulent flow features and their statistics (Visbal & Gaitonde, 1999; Wachtor *et al.*, 2013). As such, it is important to note that among the simulations performed, the minimum accuracy of the filters was 8th order accurate. The filters used were also compact, such that

$$\alpha\hat{\phi}_{i-1}+\hat{\phi}_i+\alpha\hat{\phi}_{i+1}=a_0\phi_i+\frac{a_1}{2}\left(\phi_{i+1}+\phi_{i-1}\right)+\frac{a_2}{2}\left(\phi_{i+2}+\phi_{i-2}\right)+\ldots \tag{C–12}$$

where $\hat{\phi}$ represents the filtered value of ϕ. Similarly to how to the asymmetric stencils for the compact differencing scheme can be used near the domain boundaries, asymmetric stencils can also be employed for the filter (Visbal & Gaitonde, 1999), which has been implemented into FDL3DI (Rizzetta *et al.*, 2008). The parameter used to modulate the low pass nature of the filter was $\alpha = 0.4$) which roughly correlates to needing four grid points to resolve a full wave length of some flow feature.

REFERENCES

ABDESSEMED, N., SHERWIN, S. J. & THEOFILIS, V. 2009 Linear instability analysis of low-pressure turbine flows. *Journal of Fluid Mechanics* **628**, 57.

ACARLAR, M. S. & SMITH, C. R. 1987*a* A study of hairpin vortices in a laminar boundary layer. part 1. hairpin vortices generated by a hemispherical protuberance. *Journal of Fluid Mechanics* **175**, 1–41.

ACARLAR, M. S. & SMITH, C. R. 1987*b* A study of hairpin vortices in a laminar boundary layer. part 2. hairpin vortices generated by fluid injection. *Journal of Fluid Mechanics* **175**, 43–83.

ADRIAN, R. J. 2007 Hairpin vortex organization in wall turbulence. *Physics of Fluids* **19** (4).

ADRIAN, R. J., MEINHART, C. D. & TOMKINS, C. D. 2000 Vortex organization the outer region of the turbulent boundary layer. *Journal of Fluid Mechanics* **422**, 1–54.

ÅKERVIK, E., BRANDT, L., HENNINGSON, D. S., HŒPFFNER, J., MARXEN, O. & SCHLATTER, P. 2006 Steady solutions of the navier-stokes equations by selective frequency damping. *Physics of Fluids* **18**, 068102.

ÅKERVIK, E., EHRENSTEIN, U., GALLAIRE, F. & HENNINGSON, D. S. 2008 Global two-dimensional stability measures of the flat plate boundary-layer flow. *European Journal of Mechanics-B/Fluids* **27** (5), 501–513.

ALIZARD, F. & ROBINET, J.C. 2007 Spatially convective global modes in a boundary layer. *Physics of Fluids* **19**.

AMITAY, M. & COHEN, J. 1997 Instability of a two-dimensional plane wall jet subjected to blowing or suction. *Journal of Fluid Mechanics* **344**, 67–94.

ANDERSON, E., BAI, Z., BISCHOF, C., BLACKFORD, S., DEMMEL, J., DONGARRA, J., DUCROZ, J., GREENBAUM, A., HAMMARLING, S., MCKENNEY, A. *et al.* 1987 *LAPACK Users' guide*, , vol. 9. Society for Industrial Mathematics.

ANDERSSON, P., BRANDT, L., BOTTARO, A. & HENNINGSON, D. S. 2001 On the breakdown of boundary layer streaks. *Journal of Fluid Mechanics* **428**, 29–60.

BAGHERI, S., SCHLATTER, P., SCHMID, P. J. & HENNINGSON, D. S. 2009 Global stability of a jet in crossflow. *Journal of Fluid Mechanics* **624**, 33.

BEAM, R. M. & WARMING, R. F. 1978 An implicit factored scheme for the compressible navier-stokes equations. *AIAA Journal* **16** (4), 393–402.

BERKER, A. R. 1963 Integràtion des èquations du mouvement d'un fluide visqueux incompressible. *Encyclopedia of Physics* **8** (2), 1–384.

BERMAN, A. S. 1953 Laminar flow in channels with porous walls. *Journal of Applied Physics* **24**, 1232–1235.

BERS, A. 1972 *Linear Waves and Instabilities*. Research Laboratory of Electronics, Massachusetts Institute of Technology.

BERTOLOTTI, F. P., HERBERT, T. & SPALART, P. R. 1992 Linear and nonlinear stability analysis of the blasius boundary layer. *Journal of Fluid Mechanics* **242**, 441–474.

BICKLEY, W. G. 1937 The plane jet. *The London, Edinburgh, and Dublin Philosophical Magazine and Journal of Science* **23** (156), 727–731.

B.JAYARAMAN, THAKUR, S. & SHYY, W. 2007 Modeling of fluid dynamics and heat transfer induced by dielectric barrier plasma actuator. *Journal of Heat Transfer* **129**, 517–525.

BLASIUS, H. 1908 Grenzscheichten in fl ussignkeiten mit kleiner reibung. *Z. Math. & Phys.* **56** (1).

BOEUF, J. P., LAGMICH, Y., UNFER, T., CALLEGAR, T & PITCHFORD, L. C. 2007 Electrohydrodynamic force in dielectric barrier discharge plasma actuators. *Journal of Physics D: Applied Physics* **40**, 652–662.

BRANDT, L., SIPP, D., PRALITS, J. O. & MARQUET, O. 2011 Effect of base-flow variations in noise amplifiers: the flat-plate boundary layer. *Journal of Fluid Mechanics* **687**, 503–528.

BRÈS, G. A. & COLONIUS, T. 2008 Three-dimensional instabilities in compressible flow over open cavities. *Journal of Fluid Mechanics* **599** (1), 309–339.

BRIGGS, R. J. 1964 *Electron-Stream Interaction with Plasma*. MIT Press.

BUTLER, K. M. & FARRELL, B. F. 1992 Three-dimensional optimal perturbations in viscous shear flow. *Physics of Fluids A* **4** (8), 1637–1650.

CATTAFESTA, L. N. & SHEPLAK, M. 2011 Actuators for active flow control. *Annual Review of Fluid Mechanics* **43**, 247–272.

CHEDEVERGNE, F., CASALIS, G. & FERAILLE, R. 2006 Biglobal linear stability analysis of the flow induced by wall injection. *Physics of Fluids* **18**, 014103.

CORKE, T. C., ENLOE, C. L. & WILKINSON, S. P. 2010 Dielectric barrier discharge plasma actuators for flow control. *Annual Review of Fluid Mechanics* **66**, 505–529.

DADFAR, R., SEMERARO, O., HANIFI, A. & HENNINGSON, D. S. 2013 Output feedback control of blasius flow with leading edge using plasma actuator. *AIAA journal* **51** (9), 2192–2207.

DEBIASI, M. & JIUN-MING, L. 2011 Experimental study of a dbd-plasma driven channel flow. In *AIAA-2011-0954, 50th Aerospace Sciences Meeting, Orlando, FL*.

DUCHMANN, A, GRUNDMANN, S & TROPEA, C 2013*a* Delay of natural transition with dielectric barrier discharges. *Experiments in Fluids* **54** (3), 1–12.

DUCHMANN, A., KURZ, A., WIDMANN, A., GRUNDMANN, S. & TROPEA, C. 2012 Characterization of tollmien-schlichting wave damping by dbd plasma actuators using phase-locked piv. In *AIAA-2012-0903, 50th AIAA Aerospace Sciences Meeting*.

DUCHMANN, A., REEH, A., QUADROS, R., KRIEGSEIS, J. & TROPEA, C. 2010 Linear stability analysis for manipulated boundary-layer flows using plasma actuators. In *Seventh IUTAM Symposium on Laminar-Turbulent Transition*.

DUCHMANN, A., SIMON, B., MAGIN, P., TROPEA, C. & GRUNDMANN, S. 2013*b* In-flight transition delay with dbd plasma actuators. In *AIAA-2013-0900, 51st AIAA Aerospace Sciences Meeting*.

DURSCHER, R. & ROY, S. 2012 Three-dimensional flow measurements induced from serpentine plasma actuators in quiescent air. *Journal of Physics D: Applied Physics* **45**.

DURSCHER, R., STANFIELD, S. & ROY, S. 2012 Characterization and manipulation of the saturation effect by changing the surface temperature of a dielectric barrier discharge actuator. *Applied Physics Letters* **101** (25).

ELLINGSEN, T. & PALM, E. 1975 Stability of linear flow. *Physics of Fluids* **18**, 487.

FALCO, R. E. 1977 Coherent motions in the outer region of turbulent boundary layers. *Physics of Fluids* **20** (10), 124–132.

FALKNER, V. M. & SKAN, S. W. 1931 Some approximate solutions of the boundary layer equations. *Philosophy Magazine* **12** (7), 865–896.

FARRELL, B. F. 1988 Optimal excitation of perturbations in viscous shear flow. *Physics of Fluids* **31** (8).

FASEL, H. 1976 Investigation of the stability of boundary layers by a finite-difference model of the navier-stokes equations. *Journal of Fluid Mechanics* **78** (2), 355–383.

FASEL, H. & KONZELMANN, U. 1990 Non-parallel stability of a flat-plate boundary layer using the complete navier-stokes equations. *Journal of Fluid Mechanics* **221**, 311–347.

FJØRTOFT, R. 1950 Application of integral theorems in deriving criteria of stability for laminar flows and for the baroclinic circulat vortex. *Geophysics Publication* **17** (6), 5–32.

FRANSSON, J. H. M., TALAMELLI, A., BRANDT, L. & COSSU, C. 2006 Delaying transition to turbulence by a passive mechanism. *Physical Review Letters* **96**, 064501.

Gaitonde, D., Visbal, M. & Roy, S. 2006 A coupled approach for plasma-based flow control simulations of wing sections. *AIAA paper 2006-1205, 44th AIAA Aerospace Sciences Meeting and Exhibit, Reno, NV* .

Gaster, M. 1962 A note of the relation between temporally-increasing and spatially-increasing disturbances in hydrodynamics stability. *Journal of Fluid Mechanics* **14**, 222–224.

Gaster, M. 1974 Nonparallel effects on boundary layer stability. *Journal of Fluid Mechanics* **66**, 465–480.

Gibson, B. A., Arjomandi, M. & Kelso, R. M. 2012 The response of a flat plate boundary layer to an orthogonally arranged dielectric barrier discharge actuator. *Journal of Physics D: Applied Physics* **45**.

Glauert, M. B. 1956 The wall jet. *Journal of Fluid Mechanics* **1**, 625–643.

Greenblatt, D., Sch ule, C. Y., Romann, D. & Paschereit, C. O. 2008 Dielectric barrier discharge flow control at very low flight reynolds numbers. *AIAA Journal* **46** (6), 1528–1541.

Grinstein, F. F., Margolin, L. G. & Rider, W. J. 2007 *Implicit Large Eddy Simulation*, chap. A Rationale for Implicit LES, pp. 39–58. New York - Cambridge.

Grundmann, S. & Tropea, C. 2008*a* Active cancellation of artificially induced tollmien-schlichting waves using plasma actuators. *Experiments in Fluids* **44**, 795–806.

Grundmann, S. & Tropea, C. 2008*b* Delay of boundary-layer transition using plasma actuators. In *AIAA-2008-1369, 46th AIAA Aerospace Sciences Meeting*.

Grundmann, S. & Tropea, C. 2009 Experimental damping of boundary-layer oscillations using dbd plasma actuators. *International Journal of Heat and Fluid Flow* **30**, 394–402.

Gustavsson, L. H. 1979 Initial value problem for boundary layer flows. *Physics of Fluids* **22**, 1602–1605.

Hamel, G. 1917 Spiralf ormige bewegung z aher flu ussigkeiten. *Jahresber. Deutsch. Math. Ver.* **25**, 34–60.

Hanson, R. E., Lavoie, P., Naguib, A. M. & Morrison, J. F. 2010*a* Control of transient growth induced boundary layer control using plasma actuators. In *Seventh IUTAM Symposium on Laminar-Turbulent Transition*.

Hanson, R. E., Lavoie, P., Naguib, A. M. & Morrison, J. F. 2010*b* Transient growth instability cancelation by a plasma actuator array. *Experiments in Fluids* **49** (6), 1339–1348.

HARTREE, D. R. 1937 On an equation occurring in falker and skan's approximate treatment of the equations of a boundary layer. *Proceedings of the Cambridge Philosophical Society* **33**, 223–239.

HERBERT, T. 1988 Secondary instability of boundary layers. *Annual Review of Fluid Mechanics* **20**, 487–526.

HERBERT, T. & BERTOLOTTI, F. P. 1987 Stability analysis of of nonparallel boundary layers. In *Bulletin of the American Physical Society*.

HŒPFFNER, J., BRANDT, L. & HENNINGSON, D. S. 2005 Transient growth on boundary layer streaks. *Journal of Fluid Mechanics* **537** (1), 91–100.

HOWARD, L. 1961 Note of a paper of john w. miles. *Journal of Fluid Mechanics* **10**, 509–512.

IM, S., DO, H. & CAPPELLI, M. A. 2010 Dielectric barrier discharge control of a turbulent boundary layer in a supersonic flow. *Applied Physics Letters* **97**.

VAN INGEN, J. L 1956 A suggested semi-emperical method for the calcuation of the boundary layer transition region. *Tech. Rep.*. Institute of Technology, Department of Aeronautics and Engineering. Report VTh-74, Delft.

JAFFE, N. A., OKAMURA, T. T. & SMITH, A. M. O. 1970 Determination of spatial amplification factors and their application to predicting transition. *AIAA Journal* **8** (2), 301–308.

JEFFERY, G. B. 1915 The two-dimensional steady motion of a viscous fluid. *Philosophy Magazine* **29**, 455–465.

JUKES, T. N. & CHOI, K.-S. 2009 Flow control around a circular cylinder using pulsed dielectric barrier discharge surface plasma. *Physics of Fluids* **21**.

KOTSONIS, M., GHAEMI, S., VELDHUIS, L. & SCARANO, F. 2011 Measurement of the body force field of plasma actuators. *Journal of Physics D: Applied Physics* **44**.

KRIEGSEIS, J., BARCKMANN, K., FREY, J., TROPEA, C. & GRUNDMANN, S. 2013*a* Simultaneous investigation of pressure effects and airflow influence on dbd plasma actuators. In *AIAA-2013-0756, 51st AIAA Aerospace Sciences Meeting, Grapevine, TX*.

KRIEGSEIS, J., DUCHMANN, A., TROPEA, C. & GRUNDMANN, S. 2013*b* On the classification of dielectric barrier discharge plasma actuators: A comprehensive performance evaluation study. *Journal of Applied Physics* **114** (5).

KRIEGSEIS, J., SCHWARZ, C., TROPEA, C. & GRUNDMANN, S. 2013*c* Velocity-information-based force-term estimation of dielectric-barrier discharge plasma actuators. *Journal of Physics D: Applied Physics* **46** (5).

LANDAHL, M. T. 1980 A note on an algebraic instability of invisic parallel shear flows. *Journal of Fluid Mechanics* **98** (2), 243–251.

LELE, S. K. 1992 Compact finite difference schemes with spectral-like resolution. *Journal of Computational Physics* **103** (1), 16–42.

LESIEUR, M., METAIS, O. & COMTE, P. 2005 *Large-Eddy Simulations of Turbulence*, chap. Introduction to LES, pp. 1–20. New York - Cambridge.

LUCHINI, P. 2000 Reynolds-number-independent instability of the boundary layer over a flat surface: optimal perturbations. *Journal of Fluid Mechanics* **404**, 289–309.

MADEN, I., KREIGSEI, J., MADUTA, R., JAKILRIĆ, S., GRUNDMANN, S. & TROPEA, C. 2012 Derivation of a plasma-actuator model utilizing quiescent-air piv data. *20th Annual Conference of the CFD Community of Canada, Canmore, May9-12* .

MELE, P., MORGANTI, M., SCIBILIA, M. F. & LASEK, A. 1985 Behavior of wall jet in laminar-to-turbulent transition. *AIAA Journal* **24** (6), 938–939.

MERLE, X., ALIZARD, F. & ROBINET, J.-C. 2010 Finite difference methods for viscous incompressible global stability analysis. *Computers & Fluids* **39** (6), 911–925.

MONKEWITZ, P. A., CHAUHAN, K. A. & NAGIB, H. M. 2007 Self-consistent high-reynolds-number asymptotics for zero-pressure-gradient turbulent boundary layers. *Physics of Fluids* **19**.

MOREAU, E. 2007 Airflow control by non-thermal plasma actuators. *Journal of Physics D: Applied Physics* **40**, 605–636.

MORGAN, P. & VISBAL, M. 2013 Numerical simulations exploring dielectric barrier discharge-induced steady and pulsed suction. In *AIAA-2013-2744, 43rd Fluid Dynamics Conference, San Diego, CA*.

MORKOVIN, M. V. 1969 *Viscous Drag Reduction*, chap. On the many faces of transition, pp. 1–31. New York - Plenum.

MORKOVIN, M. V., RESHOTKO, E. & HERBERT, TH. 1994 Transitions in open flow systems - a reassessment. In *Bulletin of the American Physical Society*.

NAGIB, H. M. & CHAUHAN, K. A. 2008 Variations of von karman coefficient in canonical flows. *Physics of Fluids* **20** (10).

NATARAJAN, R. & ACRIVOS, A. 1993 The instability of the steady flow past spheres and disks. *Journal of Fluid Mechanics* **254** (1), 323–344.

OPAITS, D., ZAIDI, S., SHNEIDER, M., LIKHANSKII, A., EDWARDS, M. & MACHERET, S. 2010 Surface plasma induced wall jets. *AIAA Paper 2010-0469* .

ORR, W. M. F. 1907 The stability of instability of the steady motions of a perfect liquid and of a viscous liquid. part ii: A viscous liquid. *Proceedings of the Royal Irish Academy. Section A: Mathematical and Physical Sciences* **27**, 69–138.

ORSZAG, S. A. 1971 Accurate solution to the orr-sommerfeld stability equation. *Journal of Fluid Mechanics* **50**, 689–703.

PATANKAR, S. V. 1980 *Numerical Heat Transfer and Fluid Flow*. Hemisphere Publishing Corporation.

POISEUILLE, J. L. M. 1840 Recherches expéimentelles sur le mouvement des liquids dans les tubes de trés petits diaméters. *Comptes Rendus* **11**, 961–967, 1041–1048.

POST, M. L & CORKE, T. C. 2004 Separation control on high angle of attach airfoil using plasma actuators. *AIAA Journal* **42** (11), 2177–2184.

RAYLEIGH, L. 1880 The stability, or instability, of certain fluid motions. *Proceedings of the Mathematical Society of London* pp. 57–70.

RAYLEIGH, L. 1887 The stability, or instability, of certain fluid motions, ii. *Proceedings of the Mathematical Society of London* pp. 67–74.

RESHOTKO, ELI 2001 Transient growth: A factor in bypass transition. *Physics of Fluids* **13** (5), 1067–1075.

REYNOLDS, O. 1883 An experimental investigation of the circumstances which determine whether the motion of water shall be direct or sinuous and of the resistance in parallel channels. *Philosophical Transactions of the Royal Society of London* **174**, 935–982.

RIHERD, M. & ROY, S. 2012*a* A comparison of linear and serpentine geometry plasma actuation for controlling a transitionally separated airfoil flow. *Third Annual FCAAP Symposium and Exhibition, Tallahassee, FL* .

RIHERD, M. & ROY, S. 2012*b* Measurements and simulations of a channel flow powered by plasma actuators. *Journal of Applied Physics* **112** (5).

RIHERD, M. & ROY, S. 2013*a* Damping of tollmien-schlichting waves in a boundary layer using plasma actuators. *Journal of Physics D: Applied Physics* **46** (48).

RIHERD, M. & ROY, S. 2013*b* Local and bi-global stability analysis of a plasma actuated boundary layer. In *AIAA-2012-0803, 51st AIAA Aerospace Sciences Meeting, Grapevine, TX*.

RIHERD, M. & ROY, S. 2013*c* Serpentine geometry plasma actuators for flow control. *Journal of Applied Physics* **114** (8), 1–13.

RIHERD, M. & ROY, S. 2013*d* Stabilization of boundary layer streaks by plasma actuators. *Journal of Physics D: Applied Physics (submitted* .

RIHERD, M., ROY, S. & BALACHANDAR, S. 2012 Linear stability analysis of a boundary layer with plasma actuators. In *AIAA-2011-0290, 50th AIAA Aerospace Sciences Meeting, Nashville, TN.*.

RIHERD, M., ROY, S. & BALACHANDAR, S. 2013 Local stability effects of plasma actuator on a zero pressure gradient boundary layer. *Theoretical and Computational Fluid Mechanics* .

RIZZETTA, D. P. & VISBAL, M. R. 2007 Numerical investigation of plasma-based flow control for transitional highly loaded low-pressure turbine. *AIAA Journal* **45** (10), 2554–2564.

RIZZETTA, D. P. & VISBAL, M. R. 2009 Large eddy simulation of plasma-based control strategies for bluff body flow. *AIAA Journal* **47** (3), 717–728.

RIZZETTA, D. P. & VISBAL, M. R. 2010 Large-eddy simulation of plasma-based turbulent boundary-layer separation control. *AIAA Journal* **48** (12), 2793–2810.

RIZZETTA, D. P. & VISBAL, M. R. 2011 Numerical investigation of plasma-based control for low-reynolds-number airfoil flows. *AIAA Journal* **49** (2), 411–425.

RIZZETTA, D. P., VISBAL, M. R. & MORGAN, P. E. 2008 A high-order compact finite-difference scheme for large-eddy simulations of active flow control. *Progress in Aerospace Sciences* **44**, 397–426.

ROSS, J. A., BARNES, F. H., BURNS, J. G. & ROSS, M. A. S. 1970 The flat plate boundary layer. part 3. comparison of theory with experiment. *Journal of Fluid Mechanics* **43** (4), 819.

ROTH, J. R., SHERMAN, D. M. & WILKINSON, S. P. 1998 Boundary layer flow control with a one atmosphere uniform glow discharge surface plasma. *AIAA Paper AIAA-1998-328, 36th AIAA Aerospace Sciences Meeting and Exhibit, Reno, NV* .

ROTH, J. R., SHERMAN, D. M. & WILKINSON, S. P. 2000 Electrohydrodynamic flow control with a glow-discharge surface plasma. *AIAA journal* **38** (7), 1166–1172.

ROY, S. 2005 Flow actuation using radio frequency in partially-ionized collisional plasmas. *Applied Physics Letters* **86** (10), 1–3.

ROY, S. & WANG, C. C. 2009 Bulk flow modification with horseshoe and serpentine plasma actuators. *Journal of Physics D: Applied Physics* **42**.

SALWEN, H. & GROSCH, C. E. 1981 The continuous spectrum of the orr–sommerfeld equation. part 2. eigenfunction expansions. *Journal of Fluid Mechanics* **104**, 445–465.

SANTHANAKRISHNAN, A. & JACOB, J. D. 2007 Flow control with plasma synthetic jet actuators. *Journal of Physics D: Applied Physics* **40** (3), 637.

SAYADI, T., HAMMAN, C. W. & MOIN, P. 2011 Direct numerical simulation of h-type and k-type transition to turbulence. *Center for Turbulence Research Annual Research Briefs* .

SCHATZMAN, D. M. & THOMAS, F. O. 2008 Turbulent boundary layer separation control with plasma actuators. *AIAA Paper 2008-4199* .

SCHLICHTING, H. 1933 Zur entstehung der turbulenz bei der plattenströmung. *Z. Angew. Math. Mech.* **13**, 171–174.

SCHMID, P. J. & HENNINGSON, D. S. 2000 *Stability and Transition in Shear Flows*. Springer.

SCHUBAUER, G. B. & SKRAMSTAD, H. K. 1947 Laminar boundary-layer oscillations and transition on a flat plate. *Z. Angew. Math. Mech.* **38**, 251–292.

SCHUELE, CHAN-YONG 2011 Control of stationary cross-flow modes in a mach 3.5 boundary layer using patterned passive and active roughness. *PhD Dissertation* .

SÉRAUDIE, A., VERMEERSCH, O. & ARNAL, D. 2011 Dbd plasma actuators efect on a 2d model laminar boundary layer. transition delay under ionic wind effect. In *AIAA-2011-3515, 29th AIAA Applied Aerodynamics Conference*.

SHARMA, A. S., ABDESSEMED, N., SHERWIN, S. J. & THEOFILIS, V. 2011 Transient growth mechanisms of low reynolds number flow over a low-pressure turbine blade. *Theoretical and Computational Fluid Dynamics* **25** (1), 19–30.

SHYY, W., JAYARAMAN, B. & ANDERSSON, A. 2002 Modeling of glow discharge-induced fluid dynamics. *Journal of Applied Physics* **92**, 6434–6443.

SINGH, K. P. & ROY, S. 2008 Force approximation for a plasma actuator operating in atmospheric air. *Journal of Applied Physics* **103**.

SIPP, D. & MARQUET, O. 2012 Characterization of noise amplifiers with global singular modes: the case of the leading-edge flat-plate boundary layer. *Theoretical and Computational Fluid Dynamics* pp. 1–19.

SONI, J. & ROY, S. 2013 Low pressure characterization of dielectric barrier discharge actuators. *Applied Physics Letters* **102** (11).

SPALDING, D. B. 1961 A single formula for the law of the wall. *Journal of Applied Mechanics* **28**, 455–457.

SQUIRE, H. B. 1933 On the stability of three-dimensional disturbances of viscous fluid between parallel walls. *Proceedings of the Royal Society of London A* **142**, 621–638.

SUNG, Y., KIIM, W., MUNGAL, M. G. & CAPPELLI, M. A. 2006 Aerodynamic modification of flow over bluff objects by plasma actuation. *Experiments in Fluids* **41**, 479–486.

SUZEN, Y. B., HUANG, P. G., JACOB, J. D. & ASHPIS, D. E. 2005 Numerical simulations of plasma based flow control applications. In *AIAA-2005-4633, 35th Fluid Dynamics Conference and Exhibit, Toronto, Ontario*.

TATSUMI, T. & YOSHINMURA, T. 1990 Stability of the laminar flow in a rectangular duct. *Journal of Fluid Mechanics* **212**.

THEOFILIS, V. 2003 Advances in global linear instability analysis of nonparallel and three-dimensional flows. *Progress in Aerospace Sciences* **39** (4), 249–315.

THEOFILIS, V. 2011 Global linear instability. *Annual Review of Fluid Mechanics* **43**, 319–352.

THEOFILIS, V., DUCK, P. W. & OWEN, J. 2004 Viscous linear stability analysis of rectangular duct and cavity flows. *Journal of Fluid Mechanics* **505**, 249–286.

THEOFILIS, V. & RODRIGUEZ, D. 2009 Massively parallel solution of the biglobal eigenvalue problem using dense linear algebra. *AIAA Journal* **47** (10), 2449–2459.

THOMAS, F. O., CORKE, T. C., IQBAL, M., KOZLOV, A. & SCHATZMAN, D. 2009 Optimization of dielectric barrier discharge plasma actuators for active aerodynamic flow control. *AIAA Journal* **47** (9), 2169–2178.

THOMSON, W. 1887 Stability of fluid motion - rectilinear motions of viscous fluid between two parallel plates. *Philosophy Magazine* **24** (147), 188–196.

TOLLMIEN, W. 1929 über die entstehund der turbulenz. *Nachr. Ges. Wiss. Göttingen, Math.-Phys. Kl.* pp. 21–44.

TREFETHEN, L. N. & BAU, D. 1997 *Numerical linear algebra*. Society for Industrial Mathematics.

TREFETHEN, L. N., TREFETHEN, A. E., REDDY, S. C. & DRISCOLL, T. A. 1993 Hydrodynamics stability without eigenvalues. *Science* **261**, 578–584.

TUMIN, A. & RESHOTKO, E. 2001 Spatial theory of optimal disturbances in boundary layers. *Physics of Fluids* **13** (7), 2097–2104.

VALERIOTI, J. A. & CORKE, T. C. 2012 Pressure dependence of dielectric barrier discharge plasma flow actuators. *AIAA Journal* **50** (7), 1490–1502.

VISBAL, M., GAITONDE, D. & GOGINENI, S. 1998 Direct numerical simulation of a forced transitional plane wall jet. In *AIAA-1998-2643, 36th AIAA Aerospace Sciences Meeting and Exhibit, Reno, NV*.

VISBAL, M., GAITONDE, D. & ROY, S. 2006 Control of transitional and turbulent flows using plasma-based actuators. In *AIAA-2006-3230, AIAA Fluid Dynamics and Flow Control Conference, San Francisco, CA*.

VISBAL, M. R. 2010 Strategies for control of transitional and turbulent flows using plasma-based actuators. *International Journal of Computational Fluid Dynamics* **24** (7), 237–258.

VISBAL, M. R. & GAITONDE, D. V. 1999 High-order-accurate methods for complex unsteady flows. *AIAA Journal* **37** (10), 1231–1239.

WACHTOR, A. J., GRINSTEIN, F. F., DEVORE, C. R., RISTORCELLI, J. R. & MARGOLIN, L. G. 2013 Implicit large-eddy simulation of passive scalar mixing in statistically stationary isotropic turbule nce. *Physics of Fluids* **25** (2).

WALLACE, J. M., ECKELMANN, H. & BRODKEY, R. S. 1972 The wall region in turbulent shear flow. *Journal of Fluid Mechanics* **54**, 39–48.

WANG, C. C., DURSCHER, R. & ROY, S. 2011 Three-dimensional effects of curved plasma actuators in quiescent air. *Journal of Applied Physics* **109**.

WANG, CHIN-CHENG & ROY, SUBRATA 2011 Combustion stabilization using serpentine plasma actuators. *Applied Physics Letters* **99** (4), 041502.

WANG, J.-J., CHOI, K.-S., FENG, L.-H., JUKES, T. N. & WHALLEY, R. D. 2013 Recent developments in dbd plasma flow control. *Progress in Aerospace Sciences* .

WAZZAN, A. R., GAZLEY, C. & SMITH, A. M. O 1979 Tollmien-schlichting waves and transition: heated and adiabatic wedge flows with applications to bodies of revolution. *Progress in Aerospace Sciences* **18**, 351–392.

WAZZAN, A. R., OKAMURA, T. T. & SMITH, A. M. O. 1968 Spatial and temporal stability charts for the falkner–skan boundary-layer profiles. *Tech. Rep.*. DTIC Document.

WHITE, E. B. 2002 Transient growth of stationary disturbances in a flat plate boundary layer. *Physics of Fluids* **14**, 4429.

WHITE, F. 2006 *Viscous Fluid Flow*. McGraw-Hill.

WU, X. 2010 Establishing the generality of three phenomena using a boundary layer with free-stream passing wakes. *Journal of Fluid Mechanics* **664**, 193–219.

WU, X. & MOIN, P. 2009 Direct numerical simulations of turbulence in a nominally zero-pressure-gradient flat-plate boundary layer. *Journal of Fluid Mechanics* **630**, 5–41.

ZHOU, J., ADRIAN, R., BALACHANDAR, S. & KENDALL, T. M. 1999 Mechanisms for generating coherent packets of hairpin vortices in channel flow. *Journal of Fluid Mechanics* **387**, 353–396.

ZITO, J., DURSCHER, R., SONI, J., ROY, S. & ARNOLD, D. 2012 Flow and force inducement using micro size dielectric barrier discharge actuators. *Applied Physics Letters* **100**.

BIOGRAPHICAL SKETCH

Mark Riherd is a native of Lake Butler, Florida. He performed his undergraduate work at Duke University in Durham, NC, receiving a Bachelor of Science in mechanical engineering and a minor in mathematics, graduating in May 2009. He worked for several summers during graduate school with the Air Vehicles Directorate of the Air Force Research Laboratory at Wright-Patterson Air Force Base outside of Dayton, Ohio and one summer at NASA's Flow Physics and Control Branch at the Langley Research Center in Hampton, Virginia.